SÃO PAULO STATE UNIVERSITY "JÚLIO DE MESQUITA FILHO"
SCHOOL OF ENGINEERING
CAMPUS OF ILHA SOLTEIRA

Iago Lessa de Oliveira

Using foam-extend to assess the influence of fluid-structure interaction on the rupture of intracranial aneurysms

Ilha Solteira, Brazil
2017

UNIVERSIDADE ESTADUAL PAULISTA
"JÚLIO DE MESQUITA FILHO"
CÂMPUS DE ILHA SOLTEIRA

MECHANICAL ENGINEERING GRADUATE PROGRAM OF
ILHA SOLTEIRA

Iago Lessa de Oliveira

Using foam-extend to assess the influence of fluid-structure interaction on the rupture of intracranial aneurysms

Dissertation submitted for the Master Degree of the School of Engineering of Ilha Solteira - UNESP
Mechanical Engineering Department, field of Fluid Mechanics and Thermal Sciences.

Prof. Dr. José Luiz Gasche
Supervisor

Prof. Dr. Julio Militzer
Co-supervisor

Ilha Solteira, Brazil
2017

FICHA CATALOGRÁFICA
Desenvolvido pelo Serviço Técnico de Biblioteca e Documentação

O482u

Oliveira, Iago Lessa de.
Using foam-extend to assess the influence of fluid-structure interaction on the rupture of intracranial aneurysms / Iago Lessa de Oliveira. -- Ilha Solteira: [s.n.], 2017
154 f. : il.

Dissertação (mestrado) - Universidade Estadual Paulista. Faculdade de Engenharia de Ilha Solteira. Área de conhecimento: Ciências Térmicas, 2017

Orientador: José Luiz Gasche
Co-orientador: Julio Militzer
Inclui bibliografia

1. Aneurismas intracranianos. 2. Simulação numérica. 3. Interação fluido-estrutura.

UNIVERSIDADE ESTADUAL PAULISTA

Câmpus de Ilha Solteira

CERTIFICADO DE APROVAÇÃO

TÍTULO DA DISSERTAÇÃO: **Using foam-extend to assess the influence of fluid-structure interaction on the rupture of intracranial aneurysms**

AUTOR: IAGO LESSA DE OLIVEIRA
ORIENTADOR: JOSE LUIZ GASCHE
COORIENTADOR: JULIO MILITZER

Aprovado como parte das exigências para obtenção do Título de Mestre em ENGENHARIA MECÂNICA, área: CIÊNCIAS TÉRMICAS pela Comissão Examinadora:

Prof. Dr. JOSE LUIZ GASCHE
Departamento de Engenharia Mecânica / Faculdade de Engenharia de Ilha Solteira

Prof. Dr. EMANUEL ROCHA WOISKI
Departamento de Engenharia Mecânica / Faculdade de Engenharia de Ilha Solteira

Dr. BIRAJARA SOARES MACHADO
Instituto do Cérebro / Hospital Israelita Albert Einstein

Ilha Solteira, 24 de agosto de 2017

Dedico este trabalho à minha mãe, Selma

ACKNOWLEDGEMENTS

I would like to express my sincere gratitude to my supervisors Dr. José Luiz Gasche, from FEIS/UNESP, Ilha Solteira, Brazil, and Dr. Julio Militzer, from Dalhousie University, Halifax, Nova Scotia, Canada, for all their help, support and guidance during the execution of this work.

To Dr. Carlos Eduardo Baccin from the Hospital Israelita Albert Einstein, São Paulo, Brazil, for providing the images of the aneurysms and for all the support, advices and questions during the execution of this work and, specially, regarding the medical aspects of this research.

To my family and, specially, to my mother, Selma, who provided constant support and motivation since I started to study in the university.

I am also indebted to my friends and colleagues of the Thermal and Fluid Sciences block of the Mechanical Engineering Department.

This work was conducted with a scholarship financed by CAPES – Brazilian Federal Agency for Support and Evaluation of Graduate Education within the Ministry of Education of Brazil – which is gratefully acknowledged.

I would also like to thank the financial support during my exchange period at Dalhousie University, Halifax, Nova Scotia, Canada, provided by the ELAP program – Emerging Leaders in the Americas Program – with support of the Government of Canada.

This research was partly supported by resources supplied by the Center for Scientific Computing (NCC/GridUNESP) of the São Paulo State University (UNESP) and ACENET (Dalhousie University) which are gratefully acknowledged.

Finally, I would like to thank the open-source software and CFD users communities, which have always been willing to help.

ABSTRACT

Aneurysms are abnormalities formed in some regions of the human vascular system and are characterized by dilated and thin regions of the arterial wall. One of the most common types occurs inside the brain arteries in the so-called circle of Willis. These intracranial aneurysms are extremely dangerous, because in case of rupture they can cause sub-arachnoid hemorrhage, with consequent death or presence of permanent damage to the patient. Causes of aneurysms have been investigated for a long time, and researchers agree that hemodynamic effects play a key role in the formation, growth, and rupture of brain aneurysms. However, the experimental procedures to better understand the characteristics of blood flow within the aneurysm are still difficult to perform. With the development of scanning techniques of the cerebral vascular system, it has been possible to obtain the geometry of aneurysms and then with that numerical methods for the solution of blood flow have begun to be used. Since then, several researchers have been investigating the influence of biological and hemodynamic variables on aneurysms rupture. However, it has been only in the last decade that the influence of fluid-structure interaction, due to the flexibility of the artery wall, on those variables has been investigated. In this context and using patient-specific aneurysm geometries, we simulated the blood flow using the open-source library foam-extend, which uses a partitioned methodology to numerically solve the fluid-structure interaction problem. By comparing the parameters that can lead to rupture – wall shear stress and oscillatory shear index – between the results of the simulations considering the rigid and flexible walls hypotheses, we evaluated the influence of wall flexibility on such parameters, concluding that the flexibility influences the parameters that can lead to rupture, changing the decision of treatment if made using those parameters.

Keywords: Intracranial aneurysms. Numerical simulation. Fluid-structure interaction.

RESUMO

Aneurismas são anormalidades formadas em algumas partes do sistema vascular humano e se caracterizam por regiões dilatadas e finas da parede arterial. Um dos tipos mais comuns ocorre no interior das artérias que chegam ao cérebro, no chamado círculo de Willis. Estes casos de aneurismas intracranianos são extremamente perigosos, pois em caso de rompimento podem ocasionar hemorragia cerebral, com consequente morte ou presença de sequelas permanentes no paciente. As causas dos aneurismas vêm sendo investigadas há tempos, e os pesquisadores concordam que os fenômenos hemodinâmicos têm papel fundamental na formação, crescimento e ruptura do aneurisma cerebral. Entretanto, os procedimentos experimentais para se conhecer melhor as características do escoamento de sangue no interior do aneurisma ainda são de difícil realização. A partir do desenvolvimento de técnicas de mapeamento do sistema vascular cerebral, pôde-se obter a geometria de aneurismas de modo que métodos numéricos na solução de problemas de escoamento passaram a ser utilizados. A partir de então, diversas pesquisas vêm sendo feitas visando a investigação da influência das variáveis biológicas e hemodinâmicas na ruptura do aneurisma. Entretanto, apenas recentemente foi dado foco na influência da interação fluido-estrutura que existe neste problema, devido a flexibilidade da parede da artéria. Assim, usando geometrias de aneurismas específicos de pacientes, simulamos o escoamento sanguíneo utilizando o pacote *open-source foam-extend*, que possui uma metodologia particionada implementada para resolver numericamente o problema de interação fluido-estrutura. Através de comparação dos parâmetros que podem levar a ruptura – tensão de cisalhamento na parede e índice de oscilação do cisalhamento – entre os resultados das simulações considerando as hipóteses de parede rígida e flexível, avaliamos a influência da flexibilidade da parede em tais parâmetros, concluindo que tal flexibilidade tem influência nos parâmetros que podem levar à ruptura do aneurisma a ponto de alterar a decisão de tratamento, caso ela fosse feita baseada em tais parâmetros.

Palavras-chave: Aneurismas intracranianos. Simulação numérica. Interação fluido-estrutura.

RÉSUMÉ

Les anévrismes sont des anomalies formées sur certaines régions du système vasculaire humain et sont caractérisés par des régions dilatées de la paroi artérielle, avec une petite épaisseur. L'un des types les plus communs se produit à l'intérieur des artères de la base du cerveau, dans le cercle de Willis. Ces cas d'anévrismes intracrâniens sont extrêmement dangereux car ils peuvent provoquer une hémorragie sous-arachnoïdienne en cas de rupture, avec la mort ou la présence d'un dommage définitif pour le patient. Les causes d'anévrismes sont étudiées depuis longtemps et des recherches reconnaissent que les effets hémodynamiques jouent un rôle clé dans la formation, la croissance, et la rupture des anévrismes intracrâniens. Cependant, les procédures expérimentales pour mieux comprendre les caractéristiques de l'écoulement du sang dans l'anévrisme sont encore difficiles à réaliser. Avec le développement de techniques des images du système vasculaire cérébral, il a été possible d'obtenir la géométrie des anévrismes, donc des méthodes numériques ont commencé à être utilisées pour la solution de l'écoulement dans les anévrismes, et alors plusieurs recherches ont étudié l'influence des variables biologiques et hémodynamiques sur la rupture de l'anévrisme. Cependant, ce n'est que dans la dernière décennie que l'influence de l'interaction fluide-structure, due à la flexibilité de la paroi de l'artère, sur ces variables a été étudiée. Dans ce contexte et à l'aide de géométries d'anévrismes spécifiques des patients, des simulations numériques ont été effectuées avec le logiciel *open-source* foam-extend, qui utilise une méthodologie partitionnée pour résoudre numériquement le problème d'interaction fluide-structure. En comparant les paramètres qui peuvent conduire à la rupture – tels que le cisaillement sur la paroi et l'indice d'oscillation du cisaillement – entre les résultats des simulations avec l'hypothèse de la paroi rigide et élastique, nous avons évalué l'influence de la flexibilité de la paroi de l'anévrisme sur ces paramètres, en concluant que cette flexibilité change les valeurs de ces paramètres, donc l'option de traitement peut changer si le médecin les utilise pour décider de traiter le patient.

Mots clés: Anévrismes intracrâniens. Simulation numérique. Interaction fluide-structure.

LIST OF FIGURES

1 Base of the brain: arteries tree composing the circle of Willis – internal carotid arteries (ICA) with the vertebro-basilar system, composed of the vertebral arteries (VA) and basilar artery (BA), and both their branches: middle cerebral arteries (MCA); anterior cerebral arteries (ACA) and the anterior communicating artery (ACoA). 24

2 Aneurysm dome, its parent artery and aspect ratio, A_r, definition: aneurysm dome height, h_d, divided by d_n, the neck diameter; the parent artery has diameter d_a. 25

3 Two images of the digital subtraction angiography and two reconstructed surfaces of aneurysms (indicated with arrows), respectively, (a) at the Internal Carotid Artery (ICA) bifurcation with height 5.7 mm; (b) at the Middle Cerebral Artery (MCA) bifurcation with height 3.8 mm; (c) at the MCA bifurcation with height 7.9 mm and (d) at the MCA bifurcation with height $\approx$ 18 mm. 26

4 Probability of Subarachnoid Hemorrhage (SAH) over time for a group of 1,077 patients followed up over 4.1 years who did not have previous cases of SAH, for different aneurysm sizes. 27

5 Arteries that reach the brain with some of the most common sites of aneurysm formation indicated with a blue circle. 28

6 Solid, Ω^{s}, and fluid domains, Ω^{f}, fluid-solid interface Γ^{fs} and boundaries of each region with its respective physical boundary condition. 35

7 Schematic two-dimensional representation of the coordinate systems used to describe a fluid flowing through a moving control volume $V = V(t)$: $\boldsymbol{x}$ is the fixed or spatial coordinate system, $\boldsymbol{\xi}$ is the fluid particle and $\boldsymbol{\chi}$ is the referential coordinate system, fixed to the moving control volume. 37

8 Experimental normalized flow rate for the internal carotid – normalization with respect to the temporal mean blood flow rate of each measured profile. 40

9 Mean blood flow rate through the arteries of the brain as a percentage of the total blood flow rate entering the brain: (11.95 ± 2.05) ml/s, with each respective standard deviation. 40

10 Average strain-stress curves constructed from traction tests of rectangular strips of an intracranial aneurysm wall tissue for different stages of the aneurysm: unruptured (stiff) and pre-ruptured (intermediate) or ruptured (soft). 42
11 Different measurements of stress and strain for the uniaxial case. 44
12 Schematic 2D representation of an aneurysm and arteries meshes for (a) the fluid domain and (b) the solid meshes in the partitioned context, showing each Fluid-Structure Interaction (FSI) interface and the boundary conditions applied to each domain. 49
13 Volume rendering representation of the image of a Digital Subtraction Angiography (DSA) of aneurysm case 13 – located at the ICA bifurcation – and the brain vessels (screen-shot taken using the visualization library ParaView®). 50
14 Volume rendering representation of the VOI: the *volume of interest* is extracted from the DSA image (at the upper left corner, in yellow) and includes the aneurysm and its surrounding vessels (screen-shot taken using the visualization library ParaView®). 51
15 Aneurysm and arteries surface extracted with VMTK®: (a) complete extracted surface and portion clipped with the utility `vmtksurfaceclipping` in red; (b) the final triangulated surface used subsequently for meshing (corresponds to the red portion of the surface on the item (a)). 51
16 Aneurysm geometries used: (a) case 13, an aneurysm occurring on the ICA bifurcation and (b) case17, an aneurysm occurring on the Anterior Communicating Artery (ACoA). 52
17 Fluid and solid meshes of case 13, in blue and red, respectively, with layers of refined prismatic elements adjacent to the FSI interface. 53
18 Structure of foam-extend, providing solvers and utilities for the general steps of a numerical simulation. 55
19 (a) Polygonal control volume with centroid C of a 2D finite volume mesh, and its neighbours F_i; (b) Polyhedral control volume V_C with its geometric parameters used on the finite volume discretization. 56

20 Schematic two-dimensional representation of the fluid and solid meshes of an aneurysm geometry showing each FSI interface and the interpolated variable between the solid and fluid mesh interfaces. 66
21 Interactions of FSI coupling approaches of the partitioned methodology: (a) weak FSI coupling, where the solution of the solid problem is passed directly to the next time-step and (b) strong FSI coupling where a k number of iterations are performed over the governing equations within one time-step to verify if the FSI interface displacement is correct; n and n + 1 represents two consecutive time-steps. 67
22 Representation of the fluid and solid "black-box" solvers showing their input and output variables. 69
23 Flowchart of the algorithm to solve the FSI problem in a partitioned manner using the Interface Quasi-Newton-Implicit Jacobian Least-Squares (IQN-ILS) method, showing the operators $\boldsymbol{\mathcal{F}}$ and $\boldsymbol{\mathcal{S}}$; $nIter$ is the current number of PISO iterations and $nCorr$ is its maximum number; the left arrow means attribution. 75
24 Fluid and solid meshes of case 13 decomposed in four partitions (fluid mesh partitions are darker whereas solid mesh partitions are slightly translucent and with black edges), each partition is attributed to one processor of a computational node; the decomposition is performed in such a way that the FSI interface, Γ^{fs} is distributed over all processors. 77
25 Theoretical and measured speedup, s, as function of the number of processing units, N for the simulations of the geometry of cases 13 and 17. 78
26 Wall Shear Stress (WSS) magnitude distribution on the surface of the aneurysm of case 13 for fluid meshes with (a) $\sim$ 300,000, (b) $\sim$ 600,000 and (c) $\sim$ 1,000,000. 81
27 Area-averaged WSS as a function of time for the whole surface for case 13 fluid mesh, with total number of control volumes $\sim$ 300,000, $\sim$ 600,000 and $\sim$ 1,000,000 to test mesh independence of the averaged WSS. 82
28 WSS magnitude distribution on the surface of the aneurysm of case 17 for fluid meshes with (a) $\sim$ 200,000, (b) $\sim$ 500,000 (c) $\sim$ 800,000 and (d) $\sim$ 1,200,000. 82

29 Area-averaged WSS as a function of time for the whole surface for case 17 fluid mesh, with total number of control volumes $\sim$ 200,000, $\sim$ 500,000, $\sim$ 800,000 and $\sim$ 1,200,000 to test mesh independence of the averaged WSS. . 83
30 Comparison of WSS on the surface of case 13 with (a) rigid wall and (b) linear elastic wall models at peak systole (the white arrow at the top left corner indicates the direction of the view). 85
31 Volume rendering representation of the velocity field of the aneurysm of case 13 for (a) rigid wall assumption and (b) elastic linear wall model at peak systole; arrow A indicates the region of flow impingement, for this case occurring at the aneurysm neck. 85
32 Comparison of WSS on the surface of case 17 for (a) rigid wall and (b) linear elastic wall models at peak systole (the white arrow at the top left corner indicate the direction of the view). 86
33 Volume rendering representation of the velocity field of the aneurysm of case 17 for (a) rigid wall assumption and (b) elastic linear wall model at peak systole. 86
34 Oscillatory Shear Index (OSI) field of (a) the aneurysm of case 13 with rigid wall assumption and (b) with elastic linear wall model; (c) of the aneurysm of case 17 with rigid wall model and (d) with elastic linear wall model at peak systole with indication of where occurs the highest values of OSI. . . 87
35 Wall Cauchy stress – or true stress – on the aneurysms of (a) case 13 and (b) case17. 88
36 Average strain-stress curves constructed from mechanical tests to failure of rectangular strips of an intracranial aneurysm wall tissue for different stages of the aneurysm: unruptured (stiff) and pre-ruptured or ruptured (soft). 88
37 Comparison of WSS on the surface of case 13 for (a) linear elastic wall and (b) non-linear elastic wall models at peak systole (the white arrow at the top left corner indicate the direction of the view). 90
38 Wall Cauchy stress – or true stress – on the aneurysms of case 13 for (a) linear elastic model and (b) non-linear elastic model. 90

39 Average number of iterations in a set of 100 time-steps as a function of the number of reused information from old time-steps of the IQN-ILS algorithm, q. 91
40 Time of simulation for 100 time-steps, in minutes, for (a) case 13 and (b) case 17 as a function of the reuse parameter, q. 92
A.1 Representation of the mappings between each reference system in the Arbitrary Lagrangian-Eulerian (ALE) description. 112
A.2 A material cubic element with volume $\mathrm{d}V_\xi$ change its shape and volume after $\mathrm{d}t$ to $\mathrm{d}V$: both volumes are related through the Jacobian determinant. 113
A.3 Comparison between the Eulerian, Lagrangian and ALE descriptions of a two-dimensional material motion represented by the red grid (coordinates $\boldsymbol{\xi}$) from instant $t = t_0$ (undeformed configuration) to $t = t_1$; the dashed lines represent the referential system with coordinate lines $\boldsymbol{\chi}$; the spatial coordinates $\boldsymbol{x}$ is fixed and represented by a Cartesian coordinate system. . 117
B.1 Motion of a solid deformed by a force $\boldsymbol{f}$, showing the initial (reference) configuration (left) and the current configuration (right). 126
B.2 Deformation of a solid: detail of a section under the application of a force $\boldsymbol{df}$. 128
C.1 (a) Polygonal control volume of a finite volume computational mesh, and its neighbors; (b) Polyhedral control volume V_C. 133
C.2 Choice of decomposition of normal vector $\boldsymbol{s}_f$ according to the over-relaxed approach. 138
C.3 Two adjacent control volumes with skewness and non-orthogonality between them, with vectors definitions used to calculate the gradient normal to face f, $\nabla\phi_f \bullet \boldsymbol{s}_f$ with corrections. 139
C.4 SIMPLE algorithm; index n represents the current time-step, t; the measurements of the *Residual* depends on the software, but usually includes residuals of pressure, velocity and mass balance for convergence. 152
C.5 PIMPLE algorithm: *nOuterCorr* is the number of outer corrector steps, i.e. including Semi-Implicit Method for Pressure Linked Equations (SIMPLE) and Pressure Implicit with Splitting Operators (PISO) loops; *nCorr* is the number of correctors of the PISO loop only; index n represents the current time-step, t. 153

LIST OF TABLES

1 Distribution of aneurysms size (set of 1,692 patients with unruptured aneurysms). 23

2 Percentage of ruptured aneurysms as a function of the aneurysm size for different arteries of the brain (group 1 with no previous SAH and group 2 with previous SAH and n is the number of patients in the sample). 27

3 Geometric parameters of the aneurysms studied here: parent artery and its diameter d_a, neck diameter d_n, dome height h_d and diameter d_d, aspect ratio A_r and mean blood flow rate through its parent artery, $\bar{q}_a$. 50

4 WSS and OSI mean and maximum values and maximum $\boldsymbol{\sigma}^{\mathrm{s}}$ on the *aneurysm* surface for cases 13 and 17 with different wall tissue model. 89

LIST OF ABBREVIATIONS

ICA	Internal Carotid Artery
VA	Vertebral Arteries
BA	Basilar Artery
MCA	Middle Cerebral Artery
ACA	Anterior Cerebral Artery
ACoA	Anterior Communicating Artery
SAH	Subarachnoid Hemorrhage
FSI	Fluid-Structure Interaction
DSA	Digital Subtraction Angiography
VOI	Volume of Interest
IQN-ILS	Interface Quasi-Newton-Implicit Jacobian Least-Squares
WSS	Wall Shear Stress
OSI	Oscillatory Shear Index
ALE	Arbitrary Lagrangian-Eulerian
SIMPLE	Semi-Implicit Method for Pressure Linked Equations
PISO	Pressure Implicit with Splitting Operators
CFD	Computational Fluid Dynamics
PDE	Partial Differential Equations
FVM	Finite Volume Method
FEM	Finite Element Method
FDM	Finite Differences Method

LIST OF SYMBOLS

Sign	Description	Unit
A_r	Aspect ratio of an aneurysm, defined as the ratio between dome height and neck diameter	-
h_d	Height of an aneurysm's dome	m
d_n	Diameter of an aneurysm's neck	m
d_a	Diameter of an aneurysm's parent artery section	m
V	Volume of a control volume in spatial coordinates	m^3
t	Time	s
$\boldsymbol{x}$	Eulerian or spatial coordinates system (Cartesian coordinates)	m
V_C	Volume of a cell with centroid C in a finite volume mesh	m^3
$\boldsymbol{\mathcal{F}}$	Symbolic representation of the fluid solver	-
$\boldsymbol{\mathcal{S}}$	Symbolic representation of the solid solver	-
s	Speedup	-
q	Number of time-steps reused in the IQN-ILS algorithm	-
V_ξ	Volume of an amount of particles in material coordinates	m^3
$\boldsymbol{f}$	Force vector	N
$\boldsymbol{s}_f$	Normal vector to the face f of a polyhedral cell	m^2
d_d	Diameter of an aneurysm dome	m
$\bar{q}_a$	Mean blood flow rate through an artery section	ml/s
Co	Courant number	-
E	Young's modulus of a solid	Pa
F_s	Scale factor used for scaling the residual norm	-
N^{fs}	Number of degrees of freedom on the FSI interface	-
N_{CV}	Number of control volumes in a finite volume mesh	-
Re	Reynolds number	-
S^ϕ	Source and/or sink terms of the differential transport equation of ϕ	$[\phi]/m^3/s$
S_C	Surface of a cell with centroid C in a finite volume mesh	m^2
S	Surface of control volume V in spatial coordinates	m^2
V_χ	Control volume in ALE coordinates	m^3

Sign	Description	Unit
$\bar{S}^{\phi}$	Mean source and/or sink terms of the integral transport equation of ϕ	$[\phi]/\mathrm{m}^3/\mathrm{s}$
$\boldsymbol{\mathcal{R}}$	Residual operator resulted from the fixed-point formulation of the FSI problem	m
$\tilde{\mathbf{d}}$	FSI interface position after a coupling iteration	m
$\mathbf{d}$	Position of the FSI interface	m
$\mathbf{r}$	Discrete residual vector of the coupling iterations	m
$\mathbf{r}$	Residual vector of a linear system $\mathbf{Ax} = \mathbf{b}$	-
$\mathbf{y}$	Solid solver input: traction exerted by the flow on the FSI interface	Pa
$\dot{V}_f$	Volume swept by face f of control volume V_C	m^3/s
$\dot{m}$	Mass flow rate	kg/s
$\hat{\boldsymbol{v}}$	Material velocity measured from the ALE coordinates point of view	m/s
$\mathbf{J}_{\boldsymbol{\Phi}}$	Jacobian matrix of the material-spatial mapping	-
$\mathbf{J}_{\boldsymbol{\Psi}}$	Jacobian matrix of the mesh-spatial mapping	-
$\mathrm{J}_{\boldsymbol{\Phi}}$	Jacobian of the material-spatial mapping	-
$\mathrm{J}_{\boldsymbol{\Psi}}$	Jacobian of the mesh-spatial mapping	-
$\mathbf{A}$	Coefficients matrix of a system of equations assembled for a finite volume mesh	$[\phi]$
$\boldsymbol{E}$	Green-Lagrange strain tensor	-
$\boldsymbol{F}$	Deformation gradient tensor	-
$\boldsymbol{I}$	Second order identity tensor	-
$\boldsymbol{P}$	Nominal stress tensor	Pa
$\boldsymbol{S}$	Second Piola-Kirchhoff stress tensor	Pa
$\boldsymbol{\beta}$	Vector joining the centroid of face f and the neighbor cell centroid F	-
$\boldsymbol{b}$	Body forces per unit mass	N/kg
$\boldsymbol{b}$	Source vector of the linearized momentum equations for a control volume	$[\phi]$kg/s
$\boldsymbol{c}$	Convective velocity	m/s

Sign	Description	Unit
$\boldsymbol{d}_{CF}$	Vector joining the centroids of adjacent cells in a finite volume mesh	m
$\boldsymbol{d}_{Cf}$	Vector joining the centroids of a cell V_C and the centroid of a face f	m
$\boldsymbol{f}_b$	Body forces per unit volume	$\mathrm{N/m^3}$
$\boldsymbol{g}$	Gravitational acceleration vector	$\mathrm{m/s^2}$
$\boldsymbol{n}$	Unit normal vector to the surface S pointing outwards	-
$\boldsymbol{p}$	Linear momentum vector	kg m/s
$\boldsymbol{t}$	Traction vector force	$\mathrm{N/m^2}$
$\boldsymbol{u}$	Solid displacement vector	m
$\boldsymbol{v}$	Material velocity	m/s
a_C	Diagonal coefficients of the linearized transport equation for the volume V_C	kg/s
a_F	Off-diagonal coefficients of the linearized transport equation for the volume V_C	kg/s
b	Source term of the linearized transport equation for a control volume V_C	$[\phi]$kg/s
d_{fn}	Projection of the vector $\boldsymbol{d}_{CF}$ on the face normal $\boldsymbol{n}$	m
f_χ	ALE description of a function f representing any scalar variable of the material	-
f_ξ	Function f representing any scalar variable of the material	-
f	Spatial function f representing any scalar variable of the material	-
l	Cell centroid distance to a selected boundary	m
m	Mass	kg
p'	Pressure correction field in the pressure-velocity algorithms to solve the coupled Navier-Stokes equations	Pa
p	Pressure field of a fluid flow	Pa
v_x	Velocity component on the x direction of the spatial coordinates	m/s
v_y	Velocity component on the y direction of the spatial coordinates	m/s
v_z	Velocity component on the z direction of the spatial coordinates	m/s

Greek Letters

Sign	Description	Unit
Ω	Spatial solution domain	m^3
Γ^{fs}	Fluid-solid interface $= \Gamma^f \cap \Gamma^s$	-
Γ	Boundary of the domain Ω	m^2
$\boldsymbol{\xi}$	Lagrangian or material coordinates system	m
$\boldsymbol{\chi}$	Referential coordinates system for the arbitrary Lagrangian-Eulerian description	m
ϕ	Generic intensive (per unit mass) variable transported by a fluid flow	$[\phi]$/kg
$\boldsymbol{\sigma}$	Cauchy stress tensor	Pa
$\boldsymbol{\Phi}$	Mapping of material coordinates onto spatial coordinates	-
$\boldsymbol{\Psi}$	Mapping of mesh coordinates onto spatial coordinates	-
Δt	Time-step	s
Γ^{ϕ}	Diffusivity of ϕ	m^2/s
Ω_{χ}	Solution domain as seen by the reference coordinates	m^3
Ω_{ξ}	Solution domain as seen by the material coordinates	m^3
γ	Mesh diffusivity for the Laplace equation governing the mesh motion	-
$\Gamma^{\mathrm{fs}}_{fluid}$	Fluid mesh boundary corresponding to the fluid-solid interface	-
$\Gamma^{\mathrm{fs}}_{solid}$	Solid mesh boundary corresponding to the fluid-solid interface	-
$\boldsymbol{\Xi}$	Mapping of material coordinates onto mesh coordinates	-
$\boldsymbol{\omega}_{node}$	Mesh velocity at the geometric nodes of the Finite Volume mesh	m/s
$\boldsymbol{\omega}$	Mesh velocity of a cell centroid	m/s
$\boldsymbol{\tau}$	Viscous part of the Cauchy stress tensor of a fluid flow	Pa
λ^{s}	Second Lamé's constant of a solid	Pa
μ^{f}	Dynamic viscosity of a fluid	Pa s
μ^{s}	First Lamé's constant of a solid	Pa
ν^{f}	Kinematic viscosity of a fluid	m^2/s
ν^{s}	Poisson's ratio of a solid	-
ϕ_C	ϕ at the centroid of the control volume C	-
ϕ_F	ϕ at the centroid of a neighbor control volume F	$[\phi]$

Sign	Description	Unit
ϕ_f	ϕ at the centroid of face f	$[\phi]$
ρ	Density	$\mathrm{kg/m^3}$
$\boldsymbol{\varepsilon}$	Linear or engineering strain tensor	-
$\boldsymbol{\kappa}$	Complement vector of the decomposition of $\boldsymbol{s}_f$ in $\boldsymbol{\beta}$	-
ϵ_0	Tolerance of the FSI coupling iterations	-

Others Symbols

Sign	Description	Unit
∇_0	Nabla operator in the initial material coordinates	1/m
∇	Nabla operator in Eulerian coordinates	1/m

Subscripts

C	Indicates variables evaluated at the centroid of a control volume
F	Indicates variables evaluated at the centroid of a neighbor control volume to cell V_C
k	Index for a coupling iteration of the outer loop of the IQN-ILS algorithm
f	Indicate a face of a polyhedral control volume

Superscripts

fs	Used for fluid-solid interface related variables
n	Time index
s	Used for solid related variables
f	Used for fluid related variables
0	Indicates variables at the initial instant $t = 0$

Notes about the notation

Tensors of the Euclidean three-dimensional space of rank ≥ 1 are typed in italic boldface letters, the main difference is made between first-order tensors, or vectors, which are represented by lowercase bold letters and tensors of rank ≥ 2 are represented by using uppercase boldface letters; the major exceptions are the Cauchy stress tensor $\boldsymbol{\sigma}$, and the linear or engineering strain tensor $\boldsymbol{\varepsilon}$ because these are common symbols found in the literature to represent them. Tensors of zeroth order, or scalars, are represented by italic not-boldface letters – this also includes the components of tensors of order ≥ 1.

Matrices that belong to the general $\mathbb{R}^{m\times n}$ space and vectors of $\mathbb{R}^n$, which are considered to be column vectors, are represented by boldface letters: the former in uppercase typeface and the latter in lowercase typeface. The main difference between generic matrices of $\mathbb{R}^{m\times n}$ and tensors of the three-dimensional Euclidean space is explicit in the context and/or by the operators used between them, for example, the equation $\boldsymbol{x}\bullet\boldsymbol{A}\bullet\boldsymbol{x}$, where "$\bullet$" is the commonly used notation for the scalar product, indicates that $\boldsymbol{x}$ is a vector and $\boldsymbol{A}$ is a tensor of order ≥ 2 of the Euclidean space, whereas $\mathbf{x}^{\mathrm{T}}\mathbf{A}\mathbf{x}$ indicates that $\mathbf{x}$ is a column vector and $\mathbf{A}$ a matrix. If they overlap in the text, we explicitly indicate matrices with its symbol between brackets and column vectors with braces for clarity, therefore, $\mathbf{A}$ is $[A]$, and $\mathbf{x}$ is $\{x\}$.

We use mainly vector notation to represent the equations of Continuum Mechanics instead of using Einstein's index notation, which was preferred only in demonstrations of tensorial equations where we use lowercase Latin subscripts to represent the tensor components.

CONTENTS

1 INTRODUCTION **23**

1.1 Intracranial aneurysms 23

1.2 The Role of Computational Fluid Dynamics on the Study of Aneurysms . . 30

1.3 Objectives 31

2 METHODOLOGY **32**

2.1 Fluid-Structure Interaction 32

2.1.1 Computational Fluid-Structure Interaction 33

2.2 Physical and Mathematical Modeling 35

2.2.1 Fluid Model for the Blood 36

2.2.2 Solid Model for the Aneurysm and Artery Walls Tissue 41

2.2.3 Physical Condition on the FSI interface 47

2.3 Numerical Methods 47

2.3.1 Spatial and Temporal Discretization 48

2.3.2 Discretization of the Mathematical Model 54

2.3.3 Coupling FSI Method: IQN-ILS 65

2.3.4 Solution Procedure 73

2.4 Hardware Support 74

2.5 Data Analysis 78

3 RESULTS **80**

3.1 Numerical Error and Mesh Independence Analysis 80

3.2 Simulations Results 84

3.3 Comparison between the linear and non-linear elastic models 89

3.4 Performance assessment of the IQN-ILS coupling method for the aneurysm problem 91

4 DISCUSSION AND CONCLUSIONS **93**

REFERENCES **97**

APPENDICES **110**

A Arbitrary Lagrangian-Eulerian Formulation **110**

B Total Lagrangian Formulation for a Solid Motion **126**

C The Finite Volume Discretization **132**

C.1 Spatial Discretization 135

C.2 Temporal Discretization 141

C.3 Pressure-Velocity Coupling 144

D Residuals in foam-extend **154**

1 INTRODUCTION

1.1 Intracranial aneurysms

Aneurysms are arterial abnormalities defined as dilated regions of the artery wall (the word "aneurysm" comes from the Greek word *aneurysma*: *ana*, meaning across, and *eurys*, meaning broad). These abnormalities can arise at different sites of the human vascular system, more commonly found on the abdominal aorta and arteries that reach the brain. Intracranial aneurysms generally occur on arterial bifurcations of the base of the brain, in the so-called circle of Willis – formed by the internal carotid arteries and the vertebral and basilar arteries and also by both their branches – or at nearby locations. Figure 1 presents a schematic view of the base of the brain showing the circle of Willis and its arteries. Figure 2 illustrates an aneurysm on a bifurcation: the aneurysm itself is represented by its *dome* with height h_d and the opposite artery is usually called the *parent artery*; Fig. 3 shows two computational images and two reconstructed surfaces of intracranial aneurysms.

Figure 5 presents a schematic view of the most common sites of aneurysms [2]. Their size can vary from 1 mm to 25 mm and larger, as we can see in Table 1, which shows the distribution of aneurysm size from a set of 1,692 patients with unruptured aneurysms, as reported by The International Study of Unruptured Intracranial Aneurysms Investigators [4]. In Fig. 3, the aneurysms have different sizes, ranging from 3 mm to 18 mm.

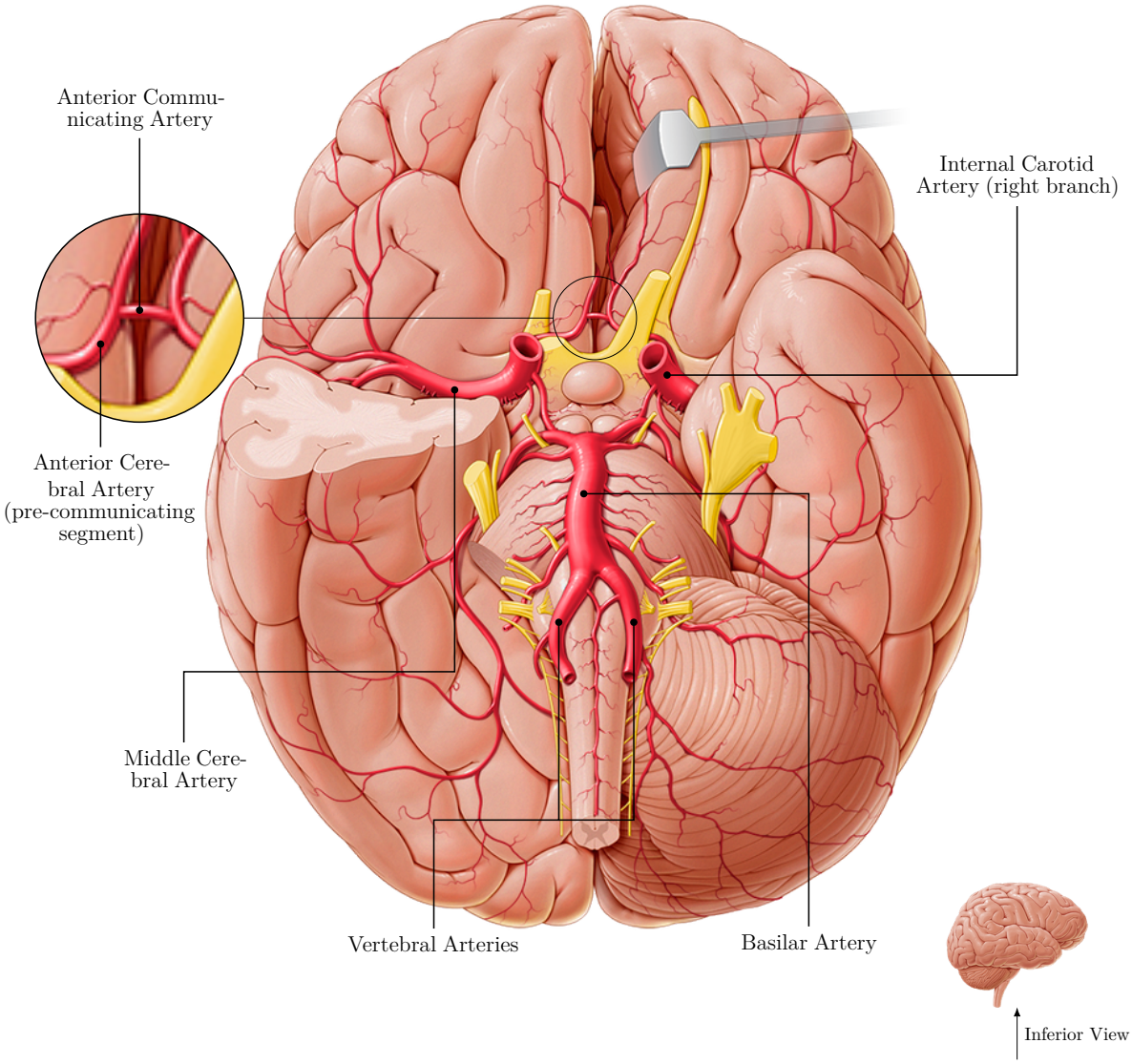
Table 1 – Distribution of aneurysms size (set of 1,692 patients with unruptured aneurysms).

Aneurysm size	2-7 mm	7-12 mm	13-24 mm	≥25 mm
Percentage of ocurrence	62%	23%	11.7%	3.2%

Source: The International Study of Unruptured Intracranial Aneurysms Investigators [4].

Intracranial aneurysms represent a high risk to the patient: they cause a mortality rate between 40 and 50% and also present high morbidity risk (permanent injury). It is also estimated that 2 to 3% of the world's population have intracranial aneurysms [5]. It is reported that 85% of Subarachnoid Hemorrhage (SAH) cases, a devastating event that can be fatal or lead to a severe neurological deficit, are caused by the rupture of these aneurysms [6, 7, 8]. Hop et al. [9] concluded that fatal cases of SAH occurred from 32 to 67% and about one-third of morbidity among the patients who survived. The work of The International Study of Unruptured Intracranial Aneurysms Investigators [4], one of the

Figure 1 – Base of the brain: arteries tree composing the circle of Willis – internal carotid arteries (ICA) with the vertebro-basilar system, composed of the vertebral arteries (VA) and basilar artery (BA), and both their branches: middle cerebral arteries (MCA); anterior cerebral arteries (ACA) and the anterior communicating artery (ACoA).

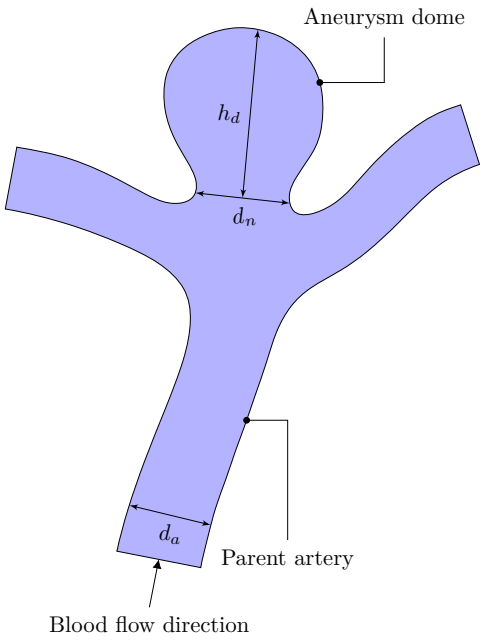


Source: prepared by the author with the brain pictures extracted from KenHub [1].

most relevant scientific work on rupture of intracranial aneurysms being used until today for the decision of their treatment, evaluated the probability of SAH over time for a group of 1,077 patients followed up over 4.1 years who did not have previous cases of SAH, for different aneurysm sizes and, according to their results, the risk of SAH increases over time and for larger aneurysms, as we can see in Fig. 4. The same study reported that, of the 193 patients who died during the follow up period, 27% died of intracranial hemorrhage.

The diagnostic of intracranial aneurysms is increasing due specially to the development of better imaging techniques such as three-dimensional (3D) Digital Subtraction

Figure 2 – Aneurysm dome, its parent artery and aspect ratio, A_r, definition: aneurysm dome height, h_d, divided by d_n, the neck diameter; the parent artery has diameter d_a.

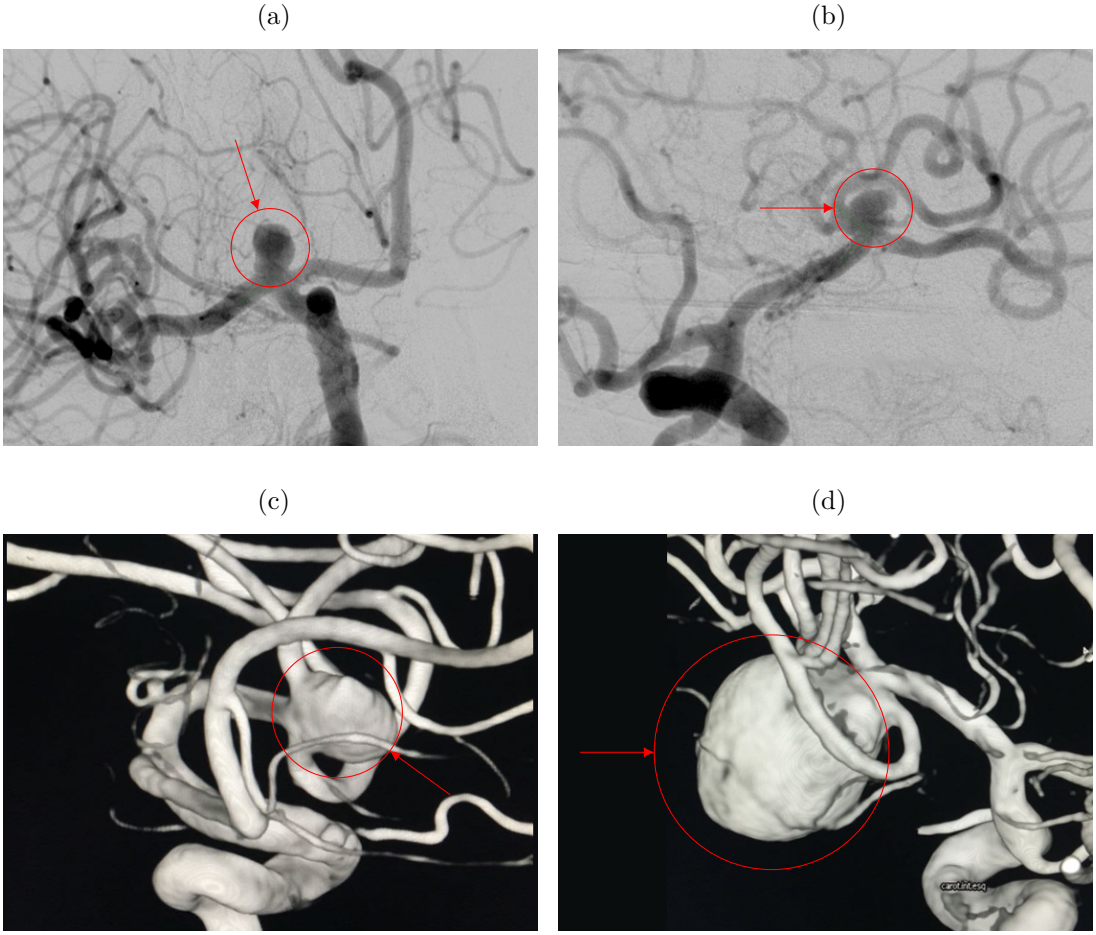


Source: prepared by the author.

Angiography (DSA), 3D Rotational Angiography, Magnetic Resonance Angiography and Computed Tomography Angiography [10, 11]. Figures 3a and 3b show images generated by DSA of intracranial aneurysms, and Figs. 3c and 3d show two reconstructed surfaces of intracranial aneurysms, of different patients and in different position of the brain vessels tree. Currently, physicians use statistical methods based primarily on the size of the aneurysm – its dome height h_d – to assess the likelihood of rupture. The work of The International Study of Unruptured Intracranial Aneurysms Investigators [4] rated the cumulative rupture rate of aneurysms according to its size and location by monitoring the patients for a period of 5 years after being detected, as presented in Table 2. The percentage of rupture increases greatly if the aneurysm is larger than 13 mm compared to the percentage if the aneurysm is smaller than 7 mm.

Currently, the two major treatment techniques for intracranial aneurysms are: surgical intervention - direct clipping, for example - and endovascular treatment - placement of coils inside the aneurysm dome and intra-vascular stent placement or occlusion of the parent vessel, for example [5]. However, these interventions also presents risks to patients. According to Torii et al. [12], risks of permanent damage and death due to treatment and post-operative procedures are about 10%. Hence, one should evaluate the best alternative for the patient. According to the data in Table 2, we can conclude that aneurysms smaller

Figure 3 – Two images of the digital subtraction angiography and two reconstructed surfaces of aneurysms (indicated with arrows), respectively, (a) at the Internal Carotid Artery (ICA) bifurcation with height 5.7 mm; (b) at the Middle Cerebral Artery (MCA) bifurcation with height 3.8 mm; (c) at the MCA bifurcation with height 7.9 mm and (d) at the MCA bifurcation with height $\approx$ 18 mm.



Source: images provided by Dr. Carlos Eduardo Baccin (Hospital Israelita Albert Einstein e Fundação Centro Médico Campinas, São Paulo, Brazil).

than 13 mm assume higher risk if treated for the first group of arteries. The major problem is for aneurysms whose size is between 7 and 12 mm and also for those smaller than 7 mm for the second group of arteries; although the risk of rupture is lower than the risk of treatment, the percentage of rupture for these sizes is not negligible when considering the risk of death. Thus, a methodology that could provide more precise criteria for the treatment decision of the patient is needed.

Weir et al. [13], for example, performed a statistical study relating the aspect ratio of the aneurysm – dome height/width of the neck, see Fig. 2 – to its rupture probability. According to the authors, chances of rupture were 20 times higher when the aspect ratio was larger than 3.47 compared to an aspect ratio lower than or equal to 1.38. In their samples, only 7% of ruptured aneurysms had an aspect ratio lower than 1.38 compared to

Table 2 – Percentage of ruptured aneurysms as a function of the aneurysm size for different arteries of the brain (group 1 with no previous SAH and group 2 with previous SAH and n is the number of patients in the sample).

Parent Artery	<7 mm		7-12mm	13-24mm	≥ 25 mm
	Group 1	Group 2			
ACA/MCA/ICA ($n = 1037$)	0%	1.5%	2.6%	14.5%	40.0%
BA/VA($n = 445$)	2.5%	3.4%	14.5%	18.4%	50.0%

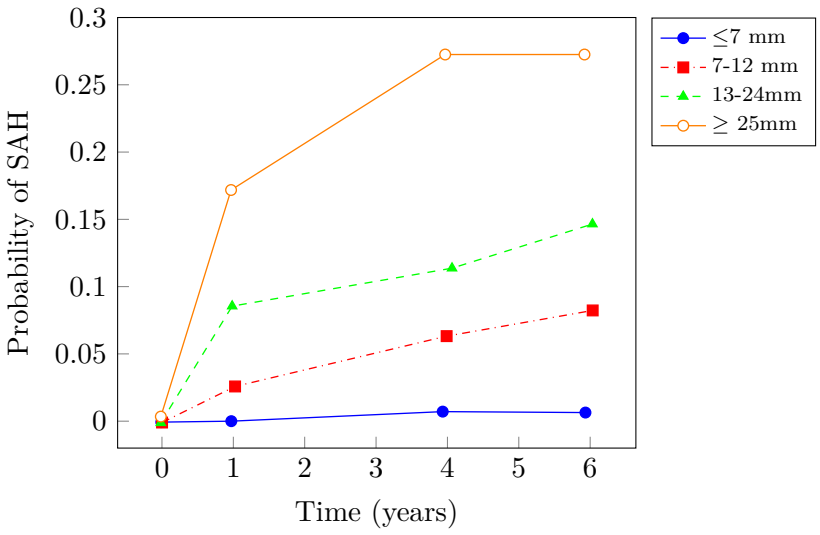
Source: The International Study of Unruptured Intracranial Aneurysms Investigators [4].

45% of unruptured aneurysms. The authors conclude that the aspect ratio is a parameter that is worth calculating and should be used as one of the decision parameters for the treatment of aneurysms. Nevertheless, for the medical practice, the most used parameter for the decision of treatment is the aneurysm size, with statistical data provided by studies such as The International Study of Unruptured Intracranial Aneurysms Investigators [4].

Although the factors that lead to the formation, growth and rupture of intracranial aneurysms are still not well understood, more recent studies agree that the effects of blood flow inside the vessels (hemodynamic) are crucial for the development of these processes [14, 15]. The most relevant hemodynamic parameters taken into account in these studies are:

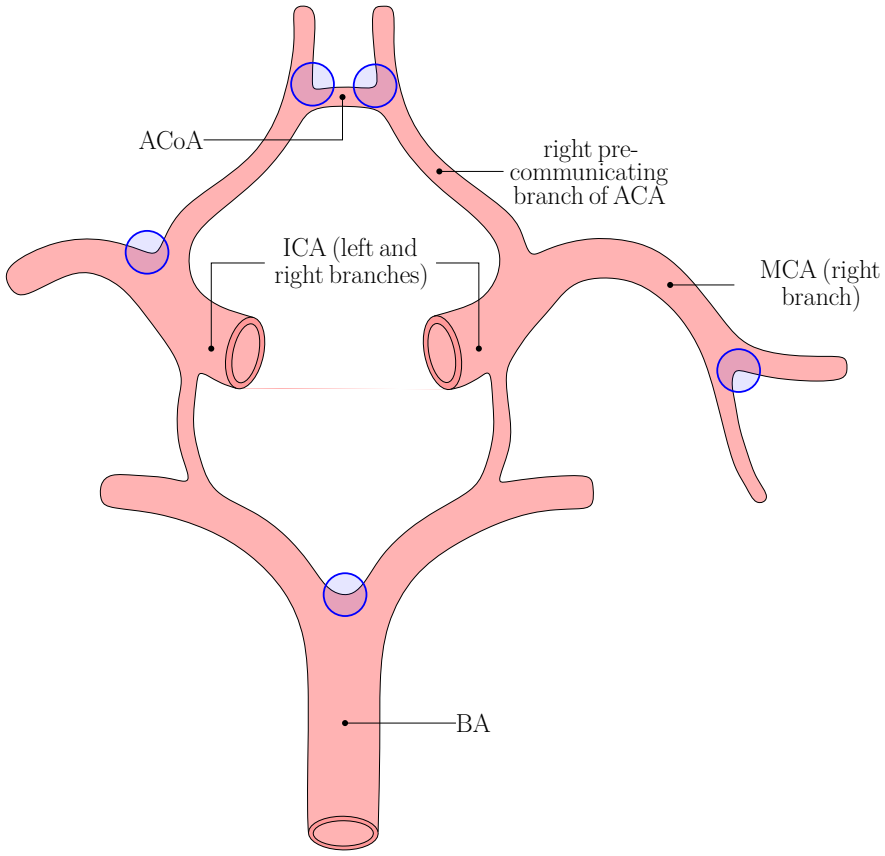
- Wall Shear Stress (WSS) due to the flow velocity gradient adjacent to the aneurysm wall and its gradient. Other important parameters are also derived from WSS like

Figure 4 – Probability of SAH over time for a group of 1,077 patients followed up over 4.1 years who did not have previous cases of SAH, for different aneurysm sizes.



Source: The International Study of Unruptured Intracranial Aneurysms Investigators [4].

Figure 5 – Arteries that reach the brain with some of the most common sites of aneurysm formation indicated with a blue circle.



Source: prepared by the author.

the Oscillatory Shear Index (OSI);

- Hydrostatic pressure;
- Transmural pressure: difference between the pressure inside and outside the artery wall;
- Flow vorticity;
- Flow impingement on the aneurysm wall.

The parameter most accepted as being associated with formation, growth and rupture is the WSS [15, 16, 17]. According to Penn et al. [14], high levels of WSS, which occurs in artery bifurcations due to the flow impingement, trigger cellular reactions, altering the cellular structure of the artery tissue, leading to aneurysm initiation.

Once the aneurysm begins to grow larger, the shape of the wall is altered, generating an irregular saccular shape, as we see in Fig. 3. Consequently, the blood flow pattern

within the vessels changes. The factors responsible for the process of growing are similar to those that give rise to the aneurysm: high WSS values are found in the aneurysm neck, hence the biological mechanisms of structural tissue modification occurring with high WSS values cause the aneurysm to grow in size [14, 16].

At the aneurysm dome, WSS levels can be low due to a slow recirculation flow usually formed. Nevertheless, the levels of WSS in this region may be related to rupture due to degradation of the endothelial cell matrix via cell death [14]. Meng et al. [15] goes further and suggests that there are two possibilities for aneurysm growth leading to rupture: one based on high levels of WSS caused by flow impingement on the aneurysm wall; and another, when the WSS levels are low, due to the recirculating flow.

Thus, since the biological mechanisms involved in aneurysm growth and rupture and their relation to hemodynamic variables have not been well defined, we can not conclude about the exact effect of WSS on those processes. Moreover, if the rupture occurs at the aneurysm wall tissue, wall variables, such as stresses and strains, must be relevant to understand the rupture event, since it is well known that arteries and veins are flexible [18].

Specialists are trying to use experimental techniques and numerical simulation to better understand the problem. However, there are currently no reliable experimental techniques for quantifying blood flow patterns and WSS in intracranial aneurysms. Although measurements of hemodynamic parameters in living patients are just becoming feasible, they are still very difficult to perform. In general, experimental studies on intracranial aneurysms were performed using idealized geometries or animal-induced aneurysms [19, 20, 21, 22, 23, 24].

On the other hand, with better imaging techniques, it is almost straightforward to generate patient-specific aneurysm geometries, from surface reconstruction – Figs. 3c and 3d show two of these surfaces – that could be used for numerical simulations of the blood flow. Moreover, numerical simulations provide more complete data of all the important variables related to aneurysms and arteries hemodynamic, therefore making it an attractive tool for investigating the blood flow in aneurysms.

1.2 The Role of Computational Fluid Dynamics on the Study of Aneurysms

Computational Fluid Dynamics (CFD) has been widely used to describe the behavior of blood flow in arteries and idealized or patient-specific aneurysms geometries. With the development of computational imaging techniques, the geometry of patient-specific intracranial aneurysm can be obtained, allowing to perform numerical simulations of the flow in realistic blood vessels and aneurysms. Several authors have used this technique to perform their simulations [16, 25, 26, 27, 28, 29, 30, 31, 32, 33]. Since the flow in aneurysms presents complex geometries, unsteady flow and complex rheological behavior, in the early simulations, limited computational power prevented the use of numerical techniques to analyze the flow in aneurysms for a large number of patients. However, with the large and fast increase in processing power of current computers, this technique is becoming suitable for studying particular cases of aneurysms. Currently, numerical simulations allow the study of patient-specific aneurysms and, in the future, proper analysis of their results may guide to their treatment and pathogenesis. In addition, using their inherent versatility, it is possible to take into account several factors that may influence the flow hemodynamic, for example, different blood rheology models [30] and different boundary conditions [34].

Shojima et al. [16] performed numerical simulations on different geometries of patient-specific aneurysms, ruptured and unruptured, to analyze the influence of WSS on rupture. The authors concluded that a minimum level of WSS should be maintained at the interface – WSS $\approx 2.0\,\mathrm{Pa}$ – to preserve the endothelial structure of the wall tissue whereas if WSS is lower than $1.5\,\mathrm{Pa}$ endothelial cells could degenerate. Therefore, WSS is one of the main factors responsible for cell degeneration and consequent structural weakness of the aneurysm wall. In addition, low levels of WSS in the dome may be responsible for the circumferential growth of the aneurysm, due to cell degeneration [14].

Cebral et al. [35] performed simulations using data of 62 aneurysms, ruptured and unruptured, collected from patients with aneurysms at different locations on the circle of Willis, and performed a statistical analysis correlating the type of flow – based on different characteristics such as area and direction of the jet colliding at the entry of the aneurysm, formation of vortex structures inside the dome – with the risk of rupture. The authors concluded that the area and direction of the jet colliding with the aneurysm dome are important for predicting rupture, but caution is recommended, since other important factors were not taken into account in their simulations, such as effects of

the wall elasticity. The same authors, in a previous study [36] carried out an analysis of the hemodynamic characteristics in aneurysms under diverse biological conditions, concluding that the vascular geometry has a large influence on the flow fields, due to the non-linearities present in the Navier-Stokes equations. We highlight at this point that all the aforementioned numerical studies considered the aneurysm wall as rigid.

In some more recent studies, researchers numerically implemented the vessel wall motion in the numerical model [27, 28, 37, 38, 39, 40, 41], therefore accounting for the interaction between the blood flow and the artery and aneurysm wall flexibility. For instance, Bazilevs et al. [28] compared the results of WSS in rigid wall and flexible wall aneurysms, and found that there is an overestimation of the WSS value of up to 36% if the vessel walls were considered rigid, indicating that, to obtain more accurate values of the hemodynamic parameters, a rigid wall may be a very crude assumption. Furthermore, they comment that the rupture event occurs on the wall tissue, then it must be related to the *wall tissue* variables. Ultimately, from a materials engineering perspective, it will occurs when the wall stress reaches a higher value than the rupture limit of the tissue. Therefore, it is important to study the wall variables to gather a deeper understanding of the aneurysm rupture event, which is not possible without a fluid (blood flow) and solid (aneurysm wall) interaction methodology.

1.3 Objectives

Dr. Carlos Eduardo Baccin (Hospital Israelita Albert Einstein e Fundação Centro Médico Campinas, São Paulo, Brazil) provided patient-specific aneurysm models, used in this work. The objective is to use the results of the numerical simulations of the aneurysms fluid-structure interaction problem to evaluate the numerical parameters related to rupture, according to the literature – WSS and OSI – for two different models: rigid and flexible wall. Since the aneurysms in this study were not ruptured, we will rely on the literature to provide reference values for the parameters related to rupture. We also aim to perform a comparison of the stress levels on the aneurysm wall resulting from the simulations with the rupture stress values which were recently measured for the wall tissue of intracranial aneurysms [42, 43].

2 METHODOLOGY

Blood flow in aneurysms and arteries fits in a general class of physical problems called *Fluid-Structure Interaction (FSI)*: the blood flow and solid – artery and aneurysm – variables are mutually dependent. This is a complex problem because, in general, both fluid and solid problems have non-linear behavior that are coupled through a physical interface, usually called fluid-solid interface or wet surface. To solve this problem numerically, we first need to develop a suitable physical model.

In this section, we present a methodology behind the FSI simulations of the aneurysms: the nature of a FSI problem and its computational approach, physical modeling of the FSI problem yielding to the governing equations and boundary conditions; spatial, temporal and governing equation discretization by the Finite Volume Method.

2.1 Fluid-Structure Interaction

Several problems in Nature deal with fluids and solids in contact. Usually, in the most common problems of Fluid Mechanics, solid interfaces in contact with the fluid flow are considered stationary, therefore the boundary conditions are directly applied for the solution of the governing equations of the fluid motion. Similarly, in a Solid Mechanics problem the flow acts on the domain by means of stress forces, which correspond to boundary conditions for the solid. However, in many situations, this kind of modeling consists in an approximation of the reality, in which one assume small or zero deformations of the solid. There are many cases in which such approximations can not be made or they would be very crude, leading to a coupled problem between the fluid and solid: the flow forces deform the solid structure that modifies the flow domain. This type of problem is called *fluid-structure interaction*.

FSI lies within a class of multi-physics problems in which models of different phenomena need to be solved together because they are dependent on each other. Several problems should be analyzed from this perspective: deflection of wind turbine blades, dynamics of reciprocating compressor valves, movement of a ship sailing on the sea, vibration of aircraft wings (phenomenon of flutter), fall of a leaf, beating wings of dragonflies and birds, cross flow on a parachute and/or flags, blood pumped through the heart valves and, as already mentioned, flow dynamics through intracranial aneurysms and arteries, which is our interest in this work.

These types of problems are present in most engineering and biomedical applications, and often their solutions are necessary for the proper design of several kinds of equipments. Performing numerical simulation of this kind of problem has led to the development and improvement of numerical techniques because it deals with dynamic meshes, non-linear systems of Partial Differential Equations (PDE) with complex boundary conditions and strong coupling between the equations. Currently, some techniques are commonly used for solving those problems. The next section gives some highlights of these techniques.

2.1.1 Computational Fluid-Structure Interaction

The equations governing FSI problems have non-linear terms, they are coupled and have an intrinsically temporal characteristic, moreover in most cases they must be solved in complex geometries. Due to such characteristics, an analytical solution is almost impossible to be found in most cases by using the existing mathematical techniques, thus the only choice is to rely on computational methods. The most common mesh-numerical methods, such as the Finite Volume Method (FVM), Finite Element Method (FEM) and Finite Differences Method (FDM), are designed to solve the governing equations using a temporal marching procedure in which the discretized equations are applied to elements or control volumes (computational mesh) into which the calculation domain is subdivided, yielding a system of linearized algebraic equations [44].

From the numerical point of view, two different methodologies are usually used to solve the system of partial differential equations of a FSI problem [45, 46]:

- Monolithic methodology: all the governing equations are solved together after their discretization in a fully coupled way that leads to only one system of linearized algebraic equations;

- Partitioned methodology: the equations for the solid and fluid domains are discretized and solved independently, in which the coupling is re-enforced through the conditions at the fluid-solid interface;

Another classification commonly found in the literature is [46]:

- Conforming mesh methods: the conditions at the solid-fluid interface are treated as physical conditions in the discretized equations. Thus, displacements of the interface

due to the solid deformations and/or rotations change the fluid field which must be taken into account and, therefore, dynamic mesh techniques must be used;

- Non-conforming mesh methods: in this technique, the conditions at the fluid-solid interface and its location are accounted as restrictions of the governing equations, so they can be solved without updating the mesh.

It is important to state that the discretization process follows the same general procedure of classical discretization methods such as the FVM and FEM, for example. The partitioned methodology fits within the conforming mesh methods because the movement of the fluid-solid interface changes the fluid domain, thus an algorithm for updating the fluid computational mesh must be used. The Immersed Boundary Method [47] can be a typical non-conforming mesh method.

Computational methods in FSI showed great development in the last two decades and many numerical simulation softwares currently solve dynamic mesh problems and multi-physics. An open-source package that is receiving much attention in academic and industrial environments for simulations in CFD is OpenFOAM® (Open Field Operation and Manipulation). One of its branches, the foam-extend package, is used here to perform the aneurysm simulations because one of its solvers is intended for FSI problems in a partitioned manner.

In the future, simulations of this type, with the most appropriate conditions as possible, could be used to analyze patient-specific aneurysms and assess whether they should be treated or not. In this sense, we opted to develop all the numerical steps with free and open-source software. This choice has several positive consequences:

1. If needed – since the source code of the applications used is publicly available – improvements and their implementation within the software can be made by any user with the ability to do it;

2. If someone wishes to follows the same approach, it only needs to download and use it, accelerating the process of improving the results and repeatability;

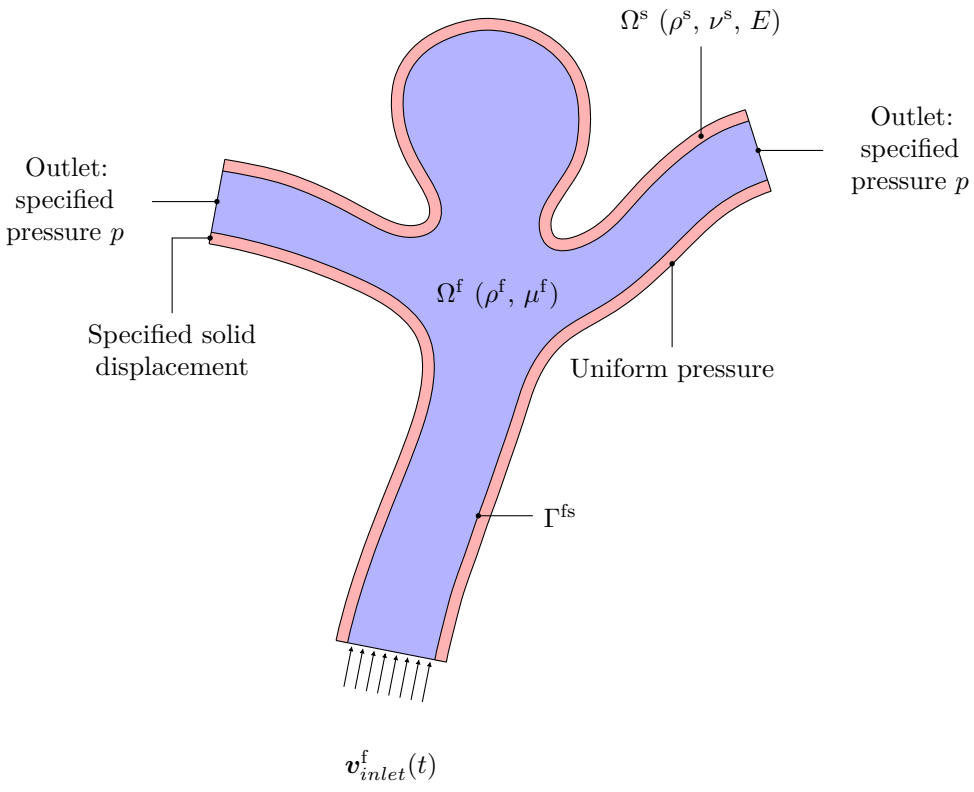
3. The whole methodology can be performed without commercial complications (inter-operability);

This choice also presents some downsides: for example, maybe the methodology needed is not fully implemented or is limited, therefore not all conditions could be tested. However, as we explain later on, we did not encounter such issues.

2.2 Physical and Mathematical Modeling

We model the geometry of the aneurysm problem as a domain Ω, with boundary Γ, composed of a solid domain Ω^{s} – the artery wall – and a fluid domain Ω^{f} – the blood flowing –, i.e. $\Omega = \Omega^{\mathrm{s}} \cup \Omega^{\mathrm{f}}$, with boundaries indicated by Γ^{s} and Γ^{f}, respectively, as shown schematically in Fig. 6 which also shows the physical conditions applied to each boundary. The figure also shows the fluid-solid interface $\Gamma^{\mathrm{fs}} = \Gamma^{\mathrm{f}} \cap \Gamma^{\mathrm{s}}$. The fluid has properties represented by its density ρ^{f} and dynamic viscosity μ^{f} (with kinematic viscosity ν^{f}), while the properties of the solid material are represented by its density ρ^{s}, Young's modulus E and Poisson's ratio ν^{s}. Below, we present the physical and mathematical modeling of the motion for each sub-domain.

Figure 6 – Solid, Ω^{s}, and fluid domains, Ω^{f}, fluid-solid interface Γ^{fs} and boundaries of each region with its respective physical boundary condition.



Source: prepared by the author.

2.2.1 Fluid Model for the Blood

Physical Modeling

We consider the blood as an incompressible Newtonian fluid with constant dynamic viscosity, in an isothermal laminar flow regime – because the velocities found in an aneurysm flow yield a Reynolds number, Re, of about 600 to 700 based on the parent artery diameter. The blood density was considered to be $1{,}000\,\mathrm{kg/m^3}$ and its kinematic viscosity $3.3 \times 10^{-6}\,\mathrm{m^2/s}$ [48].

Human blood has a mixture of different solid components (red and white blood cells, for example) suspended in a liquid formed by several different substances [49]. Different studies showed that is important to consider a non-Newtonian model for blood rheology in the overall human circulation [50, 51, 52]. However, Perktold et al. [53] showed that, for a bifurcation of the internal carotid, non-Newtonian effects are negligible for the flow velocity field. Furthermore, Valencia et al. [54] showed that predictions of flow variables on the aneurysmal wall using non-Newtonian models were similar to the predictions with the Newtonian model. Finally, several numerical studies consider the Newtonian fluid model, specially if the fluid-structure interaction is taken into account [12, 27, 28, 37, 38, 39, 48, 55], probably due to the extra complexity brought to the whole problem if a non-Newtonian behavior is considered.

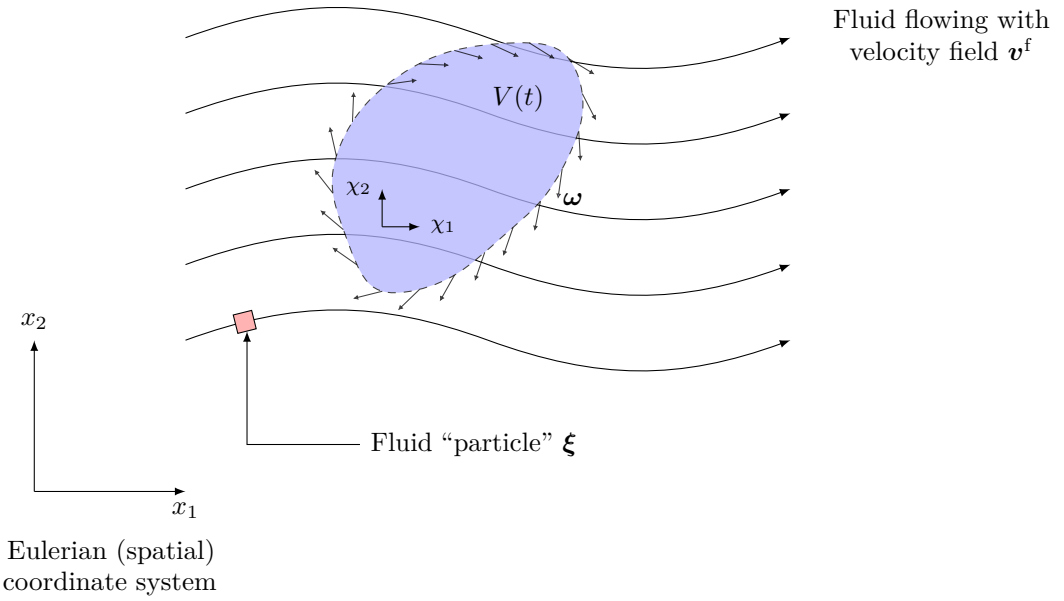
Furthermore, for this study, we are also forced to use the Newtonian model because currently it is the only fluid rheology model implemented for the FSI framework of foam-extend. Nevertheless, since this is a partitioned framework as explained later in Section 2.3.3, implementation of different models for the fluid rheology is relatively straightforward due to modularization.

Mathematical Modeling

In the fluid domain, the governing equations are derived from the mass conservation principle and the balance of linear momentum. Since the fluid domain change in time due to the artery flexibility, i.e. $\Omega^{\mathrm{f}} = \Omega^{\mathrm{f}}(t)$, we employ a moving volume integral formulation for the fluid governing principles: the so-called *Arbitrary Lagrangian-Eulerian (ALE)* description [56, 57]. This formulation introduces, combined with the material, $\boldsymbol{\xi}$, and spatial (Eulerian) coordinates, $\boldsymbol{x}$, a new coordinate frame to describe a control volume

motion, $V = V(t)$: the referential coordinates, $\boldsymbol{\chi}$, as depicted in Fig. 7. Therefore, the equations presented below hold for a moving control volume $V = V(t)$, with surface $S = S(t)$, in the fluid flow. All the equations presented here were demonstrated by the author in Appendix A.

Figure 7 – Schematic two-dimensional representation of the coordinate systems used to describe a fluid flowing through a moving control volume $V = V(t)$: $\boldsymbol{x}$ is the fixed or spatial coordinate system, $\boldsymbol{\xi}$ is the fluid particle and $\boldsymbol{\chi}$ is the referential coordinate system, fixed to the moving control volume.



Source: prepared by the author.

One of the most important variables introduced in the ALE description is the convective velocity $\boldsymbol{c}$, defined as:

$$\boldsymbol{c} = \boldsymbol{v}^{\mathrm{f}} - \boldsymbol{\omega} \tag{1}$$

where $\boldsymbol{\omega}$ is the velocity of the surface of the control volume or, equivalently, the *mesh velocity* – see Fig. 7 – and $\boldsymbol{v}^{\mathrm{f}}$ is the fluid flow velocity field. The most important modification that the ALE description brings to the equations of motion is related to this new variable: it changes the velocity that multiplies the advective transport term. In this new description, the material derivative $\dfrac{\mathrm{d}}{\mathrm{d}t}$ is related to the spatial gradient of the flow variables by the convective velocity (see Appendix A).

The equations governing the fluid motion are:

- Continuity equation for incompressible flows, derived from mass conservation principle, in differential form:

$$\nabla \bullet \left(\rho^{\mathrm{f}} \boldsymbol{v}^{\mathrm{f}}\right) = 0 \tag{2}$$

where "∇" is the nabla operator. Equation (2) can also be written in the integral form (see Appendix A):

$$\oint_{S(t)} \rho^{\mathrm{f}} \boldsymbol{v}^{\mathrm{f}} \bullet \boldsymbol{n} \mathrm{d}S = 0 \tag{3}$$

of special interest to the finite volume discretization presented below in Section 2.3.2. Is important to note, as explained in details in Appendix A, that for a moving frame of reference, mass conservation is written as in Eq. (3) if the moving control volume $V(t)$ satisfies the *space or geometric conservation law* [58]:

$$\left.\frac{\partial}{\partial t}\right|_{\boldsymbol{\chi}} \int_{V(t)} \mathrm{d}V = \oint_{S(t)} \boldsymbol{\omega} \bullet \boldsymbol{n} \mathrm{d}S \tag{4}$$

which shows that the volume of control volume V changes due to the movement of its surface S. If Eq. (4) is not satisfied by the numerical method that solves Eq. (3), source term could appear on it, leading to the divergence of the numerical procedure.

- Momentum equation, derived from the balance of linear momentum: in integral conservative ALE form, as shown in Appendix A, is written as:

$$\left.\frac{\partial}{\partial t}\right|_{\boldsymbol{\chi}} \int_{V(t)} \rho^{\mathrm{f}} \boldsymbol{v}^{\mathrm{f}}\left(\boldsymbol{x}, t\right) \mathrm{d}V + \oint_{S(t)} \rho^{\mathrm{f}} \boldsymbol{v}^{\mathrm{f}} \boldsymbol{c} \bullet \boldsymbol{n} \mathrm{d}S = \oint_{S(t)} \boldsymbol{\sigma}^{\mathrm{f}} \bullet \boldsymbol{n} \mathrm{d}S + \int_{V(t)} \boldsymbol{f}_b^{\mathrm{f}} \mathrm{d}V \tag{5}$$

where $\boldsymbol{f}_b^{\mathrm{f}}$ represents the body forces field per volume and $\boldsymbol{\sigma}^{\mathrm{f}}$ is the Cauchy stress tensor, both for the fluid flow; the bar with $\boldsymbol{\chi}$ on the temporal term means that the derivative is calculated with $\boldsymbol{\chi}$ fixed; $\boldsymbol{n}$ is the unit normal vector to S pointing outward. Note the convective velocity in the advective term.

For a Newtonian fluid, the constitutive equation relating the Cauchy stress tensor with the velocity field is:

$$\boldsymbol{\sigma}^{\mathrm{f}} = -p\boldsymbol{I} + \underbrace{\mu^{\mathrm{f}}\left(\nabla \boldsymbol{v}^{\mathrm{f}} + \nabla^T \boldsymbol{v}^{\mathrm{f}}\right) - \frac{2}{3}\mu^{\mathrm{f}}\left(\nabla \bullet \boldsymbol{v}^{\mathrm{f}}\right)\boldsymbol{I}}_{\boldsymbol{\tau}} \tag{6}$$

where $\boldsymbol{I}$ is the second order identity tensor, p is the pressure field and the under brace indicates the viscous part of $\boldsymbol{\sigma}^{\mathrm{f}}$, $\boldsymbol{\tau}$.

Substituting Eq. (6) into Eq. (5) and using Eq. (2) after rearranging we obtain:

$$\left.\frac{\partial}{\partial t}\right|_{\boldsymbol{\chi}} \int_{V(t)} \rho^{\mathrm{f}} \boldsymbol{v}^{\mathrm{f}}\left(\boldsymbol{x}, t\right) \mathrm{d}V + \oint_{S(t)} \rho^{\mathrm{f}} \boldsymbol{v}^{\mathrm{f}} \boldsymbol{c} \bullet \boldsymbol{n} \mathrm{d}S = -\oint_{S(t)} p \boldsymbol{n} \mathrm{d}S + \oint_{S(t)} \mu^{\mathrm{f}} \nabla \boldsymbol{v}^{\mathrm{f}} \bullet \boldsymbol{n} \mathrm{d}S \qquad (7)$$

These forms of the mass conservation and momentum balance principles, Eqs. (3) and (7) respectively, will be very useful for the presentation of the Finite Volume discretization.

Boundary and Initial Conditions

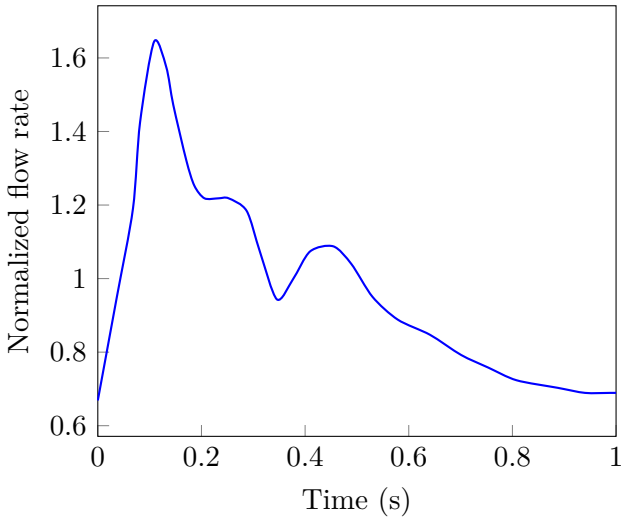
Inspecting the governing equations, we identify the flow velocity and pressure field as the unknowns, both as functions of spatial and time independent variables. Therefore, appropriate boundary conditions must be given for them.

A trivial initial condition is usually used, however we chose to use the numerical solution of the flow velocity and pressure fields from a simulation considering the aneurysm wall as rigid. As we will see in Section 2.3.3, since the coupling technique is based on a Newton method for solving non-linear systems of equations, using an initial condition closer to the solution greatly improves convergence.

The conditions at each domain boundary for velocity and pressure are:

- Inlet: the inlet is a cross section located in the parent artery of the aneurysm – see Fig. 6 – which depends on the aneurysm branch location. The condition imposed is a specified time-varying velocity, corresponding to the flow pulse from the beginning of systole until the end of the diastole. Such waveform profile is shown in Fig. 8. Since the aneurysms studied here are located in different bifurcations of the brain vessels tree, we calculated the inlet velocity considering first the pulsatile *normalized* blood flow rate profile shown in Fig. 8 as the flow waveform for the different vessels of the brain arteries tree. This profile was measured in the internal carotid by Ford et al. [59] where the normalization is made with respect to the temporal mean blood flow rate of each measured profile. Therefore, to find the *dimensional* profile we multiplied the normalized one by the mean blood flow rate of the artery of interest. The mean blood flow rate, $\bar{q}_a$, for different portions of the brain vessels tree was provided by Zarrinkoob et al. [60] who measured it as a percentage of the total blood flow rate to the brain vessels for normal subjects (11.95 ± 2.05) ml/s, as shown in Fig. 9, which presents the mean values and the standard deviation. Finally, the

Figure 8 – Experimental normalized flow rate for the internal carotid – normalization with respect to the temporal mean blood flow rate of each measured profile.

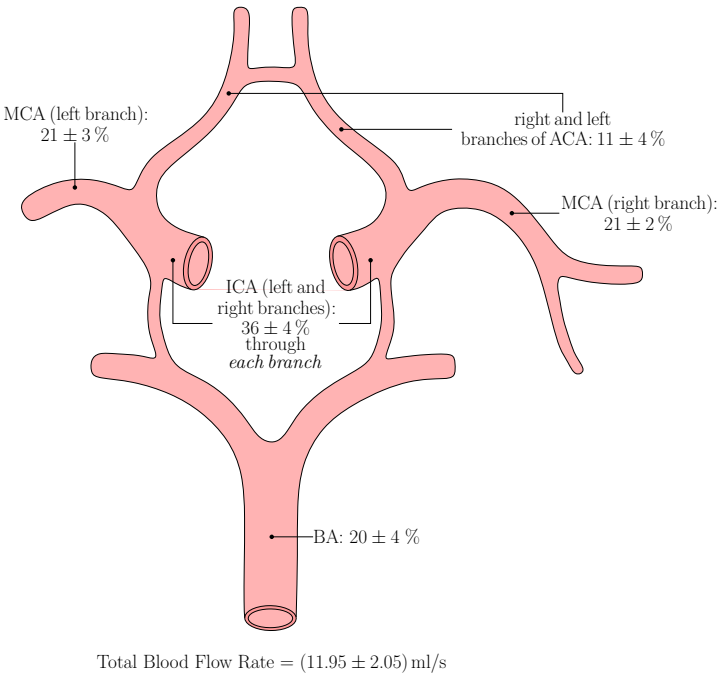


Source: Ford et al. [59].

velocity profile can be computed using the known cross sectional area of the inlet section (calculated from the fluid mesh). The pressure condition at the inlet is the locally parabolic one, i.e., pressure gradient is set to zero at the inlet;

- Outlets: the outlets are located on the vessels after the aneurysm bifurcation. Even for incompressible flow, it is important to use the real level of pressure in the FSI

Figure 9 – Mean blood flow rate through the arteries of the brain as a percentage of the total blood flow rate entering the brain: (11.95 ± 2.05) ml/s, with each respective standard deviation.



Source: prepared by the author with data from Zarrinkoob et al. [60].

context because this information is interpolated as a boundary condition for the solid problem. Therefore, we specified a constant pressure, equal to the average pressure level in the human body $\approx 100\,\text{mmHg}$ (13,333 Pa);

- Wall: This boundary corresponds to the FSI interface, Γ^{fs}. We present the details of this boundary condition below in Section 2.2.3.

2.2.2 Solid Model for the Aneurysm and Artery Walls Tissue

Physical Modeling

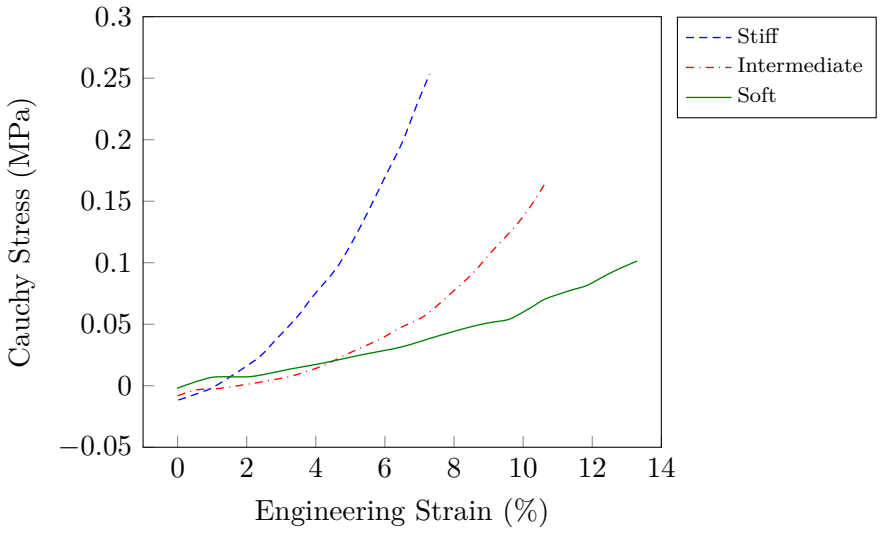
The solid domain of the problem is the artery and aneurysm walls with a specified uniform thickness found in the literature and we chose the elastic isotropic model to describe its mechanical behavior. We will analyze both the linear and non-linear (for large deformations) elastic models.

The artery wall tissue is composed of three different layers: *intima*, *media* and *adventitia*; each one having different cells in its constitution [61]. Regarding its rheology, the artery tissue does not behave as a Hookean solid, i.e., obeying Hooke's law [61, 62], on the contrary, it presents a non-linear behavior of the artery wall: models such as elastic non-linear (for large deformations) or a hyperelastic solid are usually used [27, 39, 63]. A good presentation of the constitutive relation of an artery wall can be found in Fung [61].

Recently, some studies described the mechanical behavior of a set of intracranial aneurysms' wall through traction tests to failure performed using strips of the aneurysm wall. Figure 10 presents the average stress-strain curve of an aneurysm tissue for different status of the aneurysm: unruptured (stiff tissue) and pre-ruptured (intermediate) or ruptured aneurysms (soft), as reported by Costalat et al. [42], where it is possible to see a clear non-linear behavior.

The mechanical properties of the wall tissue were considered uniform and constant: $\rho^{\text{s}} = 1{,}000\,\text{kg/m}^3$, $E = 1\,\text{MPa}$ and $\nu^{\text{s}} = 0.45$ [48]. Depending on the case, a uniform thickness of 0.1 mm or 0.15 mm for the aneurysm and artery walls were used. We relied on values found in the literature because the measurement these properties, like Young's modulus and Poisson's ratio for example, of living tissues is still difficult. Moreover, the wall thickness is also hard to measure due to poor resolution of the images used.

Figure 10 – Average strain-stress curves constructed from traction tests of rectangular strips of an intracranial aneurysm wall tissue for different stages of the aneurysm: unruptured (stiff) and pre-ruptured (intermediate) or ruptured (soft).



Source: Costalat et al. [42].

Mathematical Modeling

In Solid Mechanics, the Lagrangian description is usually used, therefore the differential operators in the following equations are calculated as functions of the material coordinates, $\boldsymbol{\xi}$. This approach is usually called *total Lagrangian* [56]: all variables such as stresses and deformations are referred to the *referential domain*, which coincides with the initial configuration of the solid (the solid at the initial time). Hence, in the total Lagrangian approach, the stress and deformation are represented by the *nominal stress tensor*, $\boldsymbol{P}$, a multiaxial extension of the engineering stress, and the deformation gradient tensor, $\boldsymbol{F}$, respectively [56]. The last one is defined as the Jacobian matrix of the solid motion, and is expressed as a function of the solid displacement, $\boldsymbol{u}$ (see Appendix B):

$$\boldsymbol{F} = \boldsymbol{I} + \nabla_0 \boldsymbol{u} \tag{8}$$

We use the lower script "0" for differential operators calculated at the initial material configuration. Therefore, using index notation:

$$\nabla_0(\bullet) \equiv \boldsymbol{e}_i \frac{\partial(\bullet)}{\partial \xi_i} \tag{9}$$

with a Cartesian coordinate system for the initial configuration with basis vector $\boldsymbol{e}_i$.

The balance of linear momentum is a widely used principle in Solid Mechanics, and it

is written in the following form for a deformable solid under defined boundary conditions:

$$\rho_0^{\mathrm{s}} \frac{\partial^2 \boldsymbol{u}}{\partial t^2} = \rho_0^{\mathrm{s}} \boldsymbol{g} + \nabla_0 \bullet \boldsymbol{P} \tag{10}$$

where $\boldsymbol{g}$ is the gravitational acceleration (accounting as a body force). It is important to note that Eq. (10) can also be written as a function of the Cauchy stress, $\boldsymbol{\sigma}^{\mathrm{s}}$, leading to the same form but, instead of $\boldsymbol{P}$, it would appear $\boldsymbol{\sigma}^{\mathrm{s}}$ and the *initial* solid density, ρ_0^{s}, would be substituted by the *current* density, ρ^{s}. The reader is referred to Belytschko et al. [56] for any further detail on this matter.

To close the problem we invoke a constitutive relation for the solid, which is intrinsic to the material itself. There are several constitutive equations suitable for different solid behavior, for example: elastic, hyperelastic, hypoelastic, plasticity, viscoelasticity. These models are described in detail in Belytschko et al. [56]. Before presenting the equation for the aneurysm model, we must mention other forms of stress and strain measurements. Tensors such as $\boldsymbol{P}$ and $\boldsymbol{F}$ are not suitable to construct constitutive relations [56] ($\boldsymbol{P}$ is not symmetric and $\boldsymbol{F}$ does not vanish for the solid rotation movement). However, the second Piola-Kirchhoff stress tensor, $\boldsymbol{S}$, and the Green-Lagrange strain tensor, $\boldsymbol{E}$, respectively, are more suitable for that purpose [56]. These two tensors are not common in Mechanical Engineering applications, but they are found in specific applications. Figure 11 shows the different measurements of strain and stress commonly found in Mechanical Engineering for one dimensional body deformation. We can see that the Green-Lagrange strain tensor presents a non-linear behavior. For further information about these variables, the total Lagrangian formulation and the equations presented below in this text consult Appendix B, where all the demonstrations are performed.

It is possible to show that the nominal stress is related to the second Piola-Kirchhoff stress in the following way (see Appendix B):

$$\boldsymbol{P} = \boldsymbol{S} \bullet \boldsymbol{F} \tag{11}$$

and the tensor $\boldsymbol{S}$ is related to the Cauchy stress through the equation:

$$\boldsymbol{\sigma}^{\mathrm{s}} = \frac{1}{det(\boldsymbol{F})} \boldsymbol{F} \bullet \boldsymbol{S} \bullet \boldsymbol{F}^T \tag{12}$$

Using the definition of the Green-Lagrange strain tensor, it is possible to show that (consult Appendix B):

$$\boldsymbol{E} = \frac{1}{2}\left(\nabla_0 \boldsymbol{u} + \nabla_0^T \boldsymbol{u} + \nabla_0 \boldsymbol{u} \bullet \nabla_0^T \boldsymbol{u}\right) \tag{13}$$

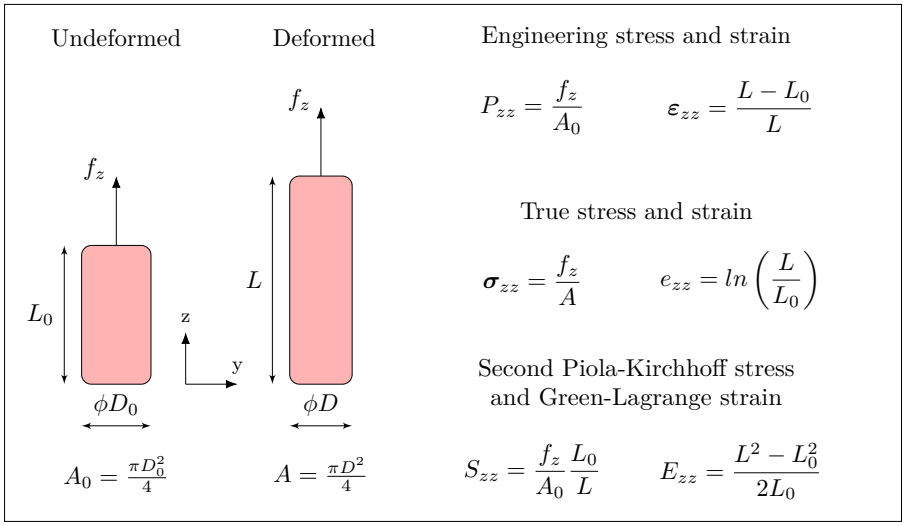
Here, we note that the strain tensor $\boldsymbol{E}$ has a linear part (the first two terms in the right-hand side of Eq. (13)) and the last term represents the non-linear part. This makes it suitable for measuring large deformations in elastic solids characterizing a non-linear behavior. In their review, Isaksen et al. [48] show that the non-linear elastic solid is the most used model for aneurysms and vessels walls. But still there are researchers trying to find the best solid model - see for example Torii et al. [27]. In this work, we use a full non-linear elastic model: the often called *Saint Venant-Kirchhoff* solid. For the isotropic case, the constitutive relation is given by:

$$\boldsymbol{S} = 2\mu^{\mathrm{s}}\boldsymbol{E} + \lambda^{\mathrm{s}} tr(\boldsymbol{E})\boldsymbol{I} \tag{14}$$

where μ^{s} and λ^{s} are the Lamé's constants related to Young's modulus and Poisson's ratio of the material:

$$\mu^{\mathrm{s}} = \frac{E}{2(1+\nu^{\mathrm{s}})} \tag{15}$$

Figure 11 – Different measurements of stress and strain for the uniaxial case.



Source: adapted from Cardiff [64].

$$\lambda^{\mathrm{s}} = \begin{cases} \frac{\nu^{\mathrm{s}} E}{(1+\nu^{\mathrm{s}})(1-\nu^{\mathrm{s}})} & \text{plane stress state} \\ \frac{\nu^{\mathrm{s}} E}{(1+\nu^{\mathrm{s}})(1-2\nu^{\mathrm{s}})} & \text{plane strain and 3D cases} \end{cases} \tag{16}$$

Substituting Eqs. (8), (11), (13) and (14) into Eq. (10), after rearrangement, we find:

$$\begin{aligned} \rho_0^{\mathrm{s}} \frac{\partial^2 \boldsymbol{u}}{\partial t^2}(\boldsymbol{\xi}, t) - \nabla_0 \bullet \left[(2\mu^{\mathrm{s}} + \lambda^{\mathrm{s}}) \nabla_0 \boldsymbol{u}\right] = & \nabla_0 \bullet \left[-\left(\mu^{\mathrm{s}} + \lambda^{\mathrm{s}}\right) \nabla_0 \boldsymbol{u} + \mu^{\mathrm{s}} \nabla_0^T \boldsymbol{u} + \lambda^{\mathrm{s}} tr(\nabla_0 \boldsymbol{u}) \boldsymbol{I} \right] + \\ & \underline{\nabla_0 \bullet \left[\mu^{\mathrm{s}} \left(\nabla_0 \boldsymbol{u} \bullet \nabla_0^T \boldsymbol{u} \right) + \frac{1}{2} \lambda^{\mathrm{s}} tr\left(\nabla_0 \boldsymbol{u} \bullet \nabla_0^T \boldsymbol{u} \right) \boldsymbol{I} \right]} + \\ & \underline{\nabla_0 \bullet \left(\boldsymbol{S} \bullet \nabla_0 \boldsymbol{u} \right)} \end{aligned} \tag{17}$$

where we dropped the body forces term since they are negligible. The first term at the right-hand side originates from the linear part of the Green-Lagrange strain tensor and the underlined terms hold the non-linear characteristics of this type of solid. Equation (17), together with Eq. (14), can be solved for the solid displacement field $\boldsymbol{u}$.

Elastic Linear Model

The non-linear elastic model presented above is a generalization of Hooke's law for large deformations. Since we will also use the elastic linear model to analyze the deformations in the aneurysm wall, we present here its constitutive equations derived as particular cases of the equations presented above.

The Green-Lagrange strain tensor, Eq. (13), is developed for large deformations, but if the deformations are small, then the quadratic term in Eq. (13) will be small compared to the linear terms. Therefore, neglecting the non-linear term, yields the classical Cauchy strain tensor for small deformations [61]:

$$\boldsymbol{\varepsilon} = \frac{1}{2} \left(\nabla_0 \boldsymbol{u} + \nabla_0^T \boldsymbol{u} \right) \tag{18}$$

In this case, it can be shown that the second Piola-Kirchhoff stress tensor reduces to Cauchy stress tensor [56]. Therefore, the constitutive equation, Eq. (14), reduces to the isotropic Hooke's law:

$$\boldsymbol{\sigma}^{\mathrm{s}} = 2\mu^{\mathrm{s}} \boldsymbol{\varepsilon} + \lambda^{\mathrm{s}} tr(\boldsymbol{\varepsilon}) \boldsymbol{I} \tag{19}$$

Following the same substitutions of last section, it can be shown that the motion governing

equation of an elastic linear solid is:

$$\rho_0^{\mathrm{s}} \frac{\partial^2 \boldsymbol{u}}{\partial t^2}(\boldsymbol{\xi}, t) - \nabla_0 \bullet \left[(2\mu^{\mathrm{s}} + \lambda^{\mathrm{s}}) \nabla_0 \boldsymbol{u}\right] = \nabla_0 \bullet \left[-(\mu^{\mathrm{s}} + \lambda^{\mathrm{s}}) \nabla_0 \boldsymbol{u} + \mu^{\mathrm{s}} \nabla_0^T \boldsymbol{u} + \lambda^{\mathrm{s}} tr(\nabla_0 \boldsymbol{u}) \boldsymbol{I}\right] \tag{20}$$

Boundary and Initial Conditions

Inspecting the governing equations, the solid displacement field is the only unknown for the solid problem, being space and time-dependent. Therefore, proper boundary conditions are provided to close the problem.

The initial condition, as for the fluid case, is the numerical solution of the simulation considering only the wall as part of the problem. Using the stress distribution on the wall from the flow solution, a displacement field is obtained and hence used as initial condition.

The following boundary conditions were used:

- For the adjacent sections of the arteries – see Fig. 6 –, the displacement was set to zero;

- Internal and external surfaces of the aneurysm and artery walls: on the internal and external surfaces of the solid domain a Neumann boundary condition was used, derived from the elastic linear constitutive relation:

$$\boldsymbol{t}^{\mathrm{s}} = \left[(2\mu^{\mathrm{s}} + \lambda^{\mathrm{s}}) \nabla_0 \boldsymbol{u} + \mu^{\mathrm{s}} \nabla_0^T \boldsymbol{u} + \lambda^{\mathrm{s}} tr(\nabla_0 \boldsymbol{u}) \boldsymbol{I} - (\lambda^{\mathrm{s}} + \mu^{\mathrm{s}}) \nabla_0 \boldsymbol{u}\right] \bullet \boldsymbol{n}^{\mathrm{s}} \tag{21}$$

  where $\boldsymbol{t}^{\mathrm{s}}$ is the traction – force per unit area – on the surface, which depends on the stresses and pressure acting on the surface and $\boldsymbol{n}^{\mathrm{s}}$ is the unit normal vector to the surface pointing outwards. Rearranging Eq. (21) yields:

$$(\nabla_0 \boldsymbol{u}) \bullet \boldsymbol{n} = \frac{\boldsymbol{t}^{\mathrm{s}} - \left[\mu^{\mathrm{s}} \nabla_0^T \boldsymbol{u} + \lambda^{\mathrm{s}} tr(\nabla_0 \boldsymbol{u}) \boldsymbol{I} - (\lambda^{\mathrm{s}} + \mu^{\mathrm{s}}) \nabla_0 \boldsymbol{u}\right] \bullet \boldsymbol{n}^{\mathrm{s}}}{2\mu^{\mathrm{s}} + \lambda^{\mathrm{s}}} \tag{22}$$

  that corresponds to a displacement gradient specification also known as a Neumann boundary condition. The gradients in the right hand side of Eq. (22) are calculated explicitly.

  On the inner surface of the aneurysm and artery walls – the FSI interface –, $\boldsymbol{t}^{\mathrm{s}}$ is evaluated using the dynamic condition at the FSI interface, as will be show in

Section 2.2.3.

On the outer surface, Eq. (22) still applies, however the traction $\boldsymbol{t}^{\mathrm{s}}$ is due only to an uniform pressure applied on it, according to:

$$\boldsymbol{t}^{\mathrm{s}} = -p\boldsymbol{n}^{\mathrm{s}} \tag{23}$$

where p on the outer surface is approximately 5 mmHg and corresponds to the intracranial pressure.

2.2.3 Physical Condition on the FSI interface

Regarding the boundary condition on the fluid-solid interface, the formulation presented is usually called *Dirichlet-Neumann formulation* of the FSI problem because the flow equations are solved for a specified velocity at Γ^{fs} due to the kinematic condition that guarantees the continuity of velocity at this boundary:

$$(\boldsymbol{v}^{\mathrm{f}})_{\Gamma^{\mathrm{fs}}} = (\boldsymbol{v}^{\mathrm{s}})_{\Gamma^{\mathrm{fs}}} = \left(\frac{\mathrm{d}\boldsymbol{u}}{\mathrm{d}t}\right)_{\Gamma^{\mathrm{fs}}} \tag{24}$$

whereas the solid equation is solved with an imposed traction on Γ^{fs} due to the dynamic condition of traction continuity at the interface, expressed as:

$$\underbrace{\left(\boldsymbol{\sigma}^{\mathrm{f}} \cdot \boldsymbol{n}^{\mathrm{f}}\right)_{\Gamma^{\mathrm{fs}}}}_{\boldsymbol{t}^{\mathrm{f}}} + \underbrace{(\boldsymbol{\sigma}^{\mathrm{s}} \cdot \boldsymbol{n}^{\mathrm{s}})_{\Gamma^{\mathrm{fs}}}}_{\boldsymbol{t}^{\mathrm{s}}} = \mathbf{0} \tag{25}$$

and therefore, this last condition gives $\boldsymbol{t}^{\mathrm{s}}$ of Eq. (22), which is a Neumann boundary condition. In Eq. (25), $\boldsymbol{n}^{\mathrm{f}}$ and $\boldsymbol{n}^{\mathrm{s}}$ are the normal vectors on Γ^{fs} pointing outwards, respectively, of the solid and fluid domain.

2.3 Numerical Methods

To solve the system of equations governing the FSI problem – Eqs. (3), (7) and (17) – under the boundary conditions presented in the Sections 2.2.1 to 2.2.3 we chose the Finite Volume Method [44, 65] since is one of the most used numerical methods for CFD applications and is beginning to be used for Solid Mechanics problems [66, 67]. We used the open-source package OpenFOAM-Extend [68] or foam-extend, as it is usually called,

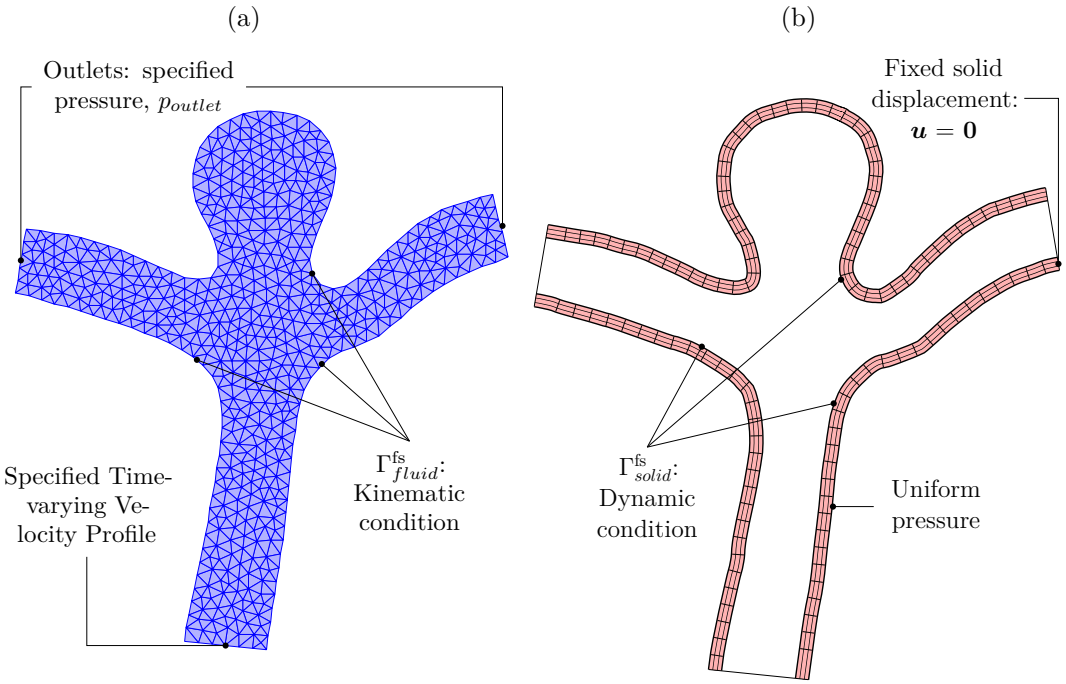
which has a specific extension providing a solver for FSI problems. We present next the discretization procedure in two parts: the discretization of the spatial and temporal domains and the discretization of the equations presented in the Section 2.2. To couple the fluid and solid problems in a partitioned context, the solver uses a method called Interface Quasi-Newton-Implicit Jacobian Least-Squares (IQN-ILS) [69].

2.3.1 Spatial and Temporal Discretization

The temporal discretization was performed splitting the time domain into a finite-number of uniform time-steps Δt and the governing equations were solved in a time-marching manner. The partitioned methodology implies the spatial discretization of the solid and fluid domains separately, yielding two computational meshes. The aneurysms geometries were obtained from reconstructed surfaces of digital subtraction angiography (DSA) provided by Dr. Carlos Eduardo Baccin and extracted using the open-source library Vascular Modeling Toolkit (VMTK®). According to its website "VMTK® is a collection of libraries and tools for 3D reconstruction, geometric analysis, mesh generation and surface data analysis for image-based modeling of blood vessels". We used VMTK® to segment the vessels and to generate the aneurysm surface. The surface can then be exported in a STL format file. The surfaces are the boundaries of the fluid domain and its computational mesh was created using VMTK®, Netgen (an open-source automatic tetrahedral mesh generator) and some utilities of the foam-extend package. The use of several softwares for generating one mesh was necessary to guarantee an initial mesh with good quality and boundary layer refinement at the aneurysm wall. The solid mesh was created extruding the aneurysm surface on its normal outward direction using the foam-extend utility `extrudeMesh`, which generates a mesh with triangular prismatic elements. Figure 12 shows a schematic two-dimensional (2D) representation of the resulting meshes.

The DSA file is a 3D pixelized image that is used to identify the brain vessels tree. Figure 13 shows a volume rendering representation of the image (visualized with ParaView®, an open-source library for data visualization, as explained in Section 2.5) for aneurysm case 13 studied here. We first used VMTK® utility `vmtkimagevoiselector` to slice a cube of the DSA image, known as the *Volume of Interest (VOI)*, that enclosures only the aneurysm and its closest surrounding vessels. Then, we used VMTK® utility `vmtklevelsetsegmentation` to extract only the image of the aneurysm and its surrounding vessels from the VOI 3D

Figure 12 – Schematic 2D representation of an aneurysm and arteries meshes for (a) the fluid domain and (b) the solid meshes in the partitioned context, showing each FSI interface and the boundary conditions applied to each domain.



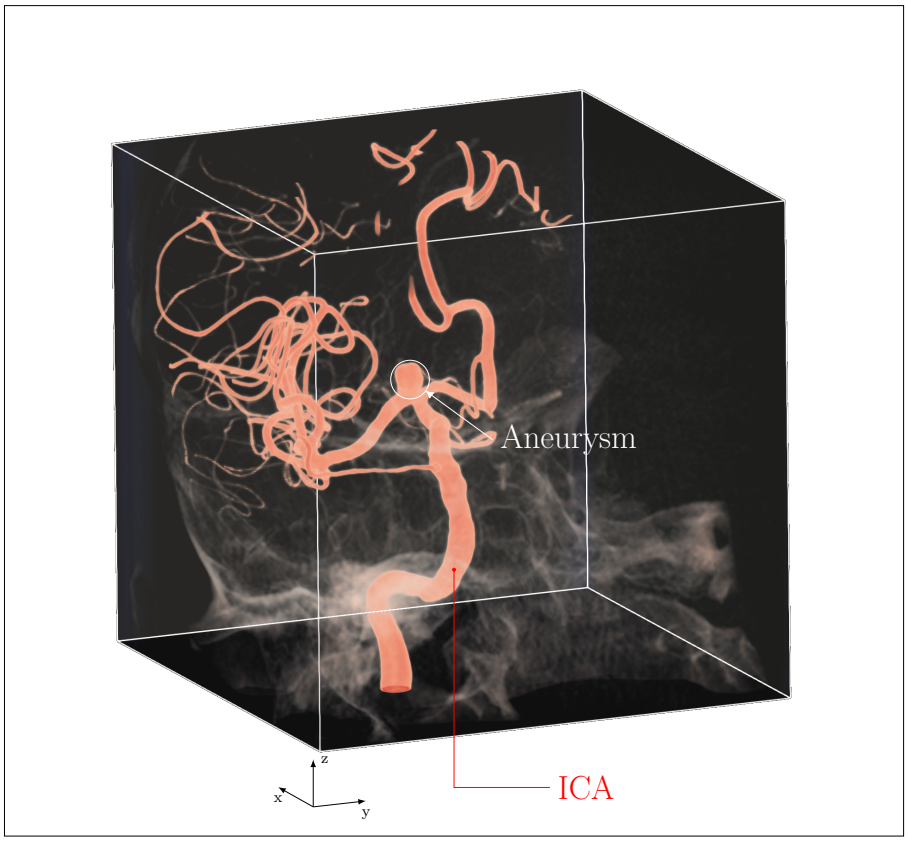
Source: prepared by the author.

image. Figure 14 shows the volume rendering representation of the VOI of case 13 where we can identify the aneurysm. Finally, a surface is constructed from the aneurysm image with the utility `vmtkmarchingcubes` as shown in Fig. 15a as a gray surface.

Before meshing, the surface quality is improved with the utility `vmtksurfacesmoothing` and the inlets and outlets are "clipped", i.e. the surrounding arteries are cut with `vmtksurfaceclipper` to correctly apply the inlet and outlets boundary conditions, yielding the final surface as a STL file used for meshing. The final surface of the two cases studied here are presented in Fig. 16 with a bounding box, showing its dimensions in millimeters. We denominated these aneurysms as "case 13" and "case 17", because it is their original enumeration in the set of aneurysms provided by Dr. Baccin. Table 3 provides the geometric characteristics of the aneurysms such as height h_d, neck diameter d_n, parent artery, aspect ratio defined in Section 1.1 and mean blood flow rate in the parent artery provided as explained in Section 2.2.1. Moreover, according to Dr. Carlos E. Baccin who provided the images, both cases are unruptured aneurysms.

Finally, the fluid and solid meshes are created from these surfaces as explained above. The fluid mesh has tetrahedral control volumes (or cells) with triangular prismatic cells

Figure 13 – Volume rendering representation of the image of a DSA of aneurysm case 13 – located at the ICA bifurcation – and the brain vessels (screen-shot taken using the visualization library ParaView®).



Source: prepared by the author with DSA images provided by Dr. Carlos E. Baccin.

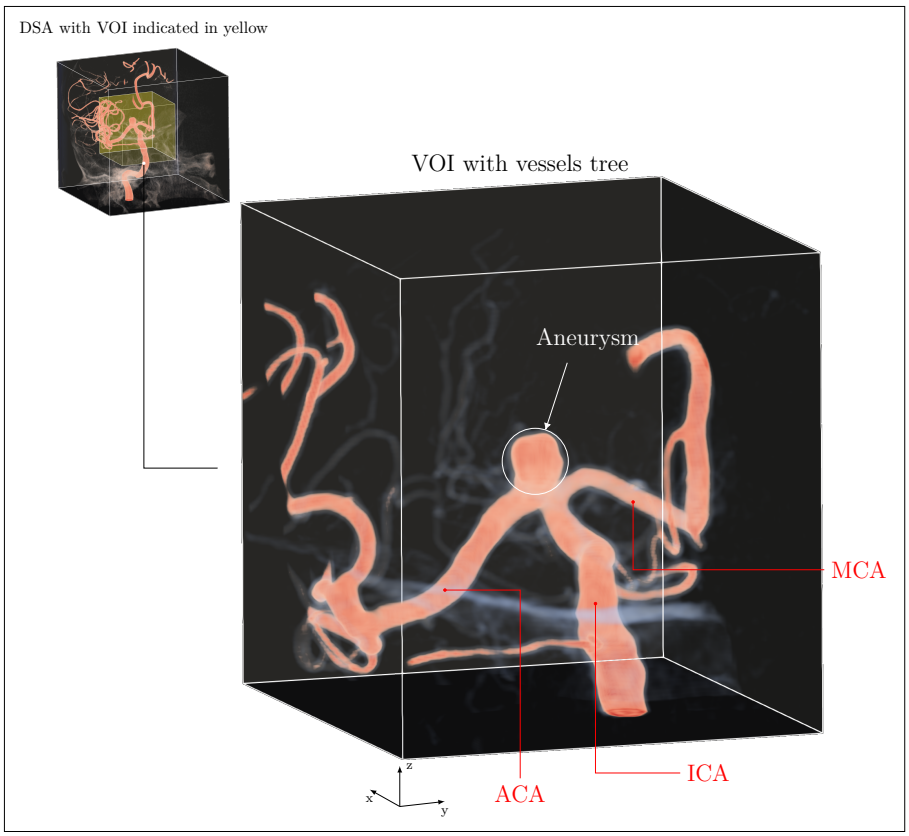
at the adjacent region of the aneurysm and arteries surfaces whereas the solid mesh is composed only by triangular prismatic cells. The final fluid and solid meshes for case 13, for example, is shown in Fig. 17, in different colors and with a detail where we can see the prismatic layer adjacent to the aneurysm wall for better resolution in the boundary-layer region and the solid mesh. The fluid and solid meshes of case 13 have 628,565 and 117,744 cells, respectively, and case 17 have 490,567 and 116,448 cells, respectively, for the fluid and solid meshes, respectively.

Table 3 – Geometric parameters of the aneurysms studied here: parent artery and its diameter d_a, neck diameter d_n, dome height h_d and diameter d_d, aspect ratio A_r and mean blood flow rate through its parent artery, $\bar{q}_a$.

	Parent Artery	d_n (mm)	h_d (mm)	d_d (mm)	d_a (mm)	A_r (-)	$\bar{q}_a$ (ml/s)
Case 13	Right ICA	4.3	5.7	5.0	3.1	1.3	4.3
Case 17	Right and Left ACA	6.1	4.3	5.0	1.8	0.7	2.5

Source: prepared by the author.

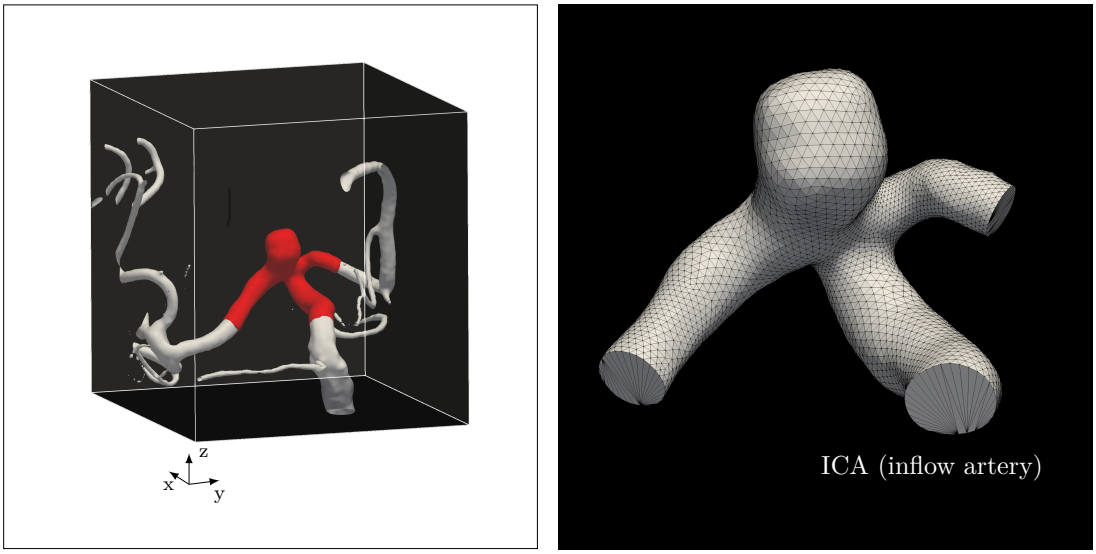
Figure 14 – Volume rendering representation of the VOI: the *volume of interest* is extracted from the DSA image (at the upper left corner, in yellow) and includes the aneurysm and its surrounding vessels (screen-shot taken using the visualization library ParaView®).



Source: prepared by the author with DSA images provided by Dr. Carlos E. Baccin.

Figure 15 – Aneurysm and arteries surface extracted with VMTK®: (a) complete extracted surface and portion clipped with the utility `vmtksurfaceclipping` in red; (b) the final triangulated surface used subsequently for meshing (corresponds to the red portion of the surface on the item (a)).

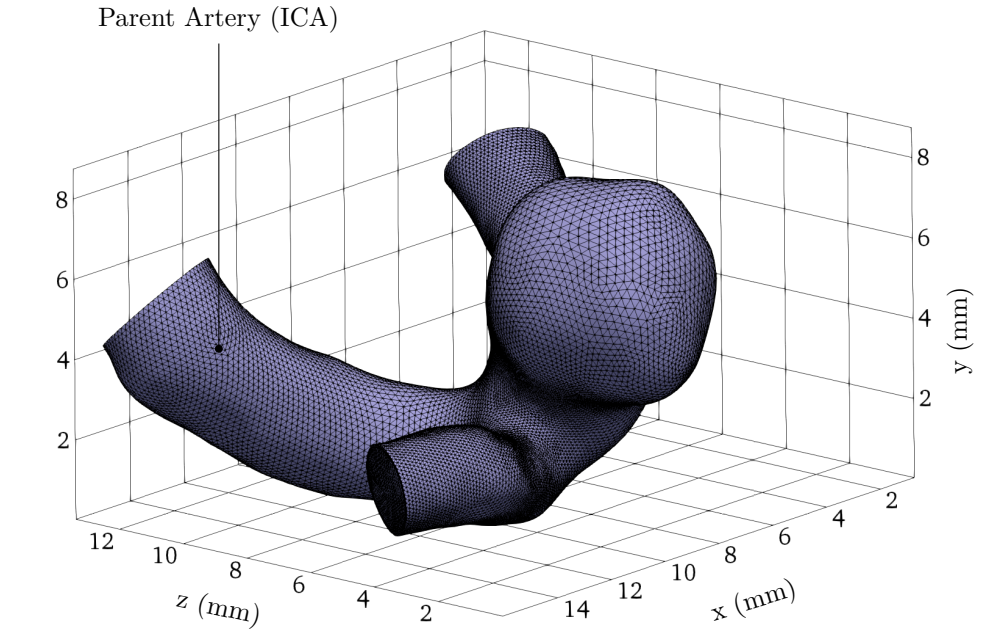
(a) (b)



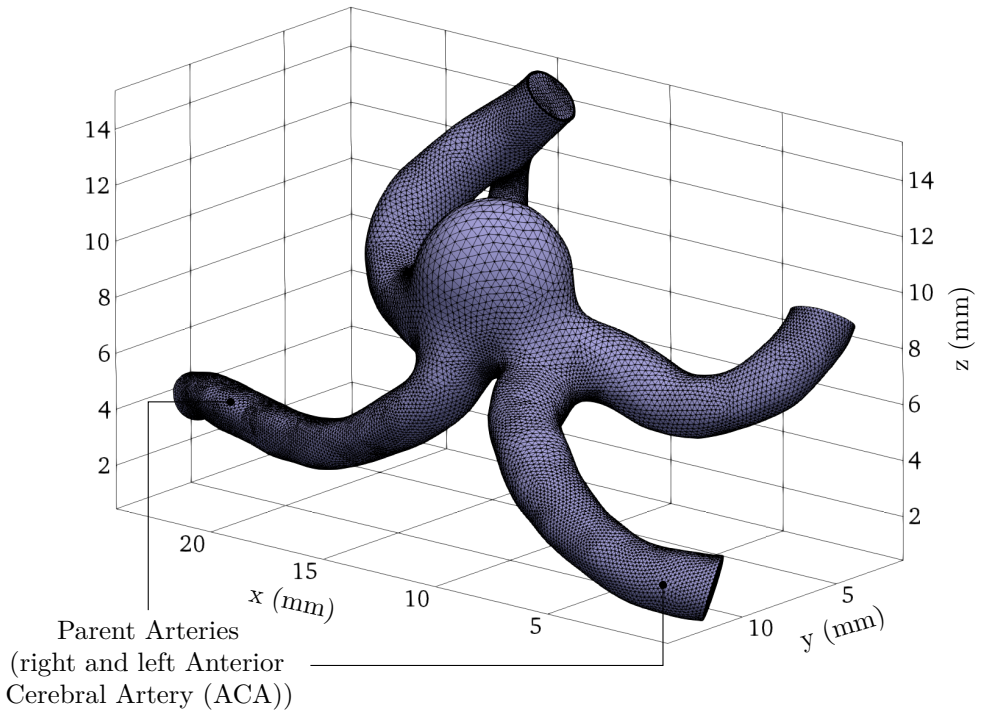
Source: prepared by the author.

Figure 16 – Aneurysm geometries used: (a) case 13, an aneurysm occurring on the ICA bifurcation and (b) case17, an aneurysm occurring on the Anterior Communicating Artery (ACoA).

(a)

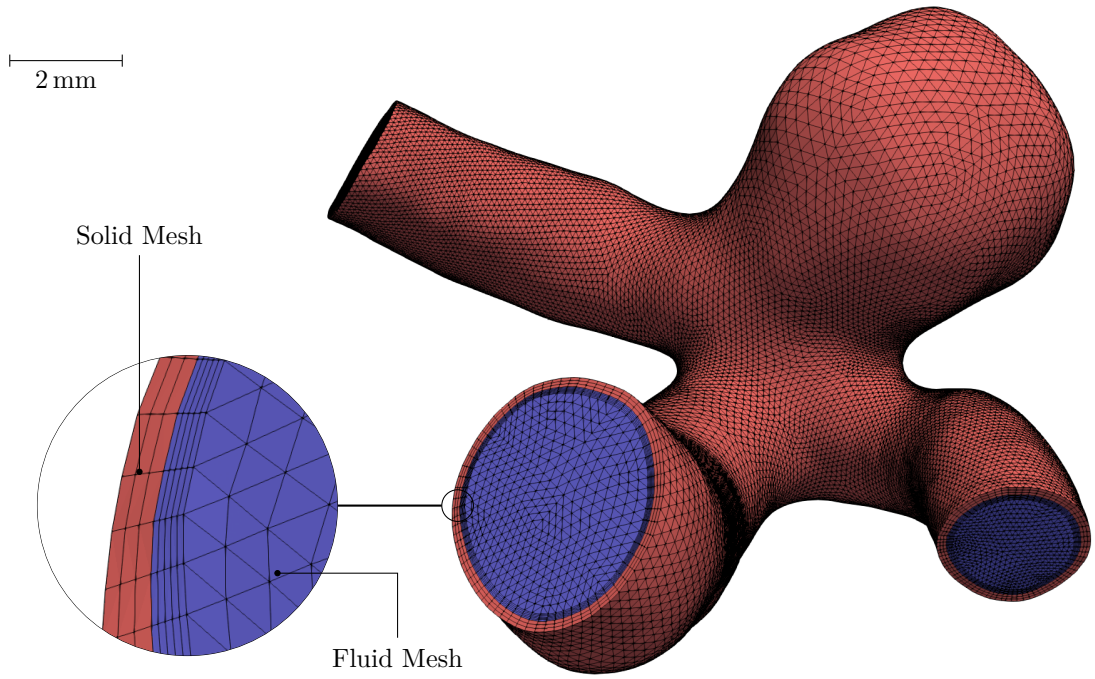


(b)



Source: prepared by the author.

Figure 17 – Fluid and solid meshes of case 13, in blue and red, respectively, with layers of refined prismatic elements adjacent to the FSI interface.



Source: prepared by the author.

Fluid Mesh Motion

The fluid mesh must be updated according to the movement of the solid (artery and aneurysm), therefore is recommended to use a dynamic mesh methodology to avoid large distortions of the cells. We used a method based on the Laplace equation's solution for the velocity of cell centroids, technique usually referred to as *Laplace smoothing*. This technique consists of solving the following equation:

$$\nabla \bullet (\gamma \nabla \boldsymbol{\omega}) = 0 \tag{26}$$

where γ is a "mesh diffusivity"; $\boldsymbol{\omega}$ is the control volume centroid velocity. Jasak and Tuković [70] and Jasak and Tuković [71] highlight that in the automatic mesh motion is important to keep the quality of the mesh, since large deformations of the moving boundaries can lead to extreme distortions of the cells, producing a solution with poor accuracy. Jasak and Tuković [70] present different ways of performing the control of the dynamic mesh quality using different functions for the diffusivity γ based on the distance to the closest moving boundary or a quality metric of the cells. We used a distance-based

approach where γ is given by:

$$\gamma = \frac{1}{l^2} \tag{27}$$

where l is the cell centroid distance to a selected moving boundary which is, for the aneurysms simulations, the aneurysm wall - the fluid-solid interface. As presented by Jasak and Tuković [70] this approach leads to a more "rigid" mesh close to the selected boundary because γ is higher, preserving the original quality of the cells. Since we used a refined layer of prismatic elements close to the aneurysm and vessels walls, this is the desired behavior.

To solve Eq. (26), the Finite Volume Method is used and its discretization is performed below in Section 2.3.2. The boundary conditions for $\boldsymbol{\omega}$ are: on inlets and outlets we specify zero velocity conditions (Dirichlet boundary condition). For the aneurysm wall, which is the fluid-solid interface, the velocity boundary condition is interpolated from the solid displacement of the last coupling iteration.

After solving Eq. (26), the cell centroid velocity, $\boldsymbol{\omega}$, is interpolated from the cell centroid to the geometric nodes. We call this interpolated velocity $\boldsymbol{\omega}_{node}$. Finally, the mesh nodes coordinates are updated by:

$$\boldsymbol{x}_{new} = \boldsymbol{x}_{old} + \boldsymbol{\omega}_{node}\Delta t \tag{28}$$

where Δt is the time-step of the fluid numerical simulation, $\boldsymbol{x}_{new}$ and $\boldsymbol{x}_{old}$ are the mesh nodes position after and before solving the equation, respectively.

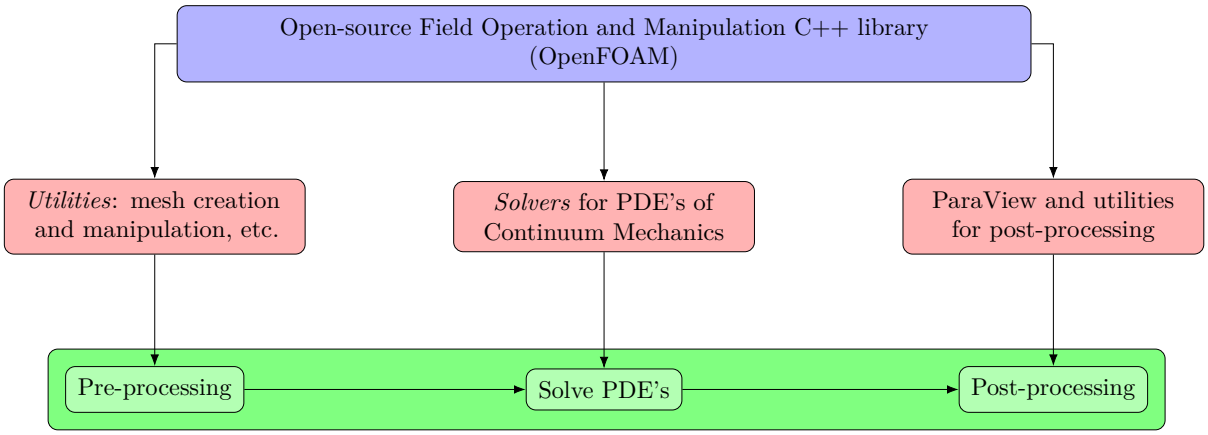
This procedure is used only for the fluid mesh because is not necessary to update the solid mesh once the formulation is the total Lagrangian (see Section 2.2.1), i.e. the motion is described with respect to the reference configuration. From the computational perspective, the solid solver implementation in foam-extend uses a non-moving mesh approach, i.e. it integrates the equations over the reference configuration.

2.3.2 Discretization of the Mathematical Model

OpenFOAM-Extend (or foam-extend) is an open-source library of classes written in C++ language (the acronym FOAM standing for "Field Operation and Manipulation"), created for executing *applications* in computer simulation of Continuum Mechanics problems. The *applications* are divided into two groups: *solvers* and *utilities*. The *solvers* contain

algorithms for solving the governing equations of problems in Continuum Mechanics. The *utilities*, in turn, are related primarily to pre- and post-processing operations: creation and manipulation of meshes, parallel processing, simulation data conversion and processing, etc. It is also possible to use other external post-processing tools such as ParaView®. Figure 18 outlines the general structure of the foam-extend. There is a third group of libraries that include generic functions and numerical models commonly used in the discretization process and/or solution of the governing equations, for example, turbulence models, non-Newtonian fluids, and dynamic mesh tools.

Figure 18 – Structure of foam-extend, providing solvers and utilities for the general steps of a numerical simulation.

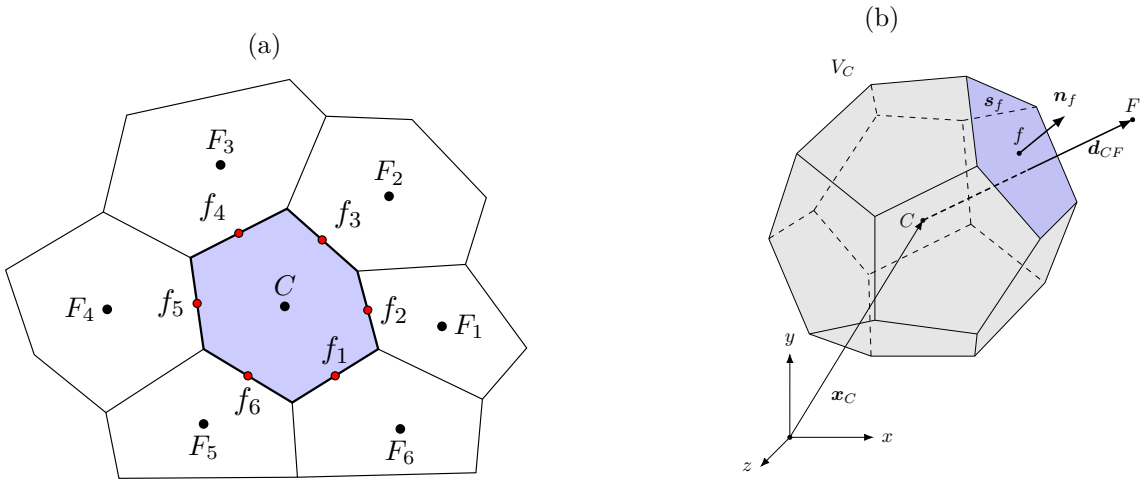


Source: prepared by the author.

OpenFOAM-Extend uses the FVM with *collocated* variables arranged in a cell-centered discretization of the governing equations, meaning that the unknown variables are stored at the computational nodes. A finite-volume mesh is composed of non-overlapping polyhedral cells with polygonal flat faces and each internal face is shared by two cells; external faces, which compose the boundaries of the domain, belong to only one cell. The meshes presented in Section 2.3.1 follow these conditions. Figure 19b shows a typical polyhedral cell with volume V_C and the centroid, or computational node, located at the point C; and Fig. 19a shows a 2D polygonal cell with its neighbours cells F's and their face centroids f's. The geometric parameters shown in these figures are needed in the finite volume discretization of the governing equations. A more detailed presentation of the FVM discretization can be found in Appendix C.

The FOAM code was started in the 1990s by a group of doctoral students at Imperial College, including Dr. Henry Weller and Dr. Hrvoje Jasak. Currently, the "OpenFOAM"

Figure 19 – (a) Polygonal control volume with centroid C of a 2D finite volume mesh, and its neighbours F_i; (b) Polyhedral control volume V_C with its geometric parameters used on the finite volume discretization.



Source: prepared by the author.

word is a registered trademark of the ESI Group, while continuing to have their code open-source under the terms of the GPL license (foam-extend-4.0, the latest release, uses version 3 of this license).

To "open the *CFD toolbox* OpenFOAM to the extensions provided by the community in the spirit of open-source development model", a branch of OpenFOAM®, the *Extend Project*, was born with Dr. Hrvoje Jasak and others contributors. The *foam-extend project*, as it is called has the same structure of the original project and, according to the *ReleaseNotes* provided with the package, "foam-extend contains bug fixes and performance improvements beyond extensions and additional features provided by community contributors". Some of these additional extensions are "missing, lost, disabled or unused by releases of the ESI Group", such as "turbomachinery applications, dynamic mesh with topological changes and support for its use with the FVM, implementation of the Finite Element Method (mainly for polyhedral mesh deformation), Finite Area Method and large contributions in Solid Mechanics modeling", and others (a complete list of the latest version, foam-extend-4.0, can be obtained from the *ReleaseNotes* of the package); it also contains FSI algorithms implemented as some of its solvers: `icoFsiFoam`, `icoFsiElasticNonLinULSolidFoam` and `fsiFoam` (this last one provided as an extension – Tuković et al. [72]). The former is used for weakly coupled FSI problems and the other two for strongly coupled ones. As we discuss in Section 2.3.3, the aneurysm FSI problem is strongly coupled. For this reason, we used in this work the solver `fsiFoam` of version foam-extend-4.0, which has implemented

the method Interface Quasi-Newton-Implicit Jacobian Least-Squares (IQN-ILS) for FSI coupling, which is also presented in Section 2.3.3.

Fluid Model Discretization

The finite volume discretization starts with the integral form of the governing equations for a control volume V_C and uses Gauss' divergence theorem to transform the volume integrals over V_C into sums of surface integrals over control volume faces. Then, to evaluate the face integrals, the classical approach is to express the fields as a linear function of space around the control volume centroid - its computational node - leading to a second-order accurate spatial discretization (see Appendix C). Our main focus here is on the discretization of Eqs. (3), (7) and (26) on a moving grid, but the complete discretization process can be found in Appendix C, where we demonstrate the finite volume discretization in detail and for further details one can consult specific literature as Moukalled et al. [44] and Versteeg and Malalasekera [73]. Furthermore, the procedure is valid only for internal cells; cells having one or more faces that belongs to the boundaries of the domain must have a special discretization for its boundary faces which depends on the type of the boundary condition. Therefore, the specific discretization procedure for boundary faces will not be presented here, but can be found in specific texts of the FVM [44, 74].

The semi-discretized momentum equation, i.e. with cell face values for the velocities of the advective and diffusive terms, and the temporal term discretized using a second-order backward Euler implicit scheme, is:

$$\begin{aligned} &\rho_C \frac{3V_C^{\mathrm{n}}(\boldsymbol{v}_C^{\mathrm{f}})^{\mathrm{n}} - 4V_C^{\mathrm{n}-1}(\boldsymbol{v}_C^{\mathrm{f}})^{\mathrm{n}-1} + V_C^{\mathrm{n}-2}(\boldsymbol{v}_C^{\mathrm{f}})^{\mathrm{n}-2}}{2\Delta t} + \sum_f \left[\dot{m}_f - (\rho^{\mathrm{f}}\boldsymbol{\omega})_f \bullet \boldsymbol{s}_f\right](\boldsymbol{v}^{\mathrm{f}})_f^{\mathrm{n}} = \\ &= \sum_f \mu_f^{\mathrm{f}} \left(\nabla \boldsymbol{v}^{\mathrm{f}}\right)_f^{\mathrm{n}} \bullet \boldsymbol{s}_f^{\mathrm{n}} + (\nabla p)_C^{\mathrm{n}} V_C^{\mathrm{n}} \end{aligned} \tag{29}$$

where the subscripts f and C represents values evaluated at a control volume faces and centroid, respectively (see Fig. 19); the superscript n represents the current time level; $\dot{m}_f = \rho^{\mathrm{f}}(\boldsymbol{v}^{\mathrm{f}})_f \bullet \boldsymbol{s}_f$ is the mass flow rate through face f which must satisfy the mass conservation principle, Eq. (3), $\boldsymbol{s}_f$ is the normal vector to face f pointing outward and $\boldsymbol{n}$ is the *unit* normal vector to f. $\dot{V}_f = \boldsymbol{\omega}_f \bullet \boldsymbol{s}_f$ is the volume swept by face f due to the spatial mesh motion per unit time; it is important to note that $\dot{V}_f$ is computed to satisfy

the discretized version of the geometric conservation law, Eq. (4):

$$\frac{\Delta V_C}{\Delta t} = \sum_f \dot{V}_f \equiv \sum_f \boldsymbol{\omega}_f \bullet \boldsymbol{s}_f \tag{30}$$

where $\frac{\Delta()}{\Delta t}$ is a discretization operator for the first order temporal derivative, using a second-order backward Euler scheme, as used for Eq. (29), it is written as:

$$\frac{\Delta V_C}{\Delta t} \equiv \frac{3V_C^{\mathrm{n}} - 4V_C^{\mathrm{n}-1} + V_C^{\mathrm{n}-2}}{2\Delta t} \tag{31}$$

as explained by Tuković and Jasak [75].

Both flow rates, $\dot{m}_f$ and $\dot{V}_f$, are evaluated using available values of the flow and mesh velocities from the last iteration to linearize the advective term (that is why we do not use superscript n on them). Note that Eq. (29) is a vector equation, i.e., it has 3 scalar equations, one for each component of $\boldsymbol{v}^{\mathrm{f}}$.

To complete the discretization procedure, face values in Eq. (29) are interpolated from cell centroid values. The velocity in the advective term, $(\boldsymbol{v}^{\mathrm{f}})_f^{\mathrm{n}}$, is interpolated using the second-order upwind scheme adapted for unstructured grids [44]:

$$(\boldsymbol{v}^{\mathrm{f}})_f = \boldsymbol{v}_C^{\mathrm{f}} + \left[2\nabla \boldsymbol{v}_C^{\mathrm{f}} - (\nabla \boldsymbol{v}^{\mathrm{f}})_f\right] \bullet \boldsymbol{d}_{Cf} \tag{32}$$

where $\boldsymbol{d}_{Cf}$ is the vector joining C and f; the velocity gradients in Eq. (32) are discretized using the least-squares method [44]. Once the gradients are discretized, $(\boldsymbol{v}^{\mathrm{f}})_f$ can be expressed in terms of the centroid values of the control volumes sharing face f:

$$(\boldsymbol{v}^{\mathrm{f}})_f = w_C \boldsymbol{v}_C^{\mathrm{f}} + w_F \boldsymbol{v}_F^{\mathrm{f}} \tag{33}$$

where w_C and w_F are weights that depends on the interpolation scheme, accounting for the influence of $\boldsymbol{v}_C^{\mathrm{f}}$ and $\boldsymbol{v}_F^{\mathrm{f}}$ on $(\boldsymbol{v}^{\mathrm{f}})_f$, respectively.

The velocity gradient normal to face f, $\left(\nabla \boldsymbol{v}^{\mathrm{f}}\right)_f \bullet \boldsymbol{s}_f^{\mathrm{n}}$, is interpolated using a skewness and non-orthogonal corrected scheme as follows (see Appendix C):

$$\nabla \phi_f \bullet \boldsymbol{s}_f = \underbrace{\frac{\phi_F - \phi_C}{d_{fn}}}_{\text{Orthogonal contribution}} + \underbrace{\frac{\boldsymbol{k}_{fF} \bullet (\nabla\phi)_F - \boldsymbol{k}_{fC} \bullet (\nabla\phi)_C}{d_{fn}}}_{\text{Non-orthogonal and skewness correction}} \tag{34}$$

where $\|\boldsymbol{d}_{fn}\| = d_{fn}\boldsymbol{n}_f$ with $d_{fn} = \boldsymbol{n}_f \bullet (\boldsymbol{x}_F - \boldsymbol{x}_C)$, where $\boldsymbol{x}_C$ and $\boldsymbol{x}_F$ are the Cartesian position vector of C and F. The correction term is due to the non-orthogonality and skewness of the unstructured mesh and is treated explicitly while the orthogonal term is evaluated implicitly. The dynamic viscosity μ_f^{f} is considered constant for the blood, but if needed could be linearly interpolated.

Substituting Eqs. (33) and (34) into Eq. (29) and after some manipulations follows the algebraic equation:

$$a_C^{\boldsymbol{v}}(\boldsymbol{v}_C^{\mathrm{f}})^{\mathrm{n}} + \sum_{F \sim NB(C)} a_F^{\boldsymbol{v}}(\boldsymbol{v}_F^{\mathrm{f}})^{\mathrm{n}} = \boldsymbol{b}_C^{\boldsymbol{v}} - (\nabla p)_C^{\mathrm{n}} V_C^{\mathrm{n}} \tag{35}$$

which is the discretized momentum equation for one finite volume or cell in *vector form* where the coefficients $a_C^{\boldsymbol{v}}$ and $a_F^{\boldsymbol{v}}$ are functions of the flow velocity. Note that the sum in Eq. (35) is computed over the neighbours of control volume C (see Fig. 19a). Since the foam-extend implementation considers the equations in a Cartesian coordinate system, the flow velocity can be written as: $\boldsymbol{v}^{\mathrm{f}} = v_x^{\mathrm{f}}\boldsymbol{i} + v_y^{\mathrm{f}}\boldsymbol{j} + v_z^{\mathrm{f}}\boldsymbol{k}$, where $\boldsymbol{i}$, $\boldsymbol{j}$ and $\boldsymbol{k}$ are vectors of the canonical basis. Therefore, the discretized momentum equation for each component of velocity is:

$$\begin{aligned}
a_C^{v_x}(v_x^{\mathrm{f}})_C^{\mathrm{n}} + \sum_F a_F^{v_x}(v_x^{\mathrm{f}})_F^{\mathrm{n}} &= b_C^{v_x} - V_C^{\mathrm{n}}\,(\nabla p_x)_C^{\mathrm{n}} \\
a_C^{v_y}(v_y^{\mathrm{f}})_C^{\mathrm{n}} + \sum_F a_F^{v_y}(v_y^{\mathrm{f}})_F^{\mathrm{n}} &= b_C^{v_y} - V_C^{\mathrm{n}}\,(\nabla p_y)_C^{\mathrm{n}} \\
a_C^{v_z}(v_z^{\mathrm{f}})_C^{\mathrm{n}} + \sum_F a_F^{v_z}(v_z^{\mathrm{f}})_F^{\mathrm{n}} &= b_C^{v_z} - V_C^{\mathrm{n}}\,(\nabla p_z)_C^{\mathrm{n}}
\end{aligned} \tag{36}$$

where the $(\nabla p_i)_C$ is the pressure gradient on direction i at the centroid C, with $i = x, y, z$. Assembling the last equations for all control volumes in the fluid mesh yields three systems of algebraic linearized equations:

$$\begin{aligned}
\mathbf{A}^{v_x}(\mathbf{v}_{\mathbf{x}}^{\mathbf{f}})^{\mathrm{n}} &= \mathbf{b}^{v_x} - V_C^{\mathrm{n}}\left\{\left(\nabla p_x\right)_C\right\} \\
\mathbf{A}^{v_y}(\mathbf{v}_{\mathbf{y}}^{\mathbf{f}})^{\mathrm{n}} &= \mathbf{b}^{v_y} - V_C^{\mathrm{n}}\left\{\left(\nabla p_y\right)_C\right\} \\
\mathbf{A}^{v_z}(\mathbf{v}_{\mathbf{z}}^{\mathbf{f}})^{\mathrm{n}} &= \mathbf{b}^{v_z} - V_C^{\mathrm{n}}\left\{\left(\nabla p_z\right)_C\right\}
\end{aligned} \tag{37}$$

where $\mathbf{A}$ is the matrix of coefficients a_C and a_F; each line of matrices $\mathbf{A}$'s presents the coefficient a_C at the diagonal element and, at the other line elements, the coefficients a_F; $\mathbf{v}_{\mathbf{x}}^{\mathbf{f}}$, $\mathbf{v}_{\mathbf{y}}^{\mathbf{f}}$ and $\mathbf{v}_{\mathbf{z}}^{\mathbf{f}}$ are the velocity solution vectors in each direction; $\mathbf{b}$ is the vector of the

source term coefficients and $\{(\nabla p_i)_C\}$ is the vector obtained from the discretization of the pressure gradient term, discussed below.

Foam-extend solves Eq. (37) in a *segregated* manner, i.e, each system is solved separately. As explained in Appendix C, Eqs. (3) and (29) represents a complex coupling problem between pressure and velocity which is solved by foam-extend using the segregated Pressure Implicit with Splitting Operators (PISO) algorithm proposed by Issa [76] (other coupling algorithms are available, consult the software User Guide for further information). This algorithm solves a pressure equation derived from the continuity equation, Eq. (3), and the discretized momentum equation, Eq. (35).

To derive the pressure equation, first we write the finite volume discretization of the continuity equation:

$$\sum_f \rho^{\mathrm{f}} (\boldsymbol{v}^{\mathrm{f}})_f \bullet \boldsymbol{s}_f = \sum_f \dot{m}_f = 0 \tag{38}$$

Then, the face velocities, $(\boldsymbol{v}^{\mathrm{f}})_f$, are evaluated from Eq. (35), which can be written for a computational node C as follows:

$$\boldsymbol{v}_C^{\mathrm{f}} + \mathbf{H}_C \left[\boldsymbol{v}^{\mathrm{f}}\right] = \mathbf{B}_C^{\boldsymbol{v}} - \mathbf{D}_C^{\boldsymbol{v}} (\nabla p)_C \tag{39}$$

where the vector operators are:

$$\mathbf{H}_C \left[\boldsymbol{v}^{\mathrm{f}}\right] \equiv \sum_F \frac{a_F^{\boldsymbol{v}}}{a_C^{\boldsymbol{v}}} \boldsymbol{v}_F^{\mathrm{f}} \tag{40}$$

$$\mathbf{B}_C^{\boldsymbol{v}} \equiv \frac{\boldsymbol{b}_C^{\boldsymbol{v}}}{a_C^{\boldsymbol{v}}} \tag{41}$$

$$\mathbf{D}_C^{\boldsymbol{v}} \equiv \frac{V_C}{a_C^{\boldsymbol{v}}} \tag{42}$$

Interpolating the flow velocity from cell centroid to face centroid is a delicate operation and it was responsible for early problems in the collocated formulation of the FVM [44, 77]. Using a linear interpolation for $(\boldsymbol{v}^{\mathrm{f}})_f$ decouples velocity and pressure, originating the known checkerboard problem. A solution was proposed by Rhie and Chow [78] and today is known as the Rhie-Chow interpolation. The original procedure starts with a

pseudo-momentum equation for the face centroid which "mimics" Eq. (39):

$$(\boldsymbol{v}^{\mathrm{f}})_f + \mathbf{H}_f\left[\boldsymbol{v}^{\mathrm{f}}\right] = \mathbf{B}_f^{\boldsymbol{v}} - \mathbf{D}_f^{\boldsymbol{v}}\left(\nabla p\right)_f \tag{43}$$

where $\mathbf{H}_f\left[\boldsymbol{v}^{\mathrm{f}}\right]$ and $\mathbf{D}_f^{\boldsymbol{v}}$ are linearly interpolated from their counterparts in the centroid of the cells sharing face f, as proposed in the original formulation. However, it is known that, if a very small time-step is used, a linear interpolation approach can produce the checkerboard problem [77, 79, 80]. Therefore, we used a *consistent* formulation presented in Tuković and Jasak [75] and implemented in foam-extend. This consistent formulation uses a modified interpolation for the terms $\mathbf{H}_f\left[\boldsymbol{v}^{\mathrm{f}}\right]$ and $\mathbf{D}_f^{\boldsymbol{v}}$ and was proposed by Yu et al. [80] which avoids the mentioned behavior for small time-steps.

Substituting Eq. (43) into Eq. (38) and rearranging yields the semi-discretized pressure equation:

$$-\sum_f (\rho^{\mathrm{f}})_f \mathbf{D}_f^{\boldsymbol{v}}\left(\nabla p\right)_f \bullet \boldsymbol{s}_f = \sum_f (\rho^{\mathrm{f}})_f \left\{\mathbf{H}_f\left[\boldsymbol{v}^{\mathrm{f}}\right] - \mathbf{B}_f^{\boldsymbol{v}}\right\} \bullet \boldsymbol{s}_f \tag{44}$$

where the right-hand side term is evaluated explicitly whereas the left hand side is made implicit. The pressure gradient normal to face f, $\left(\nabla p\right)_f \bullet \boldsymbol{s}_f$, is discretized implicitly using the skew-corrected approach, Eq. (34), which, after algebraic manipulations, can be written as a linearized algebraic equation for the pressure:

$$a_C^p p_C^{\mathrm{n}} + \sum_F a_F^p p_F^{\mathrm{n}} = b_C^p \tag{45}$$

which is the discretized pressure equation for one control volume V_C. This equation can be assembled for the whole fluid mesh, yielding a system of linearized system of equations:

$$\mathbf{A}^p \mathbf{p}^{\mathrm{n}} = \mathbf{b}^p \tag{46}$$

The PISO algorithm starts by solving the systems given by Eq. (37) using an available pressure field (at the first time-step, using an initial condition or, for later time-steps, using the values from the last iteration), generating a *momentum-satisfying* velocity field, which is considered a predictor. This predictor field is used to solve the pressure system, Eq. (46), yielding a pressure field which satisfies both momentum and continuity equations. Finally, the velocity field is updated using the new pressure solution through Eq. (39) generating a divergence-free, i.e. continuity satisfying, velocity field. The original PISO

algorithm proposed by Issa [76] recommends only two iterations over the pressure equation to achieve reasonable solution accuracy.

The system given by Eq. (37) is solved by using a preconditioned Bi-Conjugate Gradient method for asymmetric matrices [81], with convergence criterion based on a scaled normalized residual tolerance equal to 1×10^{-6} – Appendix D explains how foam-extend calculates the scaled normalized residual; the preconditioning matrix is a diagonal incomplete Cholesky for asymmetric matrices; the pressure system assembled from Eq. (44) is solved using a geometric agglomerated algebraic multi-grid solver, with scaled normalized residual tolerance equal to 1×10^{-6}.

Mesh Equation Discretization

The Laplace equation, Eq. (26), used for updating the computational and geometric nodes of the fluid mesh is also solved using the FVM. Applying the finite volume discretization to Eq. (26), i.e. integrating this equation over a moving control volume V_C yields:

$$\int_{V_C} \nabla \bullet (\gamma \nabla \boldsymbol{\omega}) \, S \mathrm{d}V = 0 \Rightarrow \oint_{\boldsymbol{s}_f} (\gamma \nabla \boldsymbol{\omega}) \bullet \boldsymbol{n} \mathrm{d}S = 0 \Rightarrow \sum_f \gamma_f \left(\nabla \boldsymbol{\omega}\right)_f \bullet \boldsymbol{s}_f = 0 \tag{47}$$

The face normal gradient is discretized using Eq. (34) with non-orthogonal and skewness correction. After substitution of Eq. (34), written for $\boldsymbol{\omega}$, in Eq. (47) and rearranging yields the discretized mesh velocity equation for V_C:

$$a_C^{\boldsymbol{\omega}} \boldsymbol{\omega}_C^{\mathrm{n}} + \sum_F a_F^{\boldsymbol{\omega}} \boldsymbol{\omega}_F^{\mathrm{n}} = \boldsymbol{b}_C^{\boldsymbol{\omega}} \tag{48}$$

As for the fluid velocity, $\boldsymbol{\omega}$ is a vector and, in the Cartesian coordinate system, can be decomposed as: $\boldsymbol{\omega} = \omega_x \boldsymbol{i} + \omega_y \boldsymbol{j} + \omega_z \boldsymbol{k}$, where $\boldsymbol{i}$, $\boldsymbol{j}$ and $\boldsymbol{k}$ are vectors of the canonical basis. Therefore, the discretized mesh velocity equation for each component of $\boldsymbol{\omega}$ is:

$$\begin{aligned} a_C^{\omega_x} (\omega_x)_C^{\mathrm{n}} + \sum_F a_F^{\omega_x} (\omega_x)_F^{\mathrm{n}} &= b_C^{\omega_x} \\ a_C^{\omega_y} (\omega_y)_C^{\mathrm{n}} + \sum_F a_F^{\omega_y} (\omega_y)_F^{\mathrm{n}} &= b_C^{\omega_y} \\ a_C^{\omega_z} (\omega_z)_C^{\mathrm{n}} + \sum_F a_F^{\omega_z} (\omega_z)_F^{\mathrm{n}} &= b_C^{\omega_z} \end{aligned} \tag{49}$$

which can be assembled for all control volumes in the fluid mesh yielding three systems of algebraic linearized equations:

$$\begin{aligned}\mathbf{A}^{\omega_x}(\boldsymbol{\omega}_\mathbf{x})^{\mathrm{n}} &= \mathbf{b}^{\omega_x}\\ \mathbf{A}^{\omega_y}(\boldsymbol{\omega}_\mathbf{y})^{\mathrm{n}} &= \mathbf{b}^{\omega_y}\\ \mathbf{A}^{\omega_z}(\boldsymbol{\omega}_\mathbf{z})^{\mathrm{n}} &= \mathbf{b}^{\omega_z}\end{aligned} \tag{50}$$

The systems in Eq. (50) are solved by a linear solver using a geometric agglomerated algebraic multi-grid solver, with scaled normalized residual tolerance equal to 1×10^{-6} – consult Appendix D for residual calculation.

Solid Model Discretization

Equation (17), governing the artery motion, is also discretized using the FVM. Integrating this equation over a polyhedral cell V_C – see Fig. 19b – gives:

$$\int_{V_C} \rho_0^{\mathrm{s}} \frac{\partial^2 \boldsymbol{u}}{\partial t^2}(\boldsymbol{\xi}, t)\mathrm{d}V - \int_{V_C} \nabla_0 \bullet [(2\mu^{\mathrm{s}} + \lambda^{\mathrm{s}})\nabla_0 \boldsymbol{u}]\mathrm{d}V = \int_{V_C} (\nabla_0 \bullet \boldsymbol{Q}_l + \nabla_0 \bullet \boldsymbol{Q}_{nl})\,\mathrm{d}V \tag{51}$$

where:

$$\boldsymbol{Q}_l = -(\mu^{\mathrm{s}} + \lambda^{\mathrm{s}})\nabla_0 \boldsymbol{u} + \mu^{\mathrm{s}}\nabla_0^T \boldsymbol{u} + \lambda^{\mathrm{s}} tr(\nabla_0 \boldsymbol{u})\boldsymbol{I} \tag{52}$$

$$\boldsymbol{Q}_{nl} = \mu^{\mathrm{s}}\left(\nabla_0 \boldsymbol{u} \bullet \nabla_0^T \boldsymbol{u}\right) + \frac{1}{2}\lambda^{\mathrm{s}} tr\left(\nabla_0 \boldsymbol{u} \bullet \nabla_0^T \boldsymbol{u}\right)\boldsymbol{I} + \boldsymbol{S} \bullet \nabla_0 \boldsymbol{u} \tag{53}$$

are the linear and non-linear parts. We can invert the order of the temporal derivative because V_C is a material control volume and $\frac{\partial^2 \boldsymbol{u}}{\partial t^2}$ is evaluated keeping the material coordinates constant; then, using the mid-point rule to evaluate the integral with second-order accuracy as follows:

$$\int_{V_C} \rho_0^{\mathrm{s}} \frac{\partial^2 \boldsymbol{u}}{\partial t^2}(\boldsymbol{\xi}, t)\mathrm{d}V = \left(\rho_0^{\mathrm{s}}\right)_C \frac{\partial^2}{\partial t^2} \underbrace{\left(\int_{V_C} \boldsymbol{u}\mathrm{d}V\right)}_{\approx \boldsymbol{u}_C V_C} = (\rho_0^{\mathrm{s}})_C V_C \frac{\partial^2 \boldsymbol{u}_C}{\partial t^2} \tag{54}$$

The second order derivative is discretized using a second-order accurate backward scheme, to unify the discretization of the temporal terms between the fluid and solid model discretization. As presented by Tuković et al. [72], this is achieved using the second-order

discretization of the first-order temporal derivative, as follows:

$$\left(\frac{\partial^2 \boldsymbol{u}_C}{\partial t^2}\right)^{\mathrm{n}} \equiv \left[\frac{\partial}{\partial t}\left(\frac{\partial \boldsymbol{u}_C}{\partial t}\right)\right]^{\mathrm{n}} \approx \frac{3\left(\frac{\partial \boldsymbol{u}_C}{\partial t}\right)^{\mathrm{n}} - 4\left(\frac{\partial \boldsymbol{u}_C}{\partial t}\right)^{\mathrm{n}-1} + \left(\frac{\partial \boldsymbol{u}_C}{\partial t}\right)^{\mathrm{n}-2}}{2\Delta t} \equiv \left(\frac{\Delta^2 \boldsymbol{u}_C}{\Delta t^2}\right)^{\mathrm{n}} \tag{55}$$

where we used the notation $\frac{\Delta^2(\,)}{\Delta t^2}$ to represent the discretized operator of the temporal term. The first-order derivatives that appear in Eq. (55) are evaluated using a second-order backward Euler scheme, as presented in Appendix C:

$$\left(\frac{\partial \boldsymbol{u}_C}{\partial t}\right)^{\mathrm{n}} \approx \frac{3\boldsymbol{u}_C^{\mathrm{n}} - 4\boldsymbol{u}_C^{\mathrm{n}-1} + \boldsymbol{u}_C^{\mathrm{n}-2}}{2\Delta t} \tag{56}$$

Applying Gauss' divergence theorem into the second integral on the left hand side of Eq. (51) and applying the discretization process for a diffusion-like term explained in Appendix C we obtain:

$$(\rho_0^{\mathrm{s}})_C V_C \left(\frac{\Delta^2 \boldsymbol{u}_C}{\Delta t^2}\right)^{\mathrm{n}} - \sum_f (2\mu^{\mathrm{s}} + \lambda^{\mathrm{s}})_f \left(\nabla_0 \boldsymbol{u}\right)_f^{\mathrm{n}} \bullet \boldsymbol{s}_f = \underbrace{\int_{V_C} \left(\nabla_0 \bullet \boldsymbol{Q}_l + \nabla_0 \bullet \boldsymbol{Q}_{nl}\right) \mathrm{d}V}_{\text{Evaluated explicitly}} \tag{57}$$

The normal gradient in the second term on the left side of Eq. (57) is interpolated using a non-orthogonal and skewness corrected scheme as shown in Eq. (34). The terms on the right hand side are explicitly evaluated by foam-extend, i.e. using values already available to make it possible to solve the problem by a segregated approach, since these terms carries the coupling between the components of the displacement.

Substituting Eqs. (34) and (55) in Eq. (57), we can write a linearized algebraic equation for a control volume V_C of the solid mesh in vector form:

$$a_C^{\boldsymbol{u}} \boldsymbol{u}_C^{\mathrm{n}} + \sum_{F \sim NB(C)} a_F^{\boldsymbol{u}} \boldsymbol{u}_F^{\mathrm{n}} = \boldsymbol{b}_C^{\boldsymbol{u}} \tag{58}$$

If we decompose $\boldsymbol{u}$ in the Cartesian coordinate system as: $\boldsymbol{u} = u_x \boldsymbol{i} + u_y \boldsymbol{j} + u_z \boldsymbol{k}$, where $\boldsymbol{i}$, $\boldsymbol{j}$ and $\boldsymbol{k}$ are vectors of the canonical basis. Therefore, the discretized solid displacement

equation for each component of $\boldsymbol{u}$ is:

$$\begin{aligned} a_C^{u_x}(u_x)_C^{\mathrm{n}} + \sum_F a_F^{u_x}(u_x)_F^{\mathrm{n}} &= b_C^{u_x} \\ a_C^{u_x}(u_y)_C^{\mathrm{n}} + \sum_F a_F^{u_y}(u_y)_F^{\mathrm{n}} &= b_C^{u_y} \\ a_C^{u_x}(u_z)_C^{\mathrm{n}} + \sum_F a_F^{u_y}(u_z)_F^{\mathrm{n}} &= b_C^{u_z} \end{aligned} \tag{59}$$

which can be assembled for all control volumes in the solid mesh yielding three systems of algebraic linearized equations:

$$\begin{aligned} \mathbf{A}^{u_x}(\mathbf{u_x})^{\mathrm{n}} &= \mathbf{b}^{u_x} \\ \mathbf{A}^{u_y}(\mathbf{u_y})^{\mathrm{n}} &= \mathbf{b}^{u_y} \\ \mathbf{A}^{u_z}(\mathbf{u_z})^{\mathrm{n}} &= \mathbf{b}^{u_z} \end{aligned} \tag{60}$$

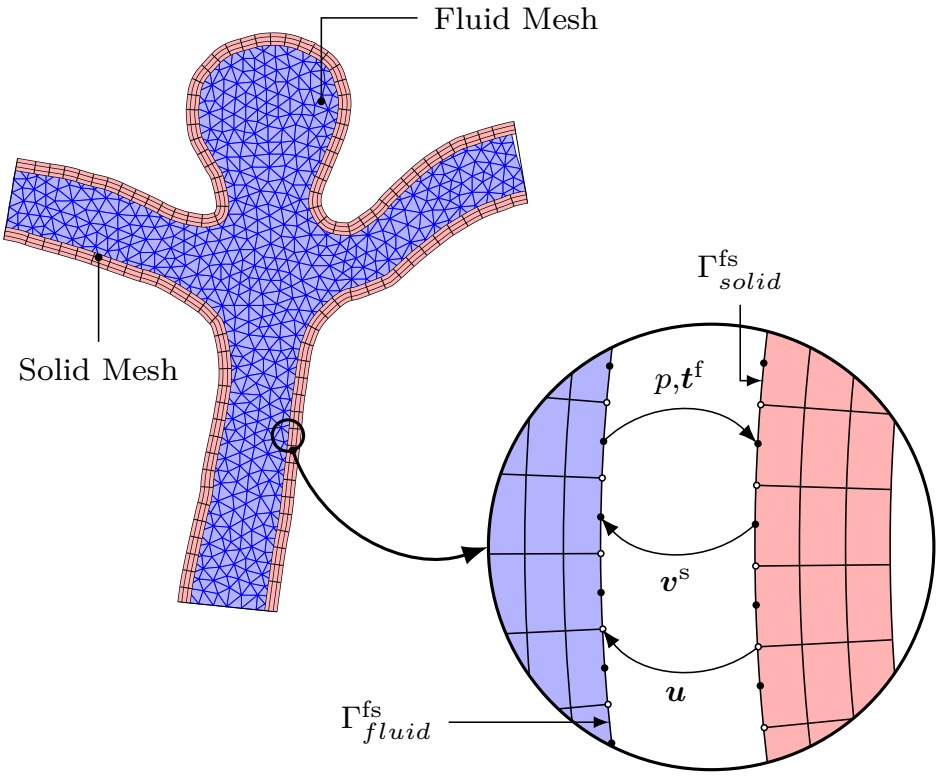
The systems in Eq. (60) are solved by a linear solver using a preconditioned Conjugate Gradient method for symmetric matrices, with scaled normalized residual tolerance equal to 1×10^{-9} – see Appendix D for residual calculation –, with the preconditioning matrix a diagonal incomplete Cholesky.

2.3.3 Coupling FSI Method: IQN-ILS

The partitioned methodology consists of solving the flow problem, Eqs. (2) and (7), the solid problem, Eq. (17), and the mesh motion equation, Eq. (26), separately and sequentially with the conditions at the fluid-solid interface, Eqs. (24) and (25), obtained interpolating each solution at this interface. One of the main advantages of this approach is the ability to re-use algorithms already developed, allowing different discretization for each domain if needed. Therefore, two computational meshes are provided and the rest of the work consists of building an algorithm that performs interpolation, or mapping, of variables between the FSI interface of each mesh. Figure 20 shows an example of a computational mesh of an aneurysm domain Ω for a FSI problem treated in a partitioned manner: the fluid and solid meshes are separated and have the FSI interface, Γ^{fs} in common; we call $\Gamma^{\mathrm{fs}}_{fluid}$ the fluid mesh boundary that corresponds to the FSI interface and $\Gamma^{\mathrm{fs}}_{solid}$ for the solid mesh. The same figure also shows the interpolation of variables between these surfaces: after solving the governing equations of the flow, the pressure p and traction $\boldsymbol{t}^{\mathrm{f}}$ fields are interpolated from $\Gamma^{\mathrm{fs}}_{fluid}$ to $\Gamma^{\mathrm{fs}}_{solid}$; on the other hand, once the solution of the governing

equation of the solid is known, the displacement $\boldsymbol{u}$ and velocity $\boldsymbol{v}^{\mathrm{s}}$ at $\Gamma^{\mathrm{fs}}_{solid}$ are interpolated to $\Gamma^{\mathrm{fs}}_{fluid}$.

Figure 20 – Schematic two-dimensional representation of the fluid and solid meshes of an aneurysm geometry showing each FSI interface and the interpolated variable between the solid and fluid mesh interfaces.



Source: prepared by the author.

Although flexible, partitioned methodologies are very unstable [45], specially for problems with strong physical couplings between the fluid and structure, e.g., high fluid and solid density ratio, which occurs when the solid is very light compared to the fluid, and/or incompressible flow leads to unconditionally instability of the computational solution [82, 83]. In general, coupling schemes are applied in these situations to improve solution stability, which is not necessary in monolithic methods as all variables are evaluated at the same time. Two computational coupling schemes are found:

- Weak coupling: in this type of scheme, the solution of the solid equation, the mesh motion and the flow equations are obtained sequentially *only once per time-step*, i.e., there is no internal loop to verify if the FSI interface displacement is correct. They are recommended for weak physical coupling between the fluid and solid domains; when the solid is very stiff, for example, in aeronautics applications like flutter of wings, where the wing has a stiff and heavier solid structure compared to the fluid

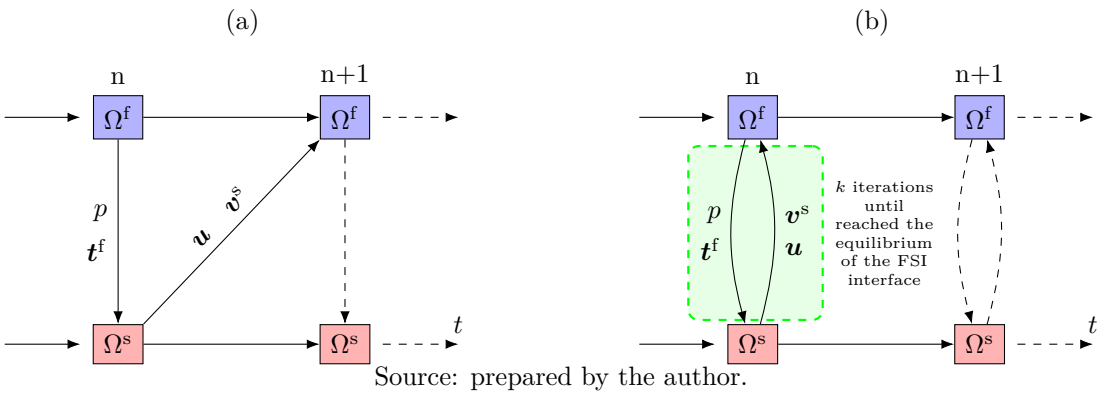
which is generally air. Figure 21a shows the sequence of interactions for this type of coupling;

- Strong coupling: in this scheme, at each time-step a coupling loop is implemented to seek the equilibrium between the displacements of the fluid and solid mesh FSI interface: with the FSI interface at position $\boldsymbol{x}|_{\Gamma^{\text{fs}}_{fluid}}$, the solution of the fluid governing equations yields a traction distribution on the solid interface which, in turn, responds with a new displacement field and a new interface position $\boldsymbol{x}|_{\Gamma^{\text{fs}}_{solid}}$, and if the result is correct then $\boldsymbol{x}|_{\Gamma^{\text{fs}}_{solid}} = \boldsymbol{x}|_{\Gamma^{\text{fs}}_{fluid}}$! However, this may not happen because, due to the strong physical coupling, solving only once the governing equations may not lead to the correct position of the FSI interface, on the contrary, the displacements are generally very large for the first calculations. In general, to achieve this convergence, relaxation factors must be applied and several coupling iterations over the governing equations are performed until, finally, the condition:

$$\left(\boldsymbol{x}|_{\Gamma^{\text{fs}}_{solid}} - \boldsymbol{x}|_{\Gamma^{\text{fs}}_{fluid}}\right) < \epsilon_0 \tag{61}$$

where ϵ_0 is a tolerance specified *a priori*, is satisfied. Figure 21b shows the sequence of interactions for this type of coupling. Information is exchanged between fluid and solid domains while the condition represented by Eq. (61) is not met, through interpolations as depicted in Fig. 20, and Eqs. (3), (7), (17) and (26) are solved in each coupling iteration.

Figure 21 – Interactions of FSI coupling approaches of the partitioned methodology: (a) weak FSI coupling, where the solution of the solid problem is passed directly to the next time-step and (b) strong FSI coupling where a k number of iterations are performed over the governing equations within one time-step to verify if the FSI interface displacement is correct; n and n + 1 represents two consecutive time-steps.



Source: prepared by the author.

Although relaxation procedures – fixed or Aitken's dynamic relaxation [84, 85] – are commonly applied in the coupling loop, for very strong interaction, which is the case of the aneurysm problem, we chose to use a more robust procedure, proposed by Degroote et al. [69] and implemented in foam-extend, called Interface Quasi-Newton-Implicit Jacobian Least-Squares (IQN-ILS). This procedure solves a residual form of the equation that governs the position of the FSI interface in each time-step, using quasi-Newton iterations and approximating the product of the *inverse* of the Jacobian by the residual vector through a least-squares method, as explained below.

Let us call $\boldsymbol{\mathcal{F}}$ a symbolic representation that gathers all operations of the "fluid solver" in a partitioned FSI procedure, i.e., the solution of the systems of equations derived in Section 2.3.2 of the fluid model, and interpolates the stresses from $\Gamma^{\text{fs}}_{fluid}$ to $\Gamma^{\text{fs}}_{solid}$, thus, its input is the new position of $\Gamma^{\text{fs}}_{fluid}$, $\mathbf{d} = \boldsymbol{x}|_{\Gamma^{\text{fs}}_{fluid}}$, and its output is the traction and pressure transmitted to the solid, $\mathbf{y} = \left\{\left(p, \boldsymbol{t}^{\text{f}}\right)|_{\Gamma^{\text{fs}}_{solid}}\right\}$. Therefore, the operator $\boldsymbol{\mathcal{F}}$ can be written as:

$$\mathbf{y} = \boldsymbol{\mathcal{F}}\left(\mathbf{d}\right) \tag{62}$$

On the other hand, we can also define a solid operator, $\boldsymbol{\mathcal{S}}$, that gathers all operations of the solid solver: solving the system of equations presented in Section 2.3.2 of the solid model, Eq. (60), and interpolates the displacement of $\Gamma^{\text{fs}}_{solid}$ to $\Gamma^{\text{fs}}_{fluid}$. Therefore, its mathematical form is written as:

$$\mathbf{d} = \boldsymbol{\mathcal{S}}\left(\mathbf{y}\right) \tag{63}$$

Figure 22 shows a schematic representation of $\boldsymbol{\mathcal{F}}$ and $\boldsymbol{\mathcal{S}}$. The representations of $\boldsymbol{\mathcal{S}}$ and $\boldsymbol{\mathcal{F}}$ are convenient because they can be any "black-box" solvers for solid and fluid problems, respectively. Hence, the IQN-ILS method does not need to know their internal structure, it only uses the FSI interface information.

With this terminology, the FSI problem, i.e. finding the FSI interface position $\mathbf{d}$, is written by substituting Eq. (62) in Eq. (63) yielding the following equation:

$$\mathbf{d} = \boldsymbol{\mathcal{S}}\left[\boldsymbol{\mathcal{F}}\left(\mathbf{d}\right)\right] = \boldsymbol{\mathcal{S}} \circ \boldsymbol{\mathcal{F}}\left(\mathbf{d}\right) \tag{64}$$

a fixed-point formulation of the FSI problem [84]. The notation "$\circ$" represents a composition of two functions, i.e., the result of $\boldsymbol{\mathcal{F}}$ is applied to $\boldsymbol{\mathcal{S}}$. Equation (64) can also be

written in a residual form:

$$\boldsymbol{\mathcal{R}}\left(\mathbf{d}\right) = \boldsymbol{\mathcal{S}} \circ \boldsymbol{\mathcal{F}}\left(\mathbf{d}\right) - \mathbf{d} = \mathbf{0} \tag{65}$$

where $\mathbf{d}$ is the FSI interface position and this last equation represents a non-linear system of equations for the coupled problem. Note that the coordinates of the FSI interface are the only explicit variable in this system.

If Newton-Raphson iterations were chosen to solve Eq. (65), the non-linear system can be linearized and written as follows:

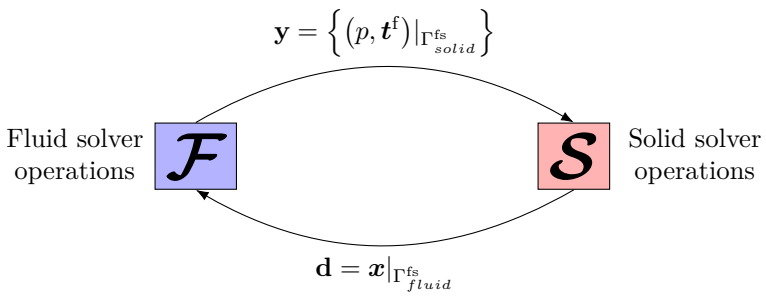
$$\left.\frac{\partial \boldsymbol{\mathcal{R}}}{\partial \mathbf{d}}\right|_{\mathbf{d}_k} \Delta\mathbf{d}_k = -\mathbf{r}_k \tag{66}$$

where $\frac{\partial \boldsymbol{\mathcal{R}}}{\partial \boldsymbol{x}}$ is the Jacobian matrix of $\boldsymbol{\mathcal{R}}$; $\Delta\mathbf{d}_k = \mathbf{d}_{k+1} - \mathbf{d}_k$ is an increment of the interface position $\mathbf{d}$ for a Newton-Raphson iteration represented by index k; the residual is evaluated by:

$$\mathbf{r}_k = \boldsymbol{\mathcal{R}}\left(\mathbf{d}_k\right) = \boldsymbol{\mathcal{S}} \circ \boldsymbol{\mathcal{F}}\left(\mathbf{d}_k\right) - \mathbf{d}_k = \tilde{\mathbf{d}}_{k+1} - \mathbf{d}_k \tag{67}$$

with the tilde indicating a variable at the end of one *iteration*, i.e., $\tilde{\mathbf{d}}_{k+1} = \boldsymbol{\mathcal{S}} \circ \boldsymbol{\mathcal{F}}\left(\mathbf{d}_k\right)$ is the result of solving the fluid and solid problems sequentially on iteration k. In one time-step, the Newton-Raphson iterations have converged when $\|\mathbf{r}_k\|_2 < \epsilon_0$, where ϵ_0 is a predefined tolerance (note that this residual is essentially the one shown in Eq. (61)). However, Eq. (66) could only be solved directly if the Jacobian $\frac{\partial \boldsymbol{\mathcal{R}}}{\partial \mathbf{d}}$ was known; since the Jacobians of $\boldsymbol{\mathcal{F}}$ and $\boldsymbol{\mathcal{S}}$ may be unknown - because the method supposes initially that $\boldsymbol{\mathcal{F}}$ and $\boldsymbol{\mathcal{S}}$ are "black-box" solvers, then their internal structure is probably unknown - we cannot calculate $\frac{\partial \boldsymbol{\mathcal{R}}}{\partial \mathbf{d}}$. Degroote et al. [69] propose to solve Eq. (66) using quasi-Newton

Figure 22 – Representation of the fluid and solid "black-box" solvers showing their input and output variables.



Source: prepared by the author.

iterations as follows:

$$\mathbf{d}_{k+1} = \mathbf{d}_k + \left(\frac{\partial \boldsymbol{\mathcal{R}}}{\partial \mathbf{d}} \Big|_{\mathbf{d}_k} \right)^{-1} (-\mathbf{r}_k) \tag{68}$$

Since the residual $\mathbf{r}_k$ is known at every iteration and $\mathbf{d}_k$ is also known from the last iteration, to obtain $\mathbf{d}_{k+1}$, the inverse of the Jacobian, $\left(\frac{\partial \boldsymbol{\mathcal{R}}}{\partial \mathbf{d}} \Big|_{\mathbf{d}_k} \right)^{-1}$, needs to be calculated. Degroote et al. [69] approximate it using a least-squares method proposed by Vierendeels et al. [86] and reproduced . Finally, once the quasi-Newton iterations converged, the new position field of the FSI interface, $\mathbf{d}_{k+1}$, is passed to the next time-step.

The implementation, in foam-extend, of the procedure to approximate the inverse Jacobian in Eq. (68) has some small differences compared to the exact steps presented in Degroote et al. [69] regarding only intermediate calculations. We present here as it is implemented on foam-extend, version 4.0. Each coupling iteration, k – a quasi-Newton one – produces a new residual vector $\mathbf{r}_k$ and a new position vector for the computational nodes of the interface, $\tilde{\mathbf{d}}_{k+1}$; these vectors are also available from previous iterations $i = 0, ..., k-1$. Defining the vectors:

$$\Delta \mathbf{r}_i = \mathbf{r}_i - \mathbf{r}_0 \tag{69}$$

$$\Delta \tilde{\mathbf{d}}_{i+1} = \tilde{\mathbf{d}}_{i+1} - \tilde{\mathbf{d}}_1 \tag{70}$$

they belong to $\mathbb{R}^{N^{\mathrm{fs}}}$ with N^{fs} the number of degrees of freedom on the FSI interface; for the current time-step level indicated as n, these vectors can be added as the columns of matrices defined as:

$$\mathbf{V}_k^{\mathrm{n}} = \begin{bmatrix} \Delta \mathbf{r}_{k-1} & \Delta \mathbf{r}_{k-2} & \cdots & \Delta \mathbf{r}_1 & \Delta \mathbf{r}_0 \end{bmatrix} \tag{71}$$

$$\mathbf{W}_k^{\mathrm{n}} = \begin{bmatrix} \Delta \tilde{\mathbf{d}}_k & \Delta \tilde{\mathbf{d}}_{k-1} & \cdots & \Delta \tilde{\mathbf{d}}_2 & \Delta \tilde{\mathbf{d}}_1 \end{bmatrix} \tag{72}$$

The matrices similar to these equations for the previous q time-steps $\mathrm{n}-1, \mathrm{n}-2, ..., \mathrm{n}-q$ can also be used; according to Degroote et al. [84], this remarkably improves convergence of the method. Thus, the matrices in Eqs. (71) and (72) can be expanded adding information

of previous q time-steps to their rightmost end:

$$\mathbf{V}_k = \begin{bmatrix} \mathbf{V}_k^{\mathrm{n}} & \mathbf{V}^{\mathrm{n}-1} & \cdots & \mathbf{V}^{\mathrm{n}-(q-1)} & \mathbf{V}^{\mathrm{n}-q} \end{bmatrix} \tag{73}$$

$$\mathbf{W}_k = \begin{bmatrix} \mathbf{W}_k^{\mathrm{n}} & \mathbf{W}^{\mathrm{n}-1} & \cdots & \mathbf{W}^{\mathrm{n}-(q-1)} & \mathbf{W}^{\mathrm{n}-q} \end{bmatrix} \tag{74}$$

According to Degroote et al. [69], the value of q can accelerate convergence, but its value for the fastest convergence is problem dependent. Note that we dropped the coupling iteration index of matrices from older time-steps, since these are complete, i.e., their columns corresponds to all coupling iterations of each previous time-step. We indicate the number of columns in $\mathbf{V}_k$ and $\mathbf{W}_k$ as v; the number of lines is N^{fs}, and usually $v \ll N^{\mathrm{fs}}$.

The final residual vector should be $\mathbf{0}$, i.e. indicating convergence. If one defines the vector $\Delta\mathbf{r} = \mathbf{0} - \mathbf{r}_k$, it can be expressed as a linear combination of the available $\Delta\mathbf{r}_k$:

$$\Delta\mathbf{r} \approx \mathbf{V}_k \mathbf{c}_k \tag{75}$$

where $\mathbf{c}_k \in \mathbb{R}^v$ is the vector formed by the coefficients of the linear combination, which must be determined solving system (75). However, $\mathbf{V}_k$ is a rectangular matrix with number of rows, N^{fs}, usually much larger than the number of columns, v. Therefore, Eq. (75) is an *overdetermined system* and hence the least-squares method is used to find $\mathbf{c}_k$ that minimizes the function:

$$\|\Delta\mathbf{r} - \mathbf{V}_k \mathbf{c}_k\|_2 \tag{76}$$

A good description of least-squares methods can be found in Golub and Van Loan [81]. For the IQN-ILS method, the QR-decomposition of $\mathbf{V}_k$ is used:

$$\mathbf{V}_k = \mathbf{Q}_k \mathbf{R}_k \tag{77}$$

calculated through the modified Gram-Schmidt method [81]; $\mathbf{Q}_k \in \mathbb{R}^{N^{\mathrm{fs}} \times N^{\mathrm{fs}}}$ is an orthogonal matrix, i.e.$\mathbf{Q}^{-1} = \mathbf{Q}^T$, and $\mathbf{R}_k \in \mathbb{R}^{N^{\mathrm{fs}} \times v}$ is upper triangular. Substituting Eq. (77) into Eq. (75) leads to:

$$\mathbf{R}_k \mathbf{c}_k = \mathbf{Q}_k^T \Delta\mathbf{r} \tag{78}$$

which can be solved for $\mathbf{c}_k$ using back substitution.

Equivalent to $\Delta\mathbf{r}$ is the vector $\Delta\tilde{\mathbf{d}} = \mathbf{d}_{k+1} - \tilde{\mathbf{d}}_{k+1}$, where $\mathbf{d}_{k+1}$ is the converged FSI interface displacement (equivalent to zero residual) and is written as a linear combination of the elements of $\mathbf{W}_k$ using the coefficients $\mathbf{c}_k$ obtained from Eq. (78):

$$\Delta\tilde{\mathbf{d}} = \mathbf{W}_k\mathbf{c}_k \tag{79}$$

From Eq. (67) and the definitions of $\Delta\mathbf{r}$ and $\Delta\tilde{\mathbf{d}}$ yields:

$$\Delta\mathbf{r} = \Delta\tilde{\mathbf{d}} - \Delta\mathbf{d} \tag{80}$$

where $\Delta\mathbf{d} = \mathbf{d}_{k+1} - \mathbf{d}_k$. Substituting Eq. (79) into the last equation follows:

$$\underbrace{\Delta\mathbf{d}}_{=\mathbf{d}_{k+1}-\mathbf{d}_k} = \mathbf{W}_k\mathbf{c}_k - \underbrace{\Delta\mathbf{r}}_{=-\mathbf{r}_k} \tag{81}$$

Since vector $\mathbf{c}_k$ is a function of $\Delta\mathbf{r}$, then Eq. (81) can be seen as an approximation of the Jacobian matrix-residual vector product of Eq. (68). Writing Eq. (81) in the form:

$$\mathbf{d}_{k+1} = \mathbf{d}_k + \mathbf{W}_k\mathbf{c}_k + \mathbf{r}_k \tag{82}$$

clarifies the comparison with Eq. (68). The form of Eq. (82) is computationally less expensive if the inverse Jacobian is explicitly written by comparison of Eq. (82) with Eq. (68), which results in:

$$\left(\left.\frac{\partial\boldsymbol{\mathcal{R}}}{\partial\mathbf{d}}\right|_{\mathbf{d}_k}\right)^{-1} = \mathbf{W}_k\mathbf{R}_k^{-1}\mathbf{Q}_k^{\mathrm{T}} - \mathbf{I} \tag{83}$$

where $\mathbf{I}$ is the identity matrix of $\mathbb{R}^{N^{\mathrm{fs}}\times N^{\mathrm{fs}}}$. Clearly, Eq. (82) involves less operations than Eq. (83) – only one matrix-vector product in the former case, whereas two matrix-matrix products in the latter case. Finally, with Eq. (82), a new value of the FSI interface position is obtained and can be passed along once convergence has been reached. Note that, for constructing Eq. (82), the most expensive computational operations are the QR-decomposition of $\mathbf{V}_k$ and the solution of the upper triangular system.

As we explained before, the reuse parameter, q, accelerates convergence. However, because there is no information to reuse at the first time-step, to avoid divergence at

the initial coupling iterations, the method includes fixed relaxation to be performed within the first time-step. Therefore, during the initial coupling iterations of the first time-step, once the residual $\mathbf{r}_k$ has been calculated, the new interface position is computed as $\mathbf{d}_{k+1} = \mathbf{d}_k + \alpha \mathbf{r}_k$

Degroote et al. [69] and Degroote et al. [84] compared the performance of the IQN-ILS method with a monolithic and other partitioned methods, respectively. While the first study was not very conclusive, the second study showed that, for example, the IQN-ILS performs better than Aitken's dynamic relaxation. We also highlight that, in these studies, the numerical experiments presented were not very representative of engineering problems arising in current industrial and biomedical applications – flow in flexible 3D pipes and flexible beam behind a cylinder in cross flow, for example –, therefore, it is still important to assess its performance in more complex problems.

2.3.4 Solution Procedure

Finally, the complete solution procedure for the simulation of the flow in aneurysms with flexible wall assumption, i.e. accounting for the fluid-solid interaction, is shown in Fig. 23 which shows a flowchart of the solution procedure where the fluid and solid "solvers" presented in Section 2.3.3 are shown in yellow boxes which enclosures its operations. A description of the flow chart is:

1. Fluid and solid fields are initialized: for the flow problem, the numerical solution of the flow with rigid wall assumption, $(\boldsymbol{v}^{\mathrm{f}})^0$ and p^0, is used as initial condition, obtained with the solver `pisoFoam` of foam-extend using the same boundary conditions described in Section 2.2.1 for the inlet and outlets; while for the solid problem, we used the wall shear stress and pressure fields of the flow problem with rigid wall to generate an initial displacement field, $\boldsymbol{u}^0$ using the solver `solidFoam` of foam-extend. It is important to note that using an initial condition (different than a trivial one) closer to the final solution is recommended since the coupling technique is based on a quasi-Newton method, as explained in Section 2.3.3.

2. Start coupling loop:

   (a) Update the displacement of the FSI interface using the IQN-ILS procedure as presented in Section 2.3.3;

(b) Updating the fluid mesh: using the last displacement and velocity of the FSI interface as boundary condition, solve Eq. (50) for mesh velocities;

(c) With the mesh velocities, solve the discretized Navier-Stokes equations: first, solve the discretized momentum equations for flow velocity components, Eq. (37), sequentially and separately, with an available pressure and velocity fields (in the first time-step, n = 0, use initial condition values; after the first time-step, n > 0, use values of the last coupling iteration); then start the PISO loop:

i. With the momentum-satisfying velocity field, solve the pressure system of equations, Eq. (46);

ii. Correct the flow velocity field with the new continuity-satisfying pressure and mass flow rate fields using Eq. (39) and iterate over the pressure equation: we used 3 iterations, one more than the suggestion of the original procedure by Issa [76] because of the non-orthogonal correction used for the pressure equation; once the number of iterations, $nIter$, is greater than the informed number of correctors step, $nCorr = 3$, skip the PISO loop;

(d) Interpolate the fluid traction $\boldsymbol{t}^{\mathrm{f}} = \boldsymbol{n}^{\mathrm{f}} \bullet \boldsymbol{\sigma}^{\mathrm{f}}$ from $\Gamma^{\mathrm{fs}}_{fluid}$ to $\Gamma^{\mathrm{fs}}_{solid}$, to be used as Neumann boundary condition – see Eq. (22) – for the solid problem;

(e) Solve the discretized momentum equation for the solid displacement, Eq. (60), which yields a new position field for $\Gamma^{\mathrm{fs}}_{solid}$;

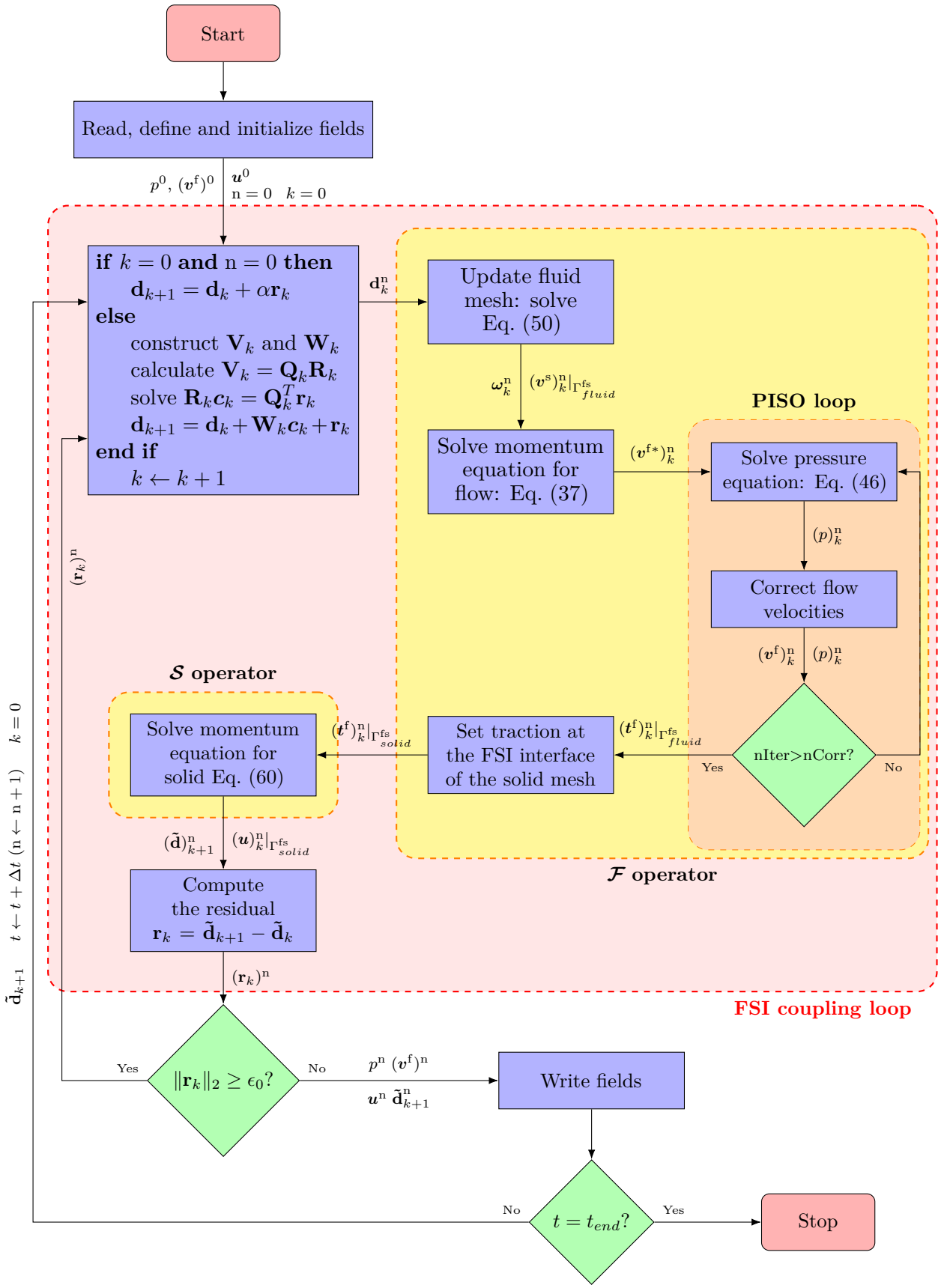
(f) Calculate the FSI residual, Eq. (67), and check for convergence of the coupling iterations – we used a scaled normalized residual tolerance equal to 1×10^{-4} – see Appendix D for residual calculation in foam-extend. If converged, skip the coupling loop, otherwise return to Item 2a;

3. Write flow velocity, pressure, solid displacement and other relevant fields to disk and move to next time-step $t \leftarrow t + \Delta t$, where the left arrow means attribution, until the last one t_{end}, is reached.

2.4 Hardware Support

The sequence presented in Fig. 23 is very time consuming for a machine running in sequential mode. Therefore, all the simulations were performed using parallel processing

Figure 23 – Flowchart of the algorithm to solve the FSI problem in a partitioned manner using the IQN-ILS method, showing the operators $\mathcal{F}$ and $\mathcal{S}$; *nIter* is the current number of PISO iterations and *nCorr* is its maximum number; the left arrow means attribution.



Source: prepared by the author.

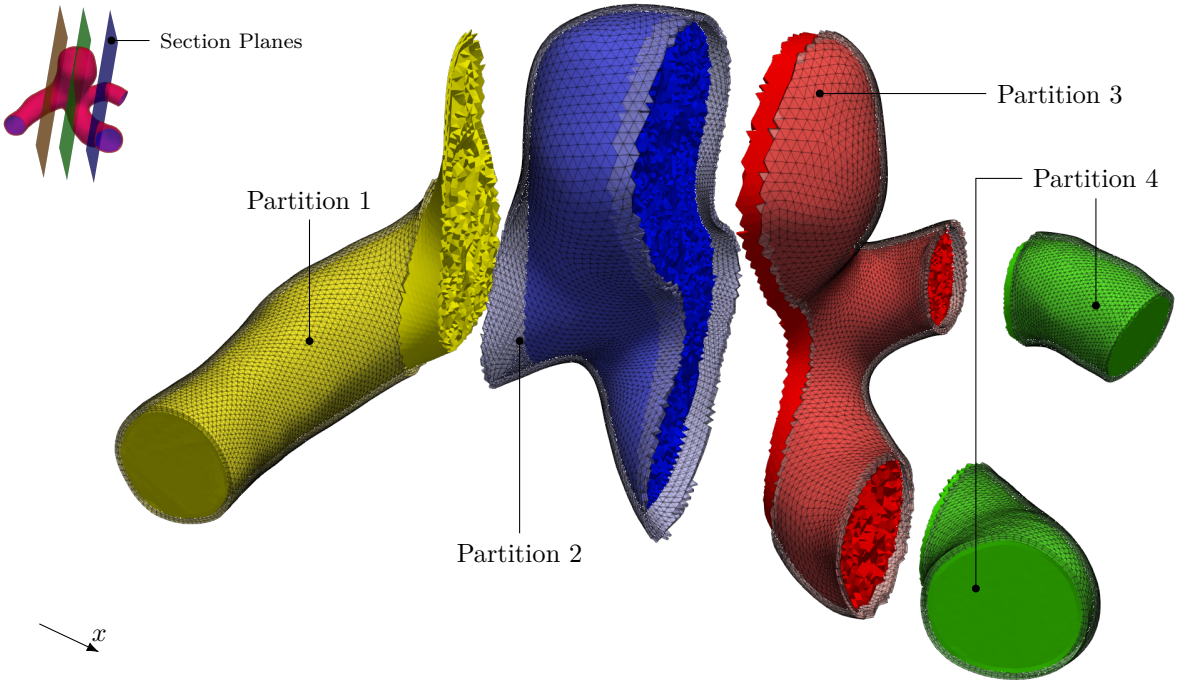
– available in the foam-extend. Because it demands a high processing power, all the simulations were performed in the following clusters via a secure shell connection:

- GridUNESP: Computational resources of the São Paulo State University, running the Linux based Operational System CentOS 6.8, and composed of the following processing structure:
  - 256 SUN X4150 servers;
  - 2,048 cores Intel Xeon 2.83 GHz;
  - 4,096 GB of RAM memory with 2GB per core;
  - Infiniband interconection 4X DDR (20 Gbps).
- ACENET clusters: according to its User Guide web-page: "ACENET is a consortium of Atlantic Canadian universities providing high-performance computing (HPC) resources, visualization and collaboration tools to participating research institutions". We used three of the four clusters located at Dalhousie University in Halifax, Nova Scotia, Canada. They run the Red Hat Enterprise Linux 6.4 and have the following processing structure:
  - 174 nodes and 2,196 total cores (AMD Opteron 280 (2.4GHz), AMD Opteron 8384 (2.7GHz) and AMD Opteron 6134 (2.3GHz));
  - With 4GB up to 128GB of the RAM memory per node.

It is important to note that both cluster were used separately. To run in parallel mode, the mesh must be decomposed into the respective number of needed processes. For the domain decomposition, we used the utility `decomposePar` of foam-extend, and, once the simulation finished, the utility `reconstructPar` was used to reconstruct the data for visualization and post-processing. The particular issue with mesh decomposition is that the fluid and solid meshes are decomposed in such a way that the FSI interface of each mesh is distributed over all processors, therefore exchange of information between $\Gamma^{\text{fs}}_{fluid}$ and $\Gamma^{\text{fs}}_{solid}$ is performed in each processor. Moreover, the partitioning is performed along axis x of each case, as shown in Fig. 24 for case 13 for four processes – see Fig. 17.

The number of processes used was estimate evaluating the *speedup* of the simulation, a parameter used to assess the scalability of a problem. The *scalability* measures if a given

Figure 24 – Fluid and solid meshes of case 13 decomposed in four partitions (fluid mesh partitions are darker whereas solid mesh partitions are slightly translucent and with black edges), each partition is attributed to one processor of a computational node; the decomposition is performed in such a way that the FSI interface, Γ^{fs} is distributed over all processors.



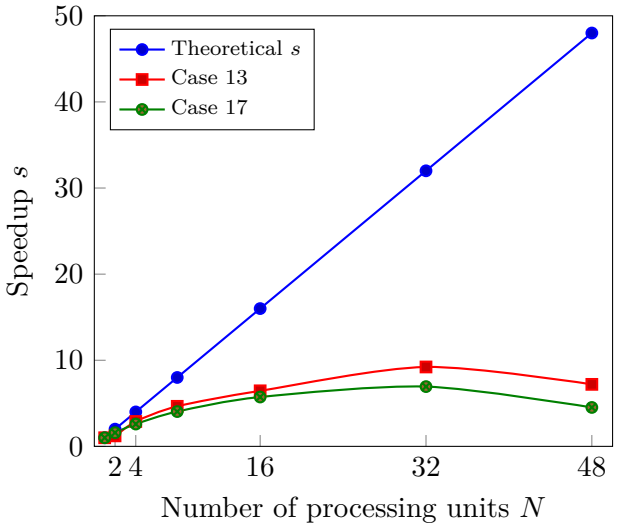
Source: prepared by the author.

problem can be solved faster by increasing the number of processing units dedicated to that task. The speedup, s, is then given by:

$$s = \frac{T_{sequential}}{T_{parallel}} \tag{84}$$

where $T_{sequential}$ is the time spent for a task running with only one processing unit and $T_{parallel}$ is the time of the same task if N processing units are used. In general, a fully parallel task have a speedup equal to the number of processing units [87]. To have the estimate of the speedup, we simulated only 20 time-steps for both cases 13 and 17 and used Eq. (84) to measure s, which is plotted in Fig. 25 together with the linear curve for the theoretical speedup. The maximum speedup for both cases occurs with 32 processes for the meshes used. Note that the observed speedup is much lower than the theoretical one. This is probably due to load balancing issues in the execution of the FSI simulation, because solving the solid part of the problem is computationally less expensive than solving the fluid part [88].

Figure 25 – Theoretical and measured speedup, s, as function of the number of processing units, N for the simulations of the geometry of cases 13 and 17.



Source: prepared by the author.

2.5 Data Analysis

Once completed the simulations, we evaluated the following quantities using ParaView®, an open-source software for post-processing of CFD simulations. This software has a large number of filters that allow processing and displaying all field variables of the flow, of the solid, and of the wall-fluid interface:

- Velocity field to determine where the flow impinges the aneurysm;
- WSS at the surface wall: the WSS is the magnitude of the traction due to the viscous part of the Cauchy stress tensor, $\boldsymbol{\tau}$, of the flow on the wall, i.e.:

$$WSS = \|\boldsymbol{WSS}\|_2 = \left(\|\boldsymbol{\tau} \cdot \boldsymbol{n}^{\mathrm{f}}\|\right)_{\Gamma^{\mathrm{fs}}} \tag{85}$$

- Wall stress: we evaluate the wall stress obtained by both linear and non-linear elastic models for the aneurysm and arteries walls. Since $\boldsymbol{\sigma}^{\mathrm{s}}$ is a second order tensor, its magnitude is defined as:

$$\sigma^{\mathrm{s}} = \|\boldsymbol{\sigma}^{\mathrm{s}}\| = \sqrt{\boldsymbol{\sigma}^{\mathrm{s}} : \boldsymbol{\sigma}^{\mathrm{s}}} \tag{86}$$

- OSI: this index measures the change of the WSS vector direction during the cardiac

cycle and it is defined as [29]:

$$OSI = \frac{1}{2}\left(1 - \frac{\left\|\int_0^T \boldsymbol{WSS}\mathrm{d}t\right\|}{\int_0^T \|\boldsymbol{WSS}\|_2\mathrm{d}t}\right) \tag{87}$$

where T is the cardiac cycle duration and $\boldsymbol{WSS}$ is the WSS vector defined on the aneurysm and arteries surface.

The WSS and OSI are the most common hemodynamic parameters related to intracranial aneurysm rupture, as explained in Section 1.1.

3 RESULTS

3.1 Numerical Error and Mesh Independence Analysis

One of the requirements in any numerical simulation code is *code verification* [89]. Foam-extend is widely used in industrial and academic research and has been tested in several fields. For FSI problems solved using an extension of the code, three benchmark cases were provided with the latest release – flow in a 3D tube, flexible beam behind a cylinder in cross flow and a beam in a cross flow. Regarding *validation* of the numerical solution, unfortunately, we were not able to validate the results experimentally; the work of setting up an experimental test for the aneurysm problem is left as a future work. The other requirement is the verification of the numerical accuracy of the simulations presented here. In the rest of this section, we analyze the numerical accuracy of our results through a mesh-independence analysis.

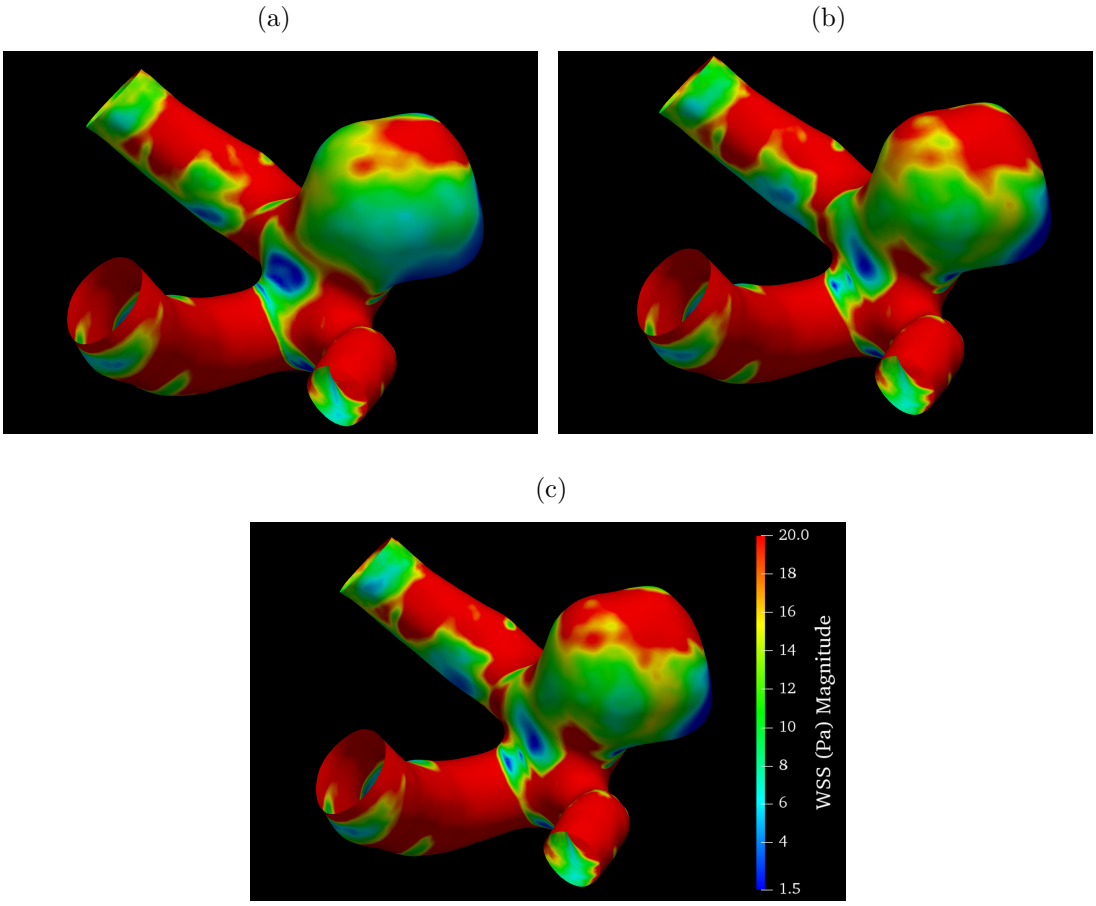
We evaluated mesh-independence of the numerical solution qualitatively, comparing the spatial distribution of WSS on the aneurysm surface, and quantitatively using the surface area averaged WSS over the surface of the geometries presented in Section 2.3.1. To perform this study, we solved the flow considering the rigid wall assumption.

Figure 26 shows the WSS on the surfaces for meshes with $\sim$ 300,000, $\sim$ 600,000 and $\sim$ 1,000,000 control volumes for the case 13. We see in the figure that there are small qualitative differences regarding the WSS for meshes with $\sim$ 600,000 and $\sim$ 1,000,000 control volumes, i.e. the overall structure of the WSS field is already established for the mesh with $\sim$ 600,000 control volumes, suggesting that this level of refinement is adequate. Figure 27, on the other hand, shows how the *area-averaged WSS* over the whole mesh surface varies with time, for two cardiac cycles. The area-averaged WSS is defined as:

$$\overline{WSS}_S = \frac{1}{A_S} \left\| \int_S (\boldsymbol{WSS}) \, \mathrm{d}S \right\|_2 \tag{88}$$

where S is the wall surface and A_S its area. The norm of the integral was calculated because WSS is a vector defined on the surface; the figure shows that there are only small differences between the three meshes. Therefore, we conclude that the fluid mesh with $\sim$ 600,000 is sufficiently refined to provided accurate results, at least for the WSS field, which is the main parameter studied here. Furthermore, this level of refinement is in close agreement with the $\sim$ 800,000 tetrahedral control volumes recommended by Khan et al.

Figure 26 – WSS magnitude distribution on the surface of the aneurysm of case 13 for fluid meshes with (a) ∼ 300,000, (b) ∼ 600,000 and (c) ∼ 1,000,000.



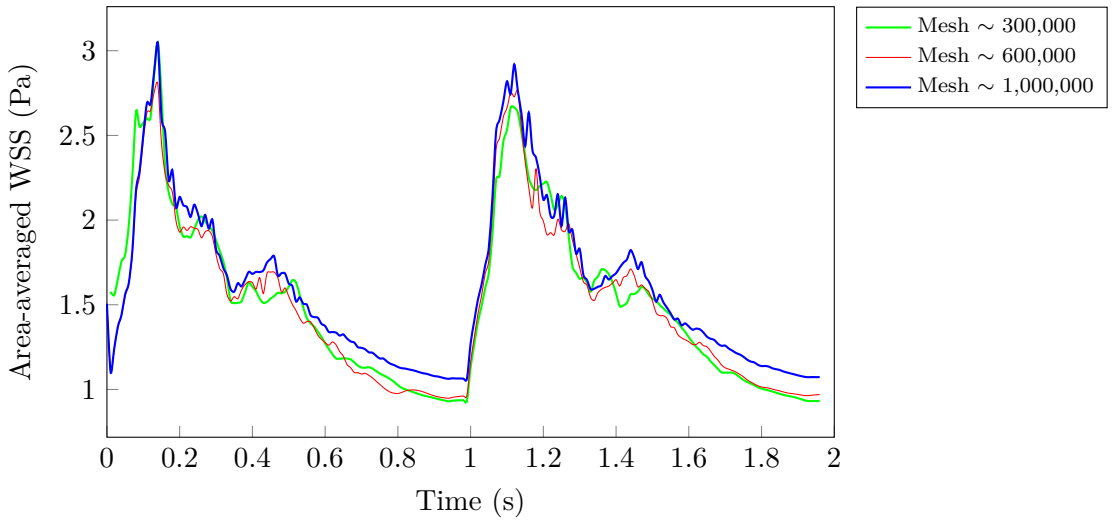
Source: prepared by the author.

[90] who studied mesh and time-step resolution for numerical simulations with aneurysms geometries.

Figure 28 presents the WSS distribution for the case 17 with fluid meshes with ∼ 200,000, ∼ 500,000, ∼ 800,000 and ∼ 1,200,000 control volumes. Comparing the WSS fields in Figs. 28b to 28d, it suggests that the overall structure of WSS is already established with a number of control volumes > 500,000. Figure 29 shows $\overline{WSS}_S$ for the case 17, for two cardiac cycles. For meshes with ∼ 500,000, ∼ 800,000 and ∼ 1,200,000 the difference between the curves is small compared to the absolute values of $\overline{WSS}_S$. Therefore, we assume that for the case 17 a mesh with ∼ 500,000 is refined enough.

Although it would be more appropriate to still use meshes with a higher degree of refinement – number of control volumes greater than 1,000,000 – however, we had to take into account a balance between *adequate accuracy and reliability* with reasonable computing time and resources requirements. For very fine meshes the required number

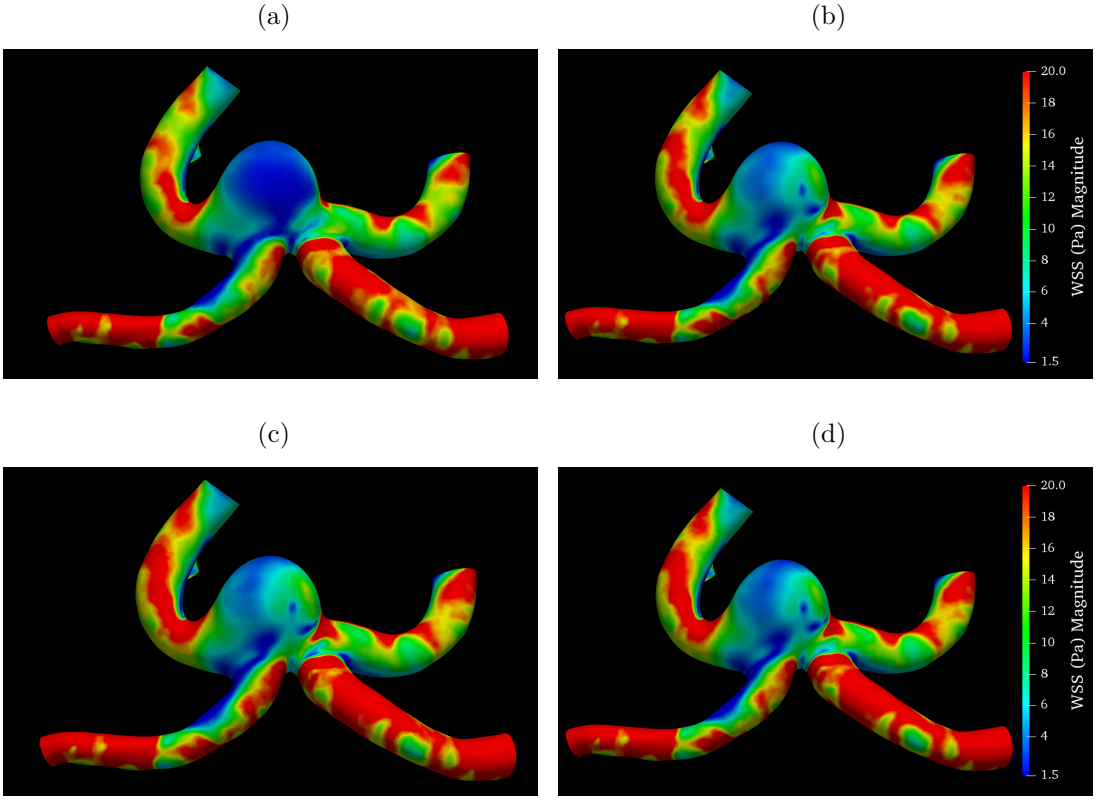
Figure 27 – Area-averaged WSS as a function of time for the whole surface for case 13 fluid mesh, with total number of control volumes ∼ 300,000, ∼ 600,000 and ∼ 1,000,000 to test mesh independence of the averaged WSS.



Source: prepared by the author.

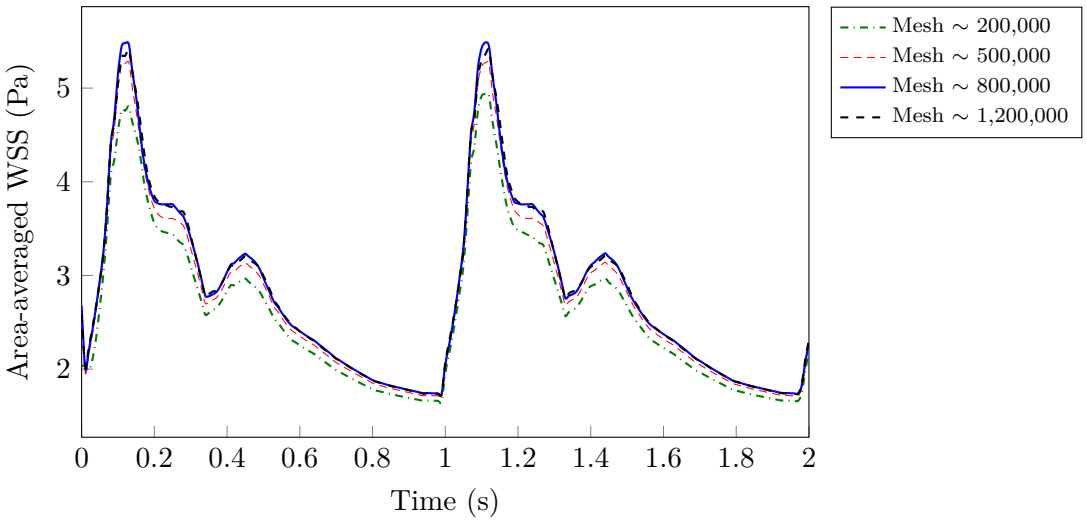
of processing units increases considerably. Furthermore, the explicitness of the IQN-ILS method for the FSI coupling requires the use of small time-steps to maintain stability

Figure 28 – WSS magnitude distribution on the surface of the aneurysm of case 17 for fluid meshes with (a) ∼ 200,000, (b) ∼ 500,000 (c) ∼ 800,000 and (d) ∼ 1,200,000.



Source: prepared by the author.

Figure 29 – Area-averaged WSS as a function of time for the whole surface for case 17 fluid mesh, with total number of control volumes $\sim$ 200,000, $\sim$ 500,000, $\sim$ 800,000 and $\sim$ 1,200,000 to test mesh independence of the averaged WSS.



Source: prepared by the author.

of the technique. The range of time-step was chosen by observing the behavior of the evolution in time of the numerical solution, which seems to be stable if the maximum *Courant number*, Co, is smaller than 1. The Courant number is defined as the ratio:

$$Co = \frac{\|(\boldsymbol{v}^{\mathrm{f}})_f\|\Delta t}{\delta} \tag{89}$$

where δ is a length defined for a cell; in one-dimensional meshes, for example, it is the cell length in the x direction, i.e. $\delta = \Delta x$; since foam-extend has support for generic polyhedral cells, δ is defined as the projection of $\boldsymbol{d}_{CF}$ on the face normal direction, $\boldsymbol{n}$, i.e. $\delta \equiv d_{fn} = \boldsymbol{d}_{CF} \bullet \boldsymbol{n}_f$ – consult Fig. 19b and Appendix C. The condition $Co < 1$ is a well know condition for the stability of explicit temporal discretization techniques for advection problems. Although we used an implicit temporal discretization of the governing equations for the fluid and solid problems, the coupling iterations diverged when $Co > 1$. We did not find any reference in the literature for this connection between the Co and the stability of coupling FSI techniques, however the literature reports that the temporal discretization approach for the solid and fluid equations has influence in the stability of partitioned techniques [91, 92], which could indicate a relation with the Courant number. Therefore, using Eq. (89) yields a time-step of 1×10^{-5} s for case 17 and 0.5×10^{-4} s for case 13.

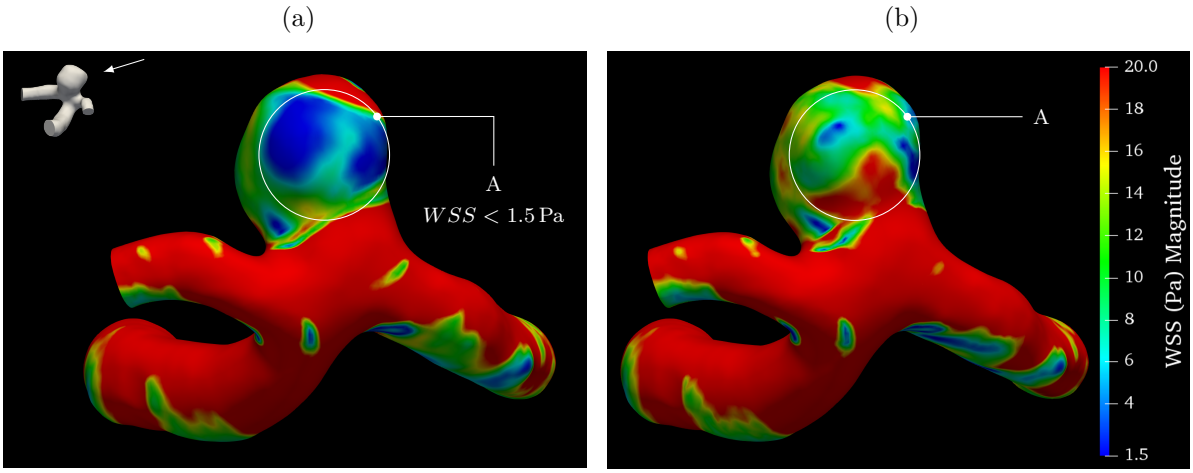
3.2 Simulations Results

In this section, we compare the solution of the aneurysm flow FSI problem for flexible and rigid wall models. The results shown below were taken at peak systole, i.e. the maximum blood flow rate at the inlet, which occurs at $t \approx 0.1\,\mathrm{s}$ – see Fig. 8. We will not present the methodology applied to the rigid-wall simulations because it is similar to the fluid model discretization derived in Section 2.3.2; the foam-extend solver used for the rigid-wall simulations was `pisoFoam` with the same setup as for the fluid part of the FSI simulations.

Figures 30 and 31 show the rigid wall versus linear elastic wall model comparison of the WSS distribution and velocity field for case 13. The scale was set up using a reference value of $WSS \approx 1.5\,\mathrm{Pa}$, below which the WSS can degenerate endothelial cells and possibly lead to rupture, as concluded by Shojima et al. [16]. In Fig. 30a we identify a large region of low WSS on the back of the aneurysm dome, caused by a large recirculation zone due to the direction of the flow jet that enters the aneurysm: the jet collides with the neck – point A in Fig. 31a – causing a recirculating flow within the dome and, more precisely, in the region indicated by point B in Fig. 31a, which is the cause of the lower levels of WSS. However, in the flexible wall simulation, the low level of WSS in that region disappears – see Fig. 30b, region A pointed by an arrow – because the flow pattern inside the aneurysm dome has changed. In Fig. 31b, the flow jet entering the aneurysm dome is less intense because part of its initial kinetic energy was lost due to the wall deformation, which changed the flow pattern inside the aneurysm dome, increasing the flow velocity in region B pointed by an arrow in Fig. 31b, hence increasing the WSS level on the aneurysm wall. It is important to note in Fig. 30 that the levels of WSS on the aneurysm's surrounding arteries remain almost the same for both rigid and elastic linear wall which could suggest that a rigid wall assumption is reasonable for modeling flows in *arteries* only.

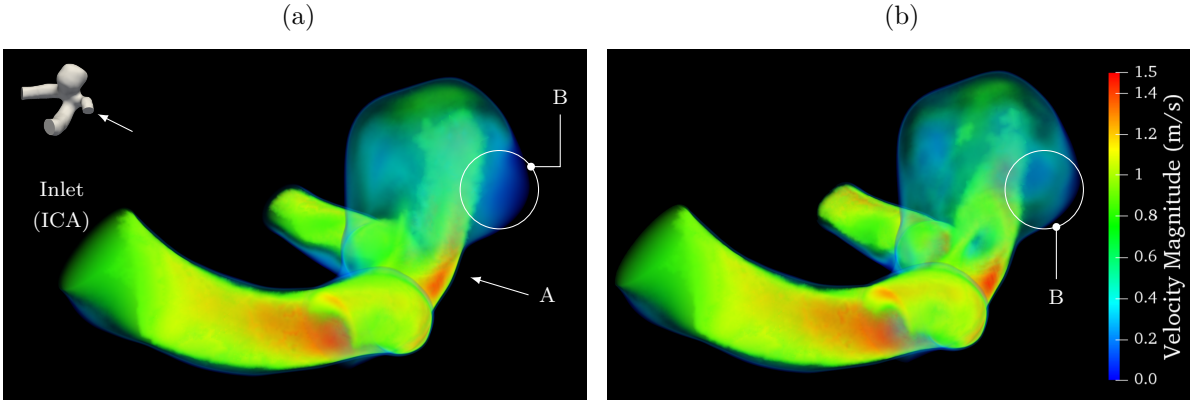
The flow velocity solution and WSS field for the case 17 are presented in Figs. 32 and 33, respectively. Figures 32a and 32b show the WSS on the wall surface for rigid and elastic linear wall assumptions, respectively. As we can see in the region indicated by circle C in Fig. 32a, there is a large area of low WSS when the rigid wall assumption is used, whereas this region is smaller when the elastic linear model is used – see Fig. 32b. Therefore, there is again an underestimation of WSS for the rigid wall. This can be explained by analyzing the velocity field, shown in Fig. 33: inside the aneurysm dome, the

Figure 30 – Comparison of WSS on the surface of case 13 with (a) rigid wall and (b) linear elastic wall models at peak systole (the white arrow at the top left corner indicates the direction of the view).



Source: prepared by the author.

Figure 31 – Volume rendering representation of the velocity field of the aneurysm of case 13 for (a) rigid wall assumption and (b) elastic linear wall model at peak systole; arrow A indicates the region of flow impingement, for this case occurring at the aneurysm neck.

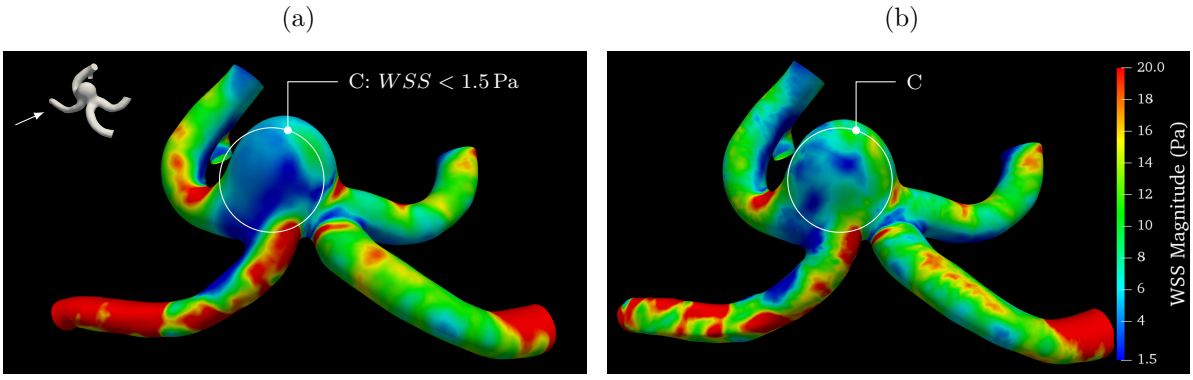


Source: prepared by the author.

velocities are higher for the flexible wall case – see Fig. 33b –, thus increasing the WSS levels on the aneurysm wall. Furthermore, the same behavior of case 13 occurs: the WSS in neighbouring arteries are almost the same for both wall models.

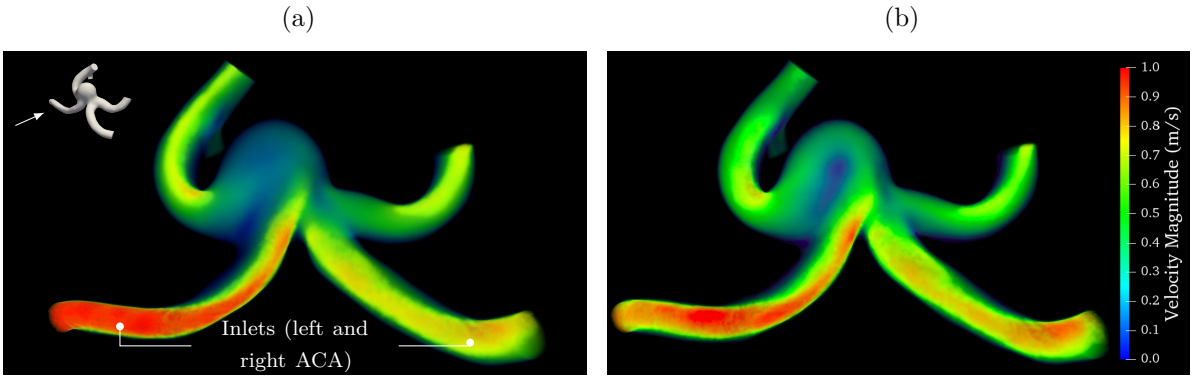
Another important parameter associated with arterial disease is the OSI, presented in Section 2.5. It has been investigated in several studies as one of the possible causes of aneurysm rupture: Meng et al. [15], for instance, propose that high values of OSI with low levels of WSS could lead to rupture; Lu et al. [29] performed numerical simulations on ruptured and unruptured aneurysms geometries and showed that, for the ruptured group, the average value of OSI was 0.0879 – compared to 0.0183 for the unruptured group. We consider here OSI $\sim$ 0.08 as a high level of OSI. Figures 34a and 34b show the OSI field

Figure 32 – Comparison of WSS on the surface of case 17 for (a) rigid wall and (b) linear elastic wall models at peak systole (the white arrow at the top left corner indicate the direction of the view).



Source: prepared by the author.

Figure 33 – Volume rendering representation of the velocity field of the aneurysm of case 17 for (a) rigid wall assumption and (b) elastic linear wall model at peak systole.



Source: prepared by the author.

for case 13 with rigid wall and flexible wall models, respectively, and Figs. 34c and 34d show the OSI for case 17.

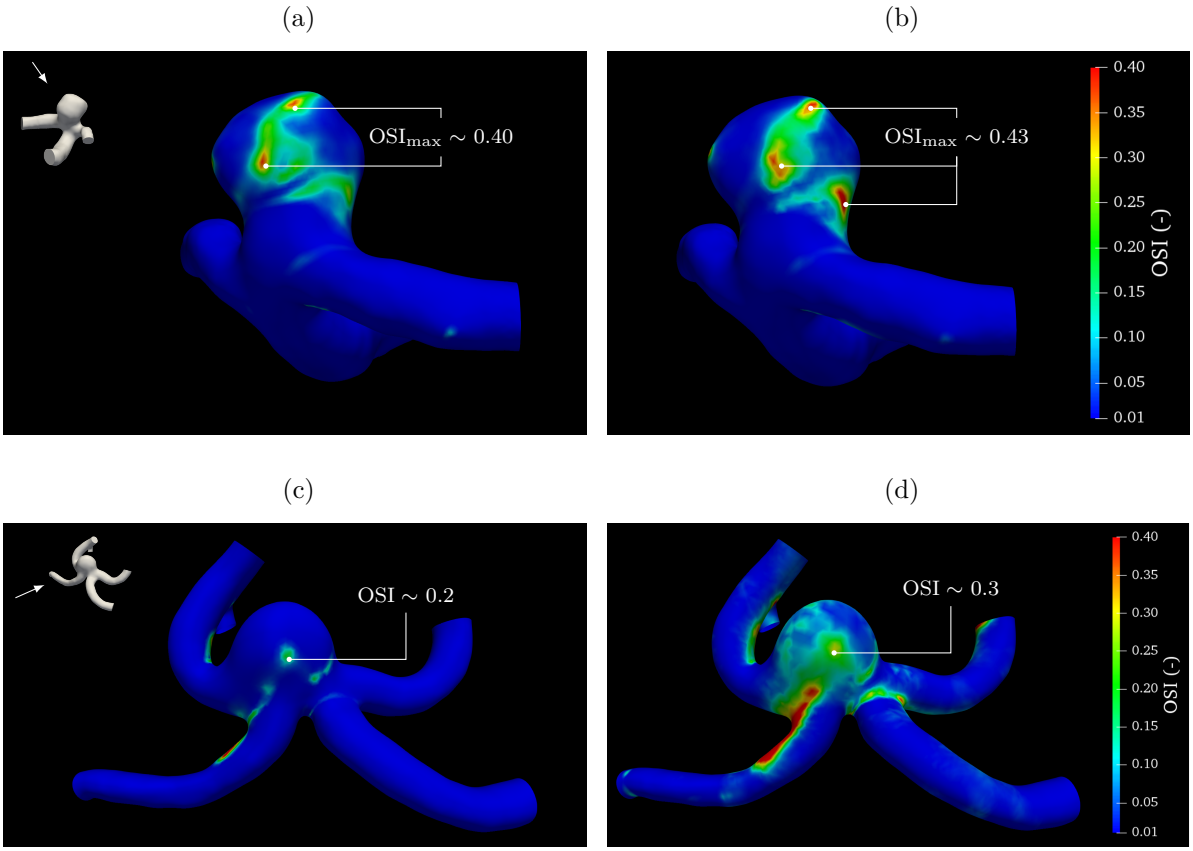
There is an increase of the areas where the OSI is already high – red regions in the figures –, with a larger maximum value (regions marked with a dot in Figs. 34a and 34b): for case 13 with rigid wall assumption the maximum value of OSI is ~ 0.40 and for the linear elastic wall model the maximum value is ~ 0.43; this difference is even larger for case17. Considering that OSI measures the temporal variation of the WSS direction, it seems that accounting for the wall movement changes this time variation, hence increasing the OSI. We note that the OSI remains very low for the arteries around the aneurysm – smaller than 0.05.

Figure 35 shows the Cauchy stress magnitude distribution – or true stress – on the aneurysm and artery walls external surface for cases 13 and 17. We see in both cases

that higher stresses occur in the aneurysm neck, probably due to the curvature of this region, whereas the overall levels of $\boldsymbol{\sigma}^{s}$ on the aneurysm dome remain low – even the maximum value of $\boldsymbol{\sigma}^{s}$ – if compared with the values for the strength limit provided by Costalat et al. [42] and Cebral et al. [43] who performed mechanical tests to failure of rectangular strips of aneurysm wall tissues. The averaged results from Costalat et al. [42] were shown in Section 2.2.2 and are reproduced here in Fig. 36. Since both aneurysms are unruptured cases, it is appropriate to compare with the blue curve of Fig. 36 because it corresponds to the average curves of unruptured cases. Cebral et al. [43] performed similar mechanical tests to failure for unruptured aneurysms and obtained higher values of strength limit: from 0.75 MPa to 2 MPa, depending on the aneurysm case. Based only on these two studies, the variability of strength limit of the aneurysm wall seems to be large.

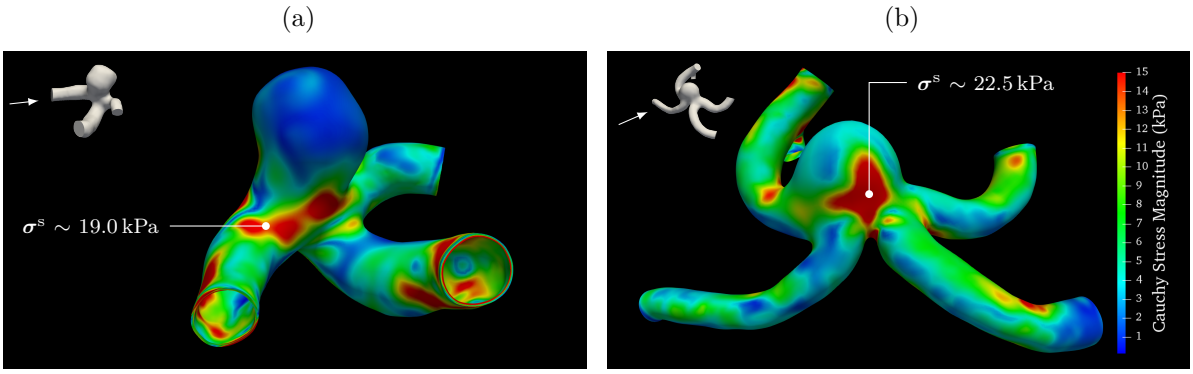
Table 4 shows a summary of mean and maximum values of WSS – at peak systole –

Figure 34 – OSI field of (a) the aneurysm of case 13 with rigid wall assumption and (b) with elastic linear wall model; (c) of the aneurysm of case 17 with rigid wall model and (d) with elastic linear wall model at peak systole with indication of where occurs the highest values of OSI.



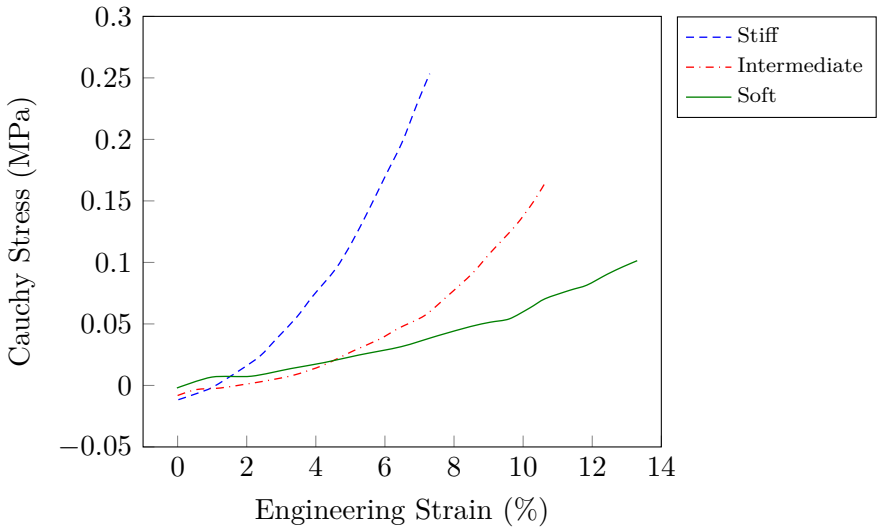
Source: prepared by the author.

Figure 35 – Wall Cauchy stress – or true stress – on the aneurysms of (a) case 13 and (b) case17.



Source: prepared by the author.

Figure 36 – Average strain-stress curves constructed from mechanical tests to failure of rectangular strips of an intracranial aneurysm wall tissue for different stages of the aneurysm: unruptured (stiff) and pre-ruptured or ruptured (soft).



Source: Costalat et al. [42].

and OSI only for the *aneurysm surface*. Averaged quantities are calculated as follows:

$$\overline{WSS}_a = \frac{1}{A_a} \left\| \int_S (\boldsymbol{WSS})\, \mathrm{d}S \right\|_2 \tag{90}$$

$$\overline{OSI}_a = \frac{1}{A_a} \int_S (OSI)\, \mathrm{d}S \tag{91}$$

where A_a is the aneurysm surface area. The table also shows the maximum Cauchy stress magnitude on the aneurysm wall. There is an overall increase in the value of WSS and OSI for case 13 while for case 17 the WSS decreases and the OSI increases considerably due to the larger area of high OSI. Depending on the criteria to define risk of rupture,

this could change the final decision. Unfortunately, since we only analyzed two cases, we cannot conclude that this is a general behavior – more cases should be studied to confirm our suggestions. However, the results reinforce the fact that it would be more appropriate to use a flexible wall model to analyze the aneurysm flow problems.

Table 4 – WSS and OSI mean and maximum values and maximum $\boldsymbol{\sigma}^{\mathrm{s}}$ on the *aneurysm* surface for cases 13 and 17 with different wall tissue model.

Case	Wall Model	WSS (Pa)		OSI (–)		σ^{s} (kPa)
		Maximum	Mean	Maximum	Mean	Maximum
Case 13	Rigid Wall	98.2	5.3	0.403	0.037	-
	Linear Elastic	101.3	15.9	0.434	0.043	18.9
Case 17	Rigid Wall	22.8	3.1	0.192	0.008	-
	Linear Elastic	21.7	2.3	0.396	0.089	22.5

Source: prepared by the author.

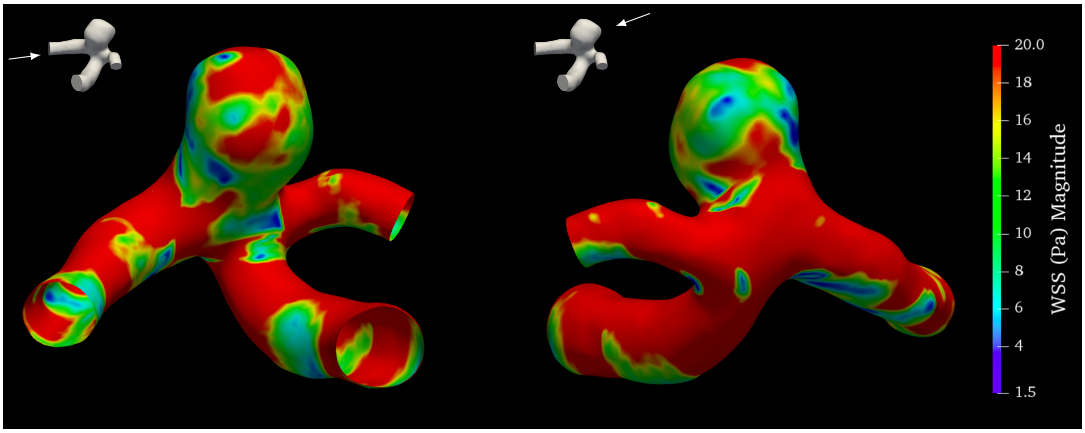
3.3 Comparison between the linear and non-linear elastic models

Simulations with the non-linear elastic solid model were also performed for the geometry of the case 13. Figure 37 shows the WSS distribution on the aneurysm wall for the elastic linear and non-linear models applied to the wall, respectively. The distributions suggest that there is no evident difference between both cases, at least not as evident as happened between the rigid and linear elastic assumptions – see Fig. 30 –, except for the region D marked on the figure, where the levels of WSS are higher for the non-linear wall case. However it seems that the overall structure of the field is the same, specially on the surface of the arteries around the aneurysm.

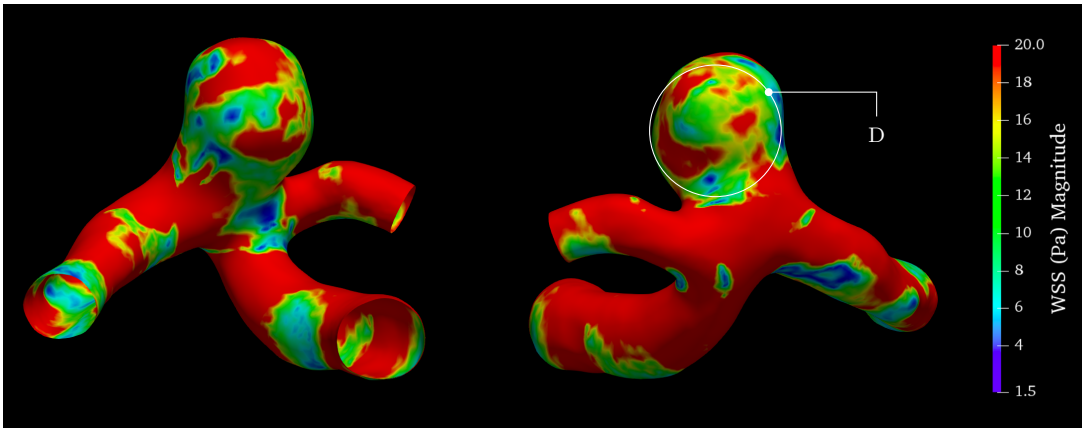
Figure 38 shows the Cauchy stress magnitude field on the wall tissue using the linear and non-linear elastic models, respectively. As with the WSS field, there are no large differences between both fields. We can see only a small increase of $\boldsymbol{\sigma}^{\mathrm{s}}$ on the top of the aneurysm dome, but it is still less than the levels of rupture limit in Fig. 36. These results suggests that both models could be used to predict the variables related to aneurysm rupture.

Figure 37 – Comparison of WSS on the surface of case 13 for (a) linear elastic wall and (b) non-linear elastic wall models at peak systole (the white arrow at the top left corner indicate the direction of the view).

(a)



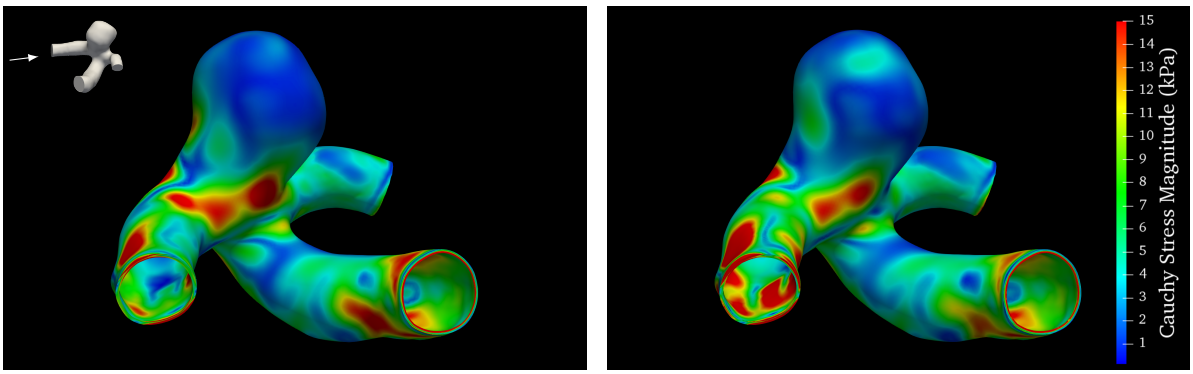
(b)



Source: prepared by the author.

Figure 38 – Wall Cauchy stress – or true stress – on the aneurysms of case 13 for (a) linear elastic model and (b) non-linear elastic model.

(a) (b)

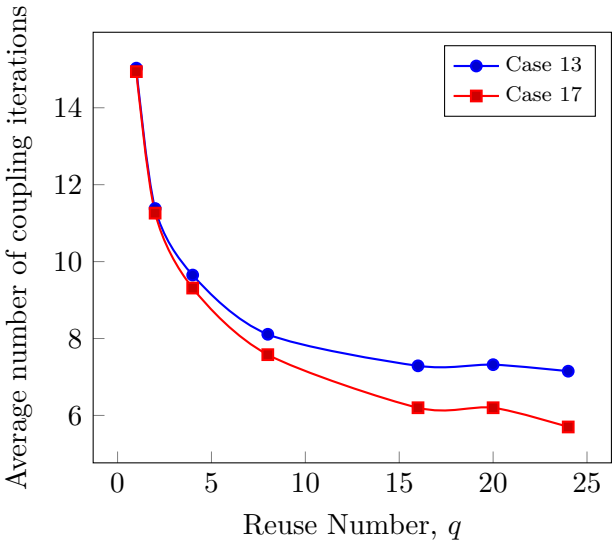


Source: prepared by the author.

3.4 Performance assessment of the IQN-ILS coupling method for the aneurysm problem

As discussed in the Section 2.3.3, the flow within aneurysms with flexible walls is a complex FSI problem due to the strong coupling between the fluid and solid phases, mainly because the flow is assumed to be incompressible and the solid and fluid densities are very close, i.e., $\frac{\rho^{s}}{\rho^{f}} \approx 1$. This yields a challenging computational problem, specially if a partitioned methodology is used to solve it. Therefore, as new techniques are created to solve strongly coupled FSI, it is interesting to assess how good the technique is for this specific problem. We try to do that here by evaluating the speed of convergence of the method through the reuse parameter, q, because as explained in the Section 2.3.3, the convergence rate depends on it. Furthermore, the reuse parameter is problem dependent. Figures 39 and 40 shows the average number of coupling iterations and running time for different values of q for both cases, respectively.

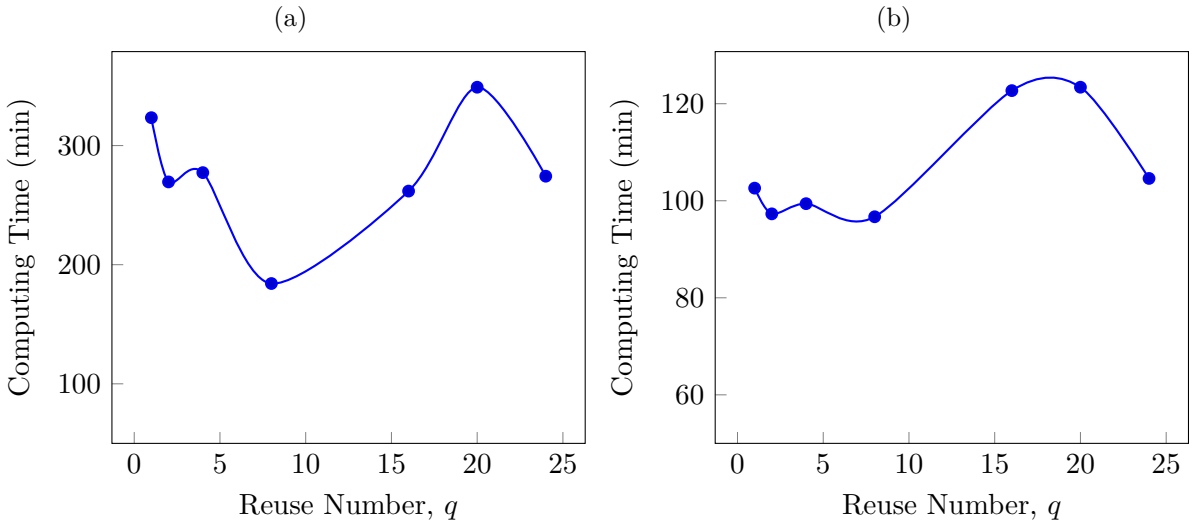
Figure 39 – Average number of iterations in a set of 100 time-steps as a function of the number of reused information from old time-steps of the IQN-ILS algorithm, q.



Source: prepared by the author.

The average number of coupling iterations decreases as q increases, but for $q > 15$ the average number of coupling iterations shows no further decrease, possibly because the information of time-steps before $n - q$ does not influence the solution anymore. On the other hand, after $q = 15$ the computing time starts to increase, probably because the number of coupling iterations is large in the initial time-steps, while the algorithm does not yet reuse data. This is valuable information if more simulations with aneurysms would be

Figure 40 – Time of simulation for 100 time-steps, in minutes, for (a) case 13 and (b) case 17 as a function of the reuse parameter, q.



Source: prepared by the author.

performed, saving time on performing analysis of this kind, because the optimum number of q does not change very much in other cases of aneurysms with similar simulation setup.

4 DISCUSSION AND CONCLUSIONS

The results show that the flexible aneurysm wall model changes the values obtained for the hemodynamic parameters that may lead to aneurysm rupture. This can be explained once we know that the aneurysm fluid-solid problem is strongly coupled: the motion of the artery changes the fluid domain sufficiently to alter the flow variables in a significant way and, most importantly, the hemodynamic parameters usually related to aneurysms rupture events; this became clear from the analysis of cases 13 and 17 flow solutions, which showed changes in the velocity field. Moreover, the reference values used here to define low or high values of WSS and OSI were obtained using numerical simulations with a rigid wall assumption [16, 29]. Therefore, it would be prudent to re-evaluate these parameters for ruptured cases using a *flexible wall model*. Finally, the rigid wall assumption seems to be a very crude approximation in a scenario where WSS and OSI are obtained from a numerical simulation of a patient-specific aneurysm would be used to assess the risk of rupture and, in a medical context, define the treatment course of action.

Despite that, as highlighted in Section 1.2, there has been fewer studies considering a flexible aneurysm and arteries wall tissue compared to studies using the rigid wall assumption, probably because taking into account the tissue movement yields a strong fluid-solid interaction problem, and numerical methods that are robust enough for solving it evolved greatly only in the last two decades, together with a fast increase in computational power and, hence, more studies of this type will appear from now on leading the way to, maybe, begin to be used in the medical practice. Nevertheless, the numerical accuracy and performance of new methods and techniques should be evaluated and tested with real world cases.

With a numerical technique to solve the aneurysm FSI problem, it was also possible to analyze the Cauchy stress on the aneurysm and artery tissue, a very important variable if we wish to have further information about the rupture event, which cannot be obtained in rigid wall aneurysm CFD simulations. From the engineering perspective, the rupture occurs when the stress in the wall reaches the strength limit of the aneurysm wall. For the cases studied, the maximum wall stress on the aneurysm dome were 18.9 kPa and 22.5 kPa for cases 13 and 17, respectively, with the linear elastic model, which is much lower than the strength limit showed in Fig. 36: ≈ 250 kPa. However, we need to consider some important factors that influence the wall stress distribution:

- Constitutive model used for the wall tissue: we only analyzed one aneurysm case with the linear and non-linear elastic wall models, which was not very conclusive with respect to the effect that the wall model plays on the hemodynamic parameters. Probably, because the non-linear elastic model used accounts for expected large deformations of the solid, it predicts whether larger distortions occur on the aneurysm wall, which could alter even more the flow field and yield great changes in the WSS and OSI distributions. Furthermore, it would be very interesting to compare different solid constitutive models of the wall tissue for *ruptured* cases of aneurysms, and compare the levels of $\boldsymbol{\sigma}^{\mathrm{s}}$ with the strength limits presented by Costalat et al. [42] and Cebral et al. [43], for example. More elaborate rheology models for solid – such as hyperelastic, viscoelastic and plastic models – were not implemented in the FSI framework of foam-extend;

- Wall thickness: the values chosen for our simulations – uniform thickness of 0.10 mm and 0.15 mm – are based on the review by Isaksen et al. [48]. According to Scott et al. [93], brain artery walls thickness lies between 0.1 mm to 0.2 mm, whereas aneurysm walls are much thinner, around 0.025 mm at the rupture site, information also confirmed by Cebral et al. [94], which goes further and concludes that not only there is a wall thinning but also a larger stiffness at rupture sites. More recent studies of the aneurysm wall tissue measured their thickness and found larger values – from 0.2 mm to 0.6 mm [42, 43]. Therefore, there seems to be a large variability of the wall thickness between different patients and a *thickness distribution* for an aneurysm. Finally, an ideal simulation should consider non-uniform wall thicknesses obtained from patient-specific images;

- Mechanical properties: while we used constant and uniform mechanical properties, Scott et al. [93] showed that the aneurysm wall stiffness is higher than the stiffness of brain arteries tissue, and Cebral et al. [94] showed that rupture sites are stiffer than the rest of the aneurysm wall. However, measuring mechanical properties of living tissue is still a complex task and we relied on values provided by the literature;

- Boundary conditions on the sections of the arteries – see Fig. 6 – are zero displacement, which is not entirely correct since, actually, there is a network of arteries after it and these are not fixed. Therefore, other boundary condition types more suitable for

theses surfaces should be explored;

- Cyclic behavior of the blood velocity leads to a cyclic pressure and stress on the aneurysm wall. From a materials engineering perspective, the wall would rupture due to fatigue with smaller values of wall stress [95];

Further investigations of the influence of these parameters on the hemodynamic and wall stress is left for future work, because most of them are not yet readily available to be used in the FSI framework of foam-extend. Regarding the non-linear solid model, when it is used, it takes more time to achieve convergence for the solid problem than using the linear elastic model, probably because the source terms in Eq. (17) are larger than those in Eq. (20). Therefore, it would be appropriate to solve it with a more robust technique to deal with the non-linear terms.

Another issue in flow simulations of the human vascular system is related to the outlet boundary conditions. We used a constant pressure condition equal to the average pressure level of the human body. However, there is some discussion in the literature about which would be the most appropriate boundary condition for outlets, because there is a network of vessels after it. One example is found in Vignon-Clementel et al. [34], who propose to use a time-varying pressure at outlets, proportional to the blood flow rate at the vessel, to account for the influence of the downstream vessels. We tried to use this time-varying profile but the simulations did not converge. This happened probably because the pressure and traction fields on the FSI boundary are very important and fluctuations in their could lead to divergence of the coupling iterations. While this is not entirely a limitation, this kind of boundary condition could have a great influence on the flow and solid solution and should be explored.

The coupling scheme IQN-ILS has proved to be a robust method to solve the strong FSI problem such as the one addressed in this work. During the initial tests with aneurysms geometries, we tried to run some simulations using dynamic relaxation – Aitken's dynamic relaxation, implemented in foam-extend –, however the tests did not reach convergence for the geometries and conditions tested. It is also important to note that, as far as the author know from the literature available, no tests of the IQN-ILS were performed on real aneurysms geometries, only benchmark cases were tested. The analysis showed in the Section 3.4 found an ideal number of reuse parameter of the IQN-ILS method for the aneurysm problem, which can be used as a starting reference for further simulations.

Some cases tested showed to be still unstable, mostly for meshes with poor quality, but improving the mesh quality and working with the setup parameters of the FSI simulations was enough to achieve convergence. One of the downsides of the method is its explicitness, which requires the use of very small time-steps for stability, and since the time-scale order of the cardiac cycle, $\sim 1\,\mathrm{s}$, a large number of time-steps must be solved.

Although there is still a lot to develop in terms of numerical simulations of biological fluid-structure interaction problems, it has an important role to play in advances on numerical simulations of coupled problems for applications in Engineering and Medicine. The results of this kind of simulations can help, in the future, the prognostic of intracranial aneurysms and other similar anomalies related to the blood flow in the human vascular system.

REFERENCES

[1] KenHub. KenHub Website. https://www.kenhub.com/, 2017. [Accessed 16-June-2017].

[2] Albert L. Rhoton. Aneurysms. *Neurosurgery*, 51(suppl_1):121–158, 2002. ISSN 0148396X. doi: 10.1227/01.NEU.0000028227.73143.A7.

[3] The International Study of Unruptured Intracranial Aneurysms Investigators. Unruptured Intracranial Aneurysms - Risk of Rupture and Risks of Surgical Intervention. *Journal of Medicine*, 339:785–791, 1998. ISSN 15334406. doi: 10.1056/NEJMoa012295.

[4] The International Study of Unruptured Intracranial Aneurysms Investigators. Unruptured intracranial aneurysms: natural history, clinical outcome, and risks of surgical and endovascular treatment. *Lancet*, 362:103–110, 2003. ISSN 1474-547X. doi: 10.1016/S0140-6736(03)13860-3. URL papers2://publication/uuid/61F1C990-D97F-4487-A3B0-3EEB7183B096.

[5] Adnan I. Qureshi, Vallabh Janardhan, Ricardo A. Hanel, and Giuseppe Lanzino. Comparison of endovascular and surgical treatments for intracranial aneurysms: an evidence-based review. *Lancet Neurology*, 6(9):816–825, 2007. ISSN 14744422. doi: 10.1016/S1474-4422(07)70217-X.

[6] J Van Gijn and G J E Rinkel. Subarachnoid haemorrhage: diagnosis, causes and management. *Brain : a journal of neurology*, 124(Pt 2):249–78, 2001. ISSN 0006-8950. doi: 10.1093/brain/124.2.249. URL http://www.ncbi.nlm.nih.gov/pubmed/11157554.

[7] Jan van Gijn, Richard S Kerr, and Gabriel J E Rinkel. Subarachnoid haemorrhage. *Lancet*, 369(9558):306–318, 2007. ISSN 1474-547X. doi: 10.1016/S0140-6736(07)60153-6.

[8] Brad E. Zacharia, Zachary L. Hickman, Bartosz T. Grobelny, Peter DeRosa, Ivan Kotchetkov, Andrew F. Ducruet, and E. Sander Connolly. Epidemiology of Aneurysmal Subarachnoid Hemorrhage. *Neurosurgery Clinics of North America*, 21(2):221–233, 2010. ISSN 10423680. doi: 10.1016/j.nec.2009.10.002. URL http://dx.doi.org/10.1016/j.nec.2009.10.002.

[9] J. W. Hop, G. J.E. Rinkel, A. Algra, and J. van Gijn. Case-Fatality Rates and Functional Outcome After Subarachnoid Hemorrhage : A Systematic Review. *Stroke*, 28(3):660–664, mar 1997. ISSN 0039-2499. doi: 10.1161/01.STR.28.3.660. URL http://stroke.ahajournals.org/cgi/content/long/28/3/660.

[10] J R Cebral and M Cerrolaza. Computational Analysis of Blood Flow Dynamics in Cerebral Aneurysms from CTA and 3D Rotational Angiography Image Data. In *International Congress on Computational Bioengineering*, 2003.

[11] George K C Wong and W. S. Poon. Current status of computational fluid dynamics for cerebral aneurysms: The clinician's perspective. *Journal of Clinical Neuroscience*, 18(10):1285–1288, 2011. ISSN 09675868. doi: 10.1016/j.jocn.2011.02.014. URL http://dx.doi.org/10.1016/j.jocn.2011.02.014.

[12] Ryo Torii, Marie Oshima, Toshio Kobayashi, Kiyoshi Takagi, and Tayfun E. Tezduyar. Fluid-structure interaction modeling of aneurysmal conditions with high and normal blood pressures. *Computational Mechanics*, 38(4-5):482–490, 2006. ISSN 01787675. doi: 10.1007/s00466-006-0065-6.

[13] Bryce Weir, Christina Amidei, Gail Kongable, J Max Findlay, Neal F Kassell, John Kelly, Lanting Dai, and Theodore G Karrison. The aspect ratio (dome/neck) of ruptured and unruptured aneurysms. *Journal of neurosurgery*, 99(3):447–451, 2003. ISSN 0022-3085. doi: 10.3171/jns.2003.99.3.0447.

[14] David L. Penn, Ricardo J. Komotar, and E. Sander Connolly. Hemodynamic mechanisms underlying cerebral aneurysm pathogenesis. *Journal of Clinical Neuroscience*, 18(11):1435–1438, 2011. ISSN 09675868. doi: 10.1016/j.jocn.2011.05.001. URL http://dx.doi.org/10.1016/j.jocn.2011.05.001.

[15] H. Meng, V. M. Tutino, J. Xiang, and A. Siddiqui. High WSS or Low WSS? Complex interactions of hemodynamics with intracranial aneurysm initiation, growth, and rupture: Toward a unifying hypothesis. *American Journal of Neuroradiology*, 35(7): 1254–1262, 2014. ISSN 1936959X. doi: 10.3174/ajnr.A3558.

[16] M. Shojima, M Oshima, Kiyoshi Takagi, Ryo Torii, Motoharu Hayakawa, Kazuhiro Katada, Akio Morita, and Takaaki Kirino. Magnitude and Role of Wall Shear

Stress on Cerebral Aneurysm: Computational Fluid Dynamic Study of 20 Middle Cerebral Artery Aneurysms. *Stroke*, 35(11):2500–2505, 2004. ISSN 0039-2499. doi: 10.1161/01.STR.0000144648.89172.0f.

[17] Daniel M Sforza, Christopher M Putman, and Juan Raul Cebral. Hemodynamics of Cerebral Aneurysms. *Annual Review of Fluid Mechanics*, 41:91–107, 2009. doi: 10.1146/annurev.fluid.40.111406.102126.Hemodynamics.

[18] Y. C. Fung. *Biomechanics*. Springer, 2nd edition, 1998. ISBN 9781441931047. doi: 10.1097/00024382-199802000-00018. URL `http://content.wkhealth.com/linkback/openurl?sid=WKPTLP:landingpage{&}an=00024382-199802000-00018`.

[19] H Nakatani, N Hashimoto, Y Kang, N Yamazoe, H Kikuchi, S Yamaguchi, and H Niimi. Cerebral blood flow patterns at major vessel bifurcations and aneurysms in rats. *Journal of neurosurgery*, 74(2):258–62, 1991. ISSN 0022-3085. doi: 10.3171/jns.1991.74.2.0258. URL `http://www.ncbi.nlm.nih.gov/pubmed/1988596`.

[20] C. F. Gonzalez, Y. I. Cho, H. V. Ortega, and J. Moret. Intracranial aneurysms: Flow analysis of their origin and progression. *American Journal of Neuroradiology*, 13(1): 181–188, 1992. ISSN 01956108.

[21] Y. P. Gobin, J. L. Counord, P. Flaud, and J. Duffaux. In vitro study of haemodynamics in a giant saccular aneurysm model: influence of flow dynamics in the parent vessel and effects of coil embolisation. *Neuroradiology*, 36(7):530–536, 1994. ISSN 00283940. doi: 10.1007/BF00593516.

[22] T M Liou and S N Liou. A review on in vitro studies of hemodynamic characteristics in terminal and lateral aneurysm models. *Proc Natl Sci Counc Repub China B*, 23 (4):133–148, 1999. ISSN 0255-6596. URL `http://www.ncbi.nlm.nih.gov/pubmed/10518314`.

[23] S Tateshima, Y Murayama, J P Villablanca, T Morino, H Takahashi, T Yamauchi, K Tanishita, and F Vinuela. Intraaneurysmal flow dynamics study featuring an acrylic aneurysm model manufactured using a computerized tomography angiogram as a mold. *Journal of neurosurgery*, 95(6):1020–1027, 2001. ISSN 0022-3085. doi: 10.3171/jns.2001.95.6.1020.

[24] Toru Satoh, Keisuke Onoda, and Shoji Tsuchimoto. Visualization of intraaneurysmal flow patterns with transluminal flow images of 3D MR angiograms in conjunction with aneurysmal configurations. *American Journal of Neuroradiology*, 24(7):1436–1445, 2003. ISSN 01956108.

[25] David A Steinman, Jaques S Milner, Chris J Norley, Stephen P Lownie, and David W Holdsworth. Image-based computational simulation of flow dynamics in a giant intracranial aneurysm. *AJNR. American journal of neuroradiology*, 24(4):559–66, 2003. ISSN 0195-6108. URL `http://www.ajnr.org/content/24/4/559.abstract`.

[26] M. A. Castro, Christopher M. Putman, and J. R. Cebral. Computational fluid dynamics modeling of intracranial aneurysms: Effects of parent artery segmentation on intra-aneurysmal hemodynamics. *American Journal of Neuroradiology*, 27(8): 1703–1709, 2006. ISSN 01956108. doi: 27/8/1703[pii].

[27] Ryo Torii, Marie Oshima, Toshio Kobayashi, Kiyoshi Takagi, and Tayfun E. Tezduyar. Fluid-structure interaction modeling of a patient-specific cerebral aneurysm: Influence of structural modeling. *Computational Mechanics*, 43(1):151–159, 2008. ISSN 01787675. doi: 10.1007/s00466-008-0325-8.

[28] Y. Bazilevs, M. C. Hsu, Y. Zhang, W. Wang, T. Kvamsdal, S. Hentschel, and J. G. Isaksen. Computational vascular fluid-structure interaction: Methodology and application to cerebral aneurysms. *Biomechanics and Modeling in Mechanobiology*, 9 (4):481–498, 2010. ISSN 16177959. doi: 10.1007/s10237-010-0189-7.

[29] G. Lu, L. Huang, X. L. Zhang, S. Z. Wang, Y. Hong, Z. Hu, and D. Y. Geng. Influence of hemodynamic factors on rupture of intracranial aneurysms: Patient-specific 3D mirror aneurysms model computational fluid dynamics simulation. *American Journal of Neuroradiology*, 32(7):1255–1261, 2011. ISSN 01956108. doi: 10.3174/ajnr.A2461.

[30] Øyvind Evju, Kristian Valen-Sendstad, and Kent André Mardal. A study of wall shear stress in 12 aneurysms with respect to different viscosity models and flow conditions. *Journal of Biomechanics*, 46(16), 2013. ISSN 00219290. doi: 10.1016/j.jbiomech.2013.09.004.

[31] C Karmonik, O Diaz, R Klucznik, R G Grossman, Y J Zhang, G Britz, N Lv, and Q Huang. Quantitative comparison of hemodynamic parameters from steady and

transient CFD simulations in cerebral aneurysms with focus on the aneurysm ostium. *Journal of neurointerventional surgery*, pages 1–6, 2014. ISSN 1759-8486. doi: 10.1136/neurintsurg-2014-011182. URL `http://jnis.bmj.com/content/early/2014/04/10/neurintsurg-2014-011182.long`.

[32] G. Byrne, F. Mut, and J. Cebral. Quantifying the large-scale hemodynamics of intracranial aneurysms. *American Journal of Neuroradiology*, 35(2):333–338, 2014. ISSN 01956108. doi: 10.3174/ajnr.A3678.

[33] Keiji Fukazawa, Fujimaro Ishida, Yasuyuki Umeda, Yoichi Miura, Shinichi Shimosaka, Satoshi Matsushima, Waro Taki, and Hidenori Suzuki. Using computational fluid dynamics analysis to characterize local hemodynamic features of middle cerebral artery aneurysm rupture points. *World Neurosurgery*, 83(1):80–86, 2015. ISSN 18788769. doi: 10.1016/j.wneu.2013.02.012. URL `http://dx.doi.org/10.1016/j.wneu.2013.02.012`.

[34] Irene E. Vignon-Clementel, C. Alberto Figueroa, Kenneth E. Jansen, and Charles A. Taylor. Outflow boundary conditions for three-dimensional finite element modeling of blood flow and pressure in arteries. *Computer Methods in Applied Mechanics and Engineering*, 195(29-32):3776–3796, 2006. ISSN 00457825. doi: 10.1016/j.cma.2005.04.014.

[35] J R Cebral, M A Castro, J E Burgess, C M Putman, R S Pergolizzi, and M J Sheridan. Characterization of Cerebral Aneurysms for Assessing Risk of Rupture by Using Patient-specific Computational Hemodynamics Models. *American Journ. Of Neuroradiology*, 26:2550–2559, 2005.

[36] J R Cebral, M A Castro, S Appanaboyina, C M Putman, D Millan, and A F Frangi. Efficient Pipeline for Image-Based Patient-Specific Analysis of Cerebral Aneurysm Hemodynamics: Technique and Sensitivity. *Transaction On Medical Imaging*, 24:457–467, 2005.

[37] Y. Bazilevs, V. M. Calo, T. J R Hughes, and Y. Zhang. Isogeometric fluid-structure interaction: Theory, algorithms, and computations. *Computational Mechanics*, 43(1):3–37, 2008. ISSN 01787675. doi: 10.1007/s00466-008-0315-x.

[38] C. J. Lee, Y. Zhang, H. Takao, Y. Murayama, and Y. Qian. A fluid–structure interaction study using patient-specific ruptured and unruptured aneurysm: The effect of aneurysm morphology, hypertension and elasticity. *Journal of Biomechanics*, 46:2402–2410, 2013. doi: 10.1002/cnm.1396.

[39] Ryo Torii, Marie Oshima, Toshio Kobayashi, Kiyoshi Takagi, and Tayfun E. Tezduyar. Influence of wall elasticity in patient-specific hemodynamic simulations. *Computers and Fluids*, 36(1):160–168, 2007. ISSN 00457930. doi: 10.1016/j.compfluid.2005.07.014.

[40] Ryo Torii, Marie Oshima, Toshio Kobayashi, Kiyoshi Takagi, and Tayfun E. Tezduyar. Fluid-structure interaction modeling of blood flow and cerebral aneurysm: Significance of artery and aneurysm shapes. *Computer Methods in Applied Mechanics and Engineering*, 198(45-46):3613–3621, 2009. ISSN 00457825. doi: 10.1016/j.cma.2008.08.020. URL `http://dx.doi.org/10.1016/j.cma.2008.08.020`.

[41] Paolo Tricerri, Luca Dedè, Simone Deparis, Alfio Quarteroni, Anne M. Robertson, and Adélia Sequeira. Fluid-structure interaction simulations of cerebral arteries modeled by isotropic and anisotropic constitutive laws. *Computational Mechanics*, 55(3), 2015. ISSN 01787675. doi: 10.1007/s00466-014-1117-y.

[42] V. Costalat, M. Sanchez, D. Ambard, L. Thines, N. Lonjon, F. Nicoud, H. Brunel, J. P. Lejeune, H. Dufour, P. Bouillot, J. P. Lhaldky, K. Kouri, F. Segnarbieux, C. A. Maurage, K. Lobotesis, M. C. Villa-Uriol, C. Zhang, A. F. Frangi, G. Mercier, A. Bonafé, L. Sarry, and F. Jourdan. Biomechanical wall properties of human intracranial aneurysms resected following surgical clipping (IRRAs Project). *Journal of Biomechanics*, 44(15):2685–2691, 2011. ISSN 00219290. doi: 10.1016/j.jbiomech.2011.07.026.

[43] J. R. Cebral, X. Duan, B. J. Chung, C. Putman, K. Aziz, and A. M. Robertson. Wall mechanical properties and hemodynamics of unruptured intracranial aneurysms. *American Journal of Neuroradiology*, 36(9):1695–1703, 2015. ISSN 1936959X. doi: 10.3174/ajnr.A4358.

[44] F. Moukalled, L. Mangani, and M. Darwish. *The Finite Volume Method in Computational Fluid Dynamics*, volume 113. Springer, 2016. ISBN 978-3-319-16873-9. doi:

10.1007/978-3-319-16874-6. URL http://www.scopus.com/inward/record.url?eid=2-s2.0-84939129919{&}partnerID=tZOtx3y1.

[45] Yuri Bazilevs, Kenji Takizawa, and Tayfun E. Tezduyar. *Computational Fluid-Structure Interaction: Methods and Applications*. John Wiley & Sons, 2012. ISBN 9780470978771. doi: 10.1002/9781118483565. URL http://eu.wiley.com/WileyCDA/WileyTitle/productCd-0470978775.html{%}5Cnhttp://doi.wiley.com/10.1002/9781118483565.

[46] Gene Hou, Jin Wang, and Anita Layton. Numerical methods for fluid-structure interaction - A review. *Communications in Computational Physics*, 12(2):337–377, 2012. ISSN 18152406. doi: 10.4208/cicp.291210.290411s.

[47] C. S. Peskin. The immersed boundary method. *Acta Numerica*, 11(January 2002): 479–517, 2002. ISSN 0962-4929. doi: 10.1017/S0962492902000077.

[48] Jørgen Gjernes Isaksen, Yuri Bazilevs, Trond Kvamsdal, Yongjie Zhang, Jon H. Kaspersen, Knut Waterloo, Bertil Romner, and Tor Ingebrigtsen. Determination of wall tension in cerebral artery aneurysms by numerical simulation. *Stroke*, 39(12): 3172–3178, 2008. ISSN 00392499. doi: 10.1161/STROKEAHA.107.503698.

[49] Taha Sochi. Non-Newtonian Rheology in Blood Circulation, 2013. URL http://arxiv.org/abs/1306.2067.

[50] F J H Gijsen, F N van de Vosse, and J D Janssen. The influence of the non-Newtonian properties of blood on the flow in large arteries: steady flow in a carotid bifurcation model. *J Biomech*, 32(6):601–608, 1999. URL http://www.sciencedirect.com/science/article/pii/S0021929099000159.

[51] Jie Chen and Xi Yun Lu. Numerical investigation of the non-Newtonian blood flow in a bifurcation model with a non-planar branch. *Journal of Biomechanics*, 37(12): 1899–1911, 2004. ISSN 00219290. doi: 10.1016/j.jbiomech.2004.02.030.

[52] J. Bernsdorf and D. Wang. Non-Newtonian blood flow simulation in cerebral aneurysms. *Computers and Mathematics with Applications*, 58(5):1024–1029, 2009. ISSN 08981221. doi: 10.1016/j.camwa.2009.02.019.

[53] K Perktold, M Resch, and H Florian. Pulsatile Non-Newtonian Flow Characteristics in a Three-Dimensional Human Carotid Bifurcation Model. *Journal of Biomechanical Engineering*, 113(4):464–475, nov 1991. ISSN 0148-0731. URL `http://dx.doi.org/10.1115/1.2895428`.

[54] Alvaro Valencia, Alvaro Zarate, Marcelo Galvez, and Lautaro Badilla. Non-Newtonian blood ow dynamics in a right internal carotid artery with a saccular aneurysm. *International Journal for Numerical Methods in Fluids*, 50:751–764, 2006.

[55] Y. Bazilevs, M. C. Hsu, Y. Zhang, W. Wang, X. Liang, T. Kvamsdal, R. Brekken, J. G. Isaksen, Y Bazylevs, Others, Y. Bazilevs, M. C. Hsu, Y. Zhang, W. Wang, X. Liang, T. Kvamsdal, R. Brekken, and J. G. Isaksen. A fully-coupled fluid-structure interaction simulation of cerebral aneurysms. *Computational Mechanics*, 46(1):3–16, 2009. ISSN 01787675. doi: 10.1007/s00466-009-0421-4.

[56] T. Belytschko, W. K. Liu, and B. Moran. *Nonlinear Finite Elements for Continua and Structures*. John Wiley & Sons, 2nd edition, 2014. ISBN 0122030532. doi: 10.1016/S0065-230X(09)04001-9. URL `http://scholar.google.com/scholar?hl=en{&}btnG=Search{&}q=intitle:Nonlinear+finite+elements+for+continua+and+structures.+2000{#}0`.

[57] J Donea, Antonio Huerta, J Ponthot, and A Rodr. Arbitrary Lagrangian – Eulerian Methods. In *Encyclopedia of Computational Mechanics*, chapter 14, pages 1–25. John Wiley & Sons, 1999. ISBN 0470846992. doi: 10.1002/0470091355.ecm009.

[58] I Demirdžić and M Perić. Space conservation law in finite volume calculations of fluid flow. *International Journal for Numerical Methods in Fluids*, 8(December 1987):1037–1050, 1988. ISSN 0271-2091. doi: 10.1002/fld.1650080906. URL `http://onlinelibrary.wiley.com/doi/10.1002/fld.1650080906/abstract{%}5Cnhttp://doi.wiley.com/10.1002/fld.1650080906`.

[59] M D Ford, N Alperin, S H Lee, D W Holdsworth, and David A Steinman. Characterization of normal cerebrovascular volumetric flow rate dynamics by PC-MRI. *The International Society for Magnetic Resonance in Medicine 13th Annual Meeting*, 13:1741, 2005.

[60] Laleh Zarrinkoob, Khalid Ambarki, Anders Wåhlin, Richard Birgander, Anders Eklund, and Jan Malm. Blood flow distribution in cerebral arteries. *Journal of cerebral blood flow and metabolism*, 35:648–654, 2015. ISSN 1559-7016. doi: 10.1038/jcbfm.2014.241. URL `http://www.ncbi.nlm.nih.gov/pubmed/25564234`.

[61] Y. C. Fung. *Biomechanics: Motion, Flow, Stress, and Growth*. Springer, 1993. ISBN 0387971246. doi: 10.1115/1.2900838.

[62] G. A. Holzapfel and R. W. Ogden. Constitutive modelling of arteries. *Proceedings of the Royal Society A: Mathematical, Physical and Engineering Sciences*, 466(2118): 1551–1597, 2010. ISSN 1364-5021. doi: 10.1098/rspa.2010.0058. URL `http://rspa.royalsocietypublishing.org/cgi/doi/10.1098/rspa.2010.0058`.

[63] Ryo Torii, Marie Oshima, Toshio Kobayashi, Kiyoshi Takagi, and Tayfun E. Tezduyar. Influence of wall thickness on fluid–structure interaction computations of cerebral aneurysms. *International Journal for Numerical Methods in Biomedical Engineering*, 26(1):336–347, 2010. ISSN 20407939. doi: 10.1002/cnm. URL `http://onlinelibrary.wiley.com/doi/10.1002/cnm.1494/full`.

[64] Philip Cardiff. Nonlinear Solid Mechanics in OpenFOAM. In *9th OpenFOAM Workshop*, 2014. doi: 10.13140/RG.2.1.3335.0481.

[65] Suhas Patankar. *Numerical heat transfer and fluid flow*. McGraw-Hill Publishing, 1980. ISBN 978-0891165224 0. doi: 10.1016/j.watres.2009.11.010.

[66] Philip Cardiff. *Development of the Finite Volume Method for Hip Joint Stress Analysis by Philip Cardiff*. PhD thesis, University College Dublin, 2012.

[67] P. Cardiff, Ž. Tuković, H. Jasak, and A. Ivanković. A block-coupled Finite Volume methodology for linear elasticity and unstructured meshes. *Computers and Structures*, 175:100–122, 2016. ISSN 00457949. doi: 10.1016/j.compstruc.2016.07.004.

[68] OpenFOAM-Extend. foam-extend Website. `https://sourceforge.net/projects/foam-extend/?source=navbar`, 2017. [Accessed 19-June-2017].

[69] Joris Degroote, Klaus Jürgen Bathe, and Jan Vierendeels. Performance of a new partitioned procedure versus a monolithic procedure in fluid-structure interaction.

Computers and Structures, 87(11-12):793–801, 2009. ISSN 00457949. doi: 10.1016/j.compstruc.2008.11.013. URL http://dx.doi.org/10.1016/j.compstruc.2008.11.013.

[70] H. Jasak and Ž. Tuković. Automatic mesh motion for the unstructured Finite Volume Method. *Transactions of Famena*, 30(2):1–20, 2006. ISSN 13331124. doi: 10.1126/science.1247727.

[71] H. Jasak and Ž. Tuković. Dynamic mesh handling in OpenFOAM applied to fluid-structure interaction simulations. In *European Conference on Computational Fluid Dynamics*, pages 1–19, Lisbon, 2010.

[72] Ž. Tuković, P. Cardiff, H. Jasak, and A. Ivankovic. OpenFOAM Library for Fluid Structure Interaction. In *9th OpenFOAM Workshop*, 2014.

[73] H. K. Versteeg and W. Malalasekera. *An Introduction to Computational Fluid Dynamics*, volume 1. Pearson Prentice Hall, 2007. ISBN 9780131274983.

[74] H Jasak. *Error Analysis and Estimation for the Finite Volume Method with Applications to Fluid Flows*. PhD thesis, Imperial College of Science, Technology and Medicine, 1996.

[75] Ž Tuković and H. Jasak. A moving mesh finite volume interface tracking method for surface tension dominated interfacial fluid flow. *Computers and Fluids*, 55:70–84, 2012. ISSN 00457930. doi: 10.1016/j.compfluid.2011.11.003.

[76] R. I. Issa. Solution of the implicitly discretised fluid flow equations by operator-splitting. *Journal of Computational Physics*, 62(1):40–65, 1986. ISSN 10902716. doi: 10.1016/0021-9991(86)90099-9.

[77] Joel H. Ferziger and Milovan Peric. *Computational Methods for Fluid Dynamics*. Springer, 3rd edition, 2002. ISBN 3540420746. doi: 10.1016/S0898-1221(03)90046-0.

[78] C M Rhie and W L Chow. Numerical study of the turbulent flow past an airfoil with trailing edge separation. *AIAA Journal*, 21(11):1525–1532, 1983. ISSN 0001-1452. doi: 10.2514/3.8284. URL http://dx.doi.org/10.2514/3.8284.

[79] B. Yu, Y Kawaguchi, WQ Tao, and H Ozoe. Checkerboard pressure predictions due to the underrelaxation factor and time step size for a nonstaggered grid with momentum interpolation method. *Numerical Heat Transfer, Part B: Fundamentals*, 41(March 2001):85–94, 2002. ISSN 1040-7790. doi: 10.1080/104077902753385027. URL http://www.tandfonline.com/doi/pdf/10.1080/104077902753385027.

[80] Bo Yu, Wen-Quan Tao, Jin-Jia Wei, Yasuo Kawaguchi, Toshio Tagawa, and Hiroyuki Ozoe. Discussion on momentum interpolation method for collocated grids of incompressible flow. *Numerical Heat*, 42:141–166, 2002. ISSN 1040-7790. doi: 10.1080/10407790190053879.

[81] Gene H Golub and Charles F Van Loan. *Matrix Computations*. The Johns Hopkins University Press, 4th edition, 2013. ISBN 9781421407944.

[82] Joris Degroote, Peter Bruggeman, Robby Haelterman, and Jan Vierendeels. Stability of a coupling technique for partitioned solvers in FSI applications. *Computers and Structures*, 86(23-24):2224–2234, 2008. ISSN 00457949. doi: 10.1016/j.compstruc.2008.05.005. URL http://dx.doi.org/10.1016/j.compstruc.2008.05.005.

[83] P. Causin, J. F. Gerbeau, and Fabio Nobile. Added-mass effect in the design of partitioned algorithms for fluid-structure problems. *Computer Methods in Applied Mechanics and Engineering*, 194(42-44):4506–4527, 2005. ISSN 00457825. doi: 10.1016/j.cma.2004.12.005.

[84] Joris Degroote, Robby Haelterman, Sebastiaan Annerel, Peter Bruggeman, and Jan Vierendeels. Performance of partitioned procedures in fluid-structure interaction. *Computers and Structures*, 88(7-8):446–457, 2010. ISSN 00457949. doi: 10.1016/j.compstruc.2009.12.006. URL http://dx.doi.org/10.1016/j.compstruc.2009.12.006.

[85] Hermann G. Matthies and Jan Steindorf. Partitioned strong coupling algorithms for fluid-structure interaction. *Computers and Structures*, 81(8-11):805–812, 2003. ISSN 00457949. doi: 10.1016/S0045-7949(02)00409-1.

[86] Jan Vierendeels, Lieve Lanoye, Joris Degroote, and Pascal Verdonck. Implicit coupling of partitioned fluid-structure interaction problems with reduced order mod-

els. *Computers and Structures*, 85(11-14):970–976, 2007. ISSN 00457949. doi: 10.1016/j.compstruc.2006.11.006.

[87] Nicolas Gourdain, Laurent Gicquel, Marc Montagnac, Olivier Vermorel, Michel Gazaix, Gabriel Staffelbach, Marta García, Jean-François J-F. Boussuge, Thierry Poinsot, Olivier Vermorel, Florent Duchaine, Jean-François J-F. Boussuge, Thierry Poinsot, Marc Montagnac, Olivier Vermorel, Michel Gazaix, Gabriel Staffelbach, M Garcia, Jean-François J-F. Boussuge, and Thierry Poinsot. High performance parallel computing of flows in complex geometries: I. Methods. *Computational Science & Discovery*, 2(1), 2009. ISSN 1749-4699. doi: 10.1088/1749-4699/2/1/015003. URL `http://stacks.iop.org/1749-4699/2/i=1/a=015003`.

[88] Miriam Mehl, Benjamin Uekermann, Hester Bijl, David Blom, Bernhard Gatzhammer, and Alexander Van Zuijlen. Parallel coupling numerics for partitioned fluid-structure interaction simulations. *Computers and Mathematics with Applications*, 71(4):869–891, 2016. ISSN 08981221. doi: 10.1016/j.camwa.2015.12.025. URL `http://dx.doi.org/10.1016/j.camwa.2015.12.025`.

[89] William L. Oberkampf and Timothy G. Trucano. Verification and validation in computational fluid dynamics. *Progress in Aerospace Sciences*, 38(3):209–272, 2002. ISSN 03760421. doi: 10.1016/S0376-0421(02)00005-2.

[90] M. O. Khan, K. Valen-Sendstad, and D. A. Steinman. Narrowing the expertise gap for predicting intracranial aneurysm hemodynamics: Impact of solver numerics versus mesh and time-step resolution. *American Journal of Neuroradiology*, 36(7), 2015. ISSN 1936959X. doi: 10.3174/ajnr.A4263.

[91] C. Förster, W.A. Wall, and E. Ramm. The artificial added mass effect in sequential staggered fluid-structure interaction algorithms. *ECCOMAS CFD 2006: Proceedings of the European Conference on Computational Fluid Dynamics*, (April): 1–20, 2006. URL `http://repository.tudelft.nl/view/conferencepapers/uuid:f6316ca6-b02a-4a6f-b5ad-4e2f6744c7de/`.

[92] Ch Förster, W. A. Wall, and E. Ramm. On the geometric conservation law in transient flow calculations on deforming domains. *International Journal for Numerical Methods in Fluids*, 50(12):1369–1379, 2006. ISSN 02712091. doi: 10.1002/fld.1093.

[93] Susan Scott, Gary G. Ferguson, and Margot R. Roach. Comparison of the Elastic Properties of Human Intracranial Arteries and Aneurysms. *Canadian Journal of Physiology and Pharmacology*, 50(4):328–332, 1972. ISSN 0008-4212. doi: 10.1139/y72-049. URL `http://www.nrcresearchpress.com/doi/abs/10.1139/y72-049{#}.VClhFBZyV0N`.

[94] Juan R Cebral, Mariano Vazquez, Daniel M Sforza, Guillaume Houzeaux, Satoshi Tateshima, Esteban Scrivano, Carlos Bleise, Pedro Lylyk, and Christopher M Putman. Analysis of hemodynamics and wall mechanics at sites of cerebral aneurysm rupture. *Journal of NeuroInterventional Surgery*, 7(7), 2015. ISSN 1759-8478. doi: 10.1136/neurintsurg-2014-011247.

[95] William D. Callister. *Fundamentals of Materials Science and Engineering*. John Wiley & Sons, Inc., 5th edition, 2001. ISBN 047139551X. URL `http://books.google.com/books?id=0TfIngEACAAJ{&}pgis=1`.

[96] Rutherford Aris. *Vectors, tensors and the basic equations of fluid mechanics*. Dover Publications, 1962.

[97] H. Jasak and H. G. Weller. Application of the finite volume method and unstructured meshes to linear elasticity. *International Journal for Numerical Methods in Engineering*, 48(2):267–287, 2000. ISSN 00295981. doi: 10.1002/(SICI)1097-0207(20000520)48:2<267::AID-NME884>3.0.CO;2-Q.

A Arbitrary Lagrangian-Eulerian Formulation

To write the physical laws that govern the motion of a continuum in space, we need to specify a coordinate system to be used, in which the variables of the motion will be described. The literature in Fluid Mechanics usually use the *Eulerian formulation*: kinematic variables of the fluid flow are related to a *spatial fixed system*; whereas the general literature of Solid Mechanics use the *Lagrangian description* in which solid variables are related to a coordinate system *fixed on the material*. Each description has their strengths and weaknesses [56, 57]. Unfortunately, problems involving moving boundaries and interfaces are not completely suitable for treatment with any of these two formulations. Thus, in FSI partitioned algorithms, hybrid techniques that combine the advantages of the Lagrangian and Eulerian descriptions are preferred. Such techniques are called *arbitrary Lagrangian-Eulerian formulations, ALE* [56, 57], arbitrary because the description is based on an *arbitrary moving control volume* inside the domain.

The basic assumption in the ALE description is the use of another coordinate system, besides the spatial and material coordinates commonly used in the Eulerian and Lagrangian descriptions. Thus, in the ALE description, one define:

- $\boldsymbol{x}$: spatial or Eulerian coordinates. Usually they are represented in the Euclidean space by a Cartesian coordinate system, i.e., $\boldsymbol{x} = x_1\boldsymbol{e}_{(1)} + x_2\boldsymbol{e}_{(2)} + x_3\boldsymbol{e}_{(3)} = x_i\boldsymbol{e}_{(i)}$ (using Einstein's tensorial notation) with $\boldsymbol{e}_{(i)}$ the canonical basis; usually, for the Cartesian coordinate system, the symbols $\boldsymbol{i} \equiv \boldsymbol{e}_{(1)}$, $\boldsymbol{j} \equiv \boldsymbol{e}_{(2)}$ and $\boldsymbol{k} \equiv \boldsymbol{e}_{(3)}$ are used to represent the vectors and x, y and z represent the coordinates directions 1, 2 and 3, respectively;

- $\boldsymbol{\xi} = (\xi_1, \xi_2, \xi_3)$: coordinate system of the material (solid or fluid) being studied, i.e. fixed on it, also called Lagrangian coordinates. In general, its coordinate lines (or coordinate surfaces) are conformed with the material domain boundaries at a predefined instant t;

- $\boldsymbol{\chi} = (\chi_1, \chi_2, \chi_3)$: referential coordinates used to track the domain motion; from the computational point of view, corresponds to the mesh coordinates.

Each of these systems are related to each other through mappings or functions. We will use these functions to derive the kinematic quantities describing the material motion. Our

main focus on this text refers to the application of the ALE formulation to Computational Fluid Dynamics using moving grids. Therefore, our *material* here is a fluid flowing, and when we use the word *particle* we mean an infinitesimal volume element $\mathrm{d}V_\xi$ of fluid, where the lower index indicates the of the particle in $\boldsymbol{\xi}$ coordinates; if $\boldsymbol{\xi}$ is a Cartesian system, for example, then $\mathrm{d}V_\xi = \mathrm{d}\xi_1\mathrm{d}\xi_2\mathrm{d}\xi_3$.

Since we defined different coordinates system, a spatial derivative can be calculated with respect to each of the coordinates presented above. Therefore, the classical "nabla" operator ∇ here is calculated with respect to *spatial coordinates*, i.e.:

$$\nabla(\bullet) = \frac{\partial(\bullet)}{\partial \boldsymbol{x}} = \boldsymbol{e}_{(i)}\frac{\partial(\bullet)}{\partial x_i} \tag{A.1}$$

whereas the nabla with respect to $\boldsymbol{\xi}$ and $\boldsymbol{\chi}$ are represented with a lower index, respectively:

$$\nabla_{\boldsymbol{\xi}}(\bullet) = \frac{\partial(\bullet)}{\partial \boldsymbol{\xi}} \tag{A.2}$$

$$\nabla_{\boldsymbol{\chi}}(\bullet) = \frac{\partial(\bullet)}{\partial \boldsymbol{\chi}} \tag{A.3}$$

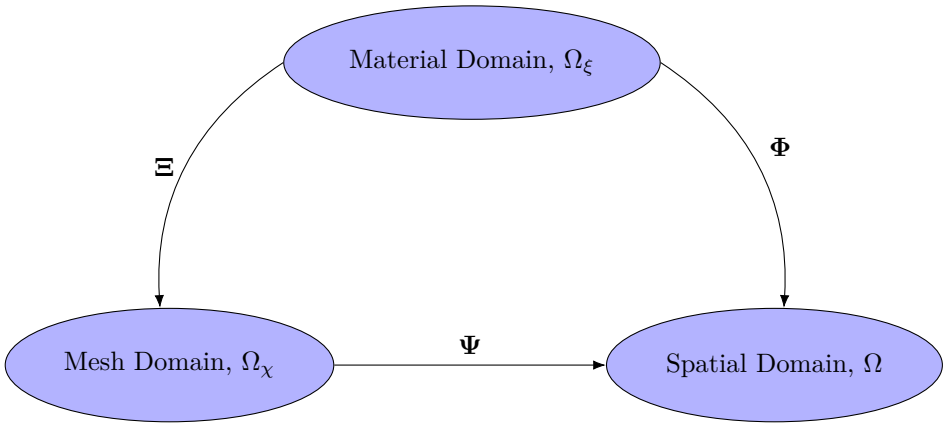
The presentation in this appendix will be as follows: first, we present the kinematic description of a material motion and its derived quantities; then, the derivatives of a generic function f are found for each coordinate system and, finally, the derivatives are used to find the *integral* relations of the principles governing a fluid flow in a moving domain. Because the process studied is time-dependent, here we suppose that time, t, evolves the same way for each coordinate system. Figure A.1 shows graphically the relation between the different systems used in the ALE description and Fig. A.3d shows a simple example of it with a generic motion of the three coordinate systems.

The material motion description on spatial or Eulerian coordinates is represented as follows:

$$(\boldsymbol{\xi}, t) \in \Omega_\xi \times [\, t_0, t_n \,[\quad \overset{\boldsymbol{\Phi}}{\longmapsto} \quad (\boldsymbol{x}, t) = \boldsymbol{\Phi}\,(\boldsymbol{\xi}, t) \in \Omega \times [\, t_0, t_n \,[\tag{A.4}$$

where Ω_ξ is the domain of the material being studied in $\boldsymbol{\xi}$ coordinates and Ω in spatial coordinates; $[\, t_0, t_n \,[$ is the temporal domain during which the domain is being studied.

Figure A.1 – Representation of the mappings between each reference system in the ALE description.



Source: prepared by the author.

Because time is the same for both variables, one can simply write:

$$\boldsymbol{x} = \boldsymbol{\Phi}\left(\boldsymbol{\xi}, t\right) \tag{A.5}$$

Function given in Eq. (A.5) represents the position of a particle located at $\boldsymbol{\xi}$ in the fluid flow – note that if we fix $\boldsymbol{\xi}$, in other words imagine you riding the particle, then you would see only $\boldsymbol{x}$ varying with time. Using block-matrix notation to ease the manipulations, we can write all the derivatives of Eq. (A.5) as:

$$\frac{\partial \boldsymbol{\Phi}}{\partial\left(\boldsymbol{\xi}, t\right)} \equiv \begin{bmatrix} \dfrac{\partial \boldsymbol{x}}{\partial \boldsymbol{\xi}}\left(\boldsymbol{\xi}, t\right) & \dfrac{\partial \boldsymbol{x}}{\partial t}\left(\boldsymbol{\xi}, t\right) \\ \mathbf{0}^T & 1 \end{bmatrix} = \begin{bmatrix} \frac{\partial x_1}{\partial \xi_1} & \frac{\partial x_1}{\partial \xi_2} & \frac{\partial x_1}{\partial \xi_3} & \frac{\partial x_1}{\partial t} \\ \frac{\partial x_2}{\partial \xi_1} & \frac{\partial x_2}{\partial \xi_2} & \frac{\partial x_2}{\partial \xi_3} & \frac{\partial x_2}{\partial t} \\ \frac{\partial x_3}{\partial \xi_1} & \frac{\partial x_3}{\partial \xi_2} & \frac{\partial x_3}{\partial \xi_3} & \frac{\partial x_1}{\partial t} \\ 0 & 0 & 0 & 1 \end{bmatrix} \tag{A.6}$$

where we see all the possible derivatives of the $\boldsymbol{\Phi}$ function. We explicitly showed the independent variables of each derivative to avoid confusion about it (this will be very helpful in future manipulations). $\dfrac{\partial \boldsymbol{x}}{\partial t}\left(\boldsymbol{\xi}, t\right)$ represents the rate of change with time of the position of particle $\boldsymbol{\xi}$, i.e. while keeping $\boldsymbol{\xi}$ constant. By definition, this is the particle velocity:

$$\boldsymbol{v}\left(\boldsymbol{\xi}, t\right) = \left.\frac{\partial \boldsymbol{x}}{\partial t}\right|_{\boldsymbol{\xi}} \equiv \frac{\mathrm{d}\boldsymbol{x}}{\mathrm{d}t} \tag{A.7}$$

$\frac{\mathrm{d}}{\mathrm{d}t}$ is the classical notation used for material derivative; some books also use $\frac{\mathrm{D}}{\mathrm{D}t}$. The

spatial gradients in Eq. (A.6) represent the *Jacobian matrix* of transformation $\mathbf{\Phi}$:

$$\mathbf{J}_{\mathbf{\Phi}} \equiv \frac{\partial \boldsymbol{x}}{\partial \boldsymbol{\xi}} (\boldsymbol{\xi}, t) \tag{A.8}$$

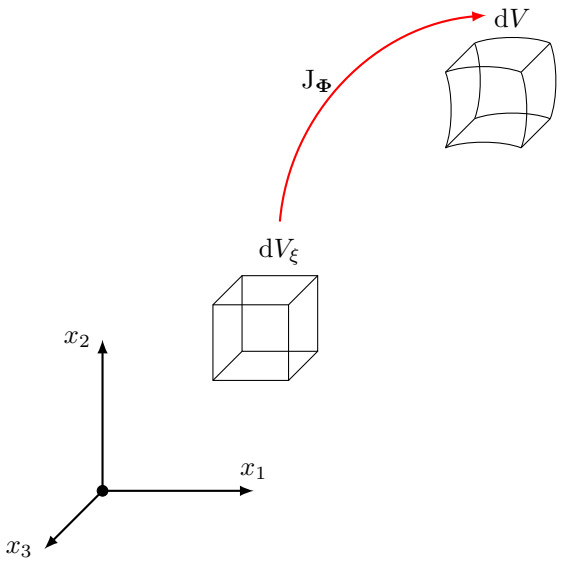
To invert function $\mathbf{\Phi}$, the determinant of its Jacobian matrix, $\mathrm{J}_{\mathbf{\Phi}} = \det \mathbf{J}_{\mathbf{\Phi}}$, must be $0 < \mathrm{J}_{\mathbf{\Phi}} < \infty$. If this is valid, one can track where particle $\boldsymbol{\xi}$ was before time t, inverting $\mathbf{\Phi}$ (a vanishing Jacobian determinant would lead to a material element collapsing into a point). Moreover, it can be shown that the Jacobian determinant gives the rate of change of the volume of the material element [96]:

$$\mathrm{d}V = \mathrm{J}_{\mathbf{\Phi}} \mathrm{d}V_{\xi} \tag{A.9}$$

therefore it is usually named *dilatation* of the movement. Figure A.2 shows a fluid element at instants $t_1 = 0$ – undeformed configuration where $\boldsymbol{\xi}$ is represented by a Cartesian coordinate system, then $\mathrm{d}V_{\xi} = \mathrm{d}\xi_1 \mathrm{d}\xi_2 \mathrm{d}\xi_3$ – and $t_2 = t_1 + \mathrm{d}t$ with the material coordinate system conformed to the material and related to $\boldsymbol{x}$ by Eq. (A.5). [96] demonstrate that the dilatation rate of change is given by:

$$\frac{\mathrm{dJ}_{\mathbf{\Phi}}}{\mathrm{d}t} = \mathrm{J}_{\mathbf{\Phi}} \nabla \bullet \boldsymbol{v} \tag{A.10}$$

Figure A.2 – A material cubic element with volume $\mathrm{d}V_{\xi}$ change its shape and volume after $\mathrm{d}t$ to $\mathrm{d}V$: both volumes are related through the Jacobian determinant.



Source: prepared by the author.

The relation between ALE coordinates and spatial coordinates is given by:

$$(\boldsymbol{\chi}, t) \in \Omega_\chi \times [\, t_0, t_n \,[\quad \overset{\boldsymbol{\Psi}}{\longmapsto} \quad (\boldsymbol{x}, t) = \boldsymbol{\Psi}(\boldsymbol{\chi}, t) \in \Omega \times [\, t_0, t_n \,[\tag{A.11}$$

which describes the motion of ALE coordinates defined on Ω_χ. Differentiation of $\boldsymbol{\Psi}$ yields:

$$\frac{\partial \boldsymbol{\Psi}}{\partial(\boldsymbol{\chi}, t)} \equiv \begin{bmatrix} \dfrac{\partial \boldsymbol{x}}{\partial \boldsymbol{\chi}}(\boldsymbol{\chi}, t) & \dfrac{\partial \boldsymbol{x}}{\partial t}(\boldsymbol{\chi}, t) \\ \mathbf{0}^T & 1 \end{bmatrix} \tag{A.12}$$

where:

$$\mathbf{J}_{\boldsymbol{\Psi}} \equiv \frac{\partial \boldsymbol{x}}{\partial \boldsymbol{\chi}}(\boldsymbol{\chi}, t) \tag{A.13}$$

is the Jacobian matrix of function $\boldsymbol{\Psi}$; the same explained before for $\mathbf{J}_{\boldsymbol{\Phi}}$ still apply here, the difference is that $\mathrm{J}_{\boldsymbol{\Psi}}$ gives the change in volume of a referential element, i.e., an element defined by ALE coordinates; thus, it is a valuable measure of *quality* of a moving grid. Also, in Eq. (A.12), the time derivative, by definition, is the velocity of the moving volume:

$$\boldsymbol{\omega}(\boldsymbol{\chi}, t) = \frac{\partial \boldsymbol{x}}{\partial t}(\boldsymbol{\chi}, t) \tag{A.14}$$

As in the material coordinates case, other kinematic quantities can be obtained from Eq. (A.11), like acceleration, for instance. Like Eq. (A.10), it is also possible to demonstrate the following relation for the rate of change of $\mathrm{J}_{\boldsymbol{\Psi}}$:

$$\left.\frac{\partial \mathrm{J}_{\boldsymbol{\Psi}}}{\partial t}\right|_{\boldsymbol{\chi}} = \mathrm{J}_{\boldsymbol{\Psi}} \nabla \bullet \boldsymbol{\omega} \tag{A.15}$$

Finally, we can also identify a map between material and ALE coordinates:

$$(\boldsymbol{\xi}, t) \in \Omega_\xi \times [\, t_0, t_n \,[\quad \overset{\boldsymbol{\Xi}}{\longmapsto} \quad (\boldsymbol{\chi}, t) = \boldsymbol{\Xi}(\boldsymbol{\xi}, t) \in \Omega_\chi \times [\, t_0, t_n \,[\tag{A.16}$$

and its derivatives can be computed as in the other two cases:

$$\frac{\partial \boldsymbol{\Xi}}{\partial(\boldsymbol{\xi}, t)} \equiv \begin{bmatrix} \dfrac{\partial \boldsymbol{\chi}}{\partial \boldsymbol{\xi}}(\boldsymbol{\xi}, t) & \dfrac{\partial \boldsymbol{\chi}}{\partial t}(\boldsymbol{\xi}, t) \\ \mathbf{0}^T & 1 \end{bmatrix} \tag{A.17}$$

Of the derivatives in Eq. (A.17), the most important is the velocity:

$$\hat{\boldsymbol{v}}\left(\boldsymbol{\xi},t\right)\equiv\frac{\partial\boldsymbol{\chi}}{\partial t}\left(\boldsymbol{\xi},t\right) \tag{A.18}$$

which, by definition, is the velocity of particles as seen by ALE coordinates reference.

Now that we already showed the most important kinematic quantities regarding each coordinate system of the ALE formulation, we turn now to the problem of relating these variables, specially the velocities. To do this, we will start with compositions of each function. Function $\boldsymbol{\Phi}$ can be decomposed into functions $\boldsymbol{\Xi}$ and $\boldsymbol{\Psi}$ (see Fig. A.1):

$$\boldsymbol{x}=\boldsymbol{\Psi}\Big(\underbrace{\boldsymbol{\chi}}_{\boldsymbol{\Xi}(\boldsymbol{\xi},t)},t\Big)=\boldsymbol{\Psi}\left[\boldsymbol{\Xi}\left(\boldsymbol{\xi},t\right),t\right]=\boldsymbol{\Phi}\left(\boldsymbol{\xi},t\right)\Rightarrow \tag{A.19}$$

$$\Rightarrow\boldsymbol{\Phi}\left(\boldsymbol{\xi},t\right)=\left(\boldsymbol{\Psi}\circ\boldsymbol{\Xi}\right)\left(\boldsymbol{\xi},t\right) \tag{A.20}$$

where "$\circ$" represents the composition of two functions, i.e. the result of one is applied to the other. Differentiating the last equation with respect to $(\boldsymbol{\xi},t)$ and applying the chain rule yields:

$$\frac{\partial\boldsymbol{\Phi}}{\partial\left(\boldsymbol{\xi},t\right)}\left(\boldsymbol{\xi},t\right)=\frac{\partial\left(\boldsymbol{\Psi}\circ\boldsymbol{\Xi}\right)}{\partial\left(\boldsymbol{\xi},t\right)}\left(\boldsymbol{\xi},t\right)=\frac{\partial\boldsymbol{\Psi}}{\partial\left(\boldsymbol{\chi},t\right)}\left(\boldsymbol{\chi},t\right)\frac{\partial\boldsymbol{\Xi}}{\partial\left(\boldsymbol{\xi},t\right)}\left(\boldsymbol{\xi},t\right) \tag{A.21}$$

Keep in mind that the derivatives in the last equation are symbolic representations of matrices (see Eq. (A.6) where we explicit the 4×4 matrix). Substituting the derivatives in Eq. (A.21) with Eqs. (A.6), (A.12) and (A.17), and using the definitions of velocities and Jacobians presented before, follows:

$$\begin{bmatrix}\mathbf{J}_{\boldsymbol{\Phi}}\left(\boldsymbol{\xi},t\right) & \boldsymbol{v}\left(\boldsymbol{\xi},t\right)\\ \mathbf{0}^{T} & 1\end{bmatrix}=\begin{bmatrix}\mathbf{J}_{\boldsymbol{\Psi}}\left(\boldsymbol{\chi},t\right) & \boldsymbol{\omega}\left(\boldsymbol{\chi},t\right)\\ \mathbf{0}^{T} & 1\end{bmatrix}\begin{bmatrix}\frac{\partial\boldsymbol{\chi}}{\partial\boldsymbol{\xi}}\left(\boldsymbol{\xi},t\right) & \hat{\boldsymbol{v}}\left(\boldsymbol{\xi},t\right)\\ \mathbf{0}^{T} & 1\end{bmatrix} \tag{A.22}$$

Matrix multiplication on the right side of the last equation yields::

$$\mathbf{J}_{\boldsymbol{\Phi}}=\mathbf{J}_{\boldsymbol{\Psi}}\frac{\partial\boldsymbol{\chi}}{\partial\boldsymbol{\xi}} \tag{A.23}$$

and

$$\boldsymbol{v}\left(\boldsymbol{\xi},t\right)=\boldsymbol{\omega}\left(\boldsymbol{\chi},t\right)+\mathrm{J}_{\boldsymbol{\Psi}}\left(\boldsymbol{\chi},t\right)\bullet\hat{\boldsymbol{v}}\left(\boldsymbol{\xi},t\right) \tag{A.24}$$

Rearranging Eq. (A.24) and defining a velocity $\boldsymbol{c}$ given by:

$$\boldsymbol{c} \equiv \boldsymbol{v}\left(\boldsymbol{\xi}, t\right) - \boldsymbol{\omega}\left(\boldsymbol{\chi}, t\right) = \mathbf{J}_{\boldsymbol{\Psi}}\left(\boldsymbol{\chi}, t\right) \bullet \hat{\boldsymbol{v}}\left(\boldsymbol{\xi}, t\right) \tag{A.25}$$

that is the so-called *convective velocity* [56, 57]. As shown below, $\boldsymbol{c}$ appears on the advective term of the governing equations of a fluid flow when a moving control volume is considered within the flow. This velocity can be interpreted as the relative velocity between the material and a moving control volume, but measured from the spatial coordinate system.

The ALE formulation can be seen as a generalization of the Eulerian and Lagrangian descriptions because these two can be deduced as special cases of the former. The Eulerian description appears when the ALE coordinate system is identified to the spatial coordinate system, i.e. the mesh is fixed in space and the material passes through it, as depicted in Fig. A.3b. Mathematically, this is equivalent to make $\boldsymbol{\Psi}$ equal to the *identity operator*, $\boldsymbol{I}$, which is a linear transformation represented by the identity matrix of order $\mathbb{R}^{3\times3}$. If we put $\boldsymbol{\Psi} \equiv \boldsymbol{I}$ in Eq. (A.11) follows:

$$\boldsymbol{\Psi} \equiv \boldsymbol{I} \Rightarrow \boldsymbol{\chi} \equiv \boldsymbol{x} \tag{A.26}$$

On the other hand, the Lagrangian formulation describes the material motion using a referential system fixed on the material at a defined instant t, which is equivalent to identify ALE and Lagrangian coordinates as Fig. A.3c shows. Then, using $\boldsymbol{\Xi} \equiv \boldsymbol{I}$ in Eq. (A.16) follows:

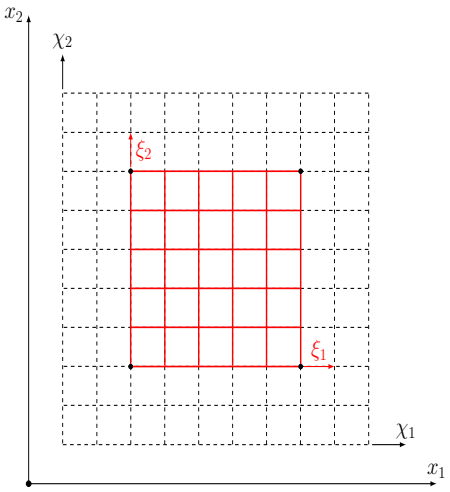
$$\boldsymbol{\Xi} \equiv \boldsymbol{I} \Rightarrow \boldsymbol{\chi} \equiv \boldsymbol{\xi} \tag{A.27}$$

Eulerian description is traditionally used in Fluid Mechanics due to the high deformation rate experienced by fluids in its motion. Lagrangian description is common in Solid Mechanics applications. The ALE formulation, however, have applications in both. In Computational Fluid Mechanics, solving the governing equations of a fluid flow in a domain whose boundaries are moving – fluid-structure interaction problems, free surface flows, for example – requires to use an automatic mesh update method and it must be accounted for in the equations that are being solved. In Solid Mechanics, the applications usually are also on the computational study of, for example, crack propagation, contact of different solids, plastic forming processes of materials.

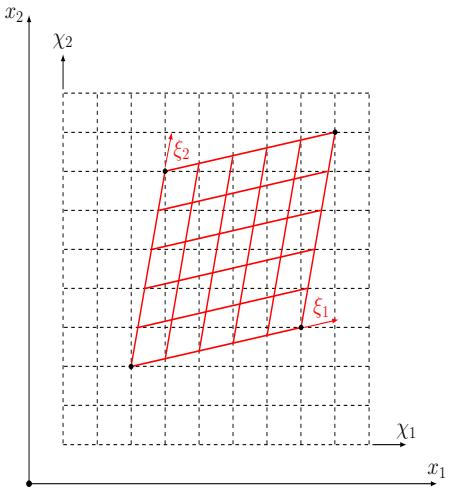
We present now how a general function f_{ξ} is described in each coordinate system,

Figure A.3 – Comparison between the Eulerian, Lagrangian and ALE descriptions of a two-dimensional material motion represented by the red grid (coordinates $\boldsymbol{\xi}$) from instant $t = t_0$ (undeformed configuration) to $t = t_1$; the dashed lines represent the referential system with coordinate lines $\boldsymbol{\chi}$; the spatial coordinates $\boldsymbol{x}$ is fixed and represented by a Cartesian coordinate system.

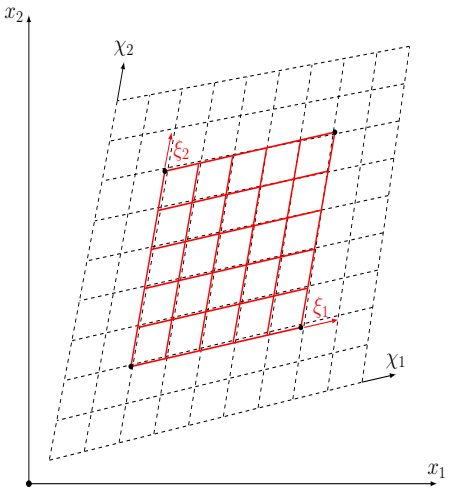
(a) Material and mesh coordinates undeformed at instant $t = t_0$;



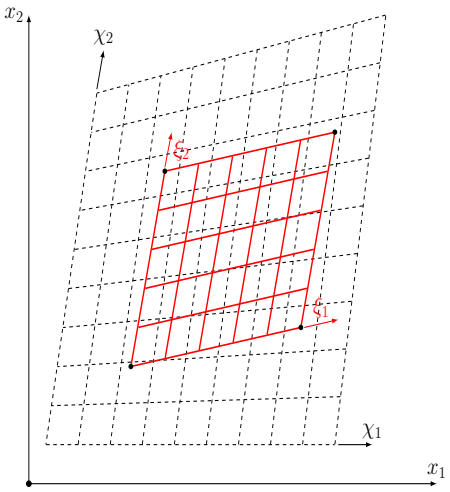
(b) Material deformation at instant $t = t_1$ on the Eulerian description;



(c) Material deformation at instant $t = t_1$ on the Lagrangian description;



(d) Material deformation at instant $t = t_1$ on the ALE description;



Source: prepared by the author.

where f_ξ can represent any property or scalar variable of the fluid or the flow. Then:

$$f_\xi = f_\xi\left(\boldsymbol{\xi}, t\right) \tag{A.28}$$

describes property f_ξ for particle $\boldsymbol{\xi}$ at time t (see, for example, Eq. (A.5) which describes the "property" position of particle $\boldsymbol{\xi}$). Using Eq. (A.5), we can regard f_ξ as a spatial

function:

$$f_\xi = f_\xi(\boldsymbol{\xi}, t) = f\Big[\underbrace{\boldsymbol{\Phi}(\boldsymbol{\xi}, t)}_{\boldsymbol{x}}, t\Big] = f(\boldsymbol{x}, t) \tag{A.29}$$

representing function f on each point in space at time t. Moreover, in the ALE formulation context, f can also be regarded as a function of ALE coordinates:

$$f_\xi = f_\xi(\boldsymbol{\xi}, t) = f_\chi\Big[\underbrace{\boldsymbol{\Xi}(\boldsymbol{\xi}, t)}_{\boldsymbol{\chi}}, t\Big] = f_\chi(\boldsymbol{\chi}, t) \tag{A.30}$$

In Eqs. (A.28) to (A.30), f was represented with different symbols as subscripts to highlight that the *mathematical form* of functions f, f_ξ and f_χ can be different, but they represent the same physical quantity; we will use this on the following manipulations to avoid confusion, but we drop the subscript once the most important relations have been found.

Our objective now is to relate the derivatives of f in each coordinate system. To this purpose, we look first to the second equality in Eq. (A.29) where we identify a composition of f and $\boldsymbol{\Phi}$. Differentiating this composite function yields:

$$\begin{aligned}
&f_\xi(\boldsymbol{\xi}, t) = f[\boldsymbol{\Phi}(\boldsymbol{\xi}, t), t] = (f \circ \boldsymbol{\Phi})(\boldsymbol{\xi}, t) \Rightarrow \\
&\Rightarrow \frac{\partial f_\xi}{\partial(\boldsymbol{\xi}, t)} = \frac{\partial[f \circ \boldsymbol{\Phi}]}{\partial(\boldsymbol{\xi}, t)}(\boldsymbol{\xi}, t) = \frac{\partial f}{\partial(\boldsymbol{x}, t)}\frac{\partial \boldsymbol{\Phi}}{\partial(\boldsymbol{\xi}, t)} \Rightarrow \\
&\Rightarrow \begin{bmatrix}\left\{\dfrac{\partial f_\xi}{\partial \boldsymbol{\xi}}\right\}^T & \dfrac{\partial f_\xi}{\partial t}\end{bmatrix} = \begin{bmatrix}\left\{\dfrac{\partial f}{\partial \boldsymbol{x}}\right\}^T & \dfrac{\partial f}{\partial t}\end{bmatrix}\begin{bmatrix}\mathbf{J}_{\boldsymbol{\Phi}}(\boldsymbol{\xi}, t) & \boldsymbol{v}(\boldsymbol{\xi}, t) \\ \mathbf{0}^T & 1\end{bmatrix}
\end{aligned} \tag{A.31}$$

leading to the following relations after matrix-vector multiplication:

$$\frac{\partial f_\xi}{\partial \boldsymbol{\xi}} = \frac{\partial f}{\partial \boldsymbol{x}}\mathrm{J}_{\boldsymbol{\Phi}}(\boldsymbol{\xi}, t) \tag{A.32}$$

which relates the gradient of f in each coordinate system; and:

$$\frac{\partial f_\xi}{\partial t}(\boldsymbol{\xi}, t) = \frac{\partial f}{\partial t}(\boldsymbol{x}, t) + \frac{\partial f}{\partial \boldsymbol{x}} \bullet \boldsymbol{v}(\boldsymbol{\xi}, t) \tag{A.33}$$

which can be rewritten on the following form:

$$\frac{\partial f_\xi}{\partial t}(\boldsymbol{\xi}, t) = \frac{\mathrm{d} f_\xi}{\mathrm{d} t} = \frac{\partial f}{\partial t} + \boldsymbol{v} \bullet \nabla f \tag{A.34}$$

because $\nabla f \equiv \dfrac{\partial f}{\partial \boldsymbol{x}}$ is the spatial gradient of f_ξ. Equation (A.34) is the classical material derivative encountered in Fluid Mechanics treatment using the Eulerian description.

The same procedure presented above relating f_ξ and f can be performed for function f_χ. We start from Eq. (A.30):

$$\begin{aligned} & f_\xi(\boldsymbol{\xi},t) = f_\chi[\boldsymbol{\Xi}(\boldsymbol{\xi},t),t] = (f_\chi \circ \boldsymbol{\Xi})(\boldsymbol{\xi},t) \Rightarrow \\ & \Rightarrow \frac{\partial f_\xi}{\partial(\boldsymbol{\xi},t)} = \frac{\partial[f \circ \boldsymbol{\Xi}]}{\partial(\boldsymbol{\xi},t)}(\boldsymbol{\xi},t) = \frac{\partial f_\chi}{\partial(\boldsymbol{\chi},t)}\frac{\partial \boldsymbol{\Xi}}{\partial(\boldsymbol{\xi},t)} \Rightarrow \\ & \Rightarrow \begin{bmatrix} \left\{\dfrac{\partial f_\xi}{\partial \boldsymbol{\xi}}\right\}^T & \dfrac{\partial f_\xi}{\partial t} \end{bmatrix} = \begin{bmatrix} \left\{\dfrac{\partial f_\chi}{\partial \boldsymbol{\chi}}\right\}^T & \dfrac{\partial f_\chi}{\partial t} \end{bmatrix} \begin{bmatrix} \dfrac{\partial \boldsymbol{\chi}}{\partial \boldsymbol{\xi}}(\boldsymbol{\xi},t) & \hat{\boldsymbol{v}}(\boldsymbol{\xi},t) \\ \mathbf{0}^T & 1 \end{bmatrix} \end{aligned} \tag{A.35}$$

leading to the following relations after matrix-vector multiplication:

$$\frac{\partial f_\xi}{\partial \boldsymbol{\xi}} = \frac{\partial f_\chi}{\partial \boldsymbol{\chi}} \bullet \frac{\partial \boldsymbol{\chi}}{\partial \boldsymbol{\xi}}(\boldsymbol{\xi},t) \tag{A.36}$$

and

$$\frac{\partial f_\xi}{\partial t}(\boldsymbol{\xi},t) = \frac{\partial f_\chi}{\partial t}(\boldsymbol{\chi},t) + \frac{\partial f_\chi}{\partial \boldsymbol{\chi}} \bullet \hat{\boldsymbol{v}} \tag{A.37}$$

Equation (A.37), similar to Eq. (A.34), relates the rate of f_ξ with changes in f_χ, i.e. in the ALE coordinates. However, the form of Eq. (A.37) is not very convenient because, in general, physical quantities are described on spatial coordinates, thus it is necessary to evaluate the gradient in terms of spatial derivatives. Substituting $\hat{\boldsymbol{v}}$ in Eq. (A.37) from Eq. (A.25), once we assumed $\boldsymbol{\Psi}$ invertible, follows:

$$\begin{aligned} \frac{\partial f_\xi}{\partial t}(\boldsymbol{\xi},t) &= \frac{\partial f_\chi}{\partial t}(\boldsymbol{\chi},t) + \left[\boldsymbol{c} \bullet \frac{\partial \boldsymbol{\chi}}{\partial \boldsymbol{x}}(\boldsymbol{x},t)\right] \bullet \frac{\partial f_\chi}{\partial \boldsymbol{\chi}}(\boldsymbol{\chi},t) \\ &= \frac{\partial f_\chi}{\partial t}(\boldsymbol{\chi},t) + \boldsymbol{c} \bullet \underbrace{\left[\frac{\partial \boldsymbol{\chi}}{\partial \boldsymbol{x}}(\boldsymbol{x},t) \bullet \frac{\partial f_\chi}{\partial \boldsymbol{\chi}}(\boldsymbol{\chi},t)\right]}_{\frac{\partial f}{\partial \boldsymbol{x}}(\boldsymbol{x},t)} \\ &= \frac{\partial f_\chi}{\partial t}(\boldsymbol{\chi},t) + \boldsymbol{c} \bullet \underbrace{\frac{\partial f}{\partial \boldsymbol{x}}(\boldsymbol{x},t)}_{\nabla f} \Rightarrow \end{aligned} \tag{A.38}$$

$$\Rightarrow \frac{\partial f_\xi}{\partial t}(\boldsymbol{\xi},t) = \frac{\partial f_\chi}{\partial t}(\boldsymbol{\chi},t) + \boldsymbol{c} \bullet \nabla f \tag{A.39}$$

Equation (A.39) is known as the *fundamental equation* of the ALE description: it relates the material time derivative with the spatial gradient of f, but taking into account the moving control volume reference system. Dropping the lower index of function f, follows:

$$\frac{\mathrm{d}f}{\mathrm{d}t} = \frac{\partial f}{\partial t}(\boldsymbol{\chi}, t) + \boldsymbol{c} \bullet \nabla f \tag{A.40}$$

Let us see how the ALE description affects the governing equations of Fluid Dynamics. The two *basic* governing equations for a fluid flow are derived from mass conservation principle and the balance of linear momentum. If the fluid has density ρ and the flow velocity field is $\boldsymbol{v}$, then the governing equations can be written as:

$$\frac{\mathrm{d}\rho}{\mathrm{d}t} + \rho \nabla \bullet \boldsymbol{v} = 0 \tag{A.41}$$

$$\rho \frac{\mathrm{d}\boldsymbol{v}}{\mathrm{d}t} = \nabla \bullet \boldsymbol{\sigma} + \boldsymbol{f}_b \tag{A.42}$$

where $\boldsymbol{\sigma}$ is the Cauchy stress tensor and $\boldsymbol{f}_b$ are the body forces acting on the fluid per unit volume; note that the divergence operator appearing on these equations is a spatial operator, while the density and velocity derivatives are material ones. In the Eulerian description, these derivatives would be replaced by Eq. (A.34) to introduce derivatives with respect to spatial coordinates. However, considering a moving frame of reference, the material derivatives in Eqs. (A.41) and (A.42) are replaced by Eq. (A.40) with f as ρ and $\boldsymbol{v}$, respectively, leading to the *differential non-conservative* governing equations:

$$\frac{\partial \rho}{\partial t}(\boldsymbol{\chi}, t) + \boldsymbol{c} \bullet \nabla \rho = -\rho \nabla \bullet \boldsymbol{v} \tag{A.43}$$

$$\rho \frac{\partial \boldsymbol{v}}{\partial t}(\boldsymbol{\chi}, t) + \boldsymbol{c} \bullet \nabla \boldsymbol{v} = \nabla \bullet \boldsymbol{\sigma} + \boldsymbol{f}_b \tag{A.44}$$

Note that the advective term now accounts for the moving control volume velocity through the convective velocity Eq. (A.25).

Of special interest to the Finite Volume Method are the *integral* governing equations, written for a finite control volume V that can be fixed or moving in space. When the volume is fixed, one identify the Eulerian description, whereas the moving volume relates

to the ALE formulation, as already shown. For that matter, we will derive a relation similar to the so-called Reynolds Transport Theorem, but applied to a control volume that is moving in space. With the notation introduced here, Reynolds' Transport Theorem for an *intensive* transport variable ϕ is written:

$$\underbrace{\frac{\mathrm{d}}{\mathrm{d}t}\int_{V(t)}\rho\phi\left(\boldsymbol{x},t\right)\mathrm{d}V}_{\substack{\text{Rate of change of } \rho\phi \text{ of}\\ \text{the particles passing in}\\ V}} = \underbrace{\int_{V(t)}\frac{\partial(\rho\phi)}{\partial t}\left(\boldsymbol{x},t\right)\mathrm{d}V}_{\text{Rate of change of } \rho\phi \text{ in } V} + \underbrace{\oint_{S(t)}\rho\phi\boldsymbol{v}\bullet\boldsymbol{n}\mathrm{d}S}_{\substack{\text{Net flow of } \rho\phi\\ \text{through } S \text{ out of } V}} \tag{A.45}$$

where S is the surface of control volume V. As showed on the equation, the first derivative – a material derivative – represents the rate of change of the total $\rho\phi$ of the *material particles* in V at instant t; which is equal to the total rate of change of $\rho\phi$ in V at t plus the net flow rate of $\rho\phi$ through surface S. A version of Eq. (A.45) to the general case of an arbitrary *moving control volume* will be derived below.

We want to evaluate the rate of change of the quantity $\rho\phi$ for an arbitrary moving control volume $V(t)$, i.e., the derivative:

$$\left.\frac{\partial}{\partial t}\right|_{\boldsymbol{\chi}}\int_{V(t)}\rho\phi\left(\boldsymbol{x},t\right)\mathrm{d}V \tag{A.46}$$

Note that the integral in Eq. (A.46) is evaluated with respect to *spatial coordinates*, but the derivative is evaluated keeping $\boldsymbol{\chi}$ constant, explicitly indicated into the last equation with the vertical bar. Therefore, derivation and integral operations can not be inverted. However, since the moving volume is fixed to the ALE coordinates, we can use mapping Eq. (A.11) to change the integration variable and, consequently, invert the derivative and integral operations:

$$\begin{aligned}\left.\frac{\partial}{\partial t}\right|_{\boldsymbol{\chi}}\int_{V(t)}\rho\phi\left(\boldsymbol{x},t\right)\mathrm{d}V =& \left.\frac{\partial}{\partial t}\right|_{\boldsymbol{\chi}}\int_{V_\chi}\rho\phi\left[\boldsymbol{x}\left(\boldsymbol{\chi},t\right),t\right]\mathrm{J}_{\boldsymbol{\Psi}}\mathrm{d}V_\chi\\ =& \int_{V_\chi}\left[\left.\frac{\partial(\rho\phi)}{\partial t}\right|_{\boldsymbol{\chi}}\mathrm{J}_{\boldsymbol{\Psi}}+\rho\phi\left.\frac{\partial \mathrm{J}_{\boldsymbol{\Psi}}}{\partial t}\right|_{\boldsymbol{\chi}}\right]\mathrm{d}V_\chi\end{aligned} \tag{A.47}$$

and substituting Eq. (A.15) into the last equation yields:

$$\begin{aligned}\left.\frac{\partial}{\partial t}\right|_{\boldsymbol{\chi}}\int_{V(t)}\rho\phi\left(\boldsymbol{x},t\right)\mathrm{d}V &= \int_{V_\chi(t)}\left[\left.\frac{\partial(\rho\phi)}{\partial t}\right|_{\boldsymbol{\chi}}\mathrm{J}_{\boldsymbol{\Psi}}+\rho\phi\mathrm{J}_{\boldsymbol{\Psi}}\nabla\bullet\boldsymbol{\omega}\right]\mathrm{d}V_\chi \\ &= \int_{V_\chi(t)}\left[\left.\frac{\partial(\rho\phi)}{\partial t}\right|_{\boldsymbol{\chi}}+\rho\phi\nabla\bullet\boldsymbol{\omega}\right]\underbrace{\mathrm{J}_{\boldsymbol{\Psi}}\mathrm{d}V_\chi}_{\mathrm{d}V} \\ &= \int_{V(t)}\left[\left.\frac{\partial(\rho\phi)}{\partial t}\right|_{\boldsymbol{\chi}}+\rho\phi\nabla\bullet\boldsymbol{\omega}\right]\mathrm{d}V\end{aligned} \tag{A.48}$$

In the last step, we turn the integrand back to spatial coordinates. However, the time derivative inside the integral is evaluated with respect to ALE coordinates. Spatial coordinates can be introduced in the integrand using the equation:

$$\left.\frac{\partial(\rho\phi)}{\partial t}\right|_{\boldsymbol{\chi}}=\left.\frac{\partial(\rho\phi)}{\partial t}\right|_{\boldsymbol{x}}+\boldsymbol{\omega}\bullet\left(\nabla\rho\phi\right) \tag{A.49}$$

which can be derived using the composition of a generic function f_χ – in this case, $f_\chi=\rho\phi$ – as presented above. Therefore, the time derivative in the last equality of Eq. (A.48) can be written:

$$\begin{aligned}\left.\frac{\partial}{\partial t}\right|_{\boldsymbol{\chi}}\int_{V(t)}\rho\phi\left(\boldsymbol{x},t\right)\mathrm{d}V &= \int_{V(t)}\left[\left.\frac{\partial(\rho\phi)}{\partial t}\right|_{\boldsymbol{\chi}}+\rho\phi\nabla\bullet\boldsymbol{\omega}\right]\mathrm{d}V \\ &= \int_{V(t)}\left[\left.\frac{\partial(\rho\phi)}{\partial t}\right|_{\boldsymbol{x}}+\underbrace{\boldsymbol{\omega}\bullet\nabla(\rho\phi)+\rho\phi\nabla\bullet\boldsymbol{\omega}}_{\nabla\bullet(\rho\phi\boldsymbol{\omega})}\right]\mathrm{d}V\Rightarrow\end{aligned} \tag{A.50}$$

$$\Rightarrow\left.\frac{\partial}{\partial t}\right|_{\boldsymbol{\chi}}\int_{V(t)}\rho\phi\left(\boldsymbol{x},t\right)\mathrm{d}V=\int_{V(t)}\left.\frac{\partial(\rho\phi)}{\partial t}\right|_{\boldsymbol{x}}\mathrm{d}V+\int_{V(t)}\nabla\bullet(\rho\phi\boldsymbol{\omega})\mathrm{d}V \tag{A.51}$$

where we used the vector identity $\nabla\bullet\left(c\boldsymbol{A}\right)=c\nabla\bullet\boldsymbol{A}+\boldsymbol{A}\bullet\nabla c$ for a scalar c and a vector field $\boldsymbol{A}$. Finally, using Gauss' divergence theorem, follows:

$$\left.\frac{\partial}{\partial t}\right|_{\boldsymbol{\chi}}\int_{V(t)}\rho\phi\left(\boldsymbol{x},t\right)\mathrm{d}V=\int_{V(t)}\left.\frac{\partial(\rho\phi)}{\partial t}\right|_{\boldsymbol{x}}\mathrm{d}V+\oint_{S(t)}\rho\phi\boldsymbol{\omega}\bullet\boldsymbol{n}\mathrm{d}S \tag{A.52}$$

Equation (A.52) does not involves the material itself, it only shows how a time derivative of an integral over a moving volume relates to the derivatives with respect to spatial coordinates. From Eq. (A.52) a very important relation can be obtained for the volume of

V, which can be written as:

$$V(t) = \int_{V(t)} \mathrm{d}V \tag{A.53}$$

Therefore, in Eq. (A.52), we can recover integral A.53 making ϕ equal to the specific volume $\frac{V}{m}$ as follows:

$$\left.\frac{\partial}{\partial t}\right|_{\boldsymbol{\chi}} \int_{V(t)} \underbrace{\rho\frac{V}{m}}_{=1} \mathrm{d}V = \int_{V(t)} \left.\frac{\partial}{\partial t}\left(\underbrace{\rho\frac{V}{m}}_{=1}\right)\right|_{\boldsymbol{x}} \mathrm{d}V + \oint_{S(t)} \underbrace{\rho\frac{V}{m}}_{=1} \boldsymbol{\omega}\bullet\boldsymbol{n}\mathrm{d}S \Rightarrow \tag{A.54}$$

$$\Rightarrow \left.\frac{\partial}{\partial t}\right|_{\boldsymbol{\chi}} \int_{V(t)} \mathrm{d}V = \int_{V(t)} \underbrace{\left.\frac{\partial(1)}{\partial t}\right|_{\boldsymbol{x}}}_{=0} \mathrm{d}V + \oint_{S(t)} \boldsymbol{\omega}\bullet\boldsymbol{n}\mathrm{d}S \tag{A.55}$$

$$\Rightarrow \left.\frac{\partial}{\partial t}\right|_{\boldsymbol{\chi}} \int_{V(t)} \mathrm{d}V = \oint_{S(t)} \boldsymbol{\omega}\bullet\boldsymbol{n}\mathrm{d}S \tag{A.56}$$

which is known as the *geometric or space conservation law* [58], it says that the volume of V changes according to the volumetric flow rate due to the movement of its surface S.

Since volume $V(t)$ is arbitrary, we can suppose that it is equal to a material volume considered on Reynolds' Transport Theorem Eq. (A.45) at instant t. In this case, the integral:

$$\int_{V(t)} \left.\frac{\partial(\rho\phi)}{\partial t}\right|_{\boldsymbol{x}} \mathrm{d}V \tag{A.57}$$

represents the same quantity in both Eqs. (A.45) and (A.52). Thus, combining both equations follows:

$$\frac{\mathrm{d}}{\mathrm{d}t}\int_{V(t)} \rho\phi\left(\boldsymbol{x},t\right)\mathrm{d}V = \left.\frac{\partial}{\partial t}\right|_{\boldsymbol{\chi}} \int_{V(t)} \rho\phi\left(\boldsymbol{x},t\right)\mathrm{d}V - \oint_{S(t)} \rho\phi\boldsymbol{\omega}\bullet\boldsymbol{n}\mathrm{d}S + \oint_{S(t)} \rho\phi\boldsymbol{v}\bullet\boldsymbol{n}\mathrm{d}S \tag{A.58}$$

$$\underbrace{\frac{\mathrm{d}}{\mathrm{d}t}\int_{V(t)} \rho\phi\left(\boldsymbol{x},t\right)\mathrm{d}V}_{\substack{\text{Rate of change of } \rho\phi \text{ of}\\ \text{the particles passing in}\\ V \text{ at instant } t}} = \underbrace{\left.\frac{\partial}{\partial t}\right|_{\boldsymbol{\chi}} \int_{V(t)} \rho\phi\left(\boldsymbol{x},t\right)\mathrm{d}V}_{\text{Rate of change of } \rho\phi \text{ in } V \text{ at } t} + \underbrace{\oint_{S(t)} \rho\phi\left(\boldsymbol{v}-\boldsymbol{\omega}\right)\bullet\boldsymbol{n}\mathrm{d}S}_{\substack{\text{Net flow of } \rho\phi\\ \text{through } S \text{ out of}\\ V \text{ at instant } t}} \tag{A.59}$$

where $\boldsymbol{c} = \boldsymbol{v} - \boldsymbol{\omega}$ is the convective velocity. Equation (A.59) is Reynolds' transport theorem for a moving control volume. We use this equation below to derive the integral governing equations for a flow in a moving domain.

Let us begin with the principle of mass conservation. For a fluid with density $\rho = \rho\left(\boldsymbol{x},t\right)$

flowing with a velocity field $\boldsymbol{v}$, a *material* volume V has total mass given by:

$$m = \int_{V(t)} \rho\left(\boldsymbol{x}, t\right) \mathrm{d}V \tag{A.60}$$

and the mass conservation principle states:

$$\frac{\mathrm{d}m}{\mathrm{d}t} = \frac{\mathrm{d}}{\mathrm{d}t} \int_{V(t)} \rho\left(\boldsymbol{x}, t\right) \mathrm{d}V = 0 \tag{A.61}$$

Substituting $\phi = 1$ in Eq. (A.59) and considering Eq. (A.61) follows:

$$\frac{\mathrm{d}}{\mathrm{d}t} \int_{V(t)} \rho\left(\boldsymbol{x}, t\right) \mathrm{d}V = \left.\frac{\partial}{\partial t}\right|_{\boldsymbol{\chi}} \int_{V(t)} \rho\left(\boldsymbol{x}, t\right) \mathrm{d}V + \oint_{S(t)} \rho\left(\boldsymbol{v} - \boldsymbol{\omega}\right) \bullet \boldsymbol{n} \mathrm{d}S = 0 \tag{A.62}$$

which is the *integral conservative* version of Eq. (A.43). For an incompressible fluid, ρ is constant and Eq. (A.62) reduces to:

$$\rho \left.\frac{\partial}{\partial t}\right|_{\boldsymbol{\chi}} \int_{V(t)} \mathrm{d}V + \rho \oint_{S(t)} \left(\boldsymbol{v} - \boldsymbol{\omega}\right) \bullet \boldsymbol{n} \mathrm{d}S = 0 \tag{A.63}$$

which can be rearranged on the following form:

$$\rho \left[\left.\frac{\partial}{\partial t}\right|_{\boldsymbol{\chi}} \int_{V(t)} \mathrm{d}V - \oint_{S(t)} \boldsymbol{\omega} \bullet \boldsymbol{n} \mathrm{d}S \right] + \rho \oint_{S(t)} \boldsymbol{v} \bullet \boldsymbol{n} \mathrm{d}S = 0 \tag{A.64}$$

the term in brackets must be zero according to the space conservation law, Eq. (A.56). Demirdžić and Perić [58] highlights that, in a dynamic mesh numerical method, satisfaction of the geometric conservation law by the moving mesh is important to avoid generation of source terms in the mass conservation equation, which can cause divergence of a numerical procedure to solve the flow governing equations. Therefore, if the control volume movement satisfies Eq. (A.56), mass conservation principle reduces to:

$$\rho \oint_{S(t)} \boldsymbol{v} \bullet \boldsymbol{n} \mathrm{d}S = 0 \tag{A.65}$$

The balance of linear momentum for a material volume in a fluid flow is written as:

$$\sum \boldsymbol{f} = \frac{\mathrm{d}\boldsymbol{p}}{\mathrm{d}t} = \frac{\mathrm{d}}{\mathrm{d}t} \int_{V(t)} \rho \boldsymbol{v}\left(\boldsymbol{x}, t\right) \mathrm{d}V \tag{A.66}$$

where $\boldsymbol{p}$ is the total linear momentum of the particles within the volume; $\sum \boldsymbol{f}$ is the sum of all forces acting on the flow, on this case, the surface forces acting on $S(t)$ due to the Cauchy stress tensor $\boldsymbol{\sigma}$ and the body forces $\boldsymbol{f}_b$ acting on the volume. Therefore:

$$\frac{\mathrm{d}}{\mathrm{d}t}\int_{V(t)} \rho \boldsymbol{v}\left(\boldsymbol{x},t\right)\mathrm{d}V = \oint_{S(t)} \boldsymbol{\sigma}\bullet\boldsymbol{n}\mathrm{d}S + \int_{V(t)} \boldsymbol{f}_b \mathrm{d}V \tag{A.67}$$

Using Eq. (A.59) on the left hand side of Eq. (A.67) with $\phi = \boldsymbol{v}$ leads to:

$$\left.\frac{\partial}{\partial t}\right|_{\boldsymbol{\chi}} \int_{V(t)} \rho \boldsymbol{v}\left(\boldsymbol{x},t\right)\mathrm{d}V + \oint_{S(t)} \rho \boldsymbol{v}\left(\boldsymbol{v}-\boldsymbol{\omega}\right)\bullet\boldsymbol{n}\mathrm{d}S = \oint_{S(t)} \boldsymbol{\sigma}\bullet\boldsymbol{n}\mathrm{d}S + \int_{V(t)} \boldsymbol{f}_b \mathrm{d}V \tag{A.68}$$

which is the integral conservative version of Eq. (A.44).

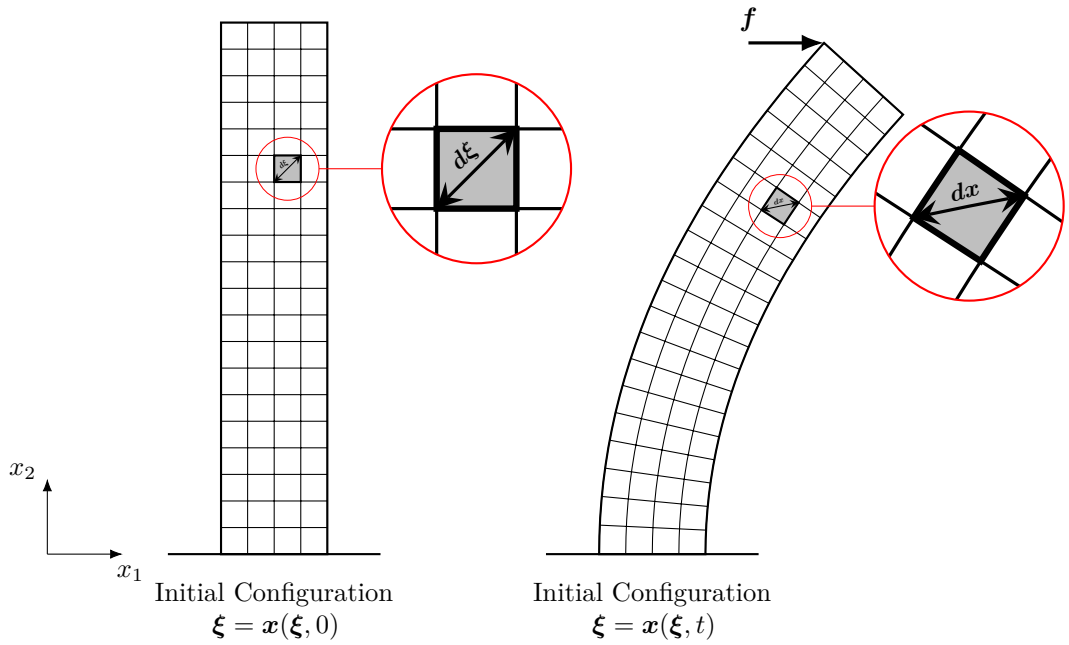
B Total Lagrangian Formulation for a Solid Motion

We present here the total Lagrangian formulation of the equation governing the motion of a solid with density ρ^{s}, Young's modulus E and Poisson's ratio ν^{s}. The field variables of the motion are described using the material coordinates, $\boldsymbol{\xi}$, at the *reference configuration* - the solid at $t = 0$ - instead of the *current configuration*; if the latter was used, then the description is called *updated Lagrangian*. The motion itself is described by:

$$\boldsymbol{x} = \boldsymbol{x}\left(\boldsymbol{\xi}, t\right) \tag{B.1}$$

Figure B.1 shows an example of a solid deformed by a force $\boldsymbol{f}$ with its initial configuration defined by a set of Cartesian coordinates as $\boldsymbol{\xi} = \boldsymbol{x}(\boldsymbol{\xi}, 0)$ and the current configuration - the solid deformed at instant t.

Figure B.1 – Motion of a solid deformed by a force $\boldsymbol{f}$, showing the initial (reference) configuration (left) and the current configuration (right).



Source: prepared by the author.

Typical measurements of stress and strain are made with respect to the initial configuration: the nominal multiaxial stress, $\boldsymbol{P}$, and the deformation gradient tensor, $\boldsymbol{F}$, defined as the Jacobian matrix of the solid motion:

$$\boldsymbol{F} = \frac{\partial \boldsymbol{x}}{\partial \boldsymbol{\xi}}\left(\boldsymbol{\xi}, t\right) \tag{B.2}$$

With the solid displacement, $\boldsymbol{u}$, given by:

$$\boldsymbol{u} = \boldsymbol{x}\left(\boldsymbol{\xi}, t\right) - \boldsymbol{x}\left(\boldsymbol{\xi}, 0\right) = \boldsymbol{x} - \boldsymbol{\xi} \tag{B.3}$$

then, Eq. (B.2) gives:

$$\boldsymbol{F} = \frac{\partial\left(\boldsymbol{u} + \boldsymbol{\xi}\right)}{\partial \boldsymbol{\xi}} = \nabla_0 \boldsymbol{u} + \boldsymbol{I} \tag{B.4}$$

where we use the subscript "0" for differential operators calculated at the initial material configuration, then, using Einstein's index notation:

$$\nabla_0(\bullet) \equiv \boldsymbol{e}_{(i)} \frac{\partial(\bullet)}{\partial \xi_i} \tag{B.5}$$

with a Cartesian coordinate system for the initial configuration with basis vector $\boldsymbol{e}_{(i)}$ and $\boldsymbol{I}$ is the second order identity tensor $\boldsymbol{I} = \delta_{ij}\boldsymbol{e}_i\boldsymbol{e}_j$, in dyadic notation, with δ_{ij} the Kronecker delta.

The total Lagrangian formulation of the solid governing equation will be derived from Newton's Second Law, one of the most used principles in Solid Mechanics, which is written as [56]:

$$\underbrace{\rho_0^{\mathrm{s}} \frac{\partial^2 \boldsymbol{u}}{\partial t^2}}_{\text{Inertial forces}} = \underbrace{\rho_0^{\mathrm{s}} \boldsymbol{g}}_{\text{Body forces}} + \underbrace{\nabla_0 \bullet \boldsymbol{P}}_{\text{Surface forces}} \tag{B.6}$$

where ρ_0^{s} is the solid density of the initial configuration and $\boldsymbol{g}$ is the gravitational acceleration. As shown in the equation, $\nabla_0 \bullet \boldsymbol{P}$ originates from the surface forces acting on a solid material element, and $\dfrac{\partial^2 \boldsymbol{u}}{\partial t^2}$ is the solid acceleration.

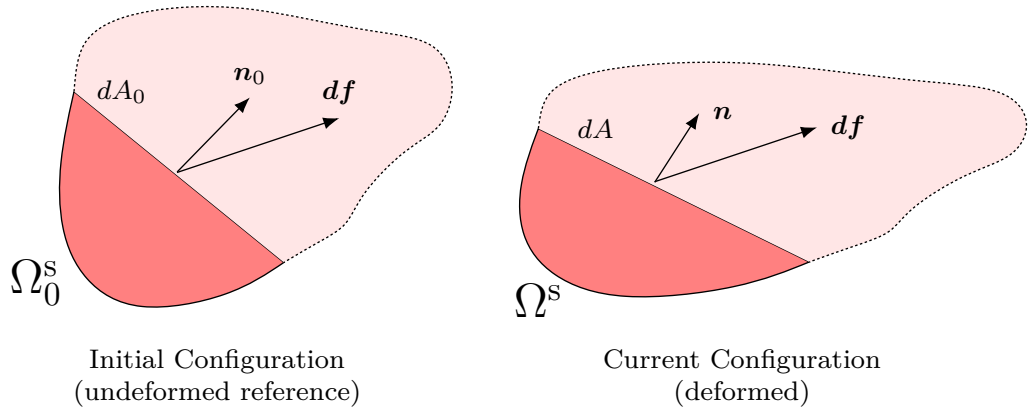
Figure B.2 depicts a solid deformation with an acting force $\boldsymbol{df}$ acting on a section $\mathrm{d}A$. Based on the figure, the multiaxial nominal stress, $\boldsymbol{P}$, on the section area, is defined by:

$$\boldsymbol{df} = \boldsymbol{t}_0 dA_0 = \boldsymbol{n}_0 \bullet \boldsymbol{P} dA_0 \tag{B.7}$$

where $\mathrm{d}A_0$ is the section area at the initial configuration and $\boldsymbol{n}_0$ the unit normal vector of section $\mathrm{d}A_0$; $\boldsymbol{t}_0$ is the traction on the undeformed configuration.

To find an equation that describes the solid motion, we must relate the nominal stress tensor in Eq. (B.6) to the solid displacement, $\boldsymbol{u}$. This can be achieved invoking a *constitutive equation* for the solid, a tensorial relation describing the material deformation under applied stresses. There are several constitutive equations suitable for different solid

Figure B.2 – Deformation of a solid: detail of a section under the application of a force $\boldsymbol{df}$.



Source: prepared by the author.

behavior: elastic, hyperelastic, hypoelastic, plasticity, viscoelasticity, etc. These models are described in detail in Belytschko et al. [56]. However, we must mention other forms of stress and strain measurements. Tensors such as $\boldsymbol{P}$ and $\boldsymbol{F}$ are not suitable to construct constitutive relations [56] because, among other reasons, $\boldsymbol{P}$ is not symmetric and $\boldsymbol{F}$ does not vanish for rotation of the solid. The second Piola-Kirchhoff stress tensor, $\boldsymbol{S}$, and the Green-Lagrange strain tensor, $\boldsymbol{E}$, respectively, are more suitable for that purpose [56]. The second Piola-Kirchhoff stress tensor is defined by (see Fig. B.2):

$$\boldsymbol{df} = \boldsymbol{F}^{-1} \bullet \boldsymbol{t}_0 \mathrm{d}A_0 = \boldsymbol{n}_0 \bullet \boldsymbol{S} \mathrm{d}A_0 \tag{B.8}$$

Combining Eqs. (B.7) and (B.8), follows:

$$\boldsymbol{P} = \boldsymbol{S} \bullet \boldsymbol{F}^T \tag{B.9}$$

a relationship between $\boldsymbol{P}$ and $\boldsymbol{S}$, which will be used in Eq. (B.6). The Green-Lagrange strain tensor is defined by [56]:

$$2\boldsymbol{d\xi} \bullet \boldsymbol{E} \bullet \boldsymbol{d\xi} = \underbrace{\boldsymbol{dx} \bullet \boldsymbol{dx}}_{\substack{\text{Square of the length } \boldsymbol{dx} \text{ in the deformed configuration}}} - \underbrace{\boldsymbol{d\xi} \bullet \boldsymbol{d\xi}}_{\substack{\text{Square of the length } \boldsymbol{d\xi} \text{ in the initial configuration}}} \tag{B.10}$$

Figure B.1 shows the vectors of a line segment at initial and current configuration, $\boldsymbol{d\xi}$ and $\boldsymbol{dx}$, respectively. From definition Eq. (B.10) and the motion equation, Eq. (B.1), is

possible to demonstrate that [56]:

$$\boldsymbol{E} = \frac{1}{2}\left(\boldsymbol{F}^T \bullet \boldsymbol{F} - \boldsymbol{I}\right) \tag{B.11}$$

Writing Eq. (B.11) in Einstein's index notation and substituting Eqs. (B.2) and (B.3) into it, a final form of $\boldsymbol{E}$ as function of $\boldsymbol{u}$ can be derived:

$$\begin{aligned}
\boldsymbol{E} =& \frac{1}{2}\left(\boldsymbol{F}^T \bullet \boldsymbol{F} - \boldsymbol{I}\right) \Rightarrow E_{ij} = \frac{1}{2}\left(F_{ik}^T F_{kj} - \delta_{ij}\right) \Rightarrow \\
\Rightarrow E_{ij} =& \frac{1}{2}\left(\frac{\partial x_k}{\partial \xi_i}\frac{\partial x_k}{\partial \xi_j} - \delta_{ij}\right) \Rightarrow \\
E_{ij} =& \frac{1}{2}\left[\left(\frac{\partial u_k}{\partial \xi_i} + \underbrace{\frac{\partial \xi_k}{\partial \xi_i}}_{\delta_{ki}}\right)\left(\frac{\partial u_k}{\partial \xi_j} + \underbrace{\frac{\partial \xi_k}{\partial \xi_j}}_{\delta_{kj}}\right) - \delta_{ij}\right] \Rightarrow \\
E_{ij} =& \frac{1}{2}\left[\frac{\partial u_k}{\partial \xi_i}\frac{\partial u_k}{\partial \xi_j} + \frac{\partial u_k}{\partial \xi_i}\delta_{kj} + \delta_{ki}\frac{\partial u_k}{\partial \xi_j} + \underbrace{\delta_{ki}\delta_{kj}}_{\delta_{ij}} - \delta_{ij}\right] \Rightarrow \\
E_{ij} =& \frac{1}{2}\left(\frac{\partial u_i}{\partial \xi_j} + \frac{\partial u_j}{\partial \xi_i} + \frac{\partial u_k}{\partial \xi_i}\frac{\partial u_k}{\partial \xi_j} + \delta_{ij} - \delta_{ij}\right) \Rightarrow \\
E_{ij} =& \frac{1}{2}\left(\frac{\partial u_i}{\partial \xi_j} + \frac{\partial u_j}{\partial \xi_i} + \frac{\partial u_k}{\partial \xi_i}\frac{\partial u_k}{\partial \xi_j}\right)
\end{aligned} \tag{B.12}$$

With the last equality in Eq. (B.12) it is easy to see that $\boldsymbol{E}$ is a symmetric second order tensor, i.e., $E_{ij} = E_{ji}$. Converting the last equality into vector notation, we finally find:

$$\boldsymbol{E} = \frac{1}{2}\left(\nabla_0 \boldsymbol{u} + \nabla_0^T \boldsymbol{u} + \nabla_0 \boldsymbol{u} \bullet \nabla_0^T \boldsymbol{u}\right) \tag{B.13}$$

It is interesting to note in Eq. (B.13) that the first two terms on the right hand side correspond to the strain when small deformations occur in the solid, i.e., linear elastic deformations, while the last term is a non-linear contribution, due to larger deformations in the solid.

The constitutive relation that we will discuss here is valid for the so-called *Saint-Venant-Kirchhoff material*, presenting an elastic non-linear behavior. Its constitutive equation relates the second order tensors $\boldsymbol{S}$ and $\boldsymbol{E}$ through an extension of Hooke's law:

$$S_{ij} = C_{ijkl} E_{kl} \tag{B.14}$$

(we will use Einstein's notation when dealing with algebraic operations on tensors to highlight their order). C_{ijkl} is a fourth order tensor called *elastic modulus*; for an isotropic solid, C_{ijkl} can be written in terms of the second order identity tensor, $\boldsymbol{I} = \delta_{ij}\boldsymbol{e}_i\boldsymbol{e}_j$:

$$C_{ijkl} = \lambda^{\mathrm{s}}\delta_{ij}\delta_{kl} + \mu^{\mathrm{s}}\left(\delta_{ik}\delta_{jl} + \delta_{il}\delta_{jk}\right) \tag{B.15}$$

where λ^{s} and μ^{s} are the Lamé's constants of the solid related to Young's modulus and Poisson's ratio of the material:

$$\mu^{\mathrm{s}} = \frac{E}{2(1+\nu^{\mathrm{s}})} \tag{B.16}$$

$$\lambda^{\mathrm{s}} = \begin{cases} \frac{\nu^{\mathrm{s}}E}{(1+\nu^{\mathrm{s}})(1-\nu^{\mathrm{s}})} & \text{plane stress state} \\ \frac{\nu^{\mathrm{s}}E}{(1+\nu^{\mathrm{s}})(1-2\nu^{\mathrm{s}})} & \text{plane strain and 3D cases} \end{cases} \tag{B.17}$$

Substituting Eq. (B.15) into Eq. (B.14) yields:

$$\begin{aligned} S_{ij} =& \lambda^{\mathrm{s}}\delta_{ij}\delta_{kl}E_{kl} + \mu^{\mathrm{s}}\delta_{ik}\delta_{jl}E_{kl} + \mu^{\mathrm{s}}\delta_{il}\delta_{jk}E_{kl} \\ S_{ij} =& \lambda^{\mathrm{s}}E_{kk}\delta_{ij} + \mu^{\mathrm{s}}E_{ij} + \mu^{\mathrm{s}}E_{ji} \end{aligned} \tag{B.18}$$

Since $\boldsymbol{E}$ is a symmetric tensor:

$$S_{ij} = 2\mu^{\mathrm{s}}E_{ij} + \lambda^{\mathrm{s}}E_{kk}\delta_{ij} \tag{B.19}$$

or, converting to vector notation:

$$\boldsymbol{S} = 2\mu^{\mathrm{s}}\boldsymbol{E} + \lambda^{\mathrm{s}}tr(\boldsymbol{E})\boldsymbol{I} \tag{B.20}$$

we find the constitutive equation for a solid with non-linear elastic behavior (large deformations).

We now have all the necessary equations to turn Eq. (B.6) into an equation in which the dependent variable is $\boldsymbol{u}$. Substituting Eqs. (B.4) and (B.9) into Eq. (B.6) follows:

$$\begin{aligned} \rho_0^{\mathrm{s}}\frac{\partial^2\boldsymbol{u}}{\partial t^2} =& \rho_0^{\mathrm{s}}\boldsymbol{g} + \nabla_0 \bullet \left(\boldsymbol{S}\bullet\boldsymbol{I} + \boldsymbol{S}\bullet\nabla_0\boldsymbol{u}\right) \Rightarrow \\ \Rightarrow \rho_0^{\mathrm{s}}\frac{\partial^2\boldsymbol{u}}{\partial t^2} =& \rho_0^{\mathrm{s}}\boldsymbol{g} + \nabla_0 \bullet \boldsymbol{S} + \nabla_0 \bullet \left(\boldsymbol{S}\bullet\nabla_0\boldsymbol{u}\right) \end{aligned} \tag{B.21}$$

where we used $\boldsymbol{S} \bullet \boldsymbol{I} = \boldsymbol{S}$. Then, substituting Eqs. (B.13) and (B.20) into the last equality:

$$\begin{aligned}
\rho_0^{\mathrm{s}} \frac{\partial^2 \boldsymbol{u}}{\partial t^2} =& \nabla_0 \bullet \left[2\mu^{\mathrm{s}} \boldsymbol{E} + \lambda^{\mathrm{s}} tr(\boldsymbol{E}) \boldsymbol{I}\right] + \nabla_0 \bullet \left(\boldsymbol{S} \bullet \nabla_0 \boldsymbol{u}\right) + \rho_0^{\mathrm{s}} \boldsymbol{g} \Rightarrow \\
\Rightarrow \rho_0^{\mathrm{s}} \frac{\partial^2 \boldsymbol{u}}{\partial t^2} =& \nabla_0 \bullet \Bigg[\mu^{\mathrm{s}} \left(\nabla_0 \boldsymbol{u} + \nabla_0^T \boldsymbol{u}\right) + \mu^{\mathrm{s}} \nabla_0 \boldsymbol{u} \bullet \nabla_0^T \boldsymbol{u} + \\
& + \frac{\lambda^{\mathrm{s}}}{2} tr\left(\nabla_0 \boldsymbol{u} + \nabla_0^T \boldsymbol{u}\right) \boldsymbol{I} + \frac{\lambda^{\mathrm{s}}}{2} tr\left(\nabla_0 \boldsymbol{u} \bullet \nabla_0^T \boldsymbol{u}\right) \boldsymbol{I}\Bigg] + \\
& + \nabla_0 \bullet \left(\boldsymbol{S} \bullet \nabla_0 \boldsymbol{u}\right) + \rho_0^{\mathrm{s}} \boldsymbol{g}
\end{aligned} \tag{B.22}$$

Last equation must be rearranged in such a way that, when solved using the Finite Volume Method, the convergence rate will be accelerated, according to Jasak and Weller [97]. Adding and subtracting $(\mu^{\mathrm{s}} \nabla_0 \boldsymbol{u} + \lambda^{\mathrm{s}} \nabla_0 \boldsymbol{u})$ to the first divergent of the last equality, after manipulating we finally find:

$$\begin{aligned}
\rho_0^{\mathrm{s}} \frac{\partial^2 \boldsymbol{u}}{\partial t^2}(\boldsymbol{\xi}, t) - \nabla_0 \bullet \left[(2\mu^{\mathrm{s}} + \lambda^{\mathrm{s}}) \nabla_0 \boldsymbol{u}\right] =& \nabla_0 \bullet \Big[-\left(\mu^{\mathrm{s}} + \lambda^{\mathrm{s}}\right) \nabla_0 \boldsymbol{u} + \mu^{\mathrm{s}} \nabla_0^T \boldsymbol{u} + \lambda^{\mathrm{s}} tr(\nabla_0 \boldsymbol{u}) \boldsymbol{I}\Big] + \\
& \nabla_0 \bullet \left[\mu^{\mathrm{s}} \left(\nabla_0 \boldsymbol{u} \bullet \nabla_0^T \boldsymbol{u}\right) + \frac{1}{2} \lambda^{\mathrm{s}} tr\left(\nabla_0 \boldsymbol{u} \bullet \nabla_0^T \boldsymbol{u}\right) \boldsymbol{I}\right] + \\
& \nabla_0 \bullet \left(\boldsymbol{S} \bullet \nabla_0 \boldsymbol{u}\right) + \rho_0^{\mathrm{s}} \boldsymbol{g}
\end{aligned} \tag{B.23}$$

which is the equation solved by the FSI solver of foam-extend for the solid part of the FSI problem.

C The Finite Volume Discretization

We present here the FVM discretization of a partial differential equation representing the transport of an intensive variable ϕ in a flow domain Ω^{f} – with boundary surface $\Gamma^{\mathrm{f}} = \partial\Omega^{\mathrm{f}}$ – with velocity field $\boldsymbol{v}$ of a fluid with density ρ. In the conservative form, this equation is written as:

$$\underbrace{\frac{\partial}{\partial t}(\rho\phi)}_{\text{Temporal term}} + \underbrace{\nabla\bullet(\rho\boldsymbol{v}\phi)}_{\text{Advective transport term}} = \underbrace{\nabla\bullet\left(\rho\Gamma^{\phi}\nabla\phi\right)}_{\text{Diffusive transport term}} + \underbrace{S^{\phi}}_{\text{Source/sink terms}} \tag{C.1}$$

where Γ^{ϕ} is the diffusivity of ϕ ($[\Gamma^{\phi}] = \mathrm{m}^2/\mathrm{s}$), "$\nabla$" is the nabla operator. We suppose that field $\boldsymbol{v}$ is known. Equation (C.1) identifies four terms:

- The temporal term, which represents the change of ϕ in time;
- The advective term: it represents the net advective flux of ϕ, i.e. the flux due to the flow velocity $\boldsymbol{v}$ over an infinitesimal control volume;
- The diffusive term: it represents the molecular transport of ϕ through the surface of an infinitesimal control volume;
- Source and/or sink terms of ϕ in the flow domain.

A set of boundary and initial conditions must be provided to close the problem and solve Eq. (C.1) for ϕ.

The FVM discretization process has the following steps:

1. Spatial domain discretization into finite volumes (computational mesh) and temporal domain discretization into a sequence of time-steps;
2. Spatial and temporal discretization of the transport equation;
3. Application and discretization of boundary and initial conditions;
4. Solution of the linearized system of equations.

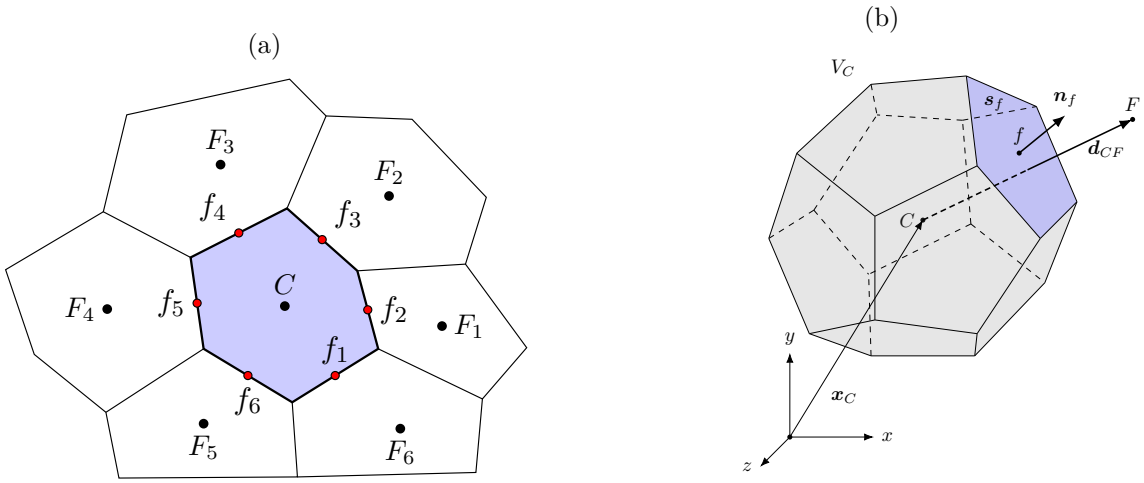
Let us consider that the spatial domain Ω^{f} is discretized in a finite number, N_{CV}, of non-overlapping control volumes of polyhedral shape, with an arbitrary number of planar faces and each face must be shared by only two adjacent cells. A typical control volume

has its centroid at point C, and volume V_C as shown in Figure C.1b, and Fig. C.1a shows a finite volume and its neighbors. Fig. C.1b also shows the geometric entities of the cell used in theFVMdiscretization: a face f, the unit normal pointing outward face f, $\boldsymbol{n}_f$, and the vector joining C and the centroid of a neighbor cell F, $\boldsymbol{d}_{CF}$. Centroid C has Cartesian coordinates $\boldsymbol{x}_C$, defined by:

$$\boldsymbol{x}_C = \frac{1}{V_C}\int_{V_C} \boldsymbol{x}\mathrm{d}V \Leftrightarrow \int_{V_C} (\boldsymbol{x} - \boldsymbol{x}_C)\mathrm{d}V = 0 \tag{C.2}$$

The cell-centered FVM stores the variables at this point [44].

Figure C.1 – (a) Polygonal control volume of a finite volume computational mesh, and its neighbors; (b) Polyhedral control volume V_C.



Source: prepared by the author.

With the domain decomposed into a finite number of control volumes, the FVM integrates Eq. (C.1) in the volume V_C, leading to:

$$\int_{V_C} \frac{\partial}{\partial t}(\rho\phi)\mathrm{d}V + \int_{V_C} \nabla\bullet(\rho\boldsymbol{v}\phi)\mathrm{d}V = \int_{V_C} \nabla\bullet\left(\rho\Gamma^{\phi}\nabla\phi\right)\mathrm{d}V + \int_{V_C} S^{\phi}\mathrm{d}V \tag{C.3}$$

We consider that control volume V_C does not change in time, (the methodology for moving computational meshes is essentially the same, the initial equation must be properly formulated, as presented in the main text, Section 2.3.2). Therefore, the order of the temporal derivative can be inverted:

$$\frac{\partial}{\partial t}\int_{V_C} \rho\phi\mathrm{d}V + \int_{V_C} \nabla\bullet(\rho\boldsymbol{v}\phi)\mathrm{d}V = \int_{V_C} \nabla\bullet\left(\rho\Gamma^{\phi}\nabla\phi\right)\mathrm{d}V + \int_{V_C} S^{\phi}\mathrm{d}V \tag{C.4}$$

Applying Gauss' divergence theorem, the volume integrals of the advective and diffusive terms can be transformed in surface integrals over the control volume surface $S_C = \partial V_C$:

$$\frac{\partial}{\partial t}\int_{V_C}\rho\phi \mathrm{d}V + \oint_{\partial V_C}\rho\phi\left(\boldsymbol{v}\bullet\boldsymbol{n}\right)\mathrm{d}S = \oint_{\partial V_C}\rho\Gamma^{\phi}\left(\boldsymbol{n}\bullet\nabla\phi\right)\mathrm{d}S + \int_{V_C}S^{\phi}\mathrm{d}V \tag{C.5}$$

where $\boldsymbol{n}$ is the outward unit normal vector of control surface S. The surface integrals can be split into a sum of integrals over the planar faces of the cell (see Fig. C.1b):

$$\frac{\partial}{\partial t}\int_{V_C}\rho\phi \mathrm{d}V + \sum_{f\sim nb(C)}\int_{S_f}\rho\phi\left(\boldsymbol{n}_f\bullet\boldsymbol{v}\right)\mathrm{d}S = \sum_{f\sim nb(C)}\int_{S_f}\rho\Gamma^{\phi}\left(\boldsymbol{n}_f\bullet\nabla\phi\right)\mathrm{d}S + \int_{V_C}S^{\phi}\mathrm{d}V \tag{C.6}$$

where S_f is the area of face f; the notation $f\sim nb(C)$ represents faces neighboring the centroid C, i.e., the faces of the cell C, as shown in Fig. C.1a. So far we adapted Eq. (C.3) to the polyhedral control volume. The discretized equation, i.e., Eq. (C.6) transformed into an algebraic equation for cell centroid values, $\phi_C = \phi(\boldsymbol{x}_C)$, is obtained assuming a linear spatial variation of ϕ around the cell centroid $\boldsymbol{x}_C$, i.e.:

$$\phi\left(\boldsymbol{x}\right) = \phi\left(\boldsymbol{x}_C\right) + \left(\nabla\phi\right)_C \bullet \left(\boldsymbol{x}-\boldsymbol{x}_C\right) \tag{C.7}$$

This linear function is second-order accurate, which is adequate because the transport equation, Eq. (C.1), is a second-order partial differential equation. The referred second-order accuracy can be verified writing the Taylor series expansion of function $\phi = \phi(\boldsymbol{x})$:

$$\begin{aligned}\phi(\boldsymbol{x}) =& \phi\left(\boldsymbol{x}_C\right) + \left(\boldsymbol{x}-\boldsymbol{x}_C\right)\bullet\left(\nabla\phi\right)_C + \frac{1}{2!}\left(\boldsymbol{x}-\boldsymbol{x}_C\right)^2 \vdots \left(\nabla\nabla\phi\right)_C + \\ & \frac{1}{3!}\left(\boldsymbol{x}-\boldsymbol{x}_C\right)^3 \vdots\vdots \left(\nabla\nabla\nabla\phi\right)_C + \cdots + \frac{1}{n!}\left(\boldsymbol{x}-\boldsymbol{x}_C\right)^n \underbrace{\vdots\vdots\ldots\vdots}_{\text{n times}} \left(\underbrace{\nabla\nabla\ldots\nabla}_{\text{n times}}\phi\right)_C + \cdots\end{aligned} \tag{C.8}$$

where $\left(\boldsymbol{x}-\boldsymbol{x}_C\right)^n$ represents the n^{th} outer product of vector $\boldsymbol{x}-\boldsymbol{x}_C$ with itself, resulting in a n^{th} order tensor; $\vdots\vdots\ldots\vdots$ represents the inner product of two n^{th} order tensors, resulting in a scalar. Truncating the series after the first order term yields:

$$\phi(\boldsymbol{x}) = \phi(\boldsymbol{x}_C) + \left(\boldsymbol{x}-\boldsymbol{x}_C\right)\bullet\left(\nabla\phi\right)_C + \mathcal{O}\left(\left\|\boldsymbol{x}-\boldsymbol{x}_C\right\|^2\right) \tag{C.9}$$

where we see that the error is of order $\left\|\boldsymbol{x}-\boldsymbol{x}_C\right\|^2$.

Using the approximation Eq. (C.7), the surface integrals in Eq. (C.6) are evaluated with second-order accuracy [44], leading to:

$$\frac{\partial}{\partial t}\int_{V_C}\rho\phi \mathrm{d}V + \sum_{f\sim nb(C)}\left[\rho_f\left(\boldsymbol{v}_f \bullet \boldsymbol{s}_f\right)\right]\phi_f = \sum_{f\sim nb(C)}\left(\rho\Gamma^{\phi}\right)_f\left(\nabla\phi_f\right)\bullet\boldsymbol{s}_f + \int_{V_C} S^{\phi}\mathrm{d}V \quad \text{(C.10)}$$

where the lower index f indicates a variable evaluated at the face centroid.

Applying Gauss' divergence theorem allowed to write the advective and diffusive terms as functions of ϕ values at face centroids. However, the variables that must be used are stored at cell centroids. The FVM interpolates the face variables, ϕ_f and $\nabla\phi_f$, from adjacent cell centroids variables, as shown in Fig. C.1a. These procedures are presented below.

C.1 Spatial Discretization

Advective Term

The advective term is:

$$\text{Advective Flow Rate of } \phi = \sum_{f\sim nb(C)}\left[\rho_f\left(\boldsymbol{v}_f \bullet \boldsymbol{s}_f\right)\right]\phi_f = \sum_{f\sim nb(C)}\dot{m}_f\phi_f \quad \text{(C.11)}$$

where $\dot{m}_f = \rho_f(\boldsymbol{v}_f \bullet \boldsymbol{s}_f)$ is the mass flow rate through face f. The FVM evaluates explicitly the mass flow rate interpolating ρ_f from known values available at adjacent cell centroids; this is important, for example, for the solution of the Navier-Stokes equations, to linearize the discretized momentum equations; ϕ_f, on the other hand, is evaluated implicitly, i.e. it is interpolated from cell centroid values, ϕ_C and ϕ_F.

The interpolation profile for ϕ_f must be carefully chosen because it is responsible for anomalous behavior of the flow solution if wrongly specified. First-order accurate profiles – "Upwind", for example – are responsible for numerical diffusion on the solution, while higher order profiles – Central Difference and second-order Upwind schemes – can cause "wiggles" on the solution – consequences of numerical dispersion causing an unbounded behavior of the solution – and the magnitude of these "wiggles" can lead to divergence of the solution process [44, 73]. Higher order and high resolution *bounded schemes* are recommended.

We describe below the scheme used for the aneurysms simulations presented on the

main text. In foam-extend, the scheme is available under the keyword `linearUpwind`: a combination of a linear profile for ϕ_f with the classical Upwind scheme. Therefore, this scheme is second-order accurate and presents less numerical dispersion than the Central Difference scheme. For unstructured meshes, ϕ_f is written as follows:

$$\phi_f = \phi_C + (2\nabla\phi_C - \nabla\phi_f) \bullet \boldsymbol{d}_{Cf} \tag{C.12}$$

where $\boldsymbol{d}_{Cf} = \boldsymbol{x}_f - \boldsymbol{x}_C$ is the vector joining centroid C and face f, $\boldsymbol{x}_f$. In Eq. (C.12) is necessary to evaluate the gradient of ϕ at C and f. We will discuss the discretization of gradients below, along with the diffusive term discretization.

Once applied the advective scheme for ϕ_f, it can be written as:

$$\phi_f = w_C\phi_C + w_F\phi_F \tag{C.13}$$

where w_C and w_F are weights that depends on the chosen interpolation scheme, accounting for the influence of ϕ_C and ϕ_F on the value of ϕ_f, respectively. For example, in the classic one-dimensional Upwind scheme, $w_C = 1$ and $w_F = 0$ or vice-versa, depending on the flow direction.

In foam-extend, the advective term is identified by the function `div()` and its discretization must be specified in the sub-dictionary `divSchemes` of the dictionary `fvSchemes` on the following sequence: the discretization method - Gauss integration, for example, if the standard discretization practice is chosen -, the interpolation profile for ϕ_f and, if required, the discretization scheme for the gradient of ϕ, as follows:

```
divSchemes
{
  default     none
  div(phi,U)  Gauss <interpolation> <gradientDiscretization>
}
```

where `phi` is the keyword in foam-extend for the mass flux at the cell faces, i.e., `phi` $\equiv \rho\boldsymbol{v}$ for incompressible flows.

Diffusive Term

The diffusive term is:

$$\text{Diffusive Flow Rate of } \phi = \sum_{f \sim nb(C)} (\rho \Gamma^{\phi})_f (\nabla \phi)_f \bullet \boldsymbol{s}_f \tag{C.14}$$

First, the density and diffusivity of ϕ of the fluid need to be evaluated. Using known values available from last iterations – or for the incompressible case, ρ is a constant – these properties are interpolated from centroid values, as follows:

$$\begin{aligned} \rho_f &= g_C \rho_C + g_F \rho_F \\ \Gamma^{\phi}_f &= g_C \Gamma^{\phi}_C + g_F \Gamma^{\phi}_F \end{aligned} \tag{C.15}$$

if a linear interpolation is chosen, where g_C and g_F are interpolation factors which can be calculated as a ratio in terms of distances between cell and face centroids given by [44]:

$$g_C = \frac{d_{fF}}{d_{Cf} + d_{fF}}; \quad g_F = \frac{d_{Cf}}{d_{Cf} + d_{fF}} = 1 - g_C \tag{C.16}$$

The gradient of ϕ normal to face f, $\nabla \phi_f \bullet \boldsymbol{s}_f$, is proportional to the directional derivative of ϕ on the direction of vector $\boldsymbol{s}_f = S_f \boldsymbol{n}_f$:

$$\nabla \phi_f \bullet \boldsymbol{s}_f = S_f \nabla \phi_f \bullet \boldsymbol{n}_f = S_f \left(\frac{\partial \phi}{\partial \boldsymbol{n}_f} \right)_f \tag{C.17}$$

If centroids C and F lied on the direction of $\boldsymbol{n}_f$, the directional derivative $\left(\frac{\partial \phi}{\partial \boldsymbol{n}_f} \right)_f$ could be evaluated, with second-order accuracy, using the Central Differences scheme, i.e. $\left(\frac{\partial \phi}{\partial \boldsymbol{n}_f} \right)_f = \frac{\phi_F - \phi_C}{\|\boldsymbol{d}_{CF}\|}$, where $\|\boldsymbol{d}_{CF}\|$ is the distance between C and F. However, for an unstructured mesh of polyhedral elements, this is not always satisfied – see, for example, in Fig. C.1b the directions of $\boldsymbol{n}_f$ and $\boldsymbol{d}_{CF}$ which do not coincide – therefore, the gradient normal to a face cannot be directly evaluated using the values of ϕ_C and ϕ_F because an error would be introduced. A solution to address the problem is to decompose vector $\boldsymbol{s}_f$ into two components:

$$\boldsymbol{s}_f = \boldsymbol{\beta} + \boldsymbol{\kappa} \tag{C.18}$$

where $\boldsymbol{\beta} = \beta \boldsymbol{e}_f$ lies on the direction of $\boldsymbol{d}_{CF}$, i.e. $\boldsymbol{e}_f = \dfrac{\boldsymbol{d}_{CF}}{\|\boldsymbol{d}_{CF}\|}$. Moukalled et al. [44] presents three ways of decomposing the vector $\boldsymbol{s}_f$: minimum correction approach, orthogonal correction approach and over-relaxed approach. With this decomposition, the gradient normal to the face is written as:

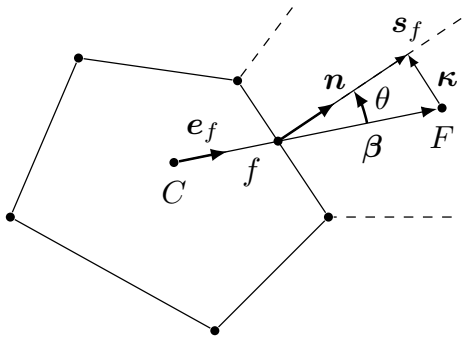
$$\begin{aligned} \nabla\phi_f \bullet \boldsymbol{s}_f &= \nabla\phi_f \bullet \boldsymbol{\beta} + \nabla\phi_f \bullet \boldsymbol{\kappa} \\ &= \|\boldsymbol{\beta}\| \nabla\phi_f \bullet \boldsymbol{e}_f + \nabla\phi_f \bullet \boldsymbol{\kappa} \\ &= \|\boldsymbol{\beta}\| \left(\frac{\partial\phi}{\partial \boldsymbol{e}_f}\right)_f + \nabla\phi_f \bullet \boldsymbol{\kappa} \end{aligned} \tag{C.19}$$

Central Differences can be used to evaluate $\left(\frac{\partial\phi}{\partial \boldsymbol{e}_f}\right)_f$, yielding:

$$\begin{aligned} \nabla\phi_f \bullet \boldsymbol{s}_f &= \|\boldsymbol{\beta}\| \frac{\phi_F - \phi_C}{\|\boldsymbol{d}_{CF}\|} + \nabla\phi_f \bullet \boldsymbol{\kappa} \Rightarrow \\ \Rightarrow \nabla\phi_f \bullet \boldsymbol{s}_f &= \underbrace{\mathrm{gDiff}_f \left(\phi_F - \phi_C\right)}_{\text{Orthogonal contribution}} + \underbrace{\nabla\phi_f \bullet \boldsymbol{\kappa}}_{\text{Non-orthogonal correction}} \end{aligned} \tag{C.20}$$

where $\mathrm{gDiff}_f = \dfrac{\|\boldsymbol{\beta}\|}{\|\boldsymbol{d}_{CF}\|}$ is a "geometric diffusivity" [44]. If the over-relaxed approach is chosen (one of the options implemented in foam-extend), then the importance of the orthogonal term is increased as the non-orthogonality increase. This is accomplished selecting $\boldsymbol{\kappa}$ to be normal to the normal direction of face f, as depicted in Fig. C.2. In this case, as shown in Moukalled et al. [44], $\boldsymbol{\beta} = \left(\dfrac{\boldsymbol{s}_f \bullet \boldsymbol{s}_f}{\boldsymbol{s}_f \bullet \boldsymbol{d}_{CF}}\right) \boldsymbol{d}_{CF}$ and $\boldsymbol{\kappa}$ is calculated according to Eq. (C.18), $\boldsymbol{\kappa} = \boldsymbol{s}_f - \boldsymbol{\beta}$. For an orthogonal mesh case, $\boldsymbol{s}_f = \boldsymbol{\beta}$ and the term $\nabla\phi_f \bullet \boldsymbol{\kappa}$ would vanish. This term is usually called non-orthogonal correction or "cross diffusion" term.

Figure C.2 – Choice of decomposition of normal vector $\boldsymbol{s}_f$ according to the over-relaxed approach.



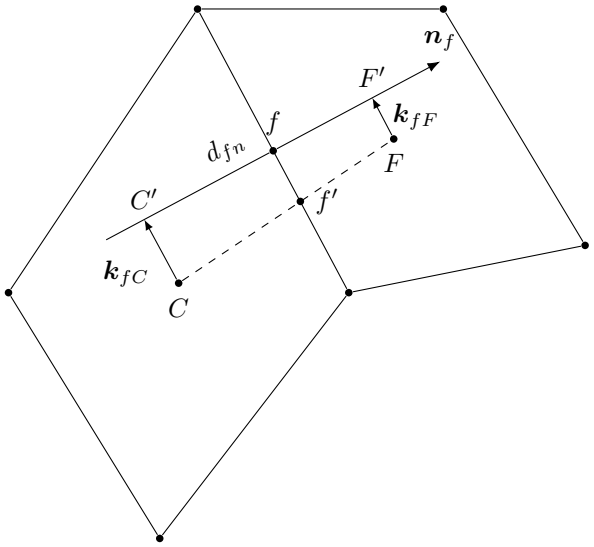
Source: prepared by the author.

However, to evaluate $\left(\frac{\partial \phi}{\partial \boldsymbol{e}_f}\right)_f$ with second-order accuracy with Central Differences, the line joining C and F must intercept face f at its centroid. This is not the general case, as we can see in Fig. C.1b, where the line segment CF does not intercept centroid f. This is called *skewness* of the mesh, and is a source of errors. In foam-extend, a discretization for $\nabla\phi_f \bullet \boldsymbol{s}_f$ presented by Tuković et al. [72] with non-orthogonal *and* skewness correction was chosen for our simulations of aneurysms – in foam-extend, this scheme is called `skewCorrected`. This scheme can be derived based on the vector quantities defined in Fig. C.3: vectors $\boldsymbol{k}_{fC}$ and $\boldsymbol{k}_{fF}$. Tuković et al. [72] presents the discretization procedure for this scheme:

$$\nabla\phi_f \bullet \boldsymbol{s}_f = \frac{\phi_F - \phi_C}{d_{fn}} + \frac{\boldsymbol{k}_{fF} \bullet (\nabla\phi)_F - \boldsymbol{k}_{fC} \bullet (\nabla\phi)_C}{d_{fn}} \tag{C.21}$$

where $d_{fn} = \boldsymbol{d}_{CF} \bullet \boldsymbol{n}_f$.

Figure C.3 – Two adjacent control volumes with skewness and non-orthogonality between them, with vectors definitions used to calculate the gradient normal to face f, $\nabla\phi_f \bullet \boldsymbol{s}_f$ with corrections.



Source: Tuković et al. [72].

In foam-extend setup, the diffusive term is identified by the function `laplacian()` and its discretization must be specified in the sub-dictionary `laplacianSchemes` of the dictionary `fvSchemes` on the sequence: the discretization method – Gauss integration is the only option available for this term –, the interpolation profile for the diffusivity and the discretization scheme for the surface normal gradient $\nabla\phi_f \bullet \boldsymbol{s}_f$, as shown below:

```
laplacianSchemes
{
  default          none
  laplacian(nu,U)  Gauss <interpolation> <surfaceNormalGradient>
}
```

Gradient Discretization

As shown above, both discretization of the advective and diffusive terms require the discretization and/or evaluation of a gradient at cell centroid, $\nabla\phi_C$, and at the face centroid, $\nabla\phi_f$. We present below one of the discretization procedures available in foam-extend.

One of the variants of Gauss' divergence theorem is the identity involving the gradient field of a variable ϕ in a volume V_C:

$$\int_{V_C} \nabla\phi \mathrm{d}V = \oint_{S=\partial V_C} \phi \boldsymbol{n} \mathrm{d}S \tag{C.22}$$

The Mean Value theorem (MVT) applied to function $\phi = \phi(\boldsymbol{x})$ in V_C is written as:

$$\nabla\phi_C = \frac{1}{V_C} \int_{V_C} \nabla\phi \mathrm{d}V \tag{C.23}$$

Combining Eqs. (C.22) and (C.23)), and substituting the FVM linear approximation of ϕ, Eq. (C.7), is possible to show that, for the polyhedral cell with faces f, the gradient of ϕ at its centroid C is:

$$\nabla\phi_C = \frac{1}{V_C} \sum_{f \sim nb(C)} \phi_f \boldsymbol{s}_f \tag{C.24}$$

where the values ϕ_f is interpolated from adjacent computational nodes.

In foam-extend, the gradient is identified by the function `grad()` and its discretization must be specified in the sub-dictionary `gradSchemes` of the dictionary `fvSchemes` on the sequence: the discretization method and the interpolation profile:

```
gradSchemes
{
  default    none
  grad(U)    Gauss <interpolation>
}
```

Other techniques for the gradient discretization – the least squares method, for example, which is also available in foam-extend – are presented by Moukalled et al. [44].

Source/Sink Terms

Using the Mean Value theorem, the volume integral of the source term in Eq. (C.10) is written as:

$$\bar{S}^{\phi} = \frac{1}{V_C} \int_{V_C} S^{\phi} \mathrm{d}V \tag{C.25}$$

$\bar{S}^{\phi}$, generally, is considered a linear function of the dependent variable: $\bar{S}^{\phi} = S_C^{\phi}\phi_C + S_F^{\phi}$. The source/sink term is particular to each differential equation and some of them could require special treatment as, for example, the pressure gradient in the momentum equations for a flow.

Before continuing with the temporal discretization, we rewrite Eq. (C.10) in the form:

$$\frac{\partial}{\partial t}\left(\rho_C \phi_C V_C\right) + \underline{\sum_{f \sim nb(C)} \left[\rho_f \left(\boldsymbol{v}_f \bullet \boldsymbol{s}_f\right)\right] \phi_f} = \underline{\sum_{f \sim nb(C)} \left(\rho \Gamma^{\phi}\right)_f \nabla \phi_f \bullet \boldsymbol{s}_f + \left(S_C^{\phi}\phi_C + S_F^{\phi}\right) V_C} \tag{C.26}$$

where we applied the Mean Value theorem for the volume integral inside the temporal derivative. The underlined terms depend on cell centroid variables, ϕ_C and ϕ_F, once applied the discretization procedures presented above. Therefore, we rewrite Eq. (C.26) into the compact form:

$$\frac{\partial}{\partial t}\left(\rho_C \phi_C V_C\right) + \mathcal{H}\left\{\phi_C, \phi_F\right\} = 0 \tag{C.27}$$

where:

$$\mathcal{H}\left\{\phi_C, \phi_F\right\} = \sum_{f \sim nb(C)} \left[\rho_f \left(\boldsymbol{v}_f \bullet \boldsymbol{s}_f\right)\right] \phi_f - \sum_{f \sim nb(C)} \left(\rho \Gamma^{\phi}\right)_f (\nabla \phi_f) \bullet \boldsymbol{s}_f - \left(S_C^{\phi}\phi_C + S_F^{\phi}\right) V_C \tag{C.28}$$

The last form of the transport equation will be useful in the presentation below.

C.2 Temporal Discretization

The procedure to discretize the temporal derivative is based on the Finite Differences Method and is a second-order Euler backward scheme because it approximates the time derivative using information of two old time-steps. Since this scheme is second-order accurate, it keeps the consistency with the spatial discretization procedures and the overall FVM discretization. We consider here a temporal domain discretization with fixed time-steps, Δt.

Let's expand function $\Phi_C = \Phi_C(t)$ in Taylor series around instants $(t - \Delta t)$ and

$(t-2\Delta t)$, where $\Phi_C = \rho_C \phi_C$:

$$\begin{aligned}\Phi_C\left(t-\Delta t\right) =& \Phi_C\left(t\right) - \frac{\partial \Phi_C}{\partial t}(t)\Delta t + \frac{1}{2!}\frac{\partial^2 \Phi_C}{\partial t^2}\left(t\right)\left(\Delta t\right)^2 + \mathcal{O}(\Delta t^3) \\ \Phi_C\left(t-2\Delta t\right) =& \Phi_C\left(t\right) - 2\frac{\partial \Phi_C}{\partial t}\left(t\right)\Delta t + \frac{4}{2!}\frac{\partial^2 \Phi_C}{\partial t^2}\left(t\right)\left(\Delta t\right)^2 + \mathcal{O}(\Delta t^3)\end{aligned} \tag{C.29}$$

To ensure second-order accuracy for the approximation of $\frac{\partial \Phi_C}{\partial t}(t)$, the second-order derivative must be eliminated of the above equations; therefore, multiplying the first equation by 4 and subtracting it from the second, follows:

$$\begin{aligned}4\Phi_C\left(t-\Delta t\right) - \Phi_C\left(t-2\Delta t\right) =& 3\Phi_C\left(t\right) - 2\frac{\partial \Phi_C}{\partial t}\left(t\right)\Delta t + \mathcal{O}(\Delta t^3) \Rightarrow \\ \Rightarrow \frac{\partial \Phi_C}{\partial t}\left(t\right) =& \frac{3\Phi_C(t) - 4\Phi_C\left(t-\Delta t\right) + \Phi_C\left(t-2\Delta t\right)}{2\Delta t} + \mathcal{O}(\Delta t^2)\end{aligned} \tag{C.30}$$

Representing variables at time t by an upper index n, last equation is rewritten as:

$$\frac{\partial\left(\rho_C \phi_C\right)}{\partial t}(t) = \frac{3\rho_C^{\mathrm{n}}\phi_C^{\mathrm{n}} - 4\rho_C^{\mathrm{n-1}}\phi_C^{\mathrm{n-1}} + \rho_C^{\mathrm{n-2}}\phi_C^{\mathrm{n-2}}}{2\Delta t} + \mathcal{O}(\Delta t^2) \tag{C.31}$$

The temporal discretization also requires a choice regarding at which instant the spatial terms, $\mathcal{H}\{\phi_C, \phi_F\}$, must be evaluated. For the aneurysms simulations, we chose to evaluate these terms implicitly, to ensure stability of the fluid flow solution regardless the time-step chosen [44].

Therefore, the discretized equation in time is written as:

$$\frac{3\rho_C^{\mathrm{n}}\phi_C^{\mathrm{n}} - 4\rho_C^{\mathrm{n-1}}\phi_C^{\mathrm{n-1}} + \rho_C^{\mathrm{n-2}}\phi_C^{\mathrm{n-2}}}{2\Delta t} + \mathcal{H}\left\{\phi_C^{\mathrm{n}}, \phi_F^{\mathrm{n}}\right\} = 0 \tag{C.32}$$

Finally, substituting Eqs. (C.13), (C.20) and (C.28) into the last equation, we obtain the linearized equation for ϕ_C in the control volume V_C:

$$\begin{aligned}&\left[\frac{3\rho_C^{\mathrm{n}}\phi_C^{\mathrm{n}} - 4\rho_C^{\mathrm{n-1}}\phi_C^{\mathrm{n-1}} + \rho_C^{\mathrm{n-2}}\phi_C^{\mathrm{n-2}}}{2\Delta t}\right] V_C + \sum_{f\sim nb(C)} \underbrace{\left[\rho_f\left(\boldsymbol{v}_f \bullet \boldsymbol{s}_f\right)\right]}_{\dot{m}_f}\left(w_C\phi_C^{\mathrm{n}} + w_F\phi_F^{\mathrm{n}}\right) = \\ &= \sum_{f\sim nb(C)} \left(\rho\Gamma^{\phi}\right)_f \left[\mathrm{gDiff}_f\left(\phi_F^{\mathrm{n}} - \phi_C^{\mathrm{n}}\right) + \nabla\phi_f \bullet \boldsymbol{\kappa}\right] + \left(S_C^{\phi}\phi_C^{\mathrm{n}} + S_F^{\phi}\right) V_C\end{aligned} \tag{C.33}$$

Rearranging the last equation, we find an algebraic linearized equation for V_C:

$$a_C^{\phi}\phi_C^{\mathrm{n}} + \sum_{F\sim NB(C)} a_F^{\phi}\phi_F^{\mathrm{n}} = b_C^{\phi} \tag{C.34}$$

where the notation $F \sim NB(C)$ indicates all control volumes F neighboring C. The coefficients in Eq. (C.34) are given by:

$$\begin{aligned} a_C^{\phi} =& \frac{3\rho_C^n V_C}{2\Delta t} + \sum_{f\sim nb(C)} \left(w_C \dot{m}_f + \rho_f \Gamma_f^{\phi} \mathrm{gDiff}_f \right) - S_C^{\phi} V_C \\ a_F^{\phi} =& w_F \dot{m}_f - \rho_f \Gamma_f^{\phi} \mathrm{gDiff}_f \\ b_C^{\phi} =& S_F^{\phi} V_C + \sum_{f\sim nb(C)} \rho_f \Gamma_f^{\phi} \nabla\phi_f \bullet \boldsymbol{\kappa} + \left(\frac{4\rho_C^{n-1} V_C}{2\Delta t} \right) \phi_C^{n-1} - \left(\frac{\rho_C^{n-2} V_C}{2\Delta t} \right) \phi_C^{n-2} \end{aligned} \tag{C.35}$$

Equation (C.34) is a discrete form of the transport partial differential equation, Eq. (C.1) for a finite control volume. Assembling the discrete equations for each control volume in the computational mesh, follows a linear system of algebraic equations:

$$\mathbf{A}^{\phi}\boldsymbol{\phi} = \mathbf{b}^{\phi} \tag{C.36}$$

where $\mathbf{A}^{\phi} \equiv (a_C^{\phi})_{N_{CV}\times N_{CV}}$ is the matrix of the coefficients a_C^{ϕ} and a_F^{ϕ}; N_{CV} is the number of control volumes in the mesh; each line of the matrix presents the coefficient a_C^{ϕ} at the diagonal element and, at the other line elements, the coefficients a_F^{ϕ}; $\boldsymbol{\phi} \in \mathbb{R}^{N_{CV}\times 1}$ is the solution vector and $\mathbf{b}^{\phi} \in \mathbb{R}^{N_{CV}\times 1}$ is the source coefficients vector.

Appropriate boundary conditions (BC) must be discretized too. Each type of BC generally has its own discretization procedure; Moukalled et al. [44] presents the implementation of the most common BC's for each term of the transport equation. In general, this implementation yields the update of coefficients Eq. (C.35).

Finally, it is important to note that Eq. (C.36) represents the spatial discretization of the transport equation for the whole domain Ω^{f} at *one time-step*. To march the solution in time, the system must be solved for each time-step, since the temporal scheme is implicit.

C.3 Pressure-Velocity Coupling

The generic transport equation, Eq. (C.1) is generally used to present the discretization process of the FVM. This presentation is convenient because the partial differential equations that describe the fluid flow phenomena – and also the motion of solids, with some small differences, like the absence of an advective term – can be written in the form of Eq. (C.1).

Note that we considered the flow velocity field $\boldsymbol{v}$ known. However, in general, $\boldsymbol{v}$ is calculated solving the continuity equation - conservation of mass - and the momentum equation that govern an isothermal fluid flow. Considering the flow of an incompressible Newtonian fluid with density ρ and dynamic viscosity μ^{f}, this system of PDE is called Navier-Stokes equations. In vector notation and for a *fixed* infinitesimal control volume, they are written, respectively:

$$\nabla \bullet (\rho \boldsymbol{v}) = 0 \tag{C.37}$$

$$\frac{\partial (\rho \boldsymbol{v})}{\partial t} + \nabla \bullet (\rho \boldsymbol{v}\boldsymbol{v}) = -\nabla p + \nabla \bullet \left[\mu^{\mathrm{f}} \left(\nabla \boldsymbol{v} + \nabla^T \boldsymbol{v}\right)\right] + \rho \boldsymbol{b} \tag{C.38}$$

where p is the hydrostatic pressure field, $\boldsymbol{b}$ are body forces acting on the flow, per mass unit. Rearranging Eq. (C.38) yields:

$$\frac{\partial (\rho \boldsymbol{v})}{\partial t} + \nabla \bullet (\rho \boldsymbol{v}\boldsymbol{v}) = \nabla \bullet \left(\mu^{\mathrm{f}} \nabla \boldsymbol{v}\right) - \nabla p + \nabla \bullet \left(\mu^{\mathrm{f}} \nabla^T \boldsymbol{v}\right) + \rho \boldsymbol{b} \tag{C.39}$$

It is evident, from Eq. (C.39), the similarity between it and the transport equation if we put $\phi \equiv \boldsymbol{v}$ – intensive version of linear momentum –, and the last three terms on the right side of Eq. (C.39) are source terms for the transport of momentum in the flow. Equations (C.37) and (C.38)) form a system of PDE with the velocity $\boldsymbol{v}$ and pressure fields p as unknowns. Equation (C.38) is actually a vector equation, i.e. can be decomposed into 3 scalar equations for each velocity component and the continuity equation can be seen as a restriction imposed to the velocity field because, in the incompressible case, the density ρ is not an unknown. However, if the momentum equations give the velocity components, then the continuity equation should provide a way to find the pressure field. Nevertheless, this is not the case because p is implicit in Eq. (C.37). The effect of pressure in mass conservation is lost towards the incompressible limit, because the fluid density is constant

on that limit; on the other hand, for the compressible case, density and pressure are related through an equation of state and the continuity equation provides a manner to find the density field. Therefore, the strong, but implicit, coupling between velocity and pressure for incompressible flows produces difficulties in solving system of Eqs. (C.37) and (C.38). Besides, note that the non-linearity in Eq. (C.38), due to the advective term, is not the hardest problem, since the FVM solves the discretized equation using an iterative process, updating the system coefficients using available values.

We present below two segregated algorithms to solve the system formed by Eqs. (C.37) and (C.38): the so-called Semi-Implicit Method for Pressure Linked Equations (SIMPLE) presented by Patankar [65] and PISO proposed by Issa [76].

The SIMPLE algorithm starts with the solution of the discretized momentum equations for each velocity component in a Cartesian coordinates system, i.e. $\boldsymbol{v} = v_x\boldsymbol{i} + v_y\boldsymbol{j} + v_z\boldsymbol{k}$, where $\boldsymbol{i}$, $\boldsymbol{j}$ and $\boldsymbol{k}$ are the vectors of the canonical basis. Applying the Finite Volume discretization to the momentum equation, follows, for the current time-step:

$$\begin{aligned} a_C^{v_x}(v_x)_C + \sum_{F\sim NB(C)} a_F^{v_x}(v_x)_F &= \hat{b}_C^{v_x} \\ a_C^{v_y}(v_y)_C + \sum_{F\sim NB(C)} a_F^{v_y}(v_y)_F &= \hat{b}_C^{v_y} \\ a_C^{v_z}(v_z)_C + \sum_{F\sim NB(C)} a_F^{v_z}(v_z)_F &= \hat{b}_C^{v_z} \end{aligned} \tag{C.40}$$

We will represent these three equations in the compact matrix form:

$$\begin{bmatrix} a_C^{v_x} & 0 & 0 \\ 0 & a_C^{v_y} & 0 \\ 0 & 0 & a_C^{v_z} \end{bmatrix} \begin{Bmatrix} (v_x)_C \\ (v_y)_C \\ (v_z)_C \end{Bmatrix} + \sum_{F\sim NB(C)} \begin{bmatrix} a_C^{v_x} & 0 & 0 \\ 0 & a_C^{v_y} & 0 \\ 0 & 0 & a_C^{v_z} \end{bmatrix} \begin{Bmatrix} (v_x)_F \\ (v_y)_F \\ (v_z)_F \end{Bmatrix} = \begin{Bmatrix} \hat{b}_C^{v_x} \\ \hat{b}_C^{v_y} \\ \hat{b}_C^{v_z} \end{Bmatrix} \Rightarrow \tag{C.41}$$

$$\Rightarrow a_C^{\boldsymbol{v}}\boldsymbol{v}_C + \sum_{F\sim NB(C)} a_F^{\boldsymbol{v}}\boldsymbol{v}_F = \hat{\boldsymbol{b}}_C^{\boldsymbol{v}} \tag{C.42}$$

where the coefficients, according to the discretization procedures presented before, are given by:

$$\begin{aligned} a_C^{\boldsymbol{v}} &= \frac{3\rho_C^{\mathrm{n}}V_C}{2\Delta t} + \sum_{f\sim nb(C)} \left(w_C\dot{m}_f + \mu_f^{\mathrm{f}}\mathrm{gDiff}_f\right) \\ a_F^{\boldsymbol{v}} &= w_F\dot{m}_f - \mu_f^{\mathrm{f}}\mathrm{gDiff}_f \end{aligned} \tag{C.43}$$

$$\hat{\boldsymbol{b}}_C^{\boldsymbol{v}} = \rho_C(\boldsymbol{b})_C V_C + \underbrace{\sum_{f\sim nb(C)} \mu_f^{\mathrm{f}} \nabla \boldsymbol{v}_f \bullet \boldsymbol{T}_f}_{\text{Cross diffusion contribution}} + \left(\frac{4\rho_C V_C}{2\Delta t}\right)\boldsymbol{v}_C^{\mathrm{n}-1} - \left(\frac{\rho_C V_C}{2\Delta t}\right)\boldsymbol{v}_C^{\mathrm{n}-2}$$
$$\underbrace{-(\nabla p_C)V_C}_{\substack{\text{Pressure gradient}\\ \text{evaluated explicitly}}} + \underbrace{\sum_{f\sim nb(C)} \mu_f^{\mathrm{f}} \nabla^T \boldsymbol{v}_f \bullet \boldsymbol{s}_f}_{\substack{\text{Cross derivative term}\\ \text{(evaluated explicitly)}}} \tag{C.44}$$

where $\mathrm{gDiff}_f = \frac{E_f}{\boldsymbol{d}_{CF}}$ is the geometric diffusivity if the over-relaxed approach is used in the surface normal gradient discretization; $\dot{m}_f = \rho_f \boldsymbol{v}_f \bullet \boldsymbol{s}_f$ is the mass flow rate through cell faces – evaluated using values from the last iteration; this eliminates the non-linear problem of solving Eq. (C.38). In the third equation of Eq. (C.43), the main differences with the general transport equation are the pressure gradient and the cross derivatives – originated from the viscous force term of the momentum equation; these are accounted as source terms and evaluated explicitly, i.e. using values of the last *iteration*. It is important to keep in mind that Eq. (C.42) does not imply that the momentum equations are solved together as an assembled large system, on the contrary, the segregated SIMPLE and PISO algorithm assumes that they are solved separately.

The mass flow rate through each cell face, $\dot{m}_f = \rho_f \boldsymbol{v}_f \bullet \boldsymbol{s}_f$, deserves some comments. The collocated FVM assumes that all the variables are stored at cell centroids. However, to evaluate $\dot{m}_f$, we need the velocity at the *face centroid*. We have already shown that this is usually performed with a linear interpolation from centroid values to face centroid. However, due to the coupling between velocity and pressure, a linear interpolation from $\boldsymbol{v}_C$ and $\boldsymbol{v}_F$ to $\boldsymbol{v}_f$ can decouple the two fields, leading to the well-known "checkerboard problem" of the collocated arrangement. One solution is to use the Rhie-Chow interpolation [78] for the velocity field. This interpolation accounts for the influence of pressure in the velocity field after constructing a pseudo-momentum equation for the velocity at cell faces.

Before presenting the SIMPLE algorithm, we will rearrange Eq. (C.42) in a more useful form to the following procedures:

$$\boldsymbol{v}_C + \sum_{F\sim NB(C)} \frac{a_F^{\boldsymbol{v}}}{a_C^{\boldsymbol{v}}} \boldsymbol{v}_F = \frac{\boldsymbol{b}_C^{\boldsymbol{v}}}{a_C^{\boldsymbol{v}}} - (\nabla p_C)\frac{V_C}{a_C^{\boldsymbol{v}}} \Rightarrow \tag{C.45}$$

$$\Rightarrow \boldsymbol{v}_C + \mathbf{H}_C[\boldsymbol{v}] = \mathbf{B}_C^{\boldsymbol{v}} - \mathbf{D}_C^{\boldsymbol{v}}(\nabla p_C) \tag{C.46}$$

where $\hat{\boldsymbol{b}}_C^{\boldsymbol{v}} = \boldsymbol{b}_C^{\boldsymbol{v}} - (\nabla p_C)\, V_C$ and the vector operators are:

$$\mathbf{H}_C\left[\boldsymbol{v}\right] \equiv \sum_{F \sim NB(C)} \frac{a_F^{\boldsymbol{v}}}{a_C^{\boldsymbol{v}}} \boldsymbol{v}_F \equiv \sum_{F \sim NB(C)} \begin{bmatrix} a_F^{v_x}/a_C^{v_x} & 0 & 0 \\ 0 & a_F^{v_y}/a_C^{v_y} & 0 \\ 0 & 0 & a_F^{v_z}/a_C^{v_z} \end{bmatrix} \begin{Bmatrix} (v_x)_F \\ (v_y)_F \\ (v_z)_F \end{Bmatrix} \tag{C.47}$$

$$\mathbf{B}_C^{\boldsymbol{v}} \equiv \frac{\boldsymbol{b}_C^{\boldsymbol{v}}}{a_C^{\boldsymbol{v}}} \equiv \begin{Bmatrix} \boldsymbol{b}_C^{v_x}/a_C^{v_x} \\ \boldsymbol{b}_C^{v_y}/a_C^{v_y} \\ \boldsymbol{b}_C^{v_z}/a_C^{v_z} \end{Bmatrix} \tag{C.48}$$

$$\mathbf{D}_C^{\boldsymbol{v}} \equiv \frac{V_C}{a_C^{\boldsymbol{v}}} \equiv \begin{bmatrix} V_C/a_C^{v_x} & 0 & 0 \\ 0 & V_C/a_C^{v_y} & 0 \\ 0 & 0 & V_C/a_C^{v_z} \end{bmatrix} \tag{C.49}$$

The $\mathbf{H}_C\left[\boldsymbol{v}\right]$ operator is related to the influence of the advective and diffusive transport of momentum for the value at C; $\mathbf{B}_C^{\boldsymbol{v}}$ gives the influence of all the source terms except pressure; and $\mathbf{D}_C^{\boldsymbol{v}}$ is a diffusivity relating the influence of pressure in the velocity field.

Finally, the SIMPLE algorithm has the following steps:

1. If $t = 0$ (n = 0), define initial values for the velocity and pressure fields, $\boldsymbol{v}^0$ and p^0, respectively, and calculates the mass flow rate through cell faces, $\dot{m}_f^{\mathrm{n}}$. If $t > 0$, use the data from the last time-step;

2. Using the available pressure field, p^{n}, solve the momentum equations discretized for a *predicted* velocity field, $\boldsymbol{v}_C^*$, which does not satisfies the continuity equation, because the pressure field is probably not correct. Therefore, $\boldsymbol{v}_C^*$ satisfies the following equation:

$$\boldsymbol{v}_C^* + \mathbf{H}_C\left[\boldsymbol{v}^*\right] = \mathbf{B}_C^{\boldsymbol{v}} - \mathbf{D}_C^{\boldsymbol{v}}(\nabla p_C^{\mathrm{n}}) \tag{C.50}$$

3. Calculate the mass flow rate in each cell face, $\dot{m}_f^*$. Therefore, is necessary to interpolate $\boldsymbol{v}_C^*$ to each cell face centroid using the Rhie-Chow interpolation, given by [44]:

$$\boldsymbol{v}_f^* = \overline{\boldsymbol{v}_f^*} - \overline{\mathbf{D}_f^{\boldsymbol{v}}} \left(\nabla p_f^{\mathrm{n}} - \overline{\nabla p_f^{\mathrm{n}}}\right) \tag{C.51}$$

where the over bar indicates a linear interpolation, i.e. $\overline{\boldsymbol{v}_f^*} = g_C \boldsymbol{v}_C^* + g_F \boldsymbol{v}_F^*$; accordingly, $\overline{\mathbf{D}_f^{\boldsymbol{v}}} = g_C \mathbf{D}_C^{\boldsymbol{v}} + g_F \mathbf{D}_F^{\boldsymbol{v}}$; the pressure gradient at the face centroid must be corrected,

and is given by:

$$\nabla p_f^{\mathrm{n}} = \overline{\nabla p_f^{\mathrm{n}}} + \underbrace{\left[\frac{p_F^{\mathrm{n}} - p_C^{\mathrm{n}}}{\|\boldsymbol{d}_{CF}\|} - \left(\overline{\nabla p_f^{\mathrm{n}}} \bullet \boldsymbol{e}_{CF}\right)\right]\boldsymbol{e}_{CF}}_{\text{Correction term}} \tag{C.52}$$

where $\boldsymbol{e}_{CF} = \frac{\boldsymbol{d}_{CF}}{\|\boldsymbol{d}_{CF}\|}$ is the unit vector in the direction of the line joining C and F and $\overline{\nabla p_f^{\mathrm{n}}} = g_C \nabla p_C^{\mathrm{n}} + g_F \nabla p_F^{\mathrm{n}}$. Equation (C.51) is derived in Moukalled et al. [44] from a momentum equation like Eq. (C.46) written for the velocity at face f.

With the correct interpolated velocity, Eq. (C.51), a "momentum satisfying" mass flow rate at the cell faces can be calculated:

$$\dot{m}_f^* = \rho_f \boldsymbol{v}_f^* \bullet \boldsymbol{s}_f = \rho_f \overline{\boldsymbol{v}_f^*} \bullet \boldsymbol{s}_f - \rho_f \overline{\mathbf{D}_f^{\boldsymbol{v}}} \left(\nabla p_f^{\mathrm{n}} - \overline{\nabla p_f^{\mathrm{n}}}\right) \bullet \boldsymbol{s}_f \tag{C.53}$$

4. In this step, a "continuity satisfying" velocity and pressure fields will be calculated. This is achieved through a pressure correction field that can be found from the continuity equation, Eq. (C.37), which if discretized, using the FVM, can be written in terms of the mass flow rate over a control volume:

$$\nabla \bullet (\rho \boldsymbol{v}) = 0 \Rightarrow \sum_{f \sim nb(C)} \dot{m}_f = 0 \tag{C.54}$$

However, $\dot{m}_f$ is the correct mass flow rate, thus we can write:

$$\dot{m}_f = \dot{m}_f^* + \dot{m}_f' \tag{C.55}$$

where $\dot{m}_f'$ is the correction mass flow rate; in a similar way, the correct velocity and pressure at cell centroids are:

$$\begin{aligned} \boldsymbol{v}_C &= \boldsymbol{v}_C^* + \boldsymbol{v}_C' \\ p_C &= p_C^{\mathrm{n}} + p_C' \end{aligned} \tag{C.56}$$

Combining Eq. (C.54) with Eq. (C.55) follows:

$$\sum_{f \sim nb(C)} \dot{m}_f = 0 \;\Rightarrow\; \sum_{f \sim nb(C)} \dot{m}_f' = -\sum_{f \sim nb(C)} \dot{m}_f * \tag{C.57}$$

The correction mass flow rate, $\dot{m}'_f$, is calculated using the correction for the velocity field at the face centroid, $\boldsymbol{v}'_f$, which is interpolated using cell centroid corrections, $\boldsymbol{v}'_C$ and $\boldsymbol{v}'_F$, with Eq. (C.51). Then, substituting $\dot{m}'_f$ in Eq. (C.57) follows:

$$\sum_{f\sim nb(C)}\left[-\rho_f\overline{\mathbf{D}^{\boldsymbol{v}}_f}\left(\nabla p'_f\right)\bullet\boldsymbol{s}_f\right]=-\sum_{f\sim nb(C)}\dot{m}^*_f+\underline{\sum_{f\sim nb(C)}\left[-\rho_f\overline{\mathbf{H}_f}[\boldsymbol{v}']\bullet\boldsymbol{s}_f\right]} \tag{C.58}$$

an equation for the pressure correction where is implicit mass conservation. In the SIMPLE algorithm, the underlined term of Eq. (C.58) is neglected – this assumption is actually what differentiate each algorithm of the SIMPLE family. Thus, the equation has only the pressure correction as unknown. After this simplification and discretization of the surface normal pressure gradient using one the approaches presented in Appendix C.1, Eq. (C.58) can be written as:

$$a^{p'}_C p'_C+\sum_{F\sim NB(C)}a^{p'}_F p'_F=b^{p'}_C \tag{C.59}$$

an algebraic equation for the pressure correction at cell centroids. Equation (C.59) can be assembled, for the whole computational mesh, in a linear system of algebraic equations. Solving this system yields the pressure correction field, which is used to correct the momentum satisfying velocity field using Eq. (C.56) with:

$$\boldsymbol{v}'_C=-\mathbf{D}^{\boldsymbol{v}}_C\left(\nabla p'_C\right) \tag{C.60}$$

Eq. (C.60) may be different because is related to the neglected terms in Eq. (C.58). The mass flow rate and pressure are also corrected:

$$\begin{aligned}\dot{m}^{**}_f&=\dot{m}^*_f+\dot{m}'_f\\ p^*_C&=p^{\mathrm{n}}_C+\lambda^p p'_C\end{aligned} \tag{C.61}$$

where $\dot{m}'_f=\rho_f\boldsymbol{v}'_f\bullet\boldsymbol{s}_f$ and $0\leq\lambda^p\leq 1$ is the pressure relaxation factor. Relaxation can also be used for the momentum equations, and is usually recommended to accelerate the convergence rate of the SIMPLE algorithm.

Figure C.4 shows the flowchart for the SIMPLE loop presented above. The loop is stopped when the residuals of the momentum and continuity equations are smaller than

the specified tolerance, ϵ. Once the velocity and pressure field are converged to the solution, other transport equations, particular to the problem studied, can be solved.

The SIMPLE algorithm has several variants, which differs from the original one depending on how the underlined term in Eq. (C.58) is treated. Another important pressure-velocity coupling algorithm is the Pressure Implicit with Splitting Operators (PISO), which incorporates a SIMPLE loop with subsequents corrections steps where only the pressure correction equation is solved implicitly. The correction steps are explained below.

Usually, the literature presents the PISO algorithm in terms of the pressure correction equation [44, 73], like SIMPLE . Therefore this approach will be presented here. However, it can also be presented in terms of a *pressure equation* (and it was in the original proposal by Issa [76]) as shown in the main text because it is the one implemented in foam-extend. However, both approaches are equivalent and are part of the so-called *projection methods* [77].

Finally, the correction steps of the PISO algorithm are:

1. Once the corrected values for velocity, mass flow rate and pressure are calculated at the last part of a SIMPLE loop, i.e. $\boldsymbol{v}_C^*$*, $\dot{m}_f^{**}$ and p_C^*, respectively, they are used to update the coefficients of the momentum equations, which then are solved *explicitly* to obtain updated values of the velocity components. We will indicate intermediate variables in each correction step with a tilde. Thus, the updated velocity is given by:

$$\tilde{\boldsymbol{v}}_C^r = -\mathbf{H}_C\left[\boldsymbol{v}^{**}\right] + \mathbf{B}_C^{\boldsymbol{v}} - \mathbf{D}_C^{\boldsymbol{v}}\left(\nabla p_C^*\right) \tag{C.62}$$

   where the upper index r represents the correction step. Remember that in Eq. (C.62) the operators $\mathbf{H}_C$, $\mathbf{B}_C^{\boldsymbol{v}}$ and $\mathbf{D}_C^{\boldsymbol{v}}$ are calculated with the updated coefficients. The following steps are exactly the same as in the SIMPLE loop.

2. Velocity $\tilde{\boldsymbol{v}}_C^r$ is interpolated using the Rhie-Chow formula and the new mass flow rate is calculated at cell faces:

$$\tilde{\dot{m}}_f^r = \rho_f \tilde{\boldsymbol{v}}_f^r \bullet \boldsymbol{s}_f \tag{C.63}$$

3. The continuity equation is discretized to obtain a system of equations for a new

pressure correction, $p_C^{r'}$:

$$a_C^{p'} p_C^{r'} + \sum_{F \sim NB(C)} a_F^{p'} p_F^{r'} = b_C^{p'} \tag{C.64}$$

Solving last system yields a new pressure correction field, which is used to correct the velocity field using:

$$\boldsymbol{v}_C^{r'} = -\mathbf{D}_C^{\boldsymbol{v}} \left(\nabla p_C^{r'} \right) \tag{C.65}$$

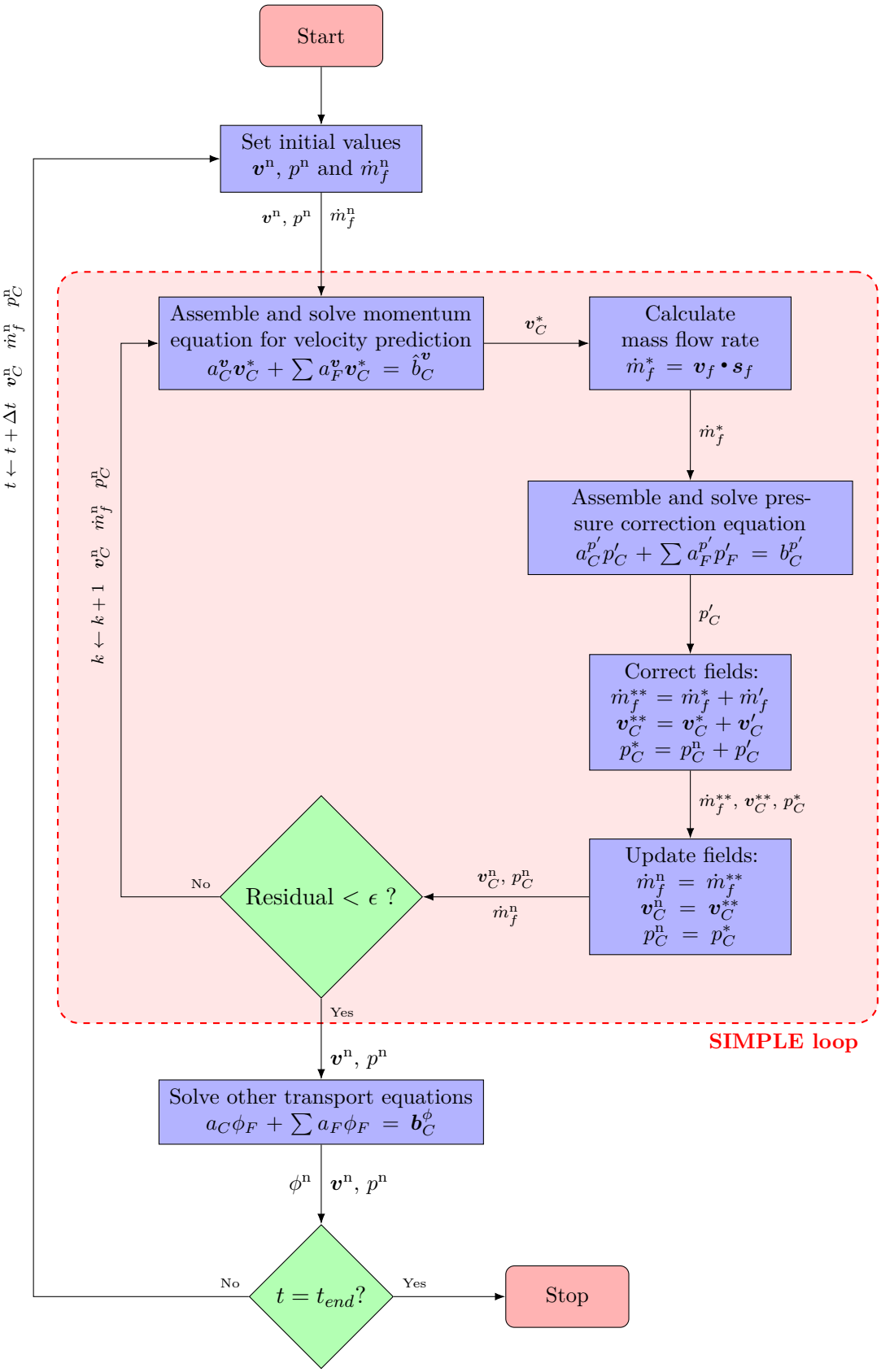
4. With the correction velocity, the mass flow rate correction can also be computed, and finally the fields are updated at the end of a correction step, r:

$$\begin{aligned} \boldsymbol{v}_C^{r+1} &= \tilde{\boldsymbol{v}}_C^{r} + \boldsymbol{v}_C^{r'} \\ \dot{m}_f^{r+1} &= \tilde{\dot{m}}_f^{r} + \dot{m}_f^{r'} \\ p_C^{r+1} &= p_C^{r} + p_C^{r'} \end{aligned} \tag{C.66}$$

where $\dot{m}_f^{r'} = \rho_f \boldsymbol{v}_f^{r'} \bullet \boldsymbol{s}_f$.

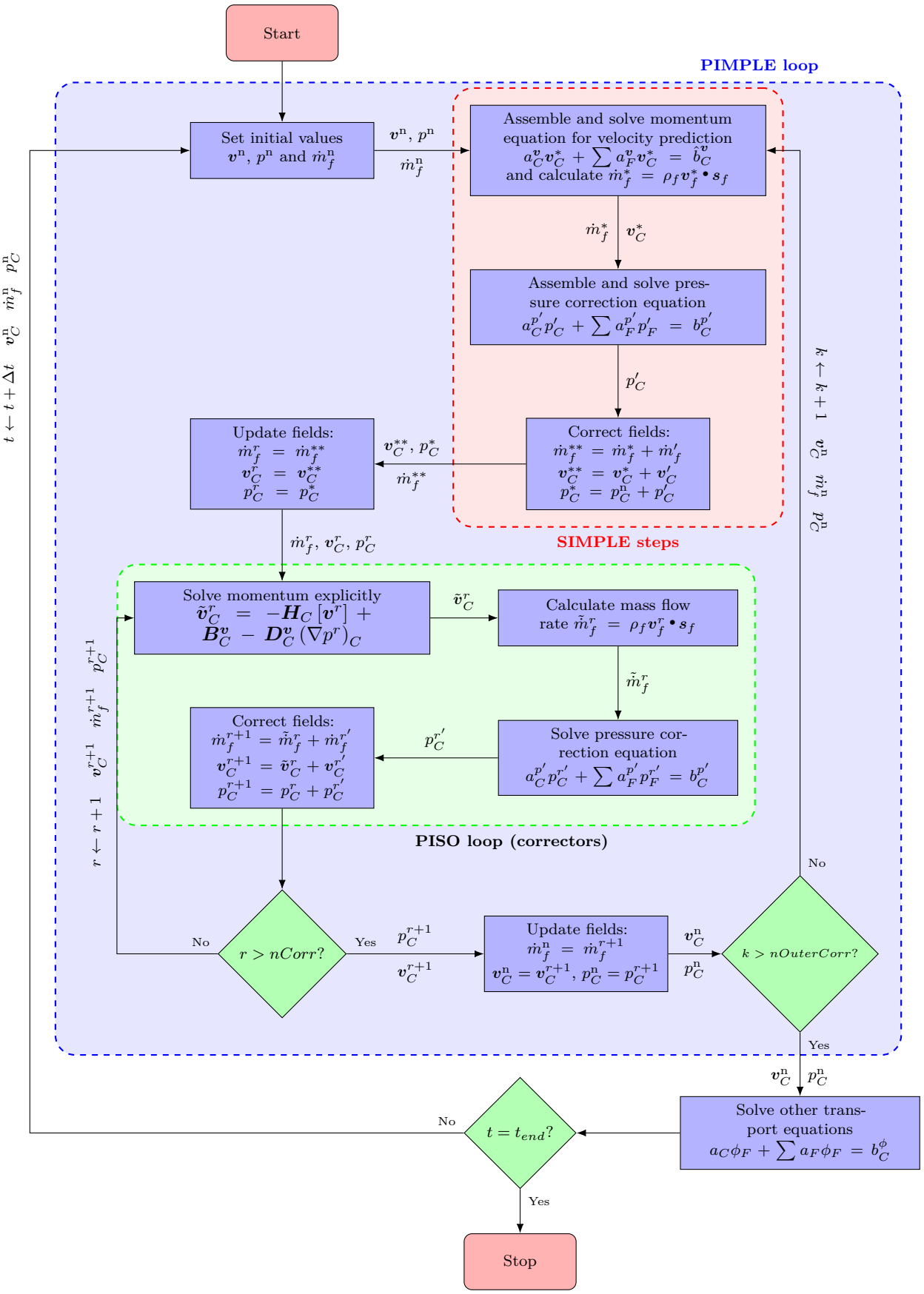
In the original PISO algorithm, Issa [76] shows that solving only once the momentum equation implicitly and iterating twice over the pressure equation are enough to yield an accurate solution. However, the steps above can be repeated as many times as desired, the loop stopping when the iteration number reaches a specified number of correctors, $nCorr$. When an *outer* loop is performed over the SIMPLE and correction steps, the algorithm has been called *PIMPLE*, because it is a combination of SIMPLE and PISO algorithms. Figure C.5 shows the flowchart of the complete algorithm, indicating the SIMPLE steps as well as the correction loop where the momentum equations are solved explicitly.

Figure C.4 – SIMPLE algorithm; index n represents the current time-step, t; the measurements of the *Residual* depends on the software, but usually includes residuals of pressure, velocity and mass balance for convergence.



Source: prepared by the author.

Figure C.5 – PIMPLE algorithm: *nOuterCorr* is the number of outer corrector steps, i.e. including SIMPLE and PISO loops; *nCorr* is the number of correctors of the PISO loop only; index n represents the current time-step, t.



Source: prepared by the author.

D Residuals in foam-extend

In every iterative solution process, it is important to keep tracking the main variables that are being solved. To this end, many techniques have been proposed [44, 73, 77]. In most common available CFD softwares, the iterative process of solving the linear system of equations originated from the discretization process is stopped based on a predefined criterion usually depending on the *residual* value for that system in an iteration. For a linear system of the form:

$$\mathbf{A}\mathbf{x} = \mathbf{b} \tag{D.1}$$

where $\mathbf{A}$ is a matrix that belongs to $\mathbb{R}^{N\times N}$, $\boldsymbol{x} \in \mathbb{R}^N$ is the solution vector and $\boldsymbol{b} \in \mathbb{R}^N$ when is solved using an iterative method, its residual, in iteration m, is defined as:

$$\mathbf{r}^m = \mathbf{b} - \mathbf{A}\mathbf{x}^m \tag{D.2}$$

In most solvers a normalized version of $\mathbf{r}^m$ is used. Besides, since $\mathbf{r}^m$ depends on the value of $\mathbf{x}$ in iteration m, the normalized residual is, in general, scaled with respect to a reference value.

In foam-extend, to verify convergence of the linear solvers, the software uses a L1-norm to normalize $\mathbf{r}^m$ and a scaling factor computed by the following procedure: set a reference value as the average of $\mathbf{x}^m$, as follows:

$$x_{ref} \equiv \overline{\mathbf{x}} = \frac{\sum_{i=1}^{N} x_i^m}{N} \tag{D.3}$$

where x_i^m is the component i of $\mathbf{x}^m$. Then, define the following vectors:

$$\mathbf{w}_\mathbf{A} = \mathbf{A}\mathbf{x}^m \tag{D.4}$$

$$\mathbf{p}_\mathbf{A} = \mathbf{A}\mathbf{x}_{ref} \tag{D.5}$$

where $\boldsymbol{x}_{ref} \in \mathbb{R}^N$ with components equal to x_{ref}. Finally, the scale factor is calculated as:

$$F_s = \|(\mathbf{w}_\mathbf{A} - \mathbf{p}_\mathbf{A}) + (\mathbf{b} - \mathbf{p}_\mathbf{A})\|_1 = \sum_{i=1}^{N} [|(w_\mathbf{A})_i - (p_\mathbf{A})_i| + |b_i - (p_\mathbf{A})_i|] \tag{D.6}$$

Using the scale factor of Eq. (D.6), the scaled normalized residual, R_s^m, is computed using a L1-norm:

$$R_s^m = \frac{\|\mathbf{r}\|_1}{F_s} = \frac{\sum_{i=1}^{N} |b_i - A_{ij}x_j|}{F_s} \tag{D.7}$$

Note that while the solution evolves in the iterative process, the numerator in Eq. (D.7) goes to zero, whereas the denominator reduces to a constant value. The form of the scaled normalized residual given by the last equation is used for all the linear solvers chosen to solve the systems of equations for velocity and pressure field, mesh motion equation and the solid equation.

On the other hand, the coupling iterations – or quasi-Newton iterations, in the case of the IQN-ILS method – uses a convergence criterion based on a L2-norm of the FSI residual vector, $\mathbf{r}$, which, for a coupling iteration k, is defined as in Eq. (61):

$$\mathbf{r}_k = \boldsymbol{x}|_{\Gamma^{\text{fs}}_{solid}} - \boldsymbol{x}|_{\Gamma^{\text{fs}}_{fluid}} \tag{D.8}$$

Therefore, the scaled normalized residual for the coupling iterations is given by:

$$\left(R_s^{\text{fs}}\right)_k = \frac{\|\mathbf{r}_k\|_2}{F_s^{\text{fs}}} = \frac{\left[\sum_{i=1}^{N^{\text{fs}}} (r_k)_i^2\right]^{1/2}}{F_s^{\text{fs}}} \tag{D.9}$$

where F_s^{fs} is the maximum value, for all k coupling iterations, of the L2-norm of total the displacement vector of the FSI interface, $\boldsymbol{u}_{tot,\Gamma^{\text{fs}}}$, i.e.:

$$F_s^{\text{fs}} = \max_k \|\boldsymbol{u}_{tot,\Gamma^{\text{fs}}}\|_2 \tag{D.10}$$